

# Radiative and Pionic Decays of Heavy-Light Mesons Using HISQ Quarks

by

**Maysam Emadi**

B.Sc., Sharif University of Technology, 2007

Thesis Submitted in Partial Fulfillment of the  
Requirements for the Degree of  
Doctor of Philosophy

in the  
Department of Physics  
Faculty of Science

© Maysam Emadi 2015  
SIMON FRASER UNIVERSITY  
Fall 2015

All rights reserved.

However, in accordance with the *Copyright Act of Canada*, this work may be reproduced without authorization under the conditions for “Fair Dealing.” Therefore, limited reproduction of this work for the purposes of private study, research, education, satire, parody, criticism, review and news reporting is likely to be in accordance with the law, particularly if cited appropriately.

# Approval

**Name:** Maysam Emadi  
**Degree:** Doctor of Philosophy (Physics)  
**Title:** *Radiative and Pionic Decays of Heavy-Light Mesons Using HISQ Quarks*

**Examining Committee:** **Chair:** Dr. B. Stelzer  
Associate Professor

**Dr. H. D. Trottier**  
Senior Supervisor  
Professor

---

**Dr. R. M. Woloshyn**  
Co-Supervisor  
Adjunct Professor

---

**Dr. I. Herbut**  
Supervisor  
Professor

---

**Dr. B. K. Jennings**  
Supervisor  
Adjunct Professor

---

**Dr. L. Pogosian**  
Internal Examiner  
Associate Professor

---

**Dr. A. X. El-Khadra**  
External Examiner  
Professor  
Department of Physics  
University of Illinois

---

**Date Defended:** 11 December 2015

# Abstract

In this thesis we use the highly improved staggered quark (HISQ) formalism to study the radiative and pionic transitions of charmed mesons within the framework of lattice QCD. The HISQ action is one of the most accurate formulations of charm quarks and is a result of a perturbative Symanzik improvement program to reduce lattice discretization errors. Decay widths are calculated in numerical simulations on an ensemble of gauge field configurations with  $N_f = 2 + 1$  asqtad sea quarks generated by the MILC collaboration. In addition we study  $H_s^*$  and charmonium radiative decays as well as meson electric form factors.

Experimental measurements of the decay ratios of vector charmed  $D^{*\pm 0}$  and charmed strange  $D_s^{*\pm}$  mesons, show a few curious features that are of great phenomenological interest in the study of low energy hadronic physics. Unlike most mesons, the strong hadronic decay modes of  $D^{*0}$  and  $D_s^{*\pm}$ , are not dominant. However, while the neutral  $D$  has a radiative mode that is competitive with its pionic mode, the charged  $D$  meson's radiative decay is highly suppressed relative to that of the neutral. This suppression provides a detailed probe of strong interactions and is apparently due to an interesting near cancellation that takes place between the photon's coupling to the charm quark and to the down antiquark.

The results are in agreement with all of the available experimental data, and in particular, we show that the HISQ action successfully accounts for the near cancellation of the charmed  $D^{*\pm}$  radiative decay. The relative suppression is demonstrated in our result for the ratio of the radiative form factors of  $D$  mesons  $V^\pm(0)/V^0(0) = 0.126(36)$  computed at heavier than physical  $u/d$  quark masses. The quoted errors are purely statistical. Evidence from other lattice studies indicate small systematic errors in continuum and sea-quark chiral extrapolations. Valence quark chiral extrapolation increases our errors by about 50%. A rough extrapolation suggests an agreement with the measured radiative width within  $2\sigma$ .

**Keywords:** Lattice QCD; HISQ; radiative decay; pionic decay

# Dedication

To Maman and Baba.

# Acknowledgements

Many people have helped me complete this thesis. I am eternally grateful to Howard Trottier for teaching me so much more than physics and to his wonderful family Loula and Alexander for treating me like a friend and for being always welcoming and generous. No one can wish for a better supervisor. I would like to thank Richard Woloshyn whose insight has been vital to this project in every step. Many thanks to Igor Herbut and Byron Jennings who supervised this project.

I have been very fortunate to have the privilege of calling Mehrdad Rastan a friend. He has been an endless source of inspiration and wisdom. Special thanks to Michael Grant-Orser for his kind and generous spirit. Many thanks to Greg Millar for numerous long discussions about life, the universe and everything. Thanks to Paul Sikora for helping me achieve progress, Jamie Horton for coffee runs, hockey games and conversations among other things, Colleen Ng for the snacks, and Arman Akbarian for being a friend. Many thanks to Avesta Rastan for her amazing artwork. I have learned plenty from many friends whom I have been lucky to know along the way and would like to thank. I would also like to especially thank Mikael Akerfeldt of Opeth for enhancing every moment of this journey.

Finally, thanks to my brother Ali and undying gratitude to mom and dad whose many sacrifices made this journey possible and whom I will never be able to thank enough.

# Table of Contents

Approval	ii
Abstract	iii
Dedication	iv
Acknowledgements	v
Table of Contents	vi
List of Tables	ix
List of Figures	x
<b>1 Introduction</b>	<b>1</b>
1.1 Invitation . . . . .	1
1.2 The Physics of Improvement . . . . .	5
1.2.1 Lattice Errors . . . . .	6
1.3 Thesis Structure . . . . .	9
<b>2 Lattice QCD</b>	<b>12</b>
2.1 Path Integrals on the Lattice . . . . .	12
2.2 Gluons on the Lattice . . . . .	15
2.2.1 The Link Variables . . . . .	15
2.2.2 Symanzik Improvements . . . . .	18
2.3 Quarks on the Lattice . . . . .	20
2.4 Simulations on the Lattice . . . . .	21
<b>3 Fermions on the Lattice</b>	<b>23</b>
3.1 The “Naive” Fermions . . . . .	23
3.1.1 The Doubling Problem . . . . .	24
3.1.2 Wilson Fermions . . . . .	31
3.1.3 Staggered Fermions . . . . .	35
3.2 Heavy Staggered Quarks; The Improvement Program . . . . .	38

3.2.1	Tree Level Symanzik Improvements . . . . .	40
3.2.2	Taste Violation; Smearing and the Asqtad Action . . . . .	41
3.2.3	Repairing Lorentz Invariance; The $\epsilon$ Coefficient . . . . .	44
3.2.4	The HISQ Action . . . . .	46
3.2.5	Loop Corrections and Higher Dimension Operators . . . . .	48
3.2.6	Diagnostics . . . . .	51
<b>4</b>	<b>The Taste Symmetry</b>	<b>52</b>
4.1	Naive and Staggered Bases . . . . .	52
4.1.1	Staggering the Action . . . . .	53
4.1.2	The Doubling Symmetry . . . . .	55
4.1.3	Meson Propagators . . . . .	58
4.2	Naive Currents; A Multitude of Mesons . . . . .	60
4.2.1	Taste Selection Rules . . . . .	61
4.3	Oscillating States . . . . .	64
4.4	Staggered Currents . . . . .	66
<b>5</b>	<b>Methodology</b>	<b>70</b>
5.1	Quark Propagators . . . . .	70
5.2	Calculating Physical Quantities . . . . .	72
5.2.1	Hadronic Masses and Two-Point Functions . . . . .	72
5.2.2	Hadronic Matrix Elements and Three-Point Functions . . . . .	76
5.2.3	The Conserved Current and the Ward Identity . . . . .	77
5.3	Lattice Calculation: Resources and Techniques . . . . .	80
5.3.1	MILC Configurations and FNAL Computing Clusters . . . . .	81
5.3.2	Random Wall Sources . . . . .	82
5.3.3	Sequential Source Technique . . . . .	88
5.4	Boundary Conditions . . . . .	89
5.4.1	Twisted Boundary Conditions . . . . .	90
5.5	Constrained Curve Fitting . . . . .	93
5.5.1	A Bayesian Approach . . . . .	93
5.5.2	Fitting Techniques . . . . .	103
5.5.3	Error Analysis: Partial Error Budgets, Bootstrap . . . . .	103
5.6	Putting It All Together; A Case Study . . . . .	105
5.6.1	Electric Form Factor and Charge Radius of Mesons . . . . .	105
<b>6</b>	<b>Radiative and Pionic Transitions</b>	<b>107</b>
6.1	Radiative Transition . . . . .	109
6.1.1	Hadronic Matrix Elements . . . . .	110
6.1.2	Lattice Correlation Functions . . . . .	112

6.2	Pionic Decay . . . . .	115
6.2.1	Theory and Definitions . . . . .	116
6.2.2	Lattice Correlation Functions . . . . .	124
6.3	Results . . . . .	125
6.3.1	Lattice Calculation . . . . .	125
6.3.2	Radiative Transition . . . . .	127
6.3.3	Pionic Decay . . . . .	137
6.4	Phenomenology . . . . .	142
6.5	Heavy-Strange . . . . .	144
<b>7</b>	<b>Conclusion</b>	<b>147</b>
7.1	Summary . . . . .	147
7.2	Further Studies . . . . .	148
	<b>Bibliography</b>	<b>151</b>
	<b>Appendix A Heavy Quarks on the Lattice</b>	<b>157</b>
A.1	NRQCD . . . . .	158
	<b>Appendix B Gamma Matrix Algebra</b>	<b>162</b>
	<b>Appendix C Fitting Details</b>	<b>164</b>
C.1	SVD . . . . .	164
C.2	Chained Fits . . . . .	165
C.3	Marginalized Fits . . . . .	166
	<b>Index</b>	<b>168</b>



# List of Tables

Table 3.1	Power counting rules for heavy-light and charmonium. . . . .	50
Table 5.1	Priors and fit results for hadronic masses from Bayesian fits to $\eta_c$ with various number of terms. . . . .	102
Table 6.1	Decay modes and branching ratios of $D^*$ and $D_s^*$ mesons [1]. . . . .	108
Table 6.2	Experimental values for meson masses and other relevant quantities [1].	108
Table 6.3	Details of the “coarse” ensemble of gauge field configurations. . . . .	126
Table 6.4	Quark masses and twisting angles used in the simulation. . . . .	126
Table 6.5	Three-point correlators computed in the simulation. . . . .	127
Table 6.6	Results for energies and masses of mesons. . . . .	129
Table 6.7	Fit results for radiative transition matrix elements and form factors. .	133
Table 6.8	Results for radiative decay widths of charged and neutral $D$ mesons. .	134
Table 6.9	Results for the radiative decay widths of $D_s^*$ and $J/\psi$ . . . . .	135
Table 6.10	Fit results for axial matrix elements and pionic form factors. . . . .	139
Table 6.11	Results for the pion coupling and pionic decay width of $D^{*+}$ . . . . .	142
Table 6.12	Results for the branching ratios of $D^{*+}$ and $D^{*0}$ mesons decay modes.	144

# List of Figures

Figure 1.1	Artwork courtesy of Avesta Rastan. . . . .	11
Figure 2.1	Low momentum quark-quark scattering amplitudes and quark self energies have loop contributions from gluons with high momenta $k > \pi/a$ that are excluded from the lattice theory. Corrections involve new interactions and renormalized masses and couplings. . . . .	13
Figure 3.1	Fermion doubling. . . . .	26
Figure 3.2	Contour integration of a naive propagator in the complex plane. . . . .	29
Figure 3.3	Tree level taste exchange interaction. . . . .	31
Figure 3.4	Energy spectra of lattice bosons and “naive” fermions. . . . .	34
Figure 3.5	Asqtad links. . . . .	42
Figure 3.6	One-loop taste exchange diagrams. . . . .	49
Figure 5.1	Random wall sources. . . . .	86
Figure 5.2	Energies from unconstrained fits to $\eta_c$ correlators plotted for various (a) $t_{\min}$ and (b) number of terms . . . . .	95
Figure 5.3	Bayesian fits to $\eta_c$ correlators with various number of terms . . . . .	100
Figure 6.1	3-point correlator corresponding to the radiative transition. . . . .	115
Figure 6.2	Coupling $g_{D^*D\pi}$ related to the form factors of the axial current. . . . .	117
Figure 6.3	Comparison of various fitting strategies. . . . .	128
Figure 6.4	Fit to 2-point correlator data. . . . .	130
Figure 6.5	Effective mass plot for pseudoscalar 2-point correlator. . . . .	131
Figure 6.6	Ratios of 3-point to 2-point correlators plotted as a function of current insertion time. . . . .	132
Figure 6.7	Radiative transition form factor $V^+(0)$ of the charged charm-light meson at various light quark masses. . . . .	136
Figure 6.8	Ratio of 3-point to 2-point axial correlators as a function of current insertion time. . . . .	138
Figure 6.9	Pion coupling of the charged $D^{*+}$ meson at various light quark masses plotted as a function of pion mass. . . . .	140
Figure 6.10	A quadratic extrapolation of the pion coupling to the chiral point. . . . .	141

Figure 6.11 Magnetic moment of heavy HISQ quarks inside heavy-strange mesons. 146

# Chapter 1

## Introduction

### 1.1 Invitation

Radiative transitions of hadrons have long been of great phenomenological interest to particle physicists. In particular, experimental measurements have shown that the radiative decay of the charged vector  $D$  meson into its pseudoscalar counterpart,  $D^{*\pm} \rightarrow D^\pm \gamma$ , is highly suppressed [1]. This strong suppression provides a very fine probe into the dynamics of quarks inside hadrons. Lattice QCD has been used to study radiative decays of mesons since the early years following its inception with increasing success [2, 3, 4, 5, 6, 7, 8]. In this thesis we would like to invite you to examine our study of this interesting physical process, among several other related quantities, within the framework of lattice QCD, using the highly improved staggered quarks (HISQ) formalism [9].

Hadrons are strongly interacting bound states made out of spin- $\frac{1}{2}$  particles called *quarks* that are bound together by massless gauge bosons called *gluons* which mediate the strong force. There are two broad classes of hadrons; (anti)-baryons typically consist of three (anti)-quarks, and *mesons* are made of a quark and an anti-quark. There are 6 quark *flavors*:

Flavor			Electric charge	Mass		
$\begin{pmatrix} u \\ d \end{pmatrix}$	$\begin{pmatrix} c \\ s \end{pmatrix}$	$\begin{pmatrix} t \\ b \end{pmatrix}$	$+\frac{2}{3}$	$2.3_{-0.5}^{+0.7}$ MeV	1.275(25) GeV	$\approx 160$ GeV
			$-\frac{1}{3}$	$4.8_{-0.3}^{+0.5}$ MeV	95(5) MeV	4.18(3) GeV

They are packaged in three *generations* with identical discrete quantum numbers but vastly different masses<sup>1</sup> spanning several orders of magnitude.

The *charmed* family of  $D$  mesons consist of a *charm* quark and either an *up* or a *down* to form the charged or the neutral members. The  $u/d$  quark flavors are frequently referred to

<sup>1</sup> These are “running” masses in the  $\overline{\text{MS}}$  scheme at a scale  $\mu \approx 2$  GeV taken from [1].

simply as the *light* quarks. The  $D_s$  mesons are the *strange* relatives of the charmed family where the light quark is replaced by a strange one.

Being made of a charm and a lighter-than-charm pair of quarks, these *heavy-light* mesons have integer spin. The spin-1 *vector* mesons, normally indicated by an asterisk, decay into their spin-0 *pseudoscalar* counterparts and other stuff [1]:

$D^{*+}$			$D^{*0}$			$D_s^{*+}$		
$m_{D^{*+}} = 2010.26(7)$ MeV			$m_{D^{*0}} = 2006.96(10)$ MeV			$m_{D_s^{*+}} = 2112.1(4)$ MeV		
$m_{D^+} = 1869.61(10)$ MeV			$m_{D^0} = 1864.84(7)$ MeV			$m_{D_s^+} = 1968.30(11)$ MeV		
Mode	Fraction	$p$ MeV	Mode	Fraction	$p$ MeV	Mode	Fraction	$p$ MeV
$D^+\gamma$	1.6(4)%	136	$D^0\gamma$	38.1(2.9)%	137	$D_s^+\gamma$	94.2(7)%	139
$D^0\pi^+$	67.7(5)%	39	$D^0\pi^0$	61.9(2.9)%	43	$D_s^+\pi^0$	5.8(7)%	48
$D^+\pi^0$	30.7(5)%	38						

There are at least three curious features in these decay processes. First, the hadronic decay modes of  $D^{*0}$  and  $D_s^{*+}$  are not as dominant as one would normally expect from strong decays. This can be explained by the kinematics of these processes. The small amount of phase space available to each of these vector mesons for it to transition into its pseudoscalar partner is just barely sufficient for a soft pion and kinematically forbids any other hadronic modes.

This can be seen in the above table where experimental values [1] for the masses of these mesons are listed. The available phase space for these decays are all in the range of 140–145 MeV, which with the neutral and charged pion masses of 135 MeV and 140 MeV respectively, leave very little room for pionic decays. As a result of the extremely tight phase space, the pionic modes are suppressed and therefore the radiative modes become competitive.

This leads to the second curious observation where the radiative decay ratio of the charged vector charmed meson  $D^{*+} = c\bar{d}$  is observed to be only 1.6(4)%, while the neutral  $D^{*0} = c\bar{u}$  decays via a photon 38.1(2.9)% of the time despite them having comparable phase spaces. This suppression is due to an accidental near cancellation between the photon's coupling to the magnetic moment of the constituent quarks. The decay rate can be written as

$$\Gamma(D^* \rightarrow D\gamma) \propto |eQ_l\mu_l - eQ_c\mu_c|^2 \quad (1.1)$$

where  $\mu_l$  and  $\mu_c$  represent the effective magnetic moments of the bound-state light and charm quarks respectively,  $Q_c = +2/3$  is the electric charge of the charm quark in units of  $e$ , and  $Q_l = (-2/3$  or  $+1/3)$  corresponds to a  $u$  or a  $d$  antiquark.

The relative minus sign in (1.1) is due to the spin flip that takes place in this kind of decay process generally referred to as a magnetic dipole (M1) transition. We conclude that the effective magnetic moment of the light quark happens to be about a factor of 2 larger than that of the charm. This combined with the electric charge coefficients  $\mathcal{Q}$  then conspire to nearly cancel out the two individual quarks' photocouplings in the charged  $D$  system by  $|\mu_d - 2\mu_c|/3$ , whereas in the neutral  $D$  they have constructive contributions due to the sum  $|2\mu_u + 2\mu_c|/3$ .

Which brings us to the third curious entry. An interesting inversion of this pattern occurs in the case of  $D_s^{*+}$ . That is, given the light mass of the  $s$  quark one would expect a similar suppression of the radiative mode due to the near cancellation between the photocouplings of the charm and that of the strange as given by (1.1). In fact, our calculation shows that the radiative decay of the  $D_s^{*+}$  is even more suppressed than that of the  $D^{*+}$ . However, despite its suppression, the radiative decay of  $D_s^{*+}$  still comes out to be dominant with a 94.2(7)% branching fraction.

This can be attributed to multiple factors that suppress its pionic decay  $D_s^{*+} \rightarrow D_s^+ \pi^0$  even more strongly. In addition to the kinematical suppression due to the small phase space of 143.8(4) MeV, this process is isospin violating [10]. To elucidate, given its quark flavor content, the pionic decay  $D_s^{*+} \rightarrow D_s^+ \pi^0$  necessarily involves the creation of the pion out of virtual gluons emitting off of the charm or the strange quark. The compound effect of this kind of *strong* suppression exacerbated by the kinematical suppression due to the small phase space, lead to the small pionic decay rate. This suggests a very narrow width for  $D_s^*$ .

The radiative decay widths of these mesons are directly calculated in this thesis through computing the radiative form factors of each constituent quark. The goal of this calculation is to demonstrate the near cancellation and show the smallness of the charged  $D$  radiative form factor relative to that of the neutral  $D$ . A corollary of this fine cancellation is that the error in the charged form factor is intrinsically larger than that of the neutral and is dominated by lattice statistical errors due to the signals almost canceling one another. Thus, the point is to resolve the fine cancellation that results in a very small yet statistically nonzero ratio of form factors  $V^+(0)/V^0(0)$ , as opposed to a precision calculation.

The  $D^{*+}$  meson's decay into a charged pion  $D^{*+} \rightarrow D^0 \pi^+$  is also directly calculated in this study using lattice QCD. However, it is much more difficult to directly calculate the decay into a neutral pion. Luckily, the approximate isospin symmetry predicts that the two pionic modes can be related to one another according to their isospin Clebsch-Gordon coefficients. Given their similar phase space factors one can write

$$\frac{\Gamma(D^{*+} \rightarrow D^0 \pi^+)}{\Gamma(D^{*+} \rightarrow D^+ \pi^0)} \approx \frac{|\langle \frac{1}{2}, \frac{1}{2} | \frac{1}{2}, -\frac{1}{2}; 1, 1 \rangle|^2}{|\langle \frac{1}{2}, \frac{1}{2} | \frac{1}{2}, \frac{1}{2}; 1, 0 \rangle|^2} = 2, \quad (1.2)$$

thereby enabling an estimate of the total width as well as the branching ratios. A direct comparison of the branching ratios of these modes indicates that invoking the isospin sym-

metry causes a systematic error of around 10%. This isospin trick cannot be extended to the  $D_s^*$  pionic decay due to the strange flavor content and hence this decay has not been studied in this work.

A recent 2013 experiment by the BaBar collaboration reported the full decay width of  $\Gamma(D^{*+}) = 83.4(1.8)$  keV [11]. This improved the accuracy of the previously available measurements by more than ten times, thereby enabling a more informative comparison of the total width. Given the somewhat large errors in the measured branching fraction of the radiative mode at 25%, our systematics are expected to be of comparable size to experimental uncertainties.

In addition, we also study charmonium ( $c\bar{c}$ ) radiative transitions, effective magnetic moments of hypothetical heavy quarks with masses larger than charm within heavy-strange systems  $H_s^*$ , as well as meson electric charge form factors and make a theoretical estimate for the “size” of charmonium and charm-light mesons.

## Quantum Chromodynamics

The Standard Model of particle physics is the standard theory that describes the interactions of elementary particles at short distances. It has enjoyed enormous success in the past several decades, which is well reflected in its name. It consists of two quantum field theories: the electroweak theory that describes the electromagnetic and the weak interactions of quarks and leptons, and quantum chromodynamics or QCD which is the theory of strong interactions of quarks.

Despite the great success of the Standard Model our knowledge of it is incomplete, in particular at the low energy hadronic physics sector described by QCD. The culprit can be attributed to a particular feature of QCD whereby the conventional *perturbative* methods that have been successfully applied to the electroweak theory become invalid in low energy QCD.

Quarks have an internal quantum degree of freedom associated with their strong interactions called *color* that can assume 3 different states. The strong interactions are symmetric under color transformations. This is codified in QCD through its local  $SU(3)$  color symmetry making it a non-Abelian gauge theory. Quarks can change colors by coupling to gluons which then transport the color differential to other quarks. Like every quantum field theory the coupling strength  $g$  changes as a function of the energy scale of the gluon. But unlike the Abelian case of QED, for instance, where the *running coupling constant* grows as the energy scale increases, a non-Abelian gauge theory allows for the reverse.

This is the case for QCD. At low energies, the strong fine structure constant  $\alpha_s(\mu) = g^2(\mu)/4\pi$  becomes increasingly large and consequently the perturbation theory breaks down. As a result, there are no free quarks or gluons; the strong coupling brings them together and in hadrons binds them. This phenomenon is called *confinement*. Conversely, as  $\mu$  increases  $\alpha_s$  drops until at energies above the so called QCD scale around  $\Lambda_{\text{QCD}} \approx 200$  MeV the

theory becomes perturbative. *Asymptotic freedom* then refers to very short distance scales where the coupling becomes weak [12].

The *nonperturbative* nature of low energy hadronic physics has represented a substantial theoretical challenge to particle physicists. Nonperturbative studies of QCD are carried out via numerical simulations on the lattice. This signifies the important role of lattice QCD not just as the first-principles method for calculating interesting physical quantities such as hadronic masses and decay rates, but also as an indispensable tool for acquiring a deeper understanding of QCD. Furthermore, precision calculations of hadronic quantities required for determination of the CKM matrix elements are essential in the search for new physics beyond the standard model.

## 1.2 The Physics of Improvement

*“I saw from this that to understand quantum field theories I would have to understand quantum field theories on a lattice.”*

Kenneth G. Wilson, *Nobel lecture, 1982.*

Lattice QCD was invented 40 years ago when Wilson first proposed a formulation of QCD on a discretized spacetime [13]. Excitement ensued at the promising prospect of carrying out nonperturbative calculations by doing numerical simulations on the computer. Particle physicists were of course well aware that there were challenges. Lattice calculations would obviously suffer from discretization errors due to a nonzero lattice spacing  $a$ .

Early enthusiasm gave way to the realization of the difficulties when it seemed that reliable simulations would require very fine lattice spacings [14]. Simulations at such small lattice spacings took too much computing power and were well beyond what was practical at the time. In fact, as the lattice spacing is decreased the computational cost grows rapidly as

$$\text{cost} \propto \left(\frac{L}{a}\right)^4 \left(\frac{1}{a}\right) \left(\frac{1}{m_\pi^2 a}\right). \quad (1.3)$$

The first factor is simply due to the number of lattice sites in a box with a fixed physical volume, and the other two are due to the “critical slowing down” of numerical algorithms which we will encounter later. This makes the lattice spacing the most important determinant of the overall computational cost of simulations. It also meant that calculations at such fine spacings were not feasible.

This implied that one would benefit from reducing errors in order to be able to work at larger lattice spacings. It became imperative in reducing the discretization errors to beat them down in the lattice action, before they showed up in the computer simulation. As a result, the simple but impractical brute force approach of reducing the lattice spacing was replaced by a more sophisticated one that has subsequently led to a much deeper understanding of lattice QCD.



An “improvement program” was embarked upon that sought to identify and systematically remove the leading finite- $a$  errors. The result is a rich set of tools and techniques, each specifically designed to tackle a particular set of challenges, that has incrementally improved each framework and thereby our understanding of lattice gauge theories. These efforts have shown remarkable success and have culminated in an accurate and reliable framework which can be employed to calculate physical quantities in a strongly coupled quantum field theory [15].

In this work we review some of the theoretical development that has taken place over the past 3-4 decades which has enabled high quality simulations of charm quarks. As part of this review we describe some of the main ideas that played a central role in construction and improvement of a theoretical framework designed to study specific physical systems in a consistent and systematic approach.

### 1.2.1 Lattice Errors

It is now clear that improvement plays a central role in the development and success of lattice QCD. Accordingly, special emphasis is placed on the physics of improvement in this thesis. Putting the ordinary continuum QCD on a discrete 4 dimensional grid leads to discretization errors. The improvement program involves finding and correcting them.

In principle, all errors can be removed by adding infinitely many new interactions to the lattice effective theory, whose couplings are tuned to precisely cancel the errors. In practice, however, this is neither practical nor is it necessary. Errors can be made sufficiently small by identifying and suppressing the leading sources, thus requiring only a finite number of corrections.

Furthermore, lattice calculations involve numerical Monte Carlo simulations which inherently have statistical uncertainties. Experimental measurements have also their own set of uncertainties. Thus, *accuracy* as pertaining to the construction of lattice actions with controlled systematic errors goes hand in hand with *precision* at the level of numerical simulations and the data analysis side of a calculation with controlled statistical errors. Exact agreement is impossible to ascertain. Neither should it be the goal.

As we begin to explore various improvement approaches, we will encounter a number of different formulations of the lattice action. Before diving in, let us pause and ponder a question that will naturally arise: why is there so many different lattice actions to simulate the same continuum theory? This is an important question whose answer lies at the heart of the improvement program.

The fundamental reason for this is that different degrees of freedom generally require different effective theories. Considering the wide range of relevant energy scales involved in hadron physics due to vastly different quark masses, physical systems with various flavors exhibit distinct dynamical features of entirely different characteristics corresponding to different underlying degrees of freedom. A clear example would be the relative scale between

a quark's 3-momentum and its energy for which the light quarks are relativistic as compared with that for a charm or a bottom which tend to be nonrelativistic in most systems of interest.

As a result, the dominant sources of error in different effective field theories will also be potentially different. Consequently, targeted improvements tailored to study different physical systems may very well result in very different formulations. Hence, several widely used formulations of lattice QCD exist today. Each has its own merits and specific domain of application for which it has been designed.

There are three primary sources of errors in lattice simulations broadly categorized as

**Discretization Errors:** These are errors due to the nonzero lattice spacing  $a$ . They can be further subcategorized into *classical* errors due to replacing continuum derivatives by approximate finite differences, and *quantum* errors resulting from the ultraviolet hard cutoff at  $\pi/a$  imposed by the lattice.

**Finite Volume:** Lattice simulations are carried out inside boxes of finite volume with some kind of boundary conditions. Hadrons can therefore interact with themselves across the lattice boundary via exchanging Yukawa pions. Typically, lattices with  $Lm_\pi > 4$  will have small such errors [16].

**Chiral Extrapolation:** Simulations of light quarks are extremely expensive at the physical up and down quark masses. Thus, they are normally done with heavier than physical light quarks and then extrapolated down to the physical point.

In this work we address in great detail the first kind, i.e. the discretization errors. Specifically, given our particular interest in heavy-light mesons we are mainly concerned with treating both heavy and light quark degrees of freedom.

Actually, until late 90s there used to be a 4th major source of error called *quenched* “approximation.” Quark vacuum polarization is by far the most expensive part of simulations. Given the computational limitations people often resorted to performing simulations that did not include any *dynamical* or *sea* quarks. This introduced *uncontrolled* systematics of varying degrees which upon unquenching turned out to be around up to 20–30% [15].

The advent of the *asqtad* improved staggered quarks [17] was a major contributing factor in unquenching lattice simulations. The computational efficiency of the staggered quarks together with the high degree of improvement of their *asqtad* incarnation played an instrumental role in enabling the inclusion of realistic quark vacuum polarization effects.

## Improvement of Discretization Errors

Various approaches have been employed to address the discretization errors in different systems. Gluons are easier to handle than fermions. Few widely used improved gluon actions currently exist. In contrast, improving the quark action is significantly more involved.

The simplest discretization of the Dirac operator in the QCD Lagrangian was proposed by Wilson in 1975 [18]. He immediately noticed that it gave rise to the *doubling* problem whereby instead of one, each fermion field on the lattice created 16 copies of the same single continuum quark. These unphysical copies are called quark *tastes*; not to be confused with flavors which are physical, have different masses and are created by their own different quark fields.

A number of different approaches were then employed to deal with the unphysical tastes. The Kogut-Susskind fermions [19, 20, 21], commonly known as the *staggered* fermions, ameliorated the problem by diagonalizing the quark action in the spin space. This showed that some spinor degrees of freedom were degenerate and uncoupled from each other, resulting in a fourfold reduction in the number of doublers down to 4.

The degeneracy between the otherwise identical remaining tastes is spoiled due to so called taste exchange interactions whereupon taste is transferred between quarks via gluons. Errors due to these taste breaking interactions turned out to be unusually large rendering staggered quarks practically useless for accurate simulations for almost two decades. That is until the asqtad improved implementation of staggered quarks significantly reduced these errors and therefore enabled high quality simulations.

Staggered quarks are numerically faster than other discretizations thanks to the fact that they have a remnant chiral symmetry and involve 4 times fewer degrees of freedom due to the spin diagonalization. Thus, as a consequence of the reduced discretization errors, large scale unquenched simulations became more practical [16]. The asqtad quarks were subsequently shown to be hugely successful for dynamical light quarks [22]. They helped lattice fulfill its promise as a tool for accurate nonperturbative calculations in hadronic physics. This development led to a shift of focus during the aughts among many lattice theorists by allowing them to perform precision calculations that were previously difficult to do.

Putting the heavy quarks<sup>2</sup> on the lattice presents its own particular set of challenges. On typical lattices currently available  $am_Q$  is of order 1. Equivalently, the Compton wavelength of the quark is of order lattice spacing  $a$ . Consequently, the heavy quark's dynamics cannot be resolved well on the lattice and the  $\mathcal{O}((am)^n)$  discretization errors will be too large.

This was dealt with by taking advantage of their large mass by noting that heavy quarks are typically nonrelativistic in most physical systems of interest. One could then exploit that fact and construct nonrelativistic effective theories where the large mass is dealt with off the lattice. Lattice NRQCD [23] in particular has been remarkably successful in highly accurate simulations of the  $b$  quark. However, it has been less successful when applied to the charm quark, which being lighter than the bottom is less nonrelativistic.

---

<sup>2</sup> Heavy quarks refer to the charm and the bottom. Top quarks are too heavy and short lived to form hadronic bound states with other quarks. Hence, all lattices are essentially without top quarks.

In fact, charm occupies an interesting position on the mass scale which makes it particularly challenging for high quality simulations. On typical lattices available today its mass is around  $am_c \approx 0.5$ . Which means that it's neither heavy enough to be nonrelativistic nor light enough to have small  $am_c$  discretization errors. As a result, accurate simulations of charm with few percent errors had been difficult to achieve. For instance, the hyperfine mass splitting of charmonium states had long been consistently underestimated in lattice calculations.

Highly accurate charm physics has been made possible by other improved theories including the Fermilab action [24] and the highly improved staggered quark action, commonly known by its acronym as the HISQ action [9]. This latest edition of the staggered quarks showed considerable success in charm physics including a correct calculation of the charmonium hyperfine mass splitting. Given its demonstrated success in simulating a variety of charmed phenomena, this work evaluates the HISQ action's ability to probe the fine near cancellation that occurs in the radiative decay of  $D^{*+}$ .

An order by order systematic improvement of the lattice theory up to some desired power in the lattice spacing  $a$  was initiated by Symanzik in early 1980s [25] and has been relentlessly pursued with tremendous success. As we move along the improvement path that leads to one of the most accurate discretizations of the charm quark which we ultimately intend to use in this work, i.e. the HISQ action, we take a couple of short detours to briefly review some of the key ideas behind other fermion actions in order to enhance our understanding of the improvement program. However, this is by no means an exhaustive history of lattice QCD. Nor do we intend to map out the entire space of effective QCD theories. We do however explore a small but major region and learn how to navigate towards the continuum QCD.

A perspective that informs this work is that lattice QCD can be viewed as the *marriage* of perturbative and nonperturbative methods and that it straddles both sides of the  $\Lambda_{\text{QCD}}$  scale. Some of the substantial evidence that have been argued to justify this position will be presented. This approach is essentially based on the idea that a lattice theory that strives to describe the confined phase nonperturbatively, is in fact informed by perturbation theory and takes full advantage of the asymptotic freedom in improving and tuning the strongly coupled theory of low energy hadrons.

### 1.3 Thesis Structure

This thesis is organized as follows. A brief description of the foundations of lattice QCD is provided in chapter 2 with a brief taste of improvements of the gluon action. Fermions are then discretized in chapter 3 which presents a detailed review of the *perturbative Symanzik improvements* applied to the staggered quarks. This chapter highlights some of the most important developments in the study of heavy quarks on the lattice.

Chapter 4 deals with the taste symmetry that underlies the appearance of the doublers with the goal of providing an intuitive understanding of its implications. To that end, we discuss the connection between the familiar Dirac basis and the spin diagonalized staggered basis. Next we describe our methodology in chapter 5 which is the most practically oriented part of this thesis. That is, with the theoretical basis in place, the nitty-gritty details of carrying out a simulation to extract actual physical quantities are explained. Some of the techniques and logistics are explained and Bayesian fitting is discussed. We will end our discussion of the methodology by putting everything together to calculate a few interesting quantities. Chapter 6 contains our main original calculations of the radiative and pionic decays. Finally, in chapter 7 we summarize our results and discuss future directions.

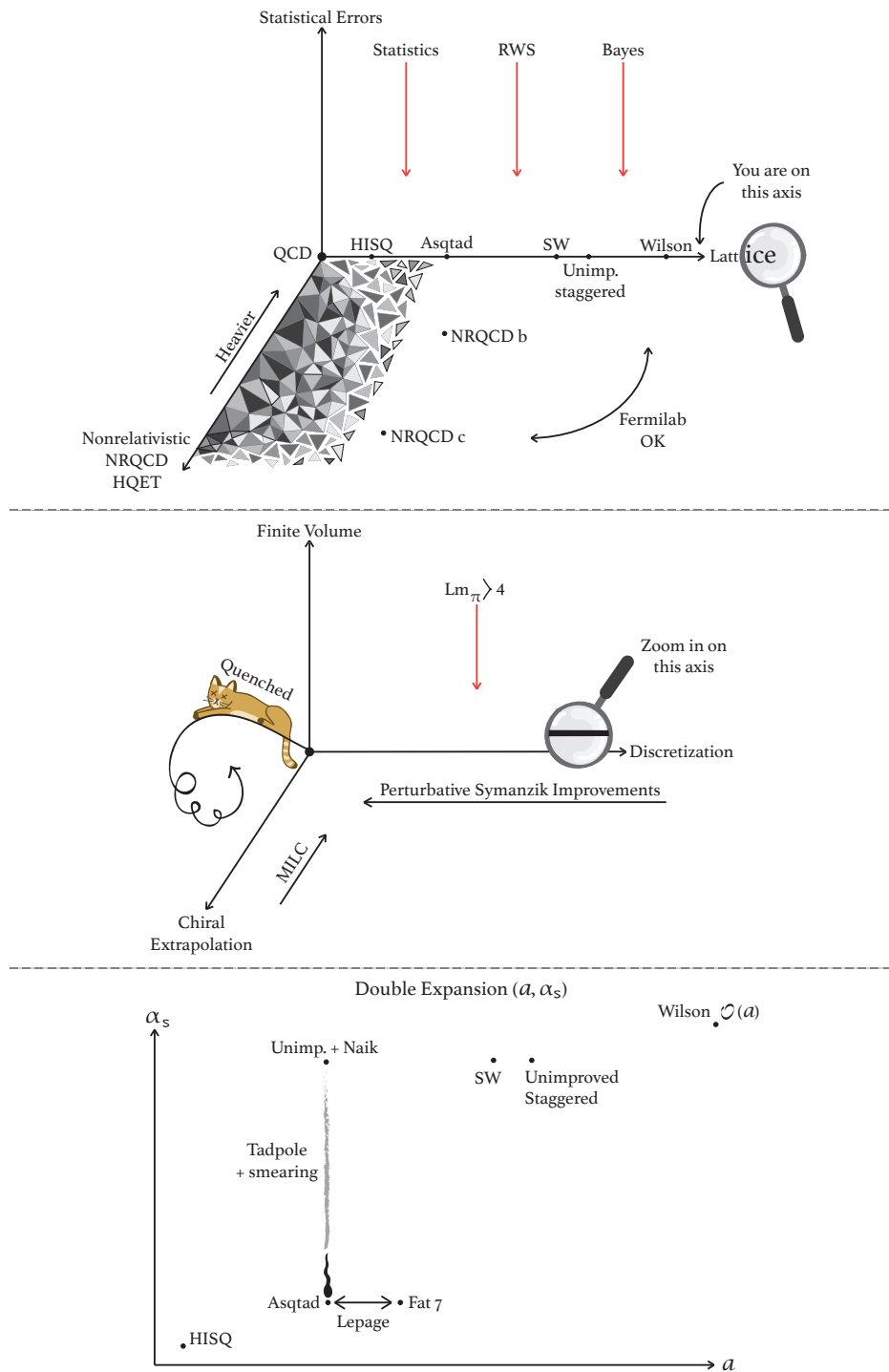


Figure 1.1: Artwork courtesy of Avesta Rastan.

## Chapter 2

# Lattice QCD

This chapter presents a quick introduction to the formulation of gauge theories on a lattice. We briefly review the general foundations but some of the details that can be found in standard textbooks such as [26, 27, 28], are omitted in favor of a discussion of the modern point of view of the physics of improvement. Our treatment draws heavily from the excellent lectures in [14, 29]. By the end of this chapter we will have seen lattice gluon actions as well as the basic ideas behind a full Monte Carlo simulation of hadronic systems. The fermion action is treated like a black box and is discussed in subsequent chapters.

Starting from the continuum, the QCD Lagrangian is given by

$$\mathcal{L}_{\text{QCD}} = \bar{\psi}(i\not{D} - m)\psi - \frac{1}{2}\text{Tr}F_{\mu\nu}^2, \quad (2.1)$$

where the covariant derivative and the field tensors are defined as

$$D_\mu = \partial_\mu - igA_\mu^a t^a, \quad F_{\mu\nu} \equiv \partial_\mu A_\nu - \partial_\nu A_\mu + ig[A_\mu, A_\nu], \quad (2.2)$$

and  $t^a$  are the traceless Hermitian generators of  $SU(3)$ . It is invariant under gauge transformations in color space. Lattice QCD is based on the path integral formulation of QCD on a 4-dimensional discretized Euclidean spacetime.

### 2.1 Path Integrals on the Lattice

Physical observables can be calculated using path integrals. These are functional integrals where all paths are represented [12]. These paths consist of all quark and gluon fields as continuous functions of spacetime each weighted by a phase determined by the action. On the lattice the integration measure turns into functionals of the discrete spacetime grid:

$$\int \mathcal{D}A_\mu \dots e^{-\int d^4x \mathcal{L}(x)} \rightarrow \int \prod_{x_i \in \text{grid}} dA_\mu(x_i) \dots e^{-a^4 \sum_{x_i} \mathcal{L}_i}. \quad (2.3)$$

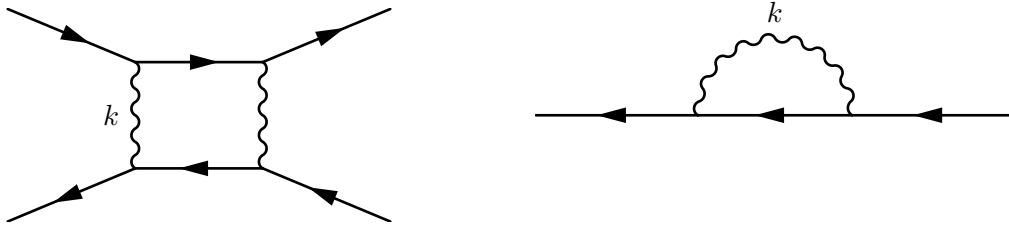


Figure 2.1: Low momentum quark-quark scattering amplitudes and quark self energies have loop contributions from gluons with high momenta  $k > \pi/a$  that are excluded from the lattice theory. Corrections involve new interactions and renormalized masses and couplings.

The integral over the continuous spacetime in the action is replaced by a discrete sum over all grid points. The ellipsis here denote additional fermion fields in the measure as well as any observables in the integrand. The path integrals are also calculated in the Euclidean space with imaginary time  $t \rightarrow it$ , in order to avoid the difficult integration of high frequency oscillations.

Broadly speaking, the nonzero lattice spacing denoted by  $a$  gives rise to two types of discretization errors. Classical errors due to approximate derivatives and quantum errors due to excluded physics at high energies as a result of the ultraviolet cutoff imposed by the lattice.

Derivatives in the continuum Lagrangian are approximated by finite differences in the lattice theory such as

$$\frac{\partial\psi(x)}{\partial x} \approx \Delta_x\psi(x) \equiv \frac{\psi(x+a) - \psi(x-a)}{2a}. \quad (2.4)$$

This particular implementation introduces errors of  $\mathcal{O}(a^2)$ . The approximation can be made more accurate for classical fields in a straightforward manner by adding correction terms. For instance, replacing

$$\partial_x\psi = \Delta_x\psi - \frac{a^2}{6}\Delta_x^3\psi + \mathcal{O}(a^4). \quad (2.5)$$

would correct the  $a^2$  error. The  $-\frac{1}{6}$  coefficient is determined from a simple Taylor expansion and is completely independent of the nature of the underlying theory.

Corrections to errors caused by the UV cutoff are not as simple though. The lattice spacing imposes a minimum wavelength of  $2a$  which excludes from the theory all momenta  $k > \pi/a$ . In an interacting quantum field theory, high energy modes affect the low energy physics through renormalizing the bare couplings and masses as well as high momentum loop contributions.

Figure 2.1 shows this for one-loop high energy contributions to low energy quark-quark scattering amplitudes and the quark self energy that are excluded from the cutoff theory. The difference between, for instance, the continuum and lattice  $qq \rightarrow qq$  scattering ampli-



tude due to these excluded UV contributions can be expanded in terms of the small external momenta  $ap_i$  in the form of  $a^2 c_4(a) \bar{u}(p_2) \gamma_\mu u(p_1) \bar{u}(p_4) \gamma^\mu u(p_3) + \dots$ . They can be brought back in by introducing new interactions into the cutoff theory that mimic their effects, such as 4-fermion contact terms, etc., Modifying the Lagrangian to compensate for the cutoff is a central idea in constructing an effective theory and its application to lattice was pioneered by Symanzik [25]. Hence, such corrections are generally referred to as ‘‘Symanzik improvements.’’

The cutoff Lagrangian is therefore modified by the addition of higher dimension correction terms such as  $c(a) a^2 \bar{\psi} \Delta^3 \cdot \gamma \psi$  already encountered in (2.5). The dimensionless coefficient  $c(a)$  is now a cutoff dependent new coupling

$$c(a) = -\frac{1}{6} + \epsilon(a) = -\frac{1}{6} + \epsilon_0 + \epsilon_1 \alpha_s(\pi/a) + \dots, \quad (2.6)$$

where the  $-\frac{1}{6}$  part is due to the finite difference corrections as before, while  $\epsilon(a)$  is from UV contributions integrated out of the theory.

The bad news is that unlike the first part, the  $\epsilon(a)$  renormalization is theory specific. The good news is the asymptotic freedom in QCD. At sufficiently high energies the running strong coupling constant becomes small enough that the theory becomes perturbative. The renormalized correction  $\epsilon$  can therefore be written in terms of a perturbative expansion where  $\epsilon_0$  denotes the tree level effects of the UV modes,  $\epsilon_1$  the one-loop effects and so on. These coefficients can then be computed to desired order through matching calculations in perturbation theory, or alternatively, tuned in nonperturbative calculations until a matching condition is satisfied.

This essentially captures the logic of *perturbative Symanzik improvements*. It involves a double expansion in terms of the lattice spacing  $a$  and the strong fine structure constant  $\alpha_s$ , and consists of *classical* and *quantum* improvements designed to correct for the approximate derivatives and the UV cutoff errors respectively. These ideas are perfectly encapsulated in a simple equation in (2.6).

For this to be viable, the lattice spacing must be small enough to satisfy two requirements so that both classical and quantum corrections will work. That is,  $a$  must be small enough for: (a) finite differences to be sufficiently accurate, and (b) the energy scale  $\mu \approx \pi/a$  be large enough so that  $\alpha_s(\pi/a)$  is small enough to be perturbative. Typical lattices currently in use have spacings of order  $a \approx 0.1 \text{ fm} \approx 2 \text{ (GeV)}^{-1}$  or smaller. Thus, given that  $\Lambda_{\text{QCD}} \approx 200 \text{ MeV}$ , at typical scales we have

$$a\Lambda_{\text{QCD}} \approx 0.1, \quad (2.7)$$

$$\alpha_s(\mu \approx \pi/a) \approx \frac{12\pi}{(33 - 2N_f) \log(\mu^2/\Lambda_{\text{QCD}}^2)} \approx 0.3.$$

The first relation indicates that with typical internal momenta of order QCD scale, first order finite difference errors are of order 10%, while the structure constant indicates that perturbation theory is marginally viable at first loop order provided that correction coefficients are small. This happy marriage between the perturbative and nonperturbative regimes is made possible by asymptotic freedom by going to a sufficiently small  $a$ .

It may seem that this approach has a serious problem due to the presence of higher order operators which are not renormalizable. That is not an issue, however. This is an effective theory with a well defined cutoff already in place and therefore needs not be renormalizable. Operators of dimension  $n + 4$  are multiplied by  $a^n$  in the Lagrangian. Therefore, higher dimension operators are referred to as “irrelevant” in the sense that they drop out in the continuum limit of the theory.

## 2.2 Gluons on the Lattice

Let us now turn to the task of discretizing QCD starting from the gluons. The pure gluonic part of the continuum action is given by

$$S_g = \int d^4x \frac{1}{2} \sum_{\mu, \nu} \text{Tr} F_{\mu\nu}^2(x). \quad (2.8)$$

The first step is then to find a discretized formulation that accurately approximates the gluon action.

### 2.2.1 The Link Variables

The lattice gluon action was originally formulated by Wilson [13] in terms of *link* variables defined by

$$U_\mu(x) \equiv \mathcal{P} \exp \left( -i \int_x^{x+a\hat{\mu}} gA \cdot dy \right) \approx e^{-iagA_\mu}, \quad (2.9)$$

where  $g$  is the coupling constant and  $\mathcal{P}$  is a path ordering operator whose role will become clear shortly. It might seem odd that instead of formulating the lattice theory directly in terms of gluon fields  $A_\mu$ , these link variables are taken as the fundamental objects. It will be helpful here to think about the geometric origin of the gauge fields in the continuum [12].

In a theory with local gauge invariance, defining field derivatives in terms of the usual infinitesimal differences like  $\partial_\mu \psi(x) = \lim (\psi(x + \epsilon\hat{\mu}) - \psi(x)) / \epsilon$  is not very sensible. This quantity does not have a clear and useful gauge transformation since each of its two terms transforms independently. A simple solution is to introduce a unitary *comparator* operator  $U(y, x)$  that transforms like

$$U(y, x) \rightarrow \Omega(y)U(y, x)\Omega^\dagger(x) \quad (2.10)$$

where  $\Omega(x)$  is a local gauge. Now with this definition  $\psi(y)$  and  $U(y, x)\psi(x)$  have the same transformation. The *covariant derivative* can then be defined in a meaningful way as

$$D_\mu\psi(x) = \lim_{\epsilon \rightarrow 0} \frac{1}{\epsilon} (\psi(x + \epsilon\hat{\mu}) - U(x + \epsilon\hat{\mu}, x)\psi(x)). \quad (2.11)$$

In its infinitesimal form this is expanded to give

$$U(x + \epsilon n, x) = 1 + i g \epsilon n^\mu A_\mu(x) + \mathcal{O}(\epsilon^2) \quad (2.12)$$

where  $n_\mu$  are unit 4-vectors and  $A_\mu$  turn out to be the gauge bosons.

In the case of a non-Abelian gauge theory such as QCD, the  $U(y, x)$  connector also known as the *Wilson line*, is defined with a path ordering operator in order to disambiguate the order in which  $A_\mu$ s are placed in the expansion of the exponential in (2.9). The leftmost fields are those closest to  $y$ . The lattice link variable therefore plays the role of a *parallel transporter* between adjacent lattice sites. This geometric description is the reason why it is often said that gluons live on the links while quarks occupy lattice sites.

Not only does this geometrical construction help make sense of derivatives in a locally gauge invariant theory, it also saves one from serious problems that would be caused by the loss of gauge invariance. Which raises the question: why go to so much length in order to rescue the gauge symmetry while we've readily given up the Lorentz symmetry by going to the lattice. There are a number of practical reason for this. A direct consequence of the gauge symmetry is that the quark-gluon, 3-gluon and 4-gluon vertex couplings must be exactly equal to one another and that gluons must be massless. Abandoning it lifts this useful constraint and consequently one will have to independently tune several more couplings. This is numerically very expensive and therefore it would be highly desirable to avoid it if at all possible.

Building a lattice theory directly in terms of  $A_\mu$  results in massive gauge bosons which wreck the gauge invariance. As a result a host of Ward identities would be invalidated. One would then have to add many new terms to the Lagrangian in order to fix those identities for every  $n$ -point correlation function [12, footnote on page 248]. Abandoning the continuum Lorentz symmetry on the other hand, causes far less severe complications. This is because unlike the gauge symmetry, the Lorentz symmetry is naturally restored in the continuum limit.

The link variables transform simply, as indicated by (2.10), according to

$$U_\mu(x) \rightarrow \Omega(x)U_\mu(x)\Omega^\dagger(x + a\hat{\mu}), \quad (2.13)$$

and are meaningful geometrical objects out of which one can construct other objects that preserve gauge invariance. One can immediately see that a *Wilson loop*, defined as

$$W(\mathcal{C}) \equiv \frac{1}{3} \text{Tr} \mathcal{P} \exp \left( -i \oint_{\mathcal{C}} gA \cdot dx \right), \quad (2.14)$$

where the integral is taken over any closed path  $\mathcal{C}$  on the lattice is a gauge invariant quantity. Such objects can therefore be used as the building blocks of a gauge invariant gluon action.

The lattice Lagrangian is therefore desired to be gauge invariant, local and respecting to what is left of the Lorentz symmetry. The smallest and most local such object on the lattice is a  $1 \times 1$  Wilson square called the *plaquette operator*

$$P_{\mu\nu}(x) \equiv \frac{1}{3} \text{Re} \text{Tr} \left( U_{\mu}(x) U_{\nu}(x + a\hat{\mu}) U_{\mu}^{\dagger}(x + a\hat{\mu} + a\hat{\nu}) U_{\nu}^{\dagger}(x) \right). \quad (2.15)$$

A simple classical expansion of this operator gives

$$\begin{aligned} P_{\mu\nu} &= \frac{1}{3} \text{Re} \text{Tr} \mathcal{P} e^{-i \oint_{\square} gA \cdot dx} \\ &= \frac{1}{3} \text{Re} \text{Tr} \left[ 1 - i \oint_{\square} gA \cdot dx - \frac{1}{2} \left( \oint_{\square} gA \cdot dx \right)^2 + \mathcal{O}(A^3) \right]. \end{aligned} \quad (2.16)$$

According to the Stoke's theorem we have

$$\begin{aligned} \oint_{\square} A \cdot dx &= \int_{-a/2}^{a/2} dx_{\mu} dx_{\nu} [\partial_{\mu} A_{\nu} - \partial_{\nu} A_{\mu}] \\ &= a^2 F_{\mu\nu} + \frac{a^4}{24} (D_{\mu}^2 + D_{\nu}^2) F_{\mu\nu} + \mathcal{O}(a^6, A^2) \end{aligned} \quad (2.17)$$

which shows that the plaquette operator can be used to approximate the field tensor

$$P_{\mu\nu} = 1 - \frac{a^4}{6} \text{Tr}(gF_{\mu\nu})^2 - \frac{a^6}{72} \text{Tr} \left( gF_{\mu\nu} (D_{\mu}^2 + D_{\nu}^2) gF_{\mu\nu} \right) + \mathcal{O}(a^8). \quad (2.18)$$

The Wilson gauge action is formulated [13] in terms of these plaquettes as

$$\mathcal{S}_g = \beta \sum_{x, \mu > \nu} (1 - P_{\mu\nu}(x)) \quad (2.19)$$

where  $\beta = 6/g^2$ . This approximates the continuum gluon action with  $\mathcal{O}(a^2)$  errors

$$\mathcal{S}_g = \int d^4x \sum_{\mu, \nu} \left\{ \frac{1}{2} \text{Tr} F_{\mu\nu}^2 + \frac{a^2}{24} \text{Tr} F_{\mu\nu} (D_{\mu}^2 + D_{\nu}^2) F_{\mu\nu} + \dots \right\}. \quad (2.20)$$

## 2.2.2 Symanzik Improvements

The  $a^2$  errors of the Wilson plaquette action can be corrected by adding new terms. The next smallest gauge invariant objects include the planar  $2 \times 1$  rectangular and the cubic  $1 \times 1 \times 1$  parallelogram Wilson loops. Rectangular Wilson loops, for instance, have a different mix of  $a^4$  and  $a^6$  terms in their expansion

$$R_{\mu\nu} = 1 - \frac{4}{6}a^4 \text{Tr}(gF_{\mu\nu})^2 - \frac{4}{72}a^6 \text{Tr}(gF_{\mu\nu}(4D_\mu^2 + D_\nu^2)gF_{\mu\nu}) - \dots \quad (2.21)$$

than that of the plaquettes in (2.18). Thus, they can be combined to cancel  $a^2$  errors in the Wilson gauge action

$$\begin{aligned} \mathcal{S}_g &= -\beta \sum_{x,\mu>\nu} \left\{ \frac{5P_{\mu\nu}}{3} - \frac{R_{\mu\nu} + R_{\nu\mu}}{12} \right\} \\ &= \int d^4x \sum_{\mu,\nu} \frac{1}{2} \text{Tr} F_{\mu\nu}^2 + \mathcal{O}(a^4). \end{aligned} \quad (2.22)$$

This is an example of a classical Symanzik improvement analogous to suggested corrections to the finite difference operator we saw in (2.5).

Improvements to quantum gluons will enter in the form of corrections to the 5/3 and 1/12 coefficients as well as additional operators. Lüscher and Weisz [30, 31] proposed an improved gauge action in the form of

$$\mathcal{S}_{\text{LW}} = -\beta \left\{ \sum_{\text{plaq.}} c_{\text{pl}} P_{\mu\nu} + \sum_{\text{rect.}} c_{\text{rt}} R_{\mu\nu} + \sum_{\text{cube}} c_{\text{cu}} C_{\mu\nu\rho} \right\}. \quad (2.23)$$

where the coefficients  $c_i = c_i^{(0)} + 4\pi\alpha_0 c_i^{(1)}$  were computed perturbatively to one-loop order.

Traditional perturbation theory in terms of the bare lattice coupling  $\alpha_0$  turned out to be slow to converge. Surprisingly, it seemed to require spacings of order  $a \approx 1/20$  fm despite evidence from continuum phenomenological applications which suggested that it should begin to work at energies around 1 GeV which correspond to  $a \approx 0.6$  fm [14]. A breakthrough was made in a landmark work by Lepage and Mackenzie [32] which showed that the perturbation theory can be made much more convergent by using the more continuum-like *tadpole improved* links and replacing the bare coupling  $\alpha_0$  by a nonperturbatively renormalized coupling  $\alpha_s$ .

The problem was that, lattice artifacts resulted in large renormalization of the bare coupling. This is a symptom of the so called tadpole problem. Tadpole diagrams arise as a result of the nonlinear dependence of the link variables  $U_\mu$  on the gauge vector potential  $A_\mu$ . But given the definition (2.9), in addition to the continuum-like vertex  $\bar{\psi}gA \cdot \gamma\psi$ , this also contains terms with any number of powers of  $agA_\mu$ .

These are pure lattice artifacts and don't exist in the continuum theory. Classically, such unphysical contributions would be suppressed by additional powers of  $ag$ . However, in a quantum theory, two of the extraneous vector fields may be contracted in divergent loops containing gluon propagators that carry momenta of order  $\pi/a$ . These UV modes then bring in factors of  $1/a^2$  that precisely cancel the  $a^2$  suppression of the tadpole pair of vector fields. As a result the tadpole contributions are only suppressed by  $g^2$ , typically with a large coefficient, which lead to uncomfortably large renormalizations and poor convergence of the perturbation theory.

Lepage and Mackenzie suggested that an effective way to deal with the tadpole problem is to cancel them out as follows [32]. The *tadpole factor* defined as the mean value of the link variable

$$u_0 \equiv \langle \frac{1}{3} \text{Re Tr } U_\mu \rangle \quad (2.24)$$

consists only of undesirable tadpoles, since the linear term in the expansion of  $U_\mu$  vanishes due to the trace. This is an effective way to compensate for tadpole renormalizations since these effects are relatively insensitive to external momenta, and are therefore process independent to a large extent? Thus, dividing every link variable by the tadpole factor

$$U_\mu \rightarrow \frac{U_\mu}{u_0} \quad (2.25)$$

will largely cancel the tadpole contributions. The tadpole factor is numerically measured by computing the expectation value of the link operator. Note, however, that this quantity is not gauge invariant and thus vanishes in simulation unless the gauge is fixed. The axis symmetric Landau gauge is commonly used. It can be shown that the Landau gauge maximizes  $u_0$  and therefore provides a lower bound for the tadpole effects.

Alternatively, one can avoid the extra trouble of fixing the gauge by using a simpler gauge invariant definition of the tadpole factor

$$u_0 \equiv \langle P_{\mu\nu} \rangle^{1/4} \quad (2.26)$$

where the 4-th root is to compensate for the 4 links forming the plaquette operator. The *tadpole improved* gauge action correct to  $\mathcal{O}(a^2\alpha_s^2, a^4)$  then takes the form

$$\mathcal{S}_g = -\beta \sum_{x,\mu>\nu} \left\{ \frac{5}{3} \frac{P_{\mu\nu}}{u_0^4} - r_g \frac{R_{\mu\nu} + R_{\nu\mu}}{12u_0^6} \right\} + c_g \beta \sum_{x,\mu>\nu>\rho} \frac{C_{\mu\nu\rho}}{u_0^6}. \quad (2.27)$$

Every link variable is divided by a nonperturbatively determined  $u_0$  factor, and the coefficients

$$\begin{aligned} r_g &= 1 + 0.48\alpha_s(\pi/a), \\ c_g &= 0.055\alpha_s(\pi/a). \end{aligned} \quad (2.28)$$

are determined by one-loop perturbative matching calculations. That is, they are tuned until an *on-shell* physical quantity such as a low energy scattering amplitude calculated using lattice perturbation theory matches that obtained from the continuum perturbation theory. The significant impact of the tadpole improvement is evident in the fact that without it one would get  $r_g = 1 + 2\alpha_s$  [14]. Compared with (2.28), this shows that the tadpole improvement reduces one-loop errors by about 75%.

## 2.3 Quarks on the Lattice

Putting fermions on the lattice is a vast subject and is significantly more involved. The next two chapters will touch upon a select subset of various frameworks that have been developed for discretizing fermions. In this section we treat the fermion action like a black box and briefly review the basic general ideas that are common to all lattice fermions.

A generic lattice fermion action looks like

$$\mathcal{S}_f = a^4 \sum_{x,y} \bar{\psi}(x) M_{x,y} \psi(y) \quad (2.29)$$

where  $M$  is some discretized implementation of the continuum Euclidean fermion operator  $\not{D} + m$ . The specific form of the discretization is encoded in the structure of this matrix and will be discussed in chapter 3.

On a lattice with  $V = L^3 T$  number of sites where  $L$  and  $T$  denote its spatial and temporal length respectively, the *fermion matrix*  $M$  generally takes the form of a  $V \times V$  matrix whose nonzero entries are  $\Gamma \otimes U$  operators connecting the spinor and color components of quark fields at different lattice sites. Here  $\Gamma$  represents a  $4 \times 4$  Dirac matrix and  $U$  an  $SU(3)$  link, overall making  $M$  a large sparse square  $12V$  dimensional matrix.

Like the continuum path integral formalism, the quark fields are represented by *anticommuting* Grassmann numbers, but only defined on the lattice sites.<sup>1</sup> Thanks to the fact that the fermion action is quadratic in the fields, the functional path integrals over the fermion fields can be calculated analytically. The fermion integration in the lattice partition function, for example, is easily performed

$$\begin{aligned} Z &\equiv \int \mathcal{D}U_\mu \mathcal{D}\bar{\psi} \mathcal{D}\psi \exp(-\mathcal{S}_f - \mathcal{S}_g) = \int \mathcal{D}U_\mu \det M \exp(-\mathcal{S}_g) \\ &= \int \mathcal{D}U_\mu \exp(-\mathcal{S}_{\text{eff.}}) \end{aligned} \quad (2.30)$$

where the lattice spacing is set to  $a = 1$ . The second line simply puts the determinant of the fermion matrix back in the exponent. It introduces  $\mathcal{S}_{\text{eff.}} = \mathcal{S}_g - \ln \det M$ , as an effective action that includes only the gluons but which also incorporates the effects of the dynamical sea quarks after they have been integrated over through the determinant.

<sup>1</sup> Details are fairly standard and won't be repeated here. See, for example, [12, Ch. 9].

The vacuum expectation value of any physical observable  $\mathcal{O}$  is then

$$\langle \mathcal{O} \rangle = \frac{1}{Z} \int \mathcal{D}U_\mu \mathcal{O}(U) \exp(-\mathcal{S}_{\text{eff}}). \quad (2.31)$$

Often, the observable of interest contains quark fields  $\psi(x)$  and  $\bar{\psi}(y)$ . Upon integration, each pair of quark fields will bring down a propagator  $M_{x,y}^{-1}$  for every possible Wick contraction. A quark propagator, for instance, is given by

$$\langle \psi(x) \bar{\psi}(y) \rangle = \frac{1}{Z} \int \mathcal{D}U_\mu M_{x,y}^{-1} e^{-\mathcal{S}_{\text{eff}}}. \quad (2.32)$$

It is worth pointing out the difference between the way the *sea* and the *valence* quarks show up in the calculation. The dynamical sea quarks result in the  $\det M$  in (2.30), while the valence quarks that are created and annihilated by quark fields in the observable operator  $\mathcal{O}$ , result in propagators and turn up as  $M^{-1}$  factors as in (2.32).

This provides the basis for carrying out Monte Carlo simulations of a strongly interacting system of quarks and gluons. The next section will outline the key ideas behind the Monte Carlo method. To go any further than that one will have to specify the fermion action which will be the primary subject of the rest of this work.

## 2.4 Simulations on the Lattice

Once the gauge and the fermion actions are chosen, observables are computed on the lattice via numerical Monte Carlo simulations. This essentially entails generating a large ensemble of *gauge field configurations*  $\{U_\mu^{(i_{\text{cf}})}(x)\}$  with a probability distribution given by

$$p(U_\mu(x)) = \frac{1}{Z} \det M(U) e^{-S_g(U)}. \quad (2.33)$$

The *statistical* expectation value of an observable  $\mathcal{O}$  over this distribution then is

$$\mathbb{E}_U[\mathcal{O}] = \int \prod_{x,\mu} dU_\mu(x) \mathcal{O}(U_\mu) p(U_\mu) \quad (2.34)$$

which is exactly the same as its *vacuum* expectation value. The average of a large number of samples from any distribution will tend to its expectation value

$$\langle \mathcal{O} \rangle = \frac{1}{N_{\text{cf}}} \sum_{i_{\text{cf}}} \mathcal{O}(U_\mu^{(i_{\text{cf}})}(x)), \quad (2.35)$$

where  $N_{\text{cf}}$  is the size of the ensemble. The central limit theorem implies that given a large number of configurations the statistical uncertainty in  $\langle \mathcal{O} \rangle$ , i.e. the sample variance, is  $\sigma^2/N_{\text{cf}}$  where  $\sigma$  is the variance of the parent probability distribution  $p(\mathcal{O}(U))$ .



For pure gauge simulations with no dynamical fermions in the sea, local updating methods such as the Metropolis algorithm can be used to generate a sequence of gauge field configurations [29]. However, they become inadequate in the presence of dynamical fermions due to the non-local nature of the  $\det M(U)$  function. Various hybrid molecular dynamics methods are used instead [16]. These are computationally intensive and become increasingly expensive with decreasing lattice spacing and lighter quark masses. Limited computing power had forced lattice theorists to ignore the sea quarks in the so called *quenched* simulations in the early days. However, several factors including significant progress in constructing highly improved actions eventually made unquenching possible. Unquenched simulations became the standard practice during the aughts.

In this work we use the gauge field configurations that have been generated and made publicly available by the MILC collaboration [16]. Details of related Monte Carlo methods will therefore not be discussed further.

## Chapter 3

# Fermions on the Lattice

The previous chapter discretized the gluons and improved them. It then introduced how Monte Carlo simulations are carried out to compute physical observables using generic lattice fermions. In this chapter we discuss the discretization of fermions.

Section 3.1 starts from scratch and immediately encounters problems that arise from the simplest discretization of Dirac fermions. It follows by introducing a few different approaches to deal with those problems. In particular the *staggered quark* formalism that we will be using in our calculations are discussed. Then, section 3.2 delves deep into the improvement of the staggered quarks that ultimately result in the HISQ action [9], which *is* used here. The emphasis is on the physics of improvements as applied to staggered quarks for the purpose of doing charm physics on the lattice.

In addition, a brief complementary overview of a couple of other lattice actions that are suitable for simulations of heavy quarks and thus are related to our study through overlapping applications is presented in Appendix A.

### 3.1 The “Naive” Fermions

Let us begin with the simplest discretization of the simplest case of free Dirac fermions, where it’s easiest to see the origin of the infamous doubling problem. This section draws from multiple standard introductory textbooks in [26, 27, 28], while occasionally deviating in order to explore improvement.

The action for free Dirac fermions in the continuum Minkowski space is given by

$$\mathcal{S}_f = \int d^4x \bar{\psi}(x) (i\gamma^\mu \partial_\mu - m) \psi(x). \quad (3.1)$$

Wick rotating into the Euclidean space by substituting  $t \rightarrow it$  then gives

$$\mathcal{S}_f^{(\text{Eucl.})} = \int d^4x \bar{\psi}(x) (\gamma_\mu^E \partial_\mu + m) \psi(x), \quad (3.2)$$

where

$$\gamma_0^E = \gamma^0, \quad \gamma_i^E = -i\gamma^i, \quad (3.3)$$

are Hermitian Euclidean Dirac matrices which satisfy the Clifford algebra

$$\{\gamma_\mu^E, \gamma_\nu^E\} = 2\delta_{\mu\nu}. \quad (3.4)$$

The superscripts indicating the Euclidean space shall be omitted henceforth.

To migrate onto the lattice, the derivative in (3.2) is replaced by a finite difference approximation. This can be done in many ways. A straightforward and natural discretization [18] takes the form of a symmetrized one-step finite difference

$$\mathcal{S}_f^{\text{latt.}} = \sum_x \bar{\psi}(x) (\gamma_\mu \Delta_\mu + m) \psi(x), \quad (3.5)$$

where

$$\Delta_\mu \psi(x) \equiv \frac{\psi(x + a\hat{\mu}) - \psi(x - a\hat{\mu})}{2a}. \quad (3.6)$$

This is widely referred to by the misnomer of “*naive*” fermions.

### 3.1.1 The Doubling Problem

Wilson noticed the problem with his formulation as soon as he wrote it down. The free fermion propagator on the lattice would take the form

$$S(x, y) = \langle \psi(x) \bar{\psi}(y) \rangle = \lim_{a \rightarrow 0} \int_{-\pi/a}^{\pi/a} \frac{d^4 p}{(2\pi)^4} G(p) e^{-ip \cdot (y-x)}, \quad (3.7)$$

where the momentum space propagator is given by

$$G(p) = \frac{1}{i \sum_\mu \frac{1}{a} \sin(ap_\mu) \gamma_\mu + m} = \frac{-i \sum_\mu \tilde{p}_\mu \gamma_\mu + m}{\sum_\mu \tilde{p}_\mu^2 + m^2}. \quad (3.8)$$

The second equality introduces the shorthand notation

$$\tilde{p}_\mu \equiv \frac{1}{a} \sin(ap_\mu) \quad (3.9)$$

for the lattice version of the “momentum” corresponding to the “derivative” operator.

The propagator in the momentum space contains the form of the lattice dispersion relation for a free Dirac fermion

$$(\tilde{p}^0)^2 = \tilde{\mathbf{p}}^2 + m^2, \quad (3.10)$$

which given (3.9) takes the form

$$\frac{1}{a^2} \sin^2(aE_{\mathbf{p}}) = \frac{1}{a^2} \sin^2(a\mathbf{p}) + m^2. \quad (3.11)$$

For small lattice spacing  $a$  and small momenta, i.e. for small  $a\mathbf{p}$ , one has

$$(aE)_{\mathbf{p}}^2 = (a\mathbf{p})^2 + (am)^2 + \mathcal{O}((ap)^2). \quad (3.12)$$

This clearly shows that in the limit of  $a \rightarrow 0$  the lattice dispersion relation obtained above reproduces the continuum dispersion relation up to  $\mathcal{O}((ap)^2)$ , provided that  $ap \ll 1$ .

However, one can immediately see that this discretization procedure adopted above leads to a problem. A direct consequence of the “naive” discretization of the Dirac action is that the momentum  $p_\mu$ , which is the Fourier transform of the continuum derivative  $\partial_\mu$ , is replaced by its sine, or more accurately by  $\tilde{p}_\mu = \frac{1}{a} \sin(ap_\mu)$ . This quantity, which plays the role of the 4-momentum on the lattice is a periodic function of the continuum 4-momentum. Figure 3.1 demonstrates that for momenta up to about half the lattice cutoff  $ap_\mu < \pi/2$ , the continuum limit is relatively well approximated. However, having replaced  $ap$  by  $\sin(ap)/a$  implies that states with momenta near  $\pi/a$  at the edge of the Brillouin zone, actually behave as low momentum states.

Given that the dispersion relation is quadratic in energy-momentum and also since  $\sin(x + \pi) = -\sin(x)$ , we have

$$E_{\mathbf{p}}^2 = E_{\mathbf{p}+\mathbf{q}_\pi}^2, \quad (3.13)$$

where  $a\mathbf{q}_\pi$  can be any of the following eight 3-momentum vectors

$$a\mathbf{q}_\pi \in \{(0, 0, 0), (\pi, 0, 0), (0, \pi, 0), (0, 0, \pi), (\pi, \pi, 0), (\pi, 0, \pi), (0, \pi, \pi), (\pi, \pi, \pi)\}, \quad (3.14)$$

which correspond to the  $2^3$  corners of the Brillouin zone along the 3 spatial directions. Similarly, one also has

$$\sin^2(aE + \pi) = \sin^2(aE), \quad (3.15)$$

which means that the two corners of the Brillouin zone corresponding to the energy component of the 4-momentum will also be equivalent on the lattice. That is

$$aE \in \{ap^0, ap^0 + \pi\} \quad (3.16)$$

will become identical.

This means that, in total, for each continuum Dirac fermion with momentum  $p_\mu$  one gets 16 distinct but identical copies on the lattice, coming from  $2^4$  corners of the Brillouin zone in the 4-momentum space. They mimic 16 different copies of the same fermion. In the continuum limit  $a \rightarrow 0$  they converge to identical copies of the same single physical fermion, or copies of the same quark flavor in the case of QCD.

These 16 copies are referred to as *tastes*, so as to avoid confusion with the usual quark *flavors* which have different masses. The 15 artificial copies are called the *doublers*. They

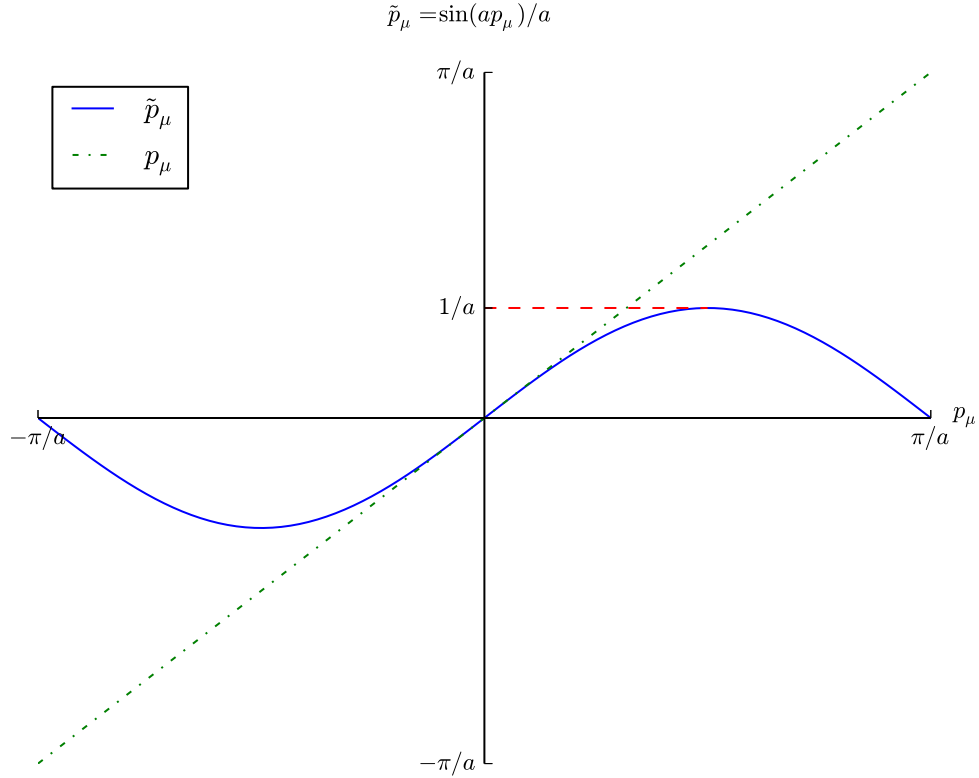


Figure 3.1: Fermion doubling. A naive lattice fermion’s momentum is plotted against the continuum momentum. As we move away from the centre of the Brillouin zone, the lattice momentum  $\frac{1}{a} \sin(ap_\mu)$  starts to split off from the correct continuum limit, quickly deviating away from it once past halfway across to the edge. Very high energy fermions at the corners essentially “double” a low energy one at the centre; hence, acting like a different “taste” of the same low energy fermion.

are pure lattice artifacts and their appearance in the Dirac (naive) discretization is called the fermion (species) doubling problem. Formally, they can be characterized by the specific corners of the Brillouin zone that they belong to through the following relation

$$p^{(\zeta)} = p + \zeta\pi/a, \quad (3.17)$$

with  $-\pi/2 \leq ap_\mu \leq \pi/2$ . Here,  $\zeta$  is a 4-vector whose components  $\zeta_\mu \in \mathbb{Z}_2$  are either 0 or 1 and labels the 16 different tastes of the Dirac fermion on the lattice.

The appearance of the doublers is evident from the sine in the dispersion relation (3.11). Additional insight can be obtained by directly examining the propagator (3.8) itself. Con-

sider a Dirac fermion with momentum  $p^{(\zeta)}$ . At this corner the propagator becomes

$$G(p^{(\zeta)}) = \frac{-i \sum_{\mu} \tilde{p}_{\mu}^{(\zeta)} \gamma_{\mu} + m}{\sum_{\mu} (\tilde{p}_{\mu}^{(\zeta)})^2 + m^2} = \frac{-i \sum_{\mu} \sin(p_{\mu} + \zeta_{\mu} \pi) \gamma_{\mu} + m}{\sum_{\mu} \sin^2(p_{\mu} + \zeta_{\mu} \pi) + m^2},$$

or equivalently

$$G(p^{(\zeta)}) = \frac{-i \sum_{\mu} (-1)^{\zeta_{\mu}} \gamma_{\mu} \sin(p_{\mu}) + m}{\sum_{\mu} \sin^2(p_{\mu}) + m^2}, \quad (3.18)$$

where the definition (3.9) is used and the lattice spacing is set to  $a = 1$  in order to declutter the equations. Notice that  $G(p^{(\zeta)} = p + \zeta\pi)$  obtained here and  $G(p)$  of (3.8) differ only in the sign of the  $\gamma_{\mu}$  terms in the numerator due to the  $(-1)^{\zeta_{\mu}}$  factor

$$\gamma_{\mu} \rightarrow \gamma_{\mu}^{(\zeta)} \equiv (-1)^{\zeta_{\mu}} \gamma_{\mu} = \pm \gamma_{\mu}.$$

These  $\pm \gamma_{\mu}$  matrices are equivalent to the original ones through the unitary transformation

$$(-1)^{\zeta_{\mu}} \gamma_{\mu} = (\gamma_{\bar{\zeta}})^{\dagger} \gamma_{\mu} \gamma_{\bar{\zeta}}, \quad (3.19)$$

where

$$\bar{\zeta}_{\mu} \equiv \sum_{\nu \neq \mu} \zeta_{\nu}. \quad (3.20)$$

These can be constructed by successive applications of

$$\gamma_{\mu} \rightarrow (i\gamma_{\rho}\gamma_5)^{\dagger} \gamma_{\mu} (i\gamma_{\rho}\gamma_5) \quad (3.21)$$

along the spacetime directions denoted by  $\rho = 0, \dots, 3$ , for every non-zero component  $\zeta_{\rho}$ .

Consequently, one can write

$$G(p^{(\zeta)}) = (\gamma_{\bar{\zeta}})^{\dagger} G(p) \gamma_{\bar{\zeta}}. \quad (3.22)$$

This is a result of an important underlying symmetry of the action known as the *doubling* symmetry which we shall see is responsible for the doublers. A comprehensive treatment of this symmetry will be presented in chapter 4. For now, let us continue to examine the propagator.

The poles of (3.7) gave the spectrum above. Evaluation of its residues will reveal another important feature of the doublers. We have

$$S(\mathbf{x}, t) = \int_{-\pi}^{\pi} \frac{d^3 \mathbf{p}}{(2\pi)^3} e^{i\mathbf{p} \cdot \mathbf{x}} \int_{-\pi}^{\pi} \frac{dp^0}{2\pi} e^{ip^0 t} \frac{-i\gamma_0 \sin(p_0) - i\gamma_i \sin(p_i) + m}{\sin^2(p_0) + \sin^2(\mathbf{p}) + m^2}. \quad (3.23)$$

The particle's energy is determined from the poles of the inner integral over the energy component  $p_0$ . This integral is taken over a finite segment of the real line  $-\pi \leq p_0 \leq \pi$ .

A clever trick can be used to turn this interval into a closed contour in the complex plane. The following change of variables

$$z \equiv e^{ip_0} \quad (3.24)$$

will accomplish that by mapping the  $[-\pi, \pi]$  interval to the unit circle. Using

$$dz = ie^{ip_0} dp_0 \quad \Rightarrow \quad dp_0 = \frac{dz}{iz}$$

and

$$\cos(p_0) = \frac{1}{2} \left( z + \frac{1}{z} \right) \quad \Rightarrow \quad \sin^2(p_0) = 1 - (z^2 + z^{-2} + 2)/4,$$

will let one rewrite the inner integral as

$$\begin{aligned} & \int_{-\pi}^{\pi} \frac{dp^0}{2\pi} e^{ip^0 t} \frac{-i\gamma_0 \sin(p_0) - i\gamma_i \sin(p_i) + m}{\sin^2(p_0) + \sin^2(\mathbf{p}) + m^2} \\ & \rightarrow \int_{S^1} \frac{dz}{2\pi iz} (z)^t \frac{-i\gamma_0(z - z^{-1})/2 - i\gamma_i \tilde{p}_i + m}{1 - (z^2 + z^{-2} + 2)/4 + \tilde{\mathbf{p}}^2 + m^2}, \end{aligned}$$

where  $S^1$  denotes the unit circle in the complex plane. Thus, the propagator (3.23) becomes

$$S(\mathbf{x}, t) = -4 \int_{-\pi}^{\pi} \frac{d^3 \mathbf{p}}{(2\pi)^3} e^{i\mathbf{p} \cdot \mathbf{x}} \int_{S^1} \frac{dz}{2\pi i} (z)^t \frac{-i\gamma_0(z^2 - 1)/2 + z(-i\gamma_i \tilde{p}_i + m)}{z^4 - 2Az^2 + 1}, \quad (3.25)$$

with

$$A = 1 + 2(\tilde{\mathbf{p}}^2 + m^2). \quad (3.26)$$

One finds that the propagator has 4 poles at  $z = \pm z_{\pm}$  given by

$$(z_{\pm})^2 = A \pm \sqrt{A^2 - 1}. \quad (3.27)$$

Figure 3.2 shows the contour along with all 4 poles. For ( $t > 0$ ) the two poles inside the unit circle, labeled  $\pm z_-$ , contribute to the propagator giving rise to a free Dirac fermion propagating forward in time and its doubler. The other two at  $\pm z_+$  outside the unit circle will then correspond to the anti-particle and its doubler. Now note that

$$z_+ z_- = (A + \sqrt{A^2 - 1})(A - \sqrt{A^2 - 1}) = 1$$

which allows one simply to write

$$z_{\pm} = e^{\pm \omega}. \quad (3.28)$$

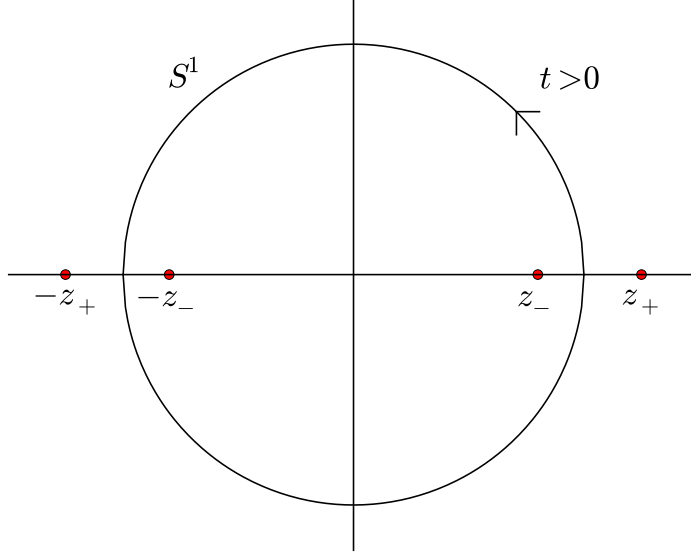


Figure 3.2: Contour integration of a free Dirac fermion propagator in the complex plane. For  $t > 0$  the two poles that fall inside the unit circle,  $\pm z_-$ , contribute to the propagator. The pole at  $-z_-$  corresponds to the energy doubler

According to (3.24), this would be equivalent to  $i\omega \equiv E$ . Using

$$\begin{aligned} \cosh(2\omega) &= \frac{e^{2\omega} + e^{-2\omega}}{2} = \frac{z_+^2 + z_-^2}{2} = A, \\ \sinh^2(\omega) &= \frac{\cosh(2\omega) - 1}{2} = \frac{A - 1}{2}, \end{aligned} \quad (3.29)$$

and substituting for  $A$  from (3.26) yields

$$\sinh^2(\omega) = \tilde{\mathbf{p}}^2 + m^2, \quad (3.30)$$

which is equivalent to the dispersion relation obtained earlier in (3.10).

With that the inner integral can then be written as

$$-4 \int \frac{dz}{2\pi i} (z)^t \frac{-i\gamma_0(z - z^{-1})/2 - i\gamma_i \tilde{p}_i + m}{(z^2 - z_+^2)(z^2 - z_-^2)},$$

with the residue from the pole at  $z = z_-$  given by

$$-4e^{-\omega t} \frac{-i\gamma_0(e^{-2\omega} - 1)/2 + e^{-\omega}(-i\gamma_i \tilde{p}_i + m)}{2e^{-\omega}(e^{-2\omega} - e^{2\omega})} = e^{-\omega t} \frac{(i\gamma_0 \sinh(\omega) - i\gamma_i \tilde{p}_i + m)}{\sinh(2\omega)}.$$



Putting this together with the contribution from the doubler pole at  $z = -z_-$ , gives the naive fermion propagator

$$\begin{aligned}
S(\mathbf{x}, t) = & \int \frac{d^3\mathbf{p}}{(2\pi)^3} \frac{e^{-\omega t + i\mathbf{p}\cdot\mathbf{x}}}{\sinh(2\omega)} (i\gamma_0 \sinh(\omega) - i\gamma_i \tilde{p}_i + m) \\
& + (-1)^t \int \frac{d^3\mathbf{p}}{(2\pi)^3} \frac{e^{-\omega t + i\mathbf{p}\cdot\mathbf{x}}}{\sinh(2\omega)} (-i\gamma_0 \sinh(\omega) - i\gamma_i \tilde{p}_i + m)
\end{aligned} \tag{3.31}$$

for forward propagation in time.

That second term is why we went through the above calculation. It corresponds to the energy doubler which we had already met. In addition, that  $(-1)^t$  reveals that the doublers oscillate in sign from even to odd time steps on the lattice.

The four poles are at  $\pm i\omega$  and  $\pm i\omega \pm \pi$  where  $p_0 = -i\omega$  and  $p_0 = -i\omega + \pi$  are relevant for  $t < 0$ . Note also that  $\omega$  depends on  $\tilde{\mathbf{p}} = \sin(\mathbf{p})$ , which means that in addition to the energy doubler, there is a momentum doubler for every spatial dimension resulting in exactly 16 copies of a single fermion in total as seen earlier in this section.

This artificial proliferation of fermions on the lattice is a problem. A very high energy fermion with  $p \approx \pi/a$ , which is the highest momentum allowed on the lattice, is actually not far off energy shell since it's identical to a low energy one with  $p \approx 0$ . As a result, the discretized theory quickly deviates from the continuum. As illustrated in Figure 3.1, the continuum limit is broken when the momentum moves past halfway through the full width of the Brillouin zone due to the lattice momentum  $\tilde{p}$  diverging from the continuum momentum  $p$  and the odd properties of the doubler states.

So far we've seen that by employing the naive discretization scheme, one gets 16 different tastes of a single physical fermion on the lattice. That's 15 too many. One may wish to ignore these extra species arguing that they are degenerate copies of the original one, while keeping in mind that the fermion's behavior on the lattice is effectively magnified 16-fold. The correct continuum limit could then be recovered by sticking factors of  $1/16$  in appropriate places to account for the presence of the doublers. For instance, in order to correct the quark vacuum polarization, one would counteract the amplification effect of having 16 tastes of each dynamical sea quark by taking the 1/16-th root of the determinant of the fermion matrix that resulted from the path integral over the quark fields

$$\det(\gamma \cdot \Delta + m) \rightarrow \det(\gamma \cdot \Delta + m)^{1/16}. \tag{3.32}$$

That would be equivalent to multiplying every quark loop by  $1/16$ .

This is possible in a non-interacting theory in which different taste states are indeed exactly degenerate. However, since momentum is only conserved modulo  $2\pi$  on the lattice, in an interacting theory taste exchange interactions may occur. Such interactions result in

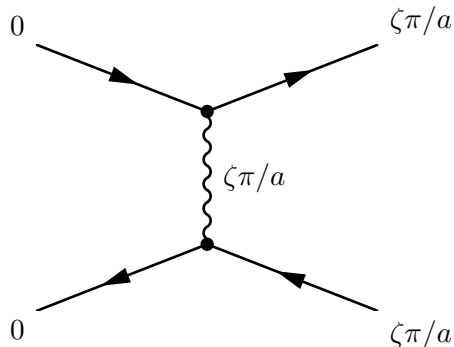


Figure 3.3: A tree level taste exchange interaction between two quarks,  $q\bar{q} \rightarrow q\bar{q}$ , through the exchange of a highly virtual gluon with momentum  $\zeta\pi/a$ , where  $\zeta^2 \neq 0$ , resulting in taste mixing in an interacting theory.

mixing between taste states and consequently splitting between their energies. Therefore, different taste states are no longer degenerate.

Figure 3.3 shows a simple tree level example of a taste changing interaction between two quarks  $q\bar{q} \rightarrow q\bar{q}$ , through the exchange of a highly virtual gluon with momentum  $\zeta\pi/a$ , for some non-zero  $\zeta \neq 0$ . Absent interactions, two quarks with momenta differing by exactly  $\zeta\pi/a$  would have been degenerate. Once interactions are turned on, however, that degeneracy is lifted. This means that the 1/16 trick may not work for an interacting theory at all. Contributions from different tastes enter with different values and therefore taking the 1/16-th root only approximates the physical fermions, leading to additional  $\mathcal{O}(a^2)$  discretization errors [33].

To recap, it should now be clear why the initial approach is called the “naive” discretization. The continuum derivative was replaced by a simple finite difference. This was basically equivalent to replacing the momentum by  $\sin(p_\mu)$ . Due to the sine function fermions with very high momenta, of the order of the lattice cutoff  $p_\mu \approx \pi/a$ , actually entered the theory pretending to be low energy fermions with  $p_\mu \approx 0$ . That gave rise to 16 different tastes of a single fermion.

Arguing that in the absence of interactions these taste states are degenerate, they can be properly dealt with by simply dividing their contributions out. However, this trick is spoiled as soon as interactions are included in the theory, enabling taste exchange and lifting the degeneracy. Additional  $\mathcal{O}(a^2)$  discretization errors arise. These unphysical tastes and their associated taste changing errors greatly complicate doing accurate simulations of fermions on the lattice. This gives rise to the vast and technically difficult subject of discretizing fermions. In the rest of this chapter we will describe a number of popular methods to ameliorate this problem.

### 3.1.2 Wilson Fermions

In the previous section we saw that the problem with the doublers is that due to the form of the lattice dispersion relation, very high energy fermions effectively become identical

to low energy fermions. One approach to treating this sickness is to push them off back to very high energies by modifying the lattice action. This can be achieved by adding a momentum dependent mass term to the action that raises the masses of the unwanted fermions to values of the order of the lattice cutoff energy and thereby decouples them from the physical fermions. Wilson proposed the following [18]

$$\begin{aligned}
m \sum_x \bar{\psi}(x)\psi(x) &\rightarrow m \sum_x \bar{\psi}(x)\psi(x) + \frac{ar}{2} \sum_{x,\mu} \partial_\mu \bar{\psi}(x) \partial_\mu \psi(x) \\
&= m \sum_x \bar{\psi}(x)\psi(x) + \frac{ar}{2} \sum_{x,\mu} \frac{1}{a^2} (\bar{\psi}(x+a\hat{\mu}) - \bar{\psi}(x)) (\psi(x+a\hat{\mu}) - \psi(x)) \\
&= \left(m + \frac{4r}{a}\right) \sum_x \bar{\psi}(x)\psi(x) - \frac{r}{2a} \sum_{x,\mu} (\bar{\psi}(x+a\hat{\mu})\psi(x) + \bar{\psi}(x)\psi(x+a\hat{\mu})),
\end{aligned} \tag{3.33}$$

where  $0 < r \leq 1$  is referred to as the Wilson parameter. The Wilson fermion action, therefore, takes the form

$$\mathcal{S}_f^{(W)} = \mathcal{S}_f - \frac{ar}{2} \sum_x \bar{\psi}(x) \square \psi(x), \tag{3.34}$$

where  $\square \equiv \sum_\mu \partial_\mu^2$  in the continuum.

In momentum space the effect of adding the Wilson term is to modify the mass as

$$m \rightarrow m + \frac{r}{a} \sum_\mu (1 - \cos(ap_\mu)), \tag{3.35}$$

effectively making it momentum dependent. In terms of the new “mass” parameter

$$M(p) \equiv m + \frac{2r}{a} \sum_\mu \sin^2(ap_\mu/2), \tag{3.36}$$

the Wilson fermion propagator will take the form

$$G^{(W)}(p) = \frac{-i\gamma_\mu \tilde{p}_\mu + M(p)}{\tilde{p}^2 + M^2(p)}, \tag{3.37}$$

where the original bare fermion mass  $m$  is simply replaced by the new coefficient of the modified mass term in the action introduced in (3.33). Now let us revisit and inspect the troublesome corners of the Brillouin zone that housed the spurious doublers. The Wilson propagator at the corner labeled by  $\zeta$  is given by

$$G^{(W)}(p^{(\zeta)}) = \frac{-i\gamma_\mu^{(\zeta)} \tilde{p}_\mu + m_\zeta}{\tilde{p}^2 + m_\zeta^2}, \tag{3.38}$$

where  $m_\zeta \equiv M(p^{(\zeta)})$  determines the location of the poles and hence gives the mass of the free Wilson fermion occupying that corner. Repeating a pole analysis exercise similar to what was done for the naive action in the previous section, one can obtain the mass of

the Wilson fermion by evaluating the propagator in the coordinate space, through finding its poles in the momentum space. This is a fairly straightforward exercise and won't be repeated here. It is easy to verify that the Wilson fermion mass at the corner labeled by  $\zeta$  turns out to be

$$m_\zeta = m + 2n_\zeta r/a, \quad n_\zeta = \zeta^2 = 0, 1, \dots, 4, \quad (3.39)$$

where  $n_\zeta = \zeta^2$  is the number of non-zero components of  $\zeta$ . For a fermion at the low energy corner of the Brillouin zone, that is for  $\zeta = 0$ , we have  $n_\zeta = 0$ , which means that its Wilson mass is equal to the bare mass in the action. In contrast, at each of the other 15 corners of the Brillouin zone that gave rise to the doublers in the naive formulation, we have  $n_\zeta > 0$  due to at least one of the 4 components of  $\zeta$  being non-zero. Consequently, in the limit of  $a \rightarrow 0$ , a fermion inhabiting any of those 15 corners becomes infinitely heavy for  $r \neq 0$ , and decouples from the continuum limit. This is precisely what the Wilson term was intended to achieve. There are no doublers in the Wilson formulation.

Note that avoiding the doublers is a direct consequence of the specific momentum dependence of the Wilson term in the form of  $\sin^2(ap_\mu/2)$ . The  $1/2$  factor in the argument of the sine function is crucial, and is responsible for driving the mass of the unwanted potential doublers with momenta  $p \approx \pi/a$  which inhabit the problem corners of the Brillouin zone, far off shell. This is the same type of momentum dependence that appear in discretized boson propagators which do not suffer from the doubling problem for the exact same reason. Figure 3.4 illustrates this by showing the energy spectrum of a boson as well as a naive fermion on the lattice along with the continuum dispersion relation.

Although the Wilson method successfully solves the doubling problem, it does so at the expense of introducing  $\mathcal{O}(a)$  discretization errors. Consider Wilson's choice of  $r = 1$ . It can be shown from (3.37) that the particle's energy is given by

$$\omega = \omega_0^- = \sqrt{m^2 + \mathbf{p}^2} + \mathcal{O}(a). \quad (3.40)$$

This has  $\mathcal{O}(a)$  errors as compared with the naive action's  $\mathcal{O}(a^2)$  errors. This represents a significant drawback for the Wilson method in practical calculations, as it would require a much smaller lattice spacing to achieve the same accuracy as that when using an  $\mathcal{O}(a^2)$  accurate method making it computationally more expensive. Time for improvement.

Sheikholeslami and Wohlert's idea was to start with adding an operator to the Dirac action that included the Wilson term as part of it but which was redundant up to  $\mathcal{O}(a^2)$  and therefore did not introduce  $\mathcal{O}(a)$  errors [34]. *Redundant* operators are operators that can be added to or removed from the action by a field redefinition and thus have no effect on physical observables. In other words, the  $\mathcal{O}(a)$  errors due to the Wilson term are canceled by another new term which then together become equivalent to the original naive action up to  $\mathcal{O}(a^2)$  through a fermion field transformation.

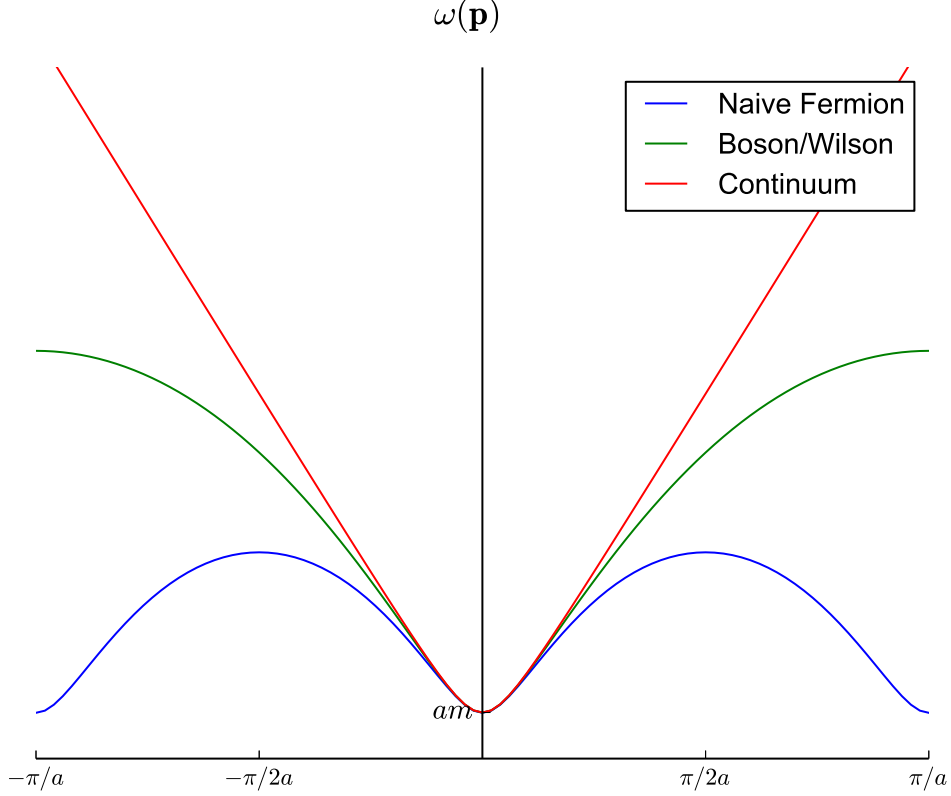


Figure 3.4: The energy spectra of lattice bosons and “naive” fermions along with that of a continuum particle, plotted as a function of momentum. The values of  $\omega$  are extracted from the poles of the lattice propagator for each particle. The continuum energy is simply obtained from the continuum dispersion relation. The addition of the Wilson term causes the Wilson fermion’s energy to qualitatively mimic a boson’s at high energies, thereby removing the unwanted doublers.

Consider the following field redefinition

$$\psi \rightarrow \left[ 1 - \frac{ra}{4}(\Delta \cdot \gamma - m_0) \right] \psi. \quad (3.41)$$

The lattice Dirac action then becomes

$$\bar{\psi}(\Delta \cdot \gamma + m_0)\psi \rightarrow \bar{\psi} \left[ \Delta \cdot \gamma + m_0 + \frac{ram_0^2}{2} - \frac{ra}{2} \left( \Delta \cdot \Delta + \frac{\sigma \cdot gF}{2} \right) \right] \psi + \mathcal{O}(a^2), \quad (3.42)$$

where  $\sigma_{\mu\nu} \equiv -\frac{i}{2}[\gamma_\mu, \gamma_\nu]$ . Nothing is changed yet. The new terms multiplied by  $a$  do not result in  $\mathcal{O}(a)$  errors since they’re redundant. But the doublers haven’t been removed yet either. The trick is now to replace the  $\Delta \cdot \Delta$  operator which vanishes at the cutoff, by the second derivative operator  $\Delta^{(2)}$  which doesn’t. These are the same up to  $\mathcal{O}(a^2)$ . This

is equivalent to replacing  $(\sin(ap)/a)^2$  by  $(2\sin(ap/2)/a)^2$  which differ by  $\mathcal{O}((ap)^2)$ . This difference is small at low momenta but near the cutoff will push the doublers far off shell.

The Sheikholeslami-Wohlert action [34] is thus formulated as

$$\mathcal{S}_{\text{SW}} = \sum \bar{\psi}(x) \left( \gamma \cdot \Delta + m - \frac{r}{2} \Delta^{(2)} + c_{\text{SW}} \sigma_{\mu\nu} F_{\mu\nu} \right) \psi(x). \quad (3.43)$$

The SW action is also referred to as the *clover* action due to the shape of the  $F_{\mu\nu}$ , with the 4 leaves being plaquette operators.

This fixes the  $\mathcal{O}(a)$  errors. However, another more serious disadvantage of Wilson type fermions persists. The Wilson term explicitly breaks the chiral symmetry of the action even for massless fermions. As a result, the chiral limit  $m = 0$  is not protected. In particular, the mass gets an additive renormalization which means that the fermion matrix  $M$  may have non-positive eigenvalues. Whether a valence quark or in the sea, a non-positive definite  $M$  is bad news for the computing budget. Configurations with negative  $\det M$  need be dealt with separately after having spent so much computing time generating them and those that are singular due to (nearly) zero eigenvalues will take too long to invert.

The Wilson method has not been used in this work, so we refrain from discussing it in more detail. In the next section we will go back to a variation of the naive discretization scheme known as staggered fermions, or less commonly as the Kogut-Susskind fermions [19, 20, 21].

### 3.1.3 Staggered Fermions

The problem with the naive formulation encountered in subsection 3.1.1 was the appearance of the undesirable doublers which popped up at the high energy corners of the Brillouin zone with near cutoff momenta. This suggested that one might be able to solve the problem by somehow cutting out the problem regions off the momentum space whence specious fermion species arose.

In other words, the idea is to crop the Brillouin zone in every direction to the halfway point across to the edge at  $p_\mu = \pi/2a$ . Breaking the entire zone down into 16 equal pieces, this reduction keeps the low energy corner and excises the other 15 populated by the doublers. The question is what exactly does that entail. Shortly after Wilson's original paper, the Kogut-Susskind fermions were proposed in [19, 20, 21].

Bounding the momentum at  $\pi/2a$  is equivalent to doubling the effective size of the lattice spacing. To that end, one could reduce the resolution of the grid by defining the fermion fields on the *elementary hypercubes* instead of on every lattice site. Each hypercube contains two sites per edge and  $2^d$  sites in total where  $d = 4$  is the number of spacetime dimensions. The  $2^{d/2}$  spinor degrees of freedom of the fermion field are said to be *staggered* over the lattice sites in the hypercube.

However, notice that in  $d = 4$ , this *blocking* still leaves a 4-fold degeneracy since 4 fermion fields are needed to populate all 16 sites of a hypercube. Thus, grouping these fields and staggering their spin degrees of freedom over elementary hypercubes reduces the number of doublers from 16 down to 4. Since they are of no practical use to us in this work, we will limit our discussion of the blocked hypercube formulation of staggered fermions to the above qualitative description.

We will take a different approach to the formulation of the staggered fermions that is equivalent to the hypercube method which is more directly related to the practical implementations of calculations. It simply involves a basis rotation.

The free Dirac fermion action is given in the spinor basis by

$$\mathcal{S} = \sum_x \bar{\psi}(x)(\gamma \cdot \Delta + m)\psi(x), \quad (3.44)$$

One can perform a unitary transformation of the fermion field variables as

$$\psi(x) \rightarrow \Omega(x)\chi(x), \quad \bar{\psi}(x) \rightarrow \bar{\chi}(x)\Omega^\dagger(x), \quad (3.45)$$

which would correspond to changing the spinor basis. Now consider the following choice for the basis rotation matrices

$$\Omega(x) \equiv \gamma_x \equiv \prod_{\mu=0}^3 (\gamma_\mu)^{x_\mu}. \quad (3.46)$$

This particular transformation is interesting because it diagonalizes the action in the spinor space. These matrices can be easily verified to satisfy the following relation

$$\Omega^\dagger(x)\gamma_\mu\Omega(x \pm a\hat{\mu}) = \alpha_\mu(x)\mathbf{1}_{\text{spinor}}, \quad (3.47)$$

where  $\alpha_\mu(x)$  is a coordinate dependent phase with values given by

$$\alpha_0(x) = 1, \quad \alpha_1(x) = (-1)^{x_0}, \quad \alpha_2(x) = (-1)^{x_0+x_1}, \quad \alpha_3(x) = (-1)^{x_0+x_1+x_2}, \quad (3.48)$$

or in a more compact notation

$$\alpha_\mu(x) \equiv (-1)^{x_0+\dots+x_{\mu-1}} \equiv (-1)^{x_\mu^<}. \quad (3.49)$$

With this change of variables, the derivative terms in the action will transform as

$$\begin{aligned} \bar{\psi}(x)\gamma_\mu\psi(x \pm a\hat{\mu}) &\rightarrow \bar{\chi}(x)\Omega^\dagger(x)\gamma_\mu\Omega(x \pm a\hat{\mu})\chi(x \pm a\hat{\mu}) \\ &= \alpha_\mu(x)\bar{\chi}(x)\chi(x \pm a\hat{\mu}). \end{aligned} \quad (3.50)$$

Notice that thanks to (3.47), the  $\gamma$  matrix is eaten up by the  $\Omega$  matrices and disappears from the action turning into a phase denoted by  $\alpha$ .

Rewriting the action in this new *staggered basis* results in

$$\mathcal{S} = \sum_{\beta=1}^4 \left[ \frac{1}{2a} \sum_{x,\mu} \alpha_{\mu}(x) \left( \bar{\chi}^{\beta}(x) \chi^{\beta}(x + a\hat{\mu}) - \bar{\chi}^{\beta}(x) \chi^{\beta}(x - a\hat{\mu}) \right) + m \sum_x \bar{\chi}^{\beta}(x) \chi^{\beta}(x) \right], \quad (3.51)$$

where the spinor indices have been made explicit. Note that there is no mixing between the four spinor degrees of freedom denoted by  $\beta = 1, \dots, 4$ . The action is diagonalized in the spin space and therefore the four spinor components are decoupled.

This means that the four field components  $\chi^{\beta}$ , become identical as a consequence of their decoupling, and the action becomes the sum of four identical terms, one for each spinor component. They lead to identical physics. Hence, one of four terms suffices to describe a fermion on the lattice. This allows one to simply truncate the sum that runs over the four spinor components in the action, discarding three and keeping only one.

Thus, in the new staggered basis the action takes the form

$$\mathcal{S} = \sum_x \bar{\chi}(x) (\alpha \cdot \Delta + m) \chi(x), \quad (3.52)$$

where the fermion fields are now represented by 1-component fields  $\chi$ , called staggered fields.<sup>1</sup> This essentially reduces the number of degrees of freedom by a factor of 4. Consequently, there are only  $16/4 = 4$  different staggered tastes as opposed to 16 “naive” tastes.

Remarkably, this reduction in the number of doublers due to the spin diagonalization of the staggered fermion survives in the interacting theory. This is surprising given that gluon interactions can cause spin flip. As a result, one would expect that adding interactions would destroy this degeneracy in the spinor components and therefore un-decouple them. However, it is easy to see that in the Dirac formulation, the quark spin degrees of freedom are packaged in a way that all such effects are encapsulated in a single spinor components.

This is readily evident by considering how interactions with gluons are introduced into the theory. Recall from chapter 2 that the gluon fields are encoded into the link variables  $U_{\mu}$  whose job was to make sense of finite differences in a locally gauge invariant theory. Thus, the lattice version of the covariant derivative  $D_{\mu} = \partial_{\mu} - igA_{\mu}$  is naturally constructed by simply connecting the fermion fields at different sites in every finite difference operator in the action by the link variables. Thus, upgrading the finite difference operator to

$$\Delta_{\mu}(U)\psi(x) \equiv \frac{1}{2a} \left( U_{\mu}(x)\psi(x + a\hat{\mu}) - U_{\mu}^{\dagger}(x - a\hat{\mu})\psi(x - a\hat{\mu}) \right) \quad (3.53)$$

---

<sup>1</sup> From now on, throughout most of the rest of this thesis “staggered fields” denoted by  $\chi$  represent the reduced 1-component spinor fields corresponding to any one of the 4 identical components of the spin diagonalized fields.



turns a free theory into an interacting one. Thus the full interacting staggered quark action simply takes the form

$$\mathcal{S} = \sum_x \bar{\chi}(x) (\alpha \cdot \Delta(U) + m) \chi(x). \quad (3.54)$$

The 4-fold reduction in the number of degrees of freedom in the spin diagonalized basis represents an enormous computational advantage for staggered quarks. What's more, and equally importantly, the staggered formulation preserves a remnant chiral symmetry and guarantees that  $M$  is positive definite. Being numerically fast and protecting the chiral limit, the staggered quarks teased with promise. However, recall that there are still three remaining doublers in the corners of the Brillouin zone that can exchange tastes and cause additional errors. More on this in section 3.2.

## 3.2 Heavy Staggered Quarks; The Improvement Program

We have now seen clearly that putting QCD on a discretized spacetime gives rise to lattice artifacts and discretization errors. These errors are expected to go away in the continuum limit. However, recall from chapter 1 that as the lattice spacing  $a \rightarrow 0$  the simulation cost grows fast as  $1/m_\pi^2 a^6$  [14]. This makes the lattice spacing the most important determinant of the simulation cost thereby significantly constraining one's ability to reduce errors through sheer brute force. In order to achieve high quality simulations, an improvement program was embarked upon whereby the leading order finite- $a$  discretization errors were identified and canceled to desired powers of the lattice spacing. Improvement of lattice effective theories was pioneered by Symanzik [25] in 1983 and has been pursued relentlessly ever since. We've seen it applied to a few theories. Here we review with greater detail the improvement of staggered fermions.

Staggered quarks have been around since mid 1970s. They are much faster to simulate than other discretizations of fermions and have the enormous advantage of preserving a remnant chiral symmetry for massless quarks. However, their unusually large  $\mathcal{O}(a^2)$  errors had rendered them practically useless for accurate simulations at typical lattice spacings for two decades until the late 1990s when it was discovered how to remove them.

The  $\mathcal{O}(a^2)$  discretization errors of the staggered quark action have two sources. The first source is the usual classical errors that arise from replacing continuum derivatives by lattice finite differences. The correction is standard and simply involves a more accurate implementation of the finite difference operator.

The second source was initially missed for almost a decade and is due to quantum effects as a results of the staggered quarks' taste changing interactions. People knew about the peculiar property of the staggered discretization where it created 4 copies of a quark field on the lattice, instead of just one. These 4 different tastes combine in a quark-antiquark pair to create 16 tastes of a single physical meson. These mesons would have been identical

had there been no mixing between different quark tastes. The correction then would have been trivial: factors of 1/16 strategically inserted in appropriate places.

The degeneracy is spoiled, however, as a result of *taste exchange* interactions whereupon taste is transferred from one quark to another through the exchange of a gluon. Instead of one  $\pi^+$ , for example, one has 16 only one of which corresponds to the Goldstone pion while all others have different masses. The smallest taste splitting between them obtained from simulations of unimproved staggered quarks on lattices with a spacing of order  $a \approx 0.1$  fm, which was until recently fairly typical, turned out to be about  $a^2 \delta m_\pi^2 \approx (300 \text{ MeV})^2$ ; twice the mass of the pion itself [16].

The generic correction for such mixing is through adding 4-quark interactions like above. The tree level improvement of the action would then require matching on-shell tree level lattice quark-quark scattering amplitudes to continuum QCD at low external momenta. This correction was missed because continuum QCD doesn't *have* any such interactions at tree level for the lattice theory to match its corresponding amplitudes to.

Normally, tree level 4-quark interactions at low external momenta would imply a low momentum exchanged gluon as well. The amplitude would then automatically match if the gluon vertices did, and hence the correction was thought unnecessary at tree level. This argument is incorrect for staggered quarks. Two low energy staggered quarks can exchange a very high energy gluon, say with  $q = (\pi/a, 0, 0, 0)$ , and subsequently turn into a pair of low energy quarks of a different taste, as illustrated in Figure 3.3.

A breakthrough was made in the late 1990s when it was observed in [35, 36] that replacing the gauge fields by “smeared” link variables in simulations greatly reduced taste splittings in the spectrum of the 16 different tastes of the pion. The empirical discovery that smeared links happen to suppress quark-quark taste exchange scattering amplitudes, led to the first correct understanding of the underlying mechanism of the taste symmetry violation [37, 38, 39, 17]. The  $a^2$  improvements subsequently proposed in a seminal work by Lepage in 1998 [17], resulted in the widely used “asqtad” action which featured corrections that were designed to restore the taste symmetry. The asqtad fermions became the basis for the first successful implementation of dynamical light quarks within the framework of the staggered quark formalism.

While hugely successful for light quarks, the asqtad action's application to heavy quarks was hindered by  $\mathcal{O}(am)$  errors as well as residual taste changing interactions which yet remained the largest source of  $a^2$  errors. High quality simulations of heavy quarks are particularly difficult because discretization errors are large unless either  $am \ll 1$  or they are highly suppressed through improvements. Accurate simulations of  $b$  quarks with few percent accuracy, for instance, would require lattice spacings of about 1/20 fm, which is much too small to be practical today. Nonrelativistic effective theories where the rest mass is removed from the lattice action, such as NRQCD, have been applied to  $b$  quarks with great success. However, they have been less successful for charm quarks since they are not

heavy enough to be adequately treated as nonrelativistic and not light enough to have small  $(am)^2$  errors. On a typical lattice currently available with  $a \approx 0.1$  fm, the charm quark mass is of order  $am_c \approx 0.5$ . Thus, achieving couple percent accuracy using staggered charm quarks is possible provided that  $\mathcal{O}((am)^4)$  errors are highly suppressed.

Therefore, it is worthwhile to fully understand taste changing interactions and further suppress them beyond tree level. While smearing can eliminate taste violation at tree level, they can be completely removed at loop level only through 4-quark contact terms, which are quite difficult to implement in dynamical simulations. However, experimenting with smearing showed that additional smearing of the gauge fields can greatly inhibit taste exchange even at loop level [40]. Finally, a rigorous analysis of all taste exchange interactions to one-loop order by the HPQCD collaboration culminated in the formulation of the highly improved staggered quark (HISQ) action [9], which made high precision simulations of staggered charm quarks possible.

This section expands upon the above mentioned developments. It presents a detailed analysis of all discretization errors of the staggered quark formalism and describes the improvements undertaken to address each. A broad overview of the procedure was outlined in section 2.1 and is described with greater detail in the rest of this section. This procedure involves various classical and quantum improvements and constitutes a double expansion in the lattice spacing  $a$  and the coupling constant  $\alpha_s$ . These methods, as organized here, are usually applied in conjunction with one another together with various other techniques and are not mutually exclusive. QCD is too difficult and so it demands lattice theorists to use every tool at their disposal.

### 3.2.1 Tree Level Symanzik Improvements

The covariant derivative in the continuum action is replaced by a symmetrical finite difference operator on the lattice given by (3.53). This approximation introduces  $\mathcal{O}(a^2)$  discretization errors. The standard and obvious correction is to include higher order terms in the Taylor expansion of the finite difference by replacing

$$\Delta_\mu \rightarrow \Delta_\mu - \frac{a^2}{6} \Delta_\mu^3. \quad (3.55)$$

The new three-link term is referred to as the ‘‘Naik’’ term [41]. This improvement reduces pure kinematical errors due to breaking the continuum rotational symmetry which are present even in the absence of interactions. However, as mentioned before, it does not remove the taste breaking errors. These are the largest remaining  $a^2$  errors at tree level, and the subject of the next section.

### 3.2.2 Taste Violation; Smearing and the Asqtad Action

We saw that the taste symmetry is broken due to interactions such as that illustrated in Figure 3.3, where taste is transferred from one quark to another in a quark-quark scattering process  $q\bar{q} \rightarrow q\bar{q}$ . As a result, the degeneracy among the otherwise identical tastes is lifted. This leads to large taste splittings among the 16 different tastes of the same meson.

The main currency in taste exchange among staggered quarks is a gluon with momentum  $\approx \pi/a$ —which incidentally is the maximum momentum allowed on the lattice—along one or more dimensions. Thus, it comes in 15 denominations of  $q \approx \zeta\pi/a$ , where  $\zeta$  is a 4-vector with  $\zeta_\mu \in \mathbb{Z}_2$  and at least one non-zero component. Meanwhile, despite absorbing such large momenta, the quarks aren't driven far off energy-shell. Instead, they just get bumped to a different corner of the Brillouin zone and turn into low energy quarks of a different taste.

The exchanged gluons are highly virtual and must be immediately reabsorbed by another quark. This has three important implications: Taste exchange interactions are inherently perturbative for sufficiently small lattice spacings. They are effectively indistinguishable from 4-quark contact interactions. And third, the dominant taste changing interactions are a one-gluon exchange with  $q \approx \zeta\pi/a$  in a process with 4 external quarks. To elaborate, one-gluon interactions are lowest order in  $\alpha_s(\pi/a)$ . And being dimension six, 4-quark operators are of order  $(ap)^2$  where  $p$  is a typical external momentum. Therefore, more external quark pairs are suppressed by additional factors of  $(ap)^3$ .

These are crucial observations in trying to restore the taste symmetry. Taste breaking interactions can be removed by adding 4-quark interactions to the lattice action. But, these are hard to implement. Alternatively, having identified the dominant source of taste violation errors, that is tree level gluon exchange with  $q \approx \zeta\pi/a$ , one can significantly reduce those errors through a targeted suppression of these unwanted interactions.

This can be achieved through modifying the quark-gluon vertex  $\bar{\psi}\gamma_\mu U_\mu\psi$ , by introducing a form factor  $f_\mu(q)$  that vanishes for all 15 taste changing gluons but remains unchanged at low momenta. In fact, since the original interaction already vanishes for  $q_\mu = \pi/a$ , the form factor need not vanish for  $\zeta_\mu = 1$ , leaving only those among the 15 taste mixing  $\zeta$ 's that have a non-zero transverse momentum. Thus the desired vertex form factor must look like

$$f_\mu(q) \rightarrow \begin{cases} 1 & \text{for } q \rightarrow 0, \\ 0 & \text{for } q \rightarrow \zeta\pi/a, \text{ where } \zeta^2 \neq 0, \zeta_\mu = 0. \end{cases} \quad (3.56)$$

Such a form factor may be engineered through applying a *smearing* operator

$$\mathcal{F}_\mu \equiv \prod_{\rho \neq \mu} \left( 1 + \frac{a^2 \delta_\rho^{(2)}}{4} \right) \Big|_{\text{symmetrized}} \quad (3.57)$$

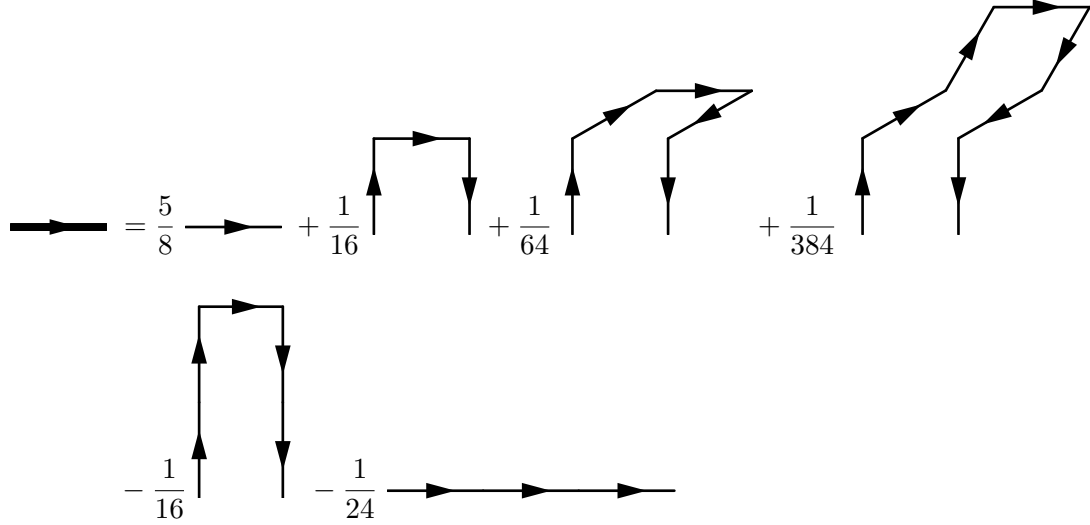


Figure 3.5: Asqtad link smearing. Up to coefficients, the first line illustrates the “fat7” smearing (3.57). It fattens  $U_\mu$  by adding 3-, 5- and 7-staples, which suppress gluons with taste changing momenta along 1, 2 and all 3 of the transverse directions respectively. The straight 5-link staple is the “Lepage” term and removes the additional  $\mathcal{O}(a^2)$  errors introduced by fat7 smearing. The straight 3-step path is due to the Naik term. The coefficients are chosen so that the symmetrized sum over all possible orderings of links in a particular smearing scheme produces the correct gluon vertex and therefore are scheme dependent.

on every link variable  $U_\mu$ , where  $\delta_\rho^{(2)}$  is like a covariant second derivative that acts on links:

$$\delta_\rho^{(2)} U_\mu(x) \equiv \frac{1}{a^2} \left( U_\rho(x) U_\mu(x + a\hat{\rho}) U_\rho^\dagger(x + a\hat{\mu}) - 2U_\mu(x) + U_\rho^\dagger(x - a\hat{\rho}) U_\mu(x - a\hat{\rho}) U_\rho(x - a\hat{\rho} + a\hat{\mu}) \right). \quad (3.58)$$

This replaces a single-link straight path by a sum of longer ones called *staples*. Each is obtained by multiplying contiguous links forming a connected path that looks like a staple and has the same overall end points as the original link. Hence, smearing respects gauge invariance.

Smearred links are also often referred to as *fat* links [42]. The operator (3.57) results in staples of length 3, 5 and 7 links in addition to the original *thin* link which are illustrated in Figure 3.5. This smearing scheme is therefore referred to as *fat7* smearing [35, 36].

It is easy to confirm that this smearing scheme has the desired effect of the form factor (3.56). Consider the effect of  $(1 + a^2 \delta_\nu^{(2)})/4$  on  $U_\mu$  in momentum space. Expanding in terms of the gluon field  $A_\mu$  to first order in  $g$ , we have

$$A_\mu(p) \rightarrow A_\mu(p) + \left[ \frac{\cos(ap_\nu) - 1}{2} A_\mu(p) + \sin(ap_\mu/2) \sin(ap_\nu/2) A_\nu(p) \right], \quad (3.59)$$

which eliminates the  $A_\mu(p)$  if  $p_\nu = \pi/a$ , thereby preventing the exchange of a taste changing gluon, while having almost no effect, up to  $\mathcal{O}(a^2)$ , on a low momentum gluon vertex. Successive applications of smearing along all transverse directions  $\rho \neq \mu$ , will therefore eliminate couplings to gluons with a taste changing momentum along any of those directions.

Though this suppresses the  $\mathcal{O}(a^2)$  tree level taste changing interactions which take place at  $p \approx \pi/a$ , it introduces new taste-*conserving* ones that pop up at  $p \approx 0$ . Those errors are in turn removed by a straight 5-link staple known as the *Lepage* term [17] resulting in the *asqtad* smearing given by

$$\mathcal{F}_\mu^{\text{ASQTAD}} \equiv \mathcal{F}_\mu - \sum_{\rho \neq \mu} \frac{a^2(\delta_\rho)^2}{4}, \quad (3.60)$$

where  $(\delta_\rho)^2$  is the square of a discretized covariant first-order derivative defined as

$$\delta_\rho U_\mu(x) \equiv \frac{1}{2a} \left( U_\rho(x) U_\mu(x + a\hat{\rho}) U_\rho^\dagger(x + a\hat{\mu}) - U_\rho^\dagger(x - a\hat{\rho}) U_\mu(x - a\hat{\rho}) U_\rho(x - a\hat{\rho} + a\hat{\mu}) \right). \quad (3.61)$$

In momentum space this has the effect of

$$A_\mu(p) \rightarrow \frac{\cos(2ap_\nu) - 1}{2} A_\mu(p) + \sin(ap_\mu/2) [\sin(ap_\nu/2) + \sin(3ap_\nu/2)] A_\nu(p), \quad (3.62)$$

which does not affect couplings to taste changing gluons while canceling the new low energy  $a^2$  errors introduced by fat7 smearing.

Finally, the  $\mathcal{O}(a^2)$  taste violation improvement is combined with the  $a^2$  improvement of the discretized derivative through the Naik term introduced in the previous section, resulting in the famous *asqtad* action

$$\mathcal{S}^{\text{ASQTAD}} = \sum_x \bar{\psi}(x) \left( \sum_\mu \gamma_\mu \left( \Delta_\mu(V) - \frac{a^2}{6} \Delta_\mu^3(U) \right) + m_0 \right) \psi(x) \quad (3.63)$$

where

$$V_\mu(x) \equiv \mathcal{F}_\mu^{\text{ASQTAD}} U_\mu(x) \quad (3.64)$$

and is illustrated by the diagram in Figure 3.5.

One might be wondering why there is not a “tad” component in the *asqtad* action presented here. This formulation actually differs slightly from the original *asqtad* action. The “asq” stands for  $a^2$  improvements in the form of smearing as well as the Naik term and is unchanged. The “tad” is for the tadpole improvement seen in subsection 2.2.2 which involves renormalization of gauge links by the so called tadpole factor:  $U_\mu \rightarrow U_\mu/u_0$ . We shall see, however, that further improvements to the staggered quarks discussed in the following sections will make the tadpole improvement unnecessary.

In short, tadpole diagrams are only important because they are UV divergent and the  $1/a^2$  due to the divergence cancels their  $a^2$  suppression. Thus, effectively lowering the hard

cutoff from  $\pi/a$  would reduce their unphysical contributions. Smearing does exactly that through the smooth form factor in (3.56). This suggests that multiple smearing would make tadpole improvement unnecessary and is why the tadpole factor  $u_0$  is omitted from the coefficients in Figure 3.5.

### 3.2.3 Repairing Lorentz Invariance; The $\epsilon$ Coefficient

The leading discretization errors of the asqtad improved fermions are of  $\mathcal{O}((ap_\mu)^4)$ , which makes simulations with  $< 1\%$  errors possible for light quarks. However, they are still too large for accurate simulations of charm. In fact, in most systems of interest the charm quark is typically nonrelativistic. That is, most of its energy is concentrated in its mass rather than its 3-momentum:  $E \approx m \gg \mathbf{p}$ . So, it's mostly the  $\mathcal{O}((am_c)^4)$  errors that one must worry about. The charm mass on typical lattices available today is of order  $am_c \approx 0.5$  for which the errors will be around 6%. More improvement is needed.

An efficient approach to removing discretization errors is to adjust parameters of the action until some condition enforced by a continuum symmetry is restored. Lorentz invariance is broken by the finite difference operator  $\gamma \cdot \Delta$  that replaces the continuum derivative. The addition of the Naik term was meant to alleviate that up to order  $a^2$ . This improvement can be enhanced by retuning the Naik term's coefficient in order to repair the broken Lorentz invariance.

The discretization errors associated with the violation of Lorentz invariance cause the speed of light, as derived from the lattice dispersion relation, to deviate from 1. These errors show up at  $\mathcal{O}((am)^4)$  at tree level in the lattice dispersion relation of asqtad improved charm quarks

$$\begin{aligned} c^2(0) &\equiv \lim_{\mathbf{p} \rightarrow 0} \frac{E^2(\mathbf{p}) - m^2}{\mathbf{p}^2} \\ &= 1 + \frac{9}{20}(am)^4 + \frac{1}{7}(am)^6 + \dots \end{aligned} \quad (3.65)$$

These errors are then removed by adjusting the Naik term's coefficient until the speed of light is fixed. This is done by introducing the  $\epsilon$  parameter into the action as follows

$$\sum_x \bar{\psi}(x) \left( \sum_\mu \gamma_\mu \left( \Delta_\mu(V) - \frac{a^2(1+\epsilon)}{6} \Delta_\mu^3(U) \right) + m_0 \right) \psi(x). \quad (3.66)$$

Setting the lattice spacing  $a = 1$  for the moment, the lattice energy and momentum are then modified according to

$$\begin{aligned} \tilde{E} &= \sinh(E) - \frac{1+\epsilon}{6} \sinh^3(E), \\ \tilde{\mathbf{p}} &= \sin(\mathbf{p}) - \frac{1+\epsilon}{6} \sin^3(\mathbf{p}), \end{aligned} \quad (3.67)$$

where  $E = -ip^0$  is the Euclidean energy. One can then calculate the  $\epsilon$  for which the lattice dispersion relation  $\tilde{E}^2 = \tilde{\mathbf{p}}^2 + m_0^2$  leads to the continuum dispersion relation  $E^2 = \mathbf{p}^2 + m^2$  up to desired orders in powers of  $am_0$ ,  $a\mathbf{p}$  and  $\alpha_s$ . Note that here  $m$  is different from the bare mass  $m_0$ .

This can be done at tree level by expanding  $\tilde{E}$ ,  $\tilde{\mathbf{p}}$  and  $\epsilon$  in powers of  $(am_0)$ , while keeping only  $(a\mathbf{p})^2$  since the momentum is small in comparison, and demanding the speed of light as defined in (3.65) to be equal to 1. This approach yields an expansion for  $\epsilon_{\text{tree}}$  in powers of  $(am_0)^2$  whose coefficients are determined order-by-order in order to cancel corresponding errors in (3.65) up to the desired order in mass.

Alternatively, one can adopt a more convenient but equivalent approach [43] whereby the “rest mass” and the “kinetic mass” are demanded to be equal. To elucidate, a nonrelativistic expansion of the lattice dispersion relation can be written as

$$E = M_1 + \frac{\mathbf{p}^2}{2M_2} + \mathcal{O}(\mathbf{p}^4), \quad (3.68)$$

where  $M_1$  is referred to as the rest mass or the “pole mass,” and  $M_2$  as the kinetic mass.

The rest/pole mass  $M_1$  is obtained from the pole condition at rest,  $\mathbf{p} = 0$ , which at tree level takes the form

$$-\sinh^2(E) \left[ 1 - \frac{1 + \epsilon}{6} \sinh^2(E) \right]^2 + m_0^2 = 0. \quad (3.69)$$

For a quark, as opposed to an anti-quark, this gives

$$\sinh(m_{\text{tree}}) \left[ 1 - \frac{1 + \epsilon_{\text{tree}}}{6} \sinh^2(m_{\text{tree}}) \right] = m_0, \quad (3.70)$$

where  $M_1$  denoted by  $m_{\text{tree}} \equiv E(0)$  is related to  $m_0$ . Note that here  $\epsilon_{\text{tree}}$  also depends on the bare mass. One can solve this relation iteratively to obtain  $\epsilon_{\text{tree}}$  and  $m_{\text{tree}}$  at a fixed bare mass  $m_0$ .

Now consider a fermion with  $p = (iE, p_x, 0, 0)$ . The kinetic mass of the on-shell particle can be defined as

$$M_2 \equiv \left[ \frac{\partial^2 E}{\partial p_x^2} \right]_{p_x=0}^{-1}. \quad (3.71)$$

Setting this equal to the rest mass, i.e.  $M_2 = M_1$ , is clearly equivalent to fixing the speed of light  $c^2(0) = 1$  as in (3.65). Using the relation (3.70), after some algebra this constraint translates into a condition on  $\epsilon_{\text{tree}}$  in the form of

$$1 + \epsilon_{\text{tree}} = \left[ 4 - \sqrt{4 + \frac{12m_{\text{tree}}}{\sinh(m_{\text{tree}}) \cosh(m_{\text{tree}})}} \right] / \sinh^2(m_{\text{tree}}). \quad (3.72)$$



Expanding this relation one gets

$$\epsilon = -\frac{27}{40}(am)^2 + \frac{327}{1120}(am)^4 - \frac{5843}{53760}(am)^6 + \frac{153607}{3942400}(am)^8 + \dots \quad (3.73)$$

We used a symbolic computation software [44] for this expansion. This gives  $c^2(0) = 1 + \mathcal{O}((am)^{12})$ . Only the first term is needed to remove  $\mathcal{O}((am)^4)$  errors. The rest remove tree level errors of higher order in  $(am)$  but only first order in  $v/c$  and are negligibly small, though trivial to include. Note that on a typical lattice the  $\epsilon$  parameter practically vanishes for light and strange quarks but becomes important for the charm.

Additionally, one can plug (3.72) into (3.70) to eliminate the  $\epsilon$  and directly relate  $m_{\text{tree}}$  to the bare mass. A similar expansion results in

$$m_{\text{tree}} = m_0 \left[ 1 - \frac{3}{80}(am_0)^4 + \frac{23}{2240}(am_0)^6 + \frac{1783}{537600}(am_0)^8 - \frac{76943}{23654400}(am_0)^{10} + \dots \right]. \quad (3.74)$$

In practice we actually compute both quantities numerically by solving (3.72) iteratively, which is much more efficient and also automatically includes all orders in  $am$ . We've included the expansion expressions (3.73) and (3.74) here only to demonstrate their mass series dependence, or as a cross check, or because we had them and why not!

Let us finally remark that, although this section focused on removing errors in the quark mass rather than its 3-momentum via a nonrelativistic expansion of the dispersion relation in (3.68), ultimately the staggered action itself remains relativistic.

### 3.2.4 The HISQ Action

So far the leading taste breaking discretization errors of the staggered quarks have been greatly suppressed by smearing the links as described in subsection 3.2.2. However, past experience with asqtad fermions has shown that residual taste changing interactions still remain the largest source of  $\mathcal{O}(a^2)$  discretization errors [9]. In addition to loop order errors, this is also partly due to leftover tree level taste changing interactions. As illustrated in Figure 3.5, even though every  $U_\mu$  is fattened along the  $\mu$  direction, in order to preserve the gauge invariance, the smearing operator introduces non-smearred links in orthogonal directions which can then smuggle undesirable taste changing gluons back into tree level interactions.

Multiple smearing will guarantee that all links are smeared, including those appearing inside the fat links. However, as usual, there are also problems that arise as a result. As pointed out earlier, smearing the links in order to suppress tree level taste-changing interactions introduces new  $\mathcal{O}(a^2)$  taste-conserving errors that grow with additional smearing. This problem is therefore exacerbated in doubly fat7 smeared actions. However, we saw that these errors can be avoided by adding the Lepage term to the fat7 operator, thereby turning it into  $\mathcal{F}_\mu^{\text{ASQTAD}}$ .

The second problem is that, the double smearing of the links by substituting

$$\mathcal{F}_\mu^{\text{ASQTAD}} \rightarrow \mathcal{F}_\mu^{\text{ASQTAD}} \mathcal{F}_\mu^{\text{ASQTAD}} \quad (3.75)$$

leads to an explosion in the number of gluon paths that replace a single thin link. The cross terms in the product of the two smearing operators blow up into a sum of many terms consisting of chained links of various lengths glued together to form the now obese staples which are comprised of any odd number of links up to  $7^2$ .

This is not a problem for single-gluon vertices by design, as the coefficients in Figure 3.5 were specifically chosen to ensure that the coupling is correct. However, it results in a huge number of terms that give rise to unphysical two-gluon vertices. Even though each is of order  $\alpha_s a^2$  in the expansion  $U_\mu = 1 + iagA_\mu - (a^2 g^2/2)A_\mu^2 + \dots$ , there are now too many of them. Thus, on aggregate they offset the suppression. This problem is easily fixed by reunitarizing the fat links before the second smearing

$$\mathcal{F}_\mu^{\text{ASQTAD}} \rightarrow \mathcal{F}_\mu^{\text{ASQTAD}} \mathcal{U} \mathcal{F}_\mu^{\text{ASQTAD}} \quad (3.76)$$

where  $\mathcal{U}$  is an implementation of the reunitarization operator that projects the once smeared links back unto  $U(3)$ . It preserves the desired effect of smearing, while preventing the undesirable explosion in the number of terms by bounding the fat links. Rearranging the order of operations for simplicity, the smearing scheme used in the highly improved staggered quarks action widely referred to by its acronym HISQ, is given by

$$\mathcal{F}_\mu^{\text{HISQ}} \equiv \left( \mathcal{F}_\mu - \sum_{\rho \neq \mu} \frac{a^2 (\delta_\rho)^2}{2} \right) \mathcal{U} \mathcal{F}_\mu, \quad (3.77)$$

where the Lepage term is pulled out of the first smearing in (3.76) and reinserted back into the second to the same overall effect.

Putting all corrections together the HISQ action is given in the naive basis by [9]

$$\mathcal{S}^{\text{HISQ}} = \sum_x \bar{\psi}(x) (\gamma \cdot \mathcal{D}^{\text{HISQ}} + m) \psi(x) \quad (3.78)$$

where all the improvements discussed above are encapsulated within the covariant derivative operator

$$\mathcal{D}_\mu^{\text{HISQ}} \equiv \Delta_\mu(W) - \frac{a^2}{6} (1 + \epsilon) \Delta_\mu^3(X). \quad (3.79)$$

The links are smeared according to

$$\begin{aligned} W_\mu(x) &\equiv \mathcal{F}_\mu^{\text{HISQ}} U_\mu(x), \\ X_\mu(x) &\equiv \mathcal{U} \mathcal{F}_\mu U_\mu(x). \end{aligned} \quad (3.80)$$

The links in the one-step difference operator are doubly smeared and the Naik term is made of straight three-step paths of reunitarized fat7 links.

The perturbative Symanzik improvements undertaken thus far resulting in the HISQ action, remove all tree level  $\mathcal{O}(a^2)$  errors as well as tree level  $\mathcal{O}((am)^4)$  errors to first order in quark's velocity  $v/c$ . The leading discretization errors, therefore, come in at  $\mathcal{O}((am)^4(v/c)^2, (a\mathbf{p})^4, \epsilon(a\mathbf{p})^2/6)$  at tree level and  $\mathcal{O}(\alpha_s(ap)^2)$  at one-loop level. On current lattices where  $am_c \approx 0.5$ , the tree level errors are in the range of 0.5% to  $\approx 2\%$  or less for charm quarks in systems of interest such as charmonium and  $D$  physics [9].

What's more, as will be discussed in the next section, the leading loop level errors of order  $\mathcal{O}(\alpha_s(ap)^2)$  turn out to be already highly suppressed thanks to the multiple smearing. Studies of other quantities show that this makes the HISQ action one of the most accurate discretizations of the staggered quarks to date and the first relativistic treatment of the charm quark to achieve few percent accuracy on the lattice.

### 3.2.5 Loop Corrections and Higher Dimension Operators

The next step in improving the lattice action will be the leading order loop corrections. The  $\mathcal{O}(\alpha_s(ap)^2)$  errors should generally be small for light quarks. However, the taste changing errors of pre-HISQ staggered actions turned out to be larger than expected. In order to assess the error due to taste violation beyond the suppression achieved at tree level by smearing, one-loop contributions to taste exchange were analyzed.

Figure 3.6 shows the only one-loop taste exchange diagrams that contribute to these errors. The rest are already highly suppressed by smearing. The corrections then involve adding current-current interactions shown in Figure 3.6f to the lattice action. There is a total of 28 such taste changing terms. Coupling constants of the corresponding 4-quark contact counter-terms were calculated in the massless limit for a number of tree level improved staggered actions in the original HISQ paper. It turned out that on average HISQ coefficients were smaller than asqtad coefficients by about an order of magnitude [9, TABLE II].

Given the perturbative origin of these interactions, which involve very high momenta transferred between quarks via gluons, this isn't surprising. The dominant contributions from the diagrams in Figure 3.6 come from loops with momenta of order  $\zeta\pi/2a$ . The smearing form factor introduced in subsection 3.2.2 suppresses large-momentum vertices and leaves soft vertices unchanged. Thus, the multiple smearing undertaken in the HISQ action suppresses loop level taste exchange interactions to a greater extent than the once-smeared asqtad action does.

The HISQ coefficients being so small—of order 0.1 or less on current lattices—is good news given that current-current interactions are complicated to implement. These coefficients are a direct measure of the size of one-loop taste breaking interactions. Therefore, the size of these errors is expected to be proportional to the couplings unless they are so highly

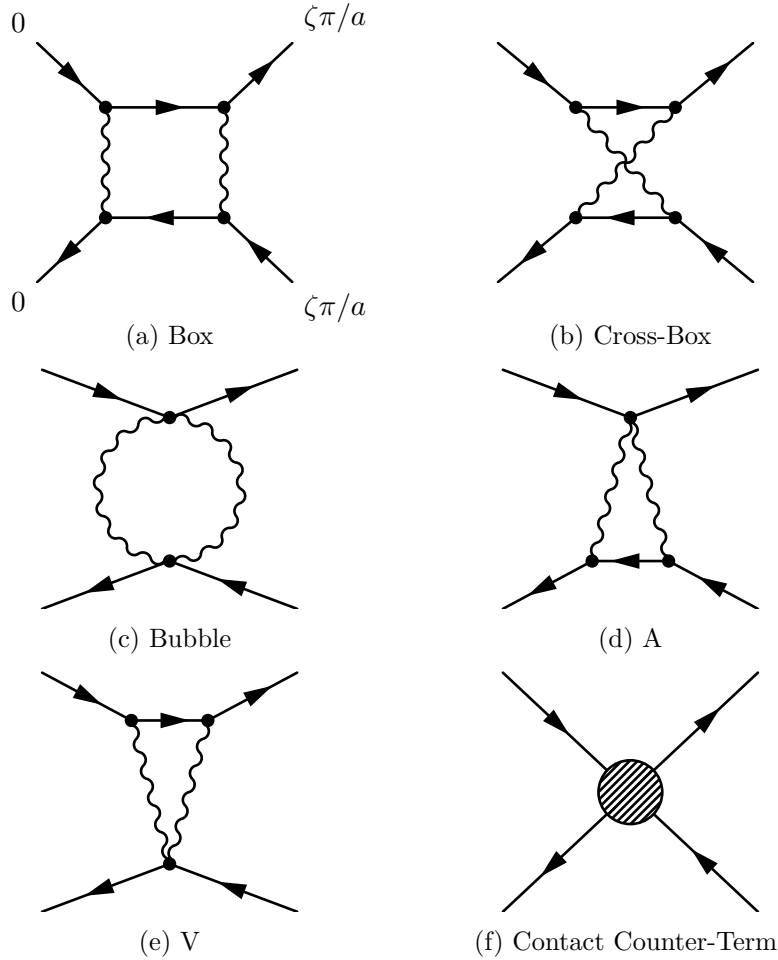


Figure 3.6: (a)–(e) One-loop taste exchange diagrams in quark-quark scattering processes. These are the only diagrams that contribute to taste violation at one-loop level. The rest involve gluon vertices with  $q \approx \pi/a$  which are already highly suppressed by smearing. (f) Four-quark contact counter-terms are needed in order to completely remove loop-level taste exchange interactions.

suppressed that higher order taste breaking effects start to take over. These expectations were also confirmed in [9] where the observed pion taste splittings in simulations with different implementations of staggered quarks were shown to exhibit the suggested pattern. In particular, pion taste splittings with HISQ came out more than 3 times smaller than with asqtad. Given that the only difference between them is the additional smearing in HISQ, this important result constitutes another *nonperturbative evidence for the perturbative origins of taste violation* and therefore reinforces one’s confidence in the validity as well as effectiveness of perturbative Symanzik improvements. This three-fold reduction is consistent with a factor of  $\alpha_s \approx 0.3$  as expected from the suppression of taste exchange at one-loop order due to the double smearing of the HISQ.

The  $\mathcal{O}(\alpha_s a^2)$  taste conserving errors are irrelevant at few percent level for light quarks. For charm quarks with  $am_c \approx 0.5$  on current lattices at  $a \approx 0.1$  fm and  $\alpha_s \approx 1/3$ , however,

Table 3.1: Power counting rules for heavy-light and charmonium [9]. The error associated with each operator is estimated in terms of  $(am)^2 \approx 1/4$ ,  $\alpha_s \approx 1/3$  and  $(v/c)^2 \approx 0.3$  for  $\psi$  and  $(v/c)^2 \approx 0.1$  for  $D$  on a lattice with  $a \approx 0.1$  fm.

Operator	$\psi$	$D$
$a^2 \bar{\psi} \gamma_\mu D_\mu^3 \psi$	$\alpha_s (am)^2$	$\alpha_s (am)^2$
$a^2 m \bar{\psi} \sigma \cdot gF \psi$	$\alpha_s (v/c)^2 (am)^2$	$\alpha_s (v/c) (am)^2$
$a^2 \bar{\psi} D^2 D \cdot \gamma \psi$		
$a^2 \bar{\psi} (D \cdot \gamma)^3 \psi$		
$a^2 m \bar{\psi} D^2 \psi$		
$a^2 \bar{\psi} \sigma \cdot gF D \cdot \gamma \psi$		
$a^2 \bar{\psi} D \sigma \cdot gF \cdot \gamma \psi$	$\alpha_s (v/c)^2 (am)^2$	$\alpha_s (v/c)^2 (am)^2$
$a^2 (\bar{\psi} \gamma \psi)^2$		
$a^2 (\bar{\psi} \gamma \gamma_5 \psi)^2$		

they can be as large as 5 – 10% and thus must be suppressed for high precision calculations. Many taste conserving operators contribute to such errors.

Using power counting rules for heavy-light mesons and charmonium states given in Table 3.1 similar to those developed for NRQCD in section A.1, in a nonrelativistic expansion one finds that the only operator with a sizable contribution at  $\mathcal{O}(\alpha_s a^2)$  is actually the Naik term. Others are suppressed by additional powers of  $v/c$  and thus contribute at 1 – 2% level or less in systems of interest given that  $(v/c)^2 \approx 1/3$  in charmonium, for instance, and  $\approx 1/10$  in  $D$  physics; see [9, TABLE III].

Radiative corrections to the Naik term’s renormalization parameter  $\epsilon$  can be done in two different ways. It can be tuned nonperturbatively by adjusting it until the dispersion relation for, say,  $\eta_c$  is corrected. Alternatively, one can calculate it perturbatively by extending the analysis of subsection 3.2.3 to one-loop order. Starting with

$$\begin{aligned}
 E &= m_{\text{tree}} + m_1 \alpha_s, \\
 \epsilon &= \epsilon_{\text{tree}} + \epsilon_1 \alpha_s,
 \end{aligned}
 \tag{3.81}$$

the one-loop corrections for a quark then take the form

$$\epsilon = -\frac{27}{40} (am)^2 + \epsilon_1 \alpha_s + \mathcal{O}(\alpha_s^2, (am)^4).
 \tag{3.82}$$

It turns out that  $\epsilon_1$  is negligibly small for HISQ but not for asqtad [9].

### 3.2.6 Diagnostics

The second half of a systematic improvement program is therefore to establish a set of diagnostics to investigate the effects of those corrections and assess the extent to which they improved the theory. So let us close this chapter by asking that question. At the risk of spoiling the ending, the short answer is: they’ve worked quite well.

For instance, mass splittings between the 16 tastes of a meson may be used to indicate the size of the taste symmetry violation errors.<sup>2</sup> Creators of HISQ presented numerical evidence to demonstrate the efficacy of double smearing in reducing loop order taste breaking errors [9]. In particular for staggered charm, they showed small splittings between different tastes of various charmonium states [9, FIG. 7]. The maximum spread between tastes of  $\eta_c$  was shown to be only 9 MeV. In contrast the mass splitting between the local and the 1-temporal-link<sup>3</sup> tastes of the  $\eta_c$  with asqtad charm is 40 MeV, whereas the same splitting is only 3 MeV with HISQ.

Furthermore, as argued in the previous section, taste splitting comparisons between HISQ and asqtad can be used to bound taste breaking errors and to assess the effect of smearing on suppressing them since the two only differ in the second smearing of HISQ.

Lorentz symmetry was broken by the discretization of the  $\not{D}$  operator. The Naik term was meant to reduce the resulting errors while the  $\epsilon$  in its coupling was perturbatively renormalized to fix the symmetry through fixing the dispersion relation obtained from the quark propagator. Inspecting the dispersion relation of simulated mesons at various momenta reveals [9, FIG. 6] that the speed of light well satisfies  $c^2 = 1$  within errors.

Perhaps one of the most severe tests of the HISQ action would be its ability to calculate accurately the until-then-consistently-underestimated hyperfine mass splitting of charmonium states. Early results reported in [9] showed good agreement with experimental measurements. A more recent precision calculation carried out by the HPQCD collaboration obtained  $m_{J/\psi} - m_{\eta_c} = 116.5(3.2)$  MeV [4], in excellent agreement with the observed value of 113.32(70) MeV [1].

In this work we further test the HISQ action’s ability to probe a very fine near cancellation between destructive contributions of a charm-light quark-antiquark pair. We will present our calculation of the radiative and pionic decays of  $D$  mesons in chapter 6. But first we need to better understand the doubling symmetry, the implications of the resulting doublers on mesons and how to work with them in the spinor basis as well as the staggered basis. This will be the subject of our next chapter.

---

<sup>2</sup> Though, since there are 28 current-current 4-quark couplings required to remove taste exchange interactions one would need more diagnostic tests to cover all sources. Which is why these couplings were calculated in [9].

<sup>3</sup> That is an  $\eta_c$  created by a bilinear operator with one field shifted relative to the other by one step along the temporal direction:  $\bar{\psi}(x)\gamma_5 U_0(x)\psi(x + a\hat{0})$ . More on meson tastes in the next chapter.

## Chapter 4

# The Taste Symmetry

We met the doublers in chapter 3. Various approaches to improving discretization errors of lattice fermions in general were reviewed. In particular, a large chunk of the discussion was dedicated to reducing the errors due to the creation of and interactions between different quark tastes. The perturbative Symanzik improvement of staggered quarks that culminated in the HISQ action [9] was explained and shown to be successful, thereby making it an accurate and efficient tool for high quality simulations of charm.

In this chapter we introduce the doubling symmetry of the naive action that is responsible for the creation of the doublers. Section 4.1 describes the spinor (or naive) and the staggered (or spin-diagonalized) bases.

Being made of two quarks, mesons also come in many different tastes which will be identified in section 4.2. The physical implications of the doubling symmetry on meson states are explained in section 4.3 where we reconcile with oscillating states and learn to like them. Most of this chapter is presented in the familiar spinor basis. Section 4.4 provides the connection to meson operators in the staggered basis.

The primary goal of this chapter is to understand taste in the spinor basis which is formally equivalent to the staggered basis but which we find more intuitive. Computer simulations, however, take place in the staggered basis which is significantly more efficient due to the 4-fold reduction in the number of degrees of freedom. By the end of this chapter we hope to be able to relate a physical process as understood in terms of continuum fields to one on the lattice in the familiar spinor basis, translate it into the staggered basis where the simulation is designed and ultimately carried out and finally interpret the results.

### 4.1 Naive and Staggered Bases

Let us begin by a more detailed discussion of the doubling symmetry we caught a brief glimpse of earlier in subsection 3.1.1. The following discussion closely follows that presented

in [9]. In this chapter, and most of the rest of the thesis, we work in lattice units where the lattice spacing is set to  $a = 1$ , unless stated otherwise.

### 4.1.1 Staggering the Action

Starting from the spinor basis the quark action can be written as

$$\mathcal{S} = \sum_x \bar{\psi}(x)(\gamma \cdot \Delta + m)\psi(x), \quad (4.1)$$

where  $\Delta_\mu$  represents some finite difference operator that replaces the continuum covariant derivative  $D_\mu$ . In its simplest form (the naive discretization), it is given by

$$\Delta_\mu \psi(x) \equiv \frac{1}{2} \left( U_\mu(x)\psi(x + \hat{\mu}) - U_\mu^\dagger(x - \hat{\mu})\psi(x - \hat{\mu}) \right), \quad (4.2)$$

where  $U_\mu(x)$  are  $SU(3)$  gauge field matrices, called the link variables or the parallel transporters, which encode the gluon fields and are responsible for the strong interactions. As before the Euclidean gamma matrices are Hermitian and satisfy the following algebra

$$\gamma_\mu^\dagger = \gamma_\mu, \quad \gamma_\mu^2 = 1, \quad \{\gamma_\mu, \gamma_\nu\} = 2\delta_{\mu\nu}, \quad (4.3)$$

for  $\mu, \nu = 0, \dots, 3$ . Let us define a set of 16 Hermitian matrices as follows

$$\gamma_n \equiv \prod_{\mu=0}^3 \gamma_\mu^{n_\mu}, \quad (4.4)$$

which form a complete set of spinor matrices and are labeled by a four-component vector  $n$  whose elements are either 0 or 1, or equivalently  $n_\mu \in \mathbb{Z}_2$ . Using these matrices, one can then spin diagonalize the quark action through carrying out a unitary transformation of the quark fields as follows

$$\psi(x) \rightarrow \Omega(x)\chi(x), \quad \bar{\psi}(x) \rightarrow \bar{\chi}(x)\Omega^\dagger(x), \quad (4.5)$$

where the  $\Omega(x)$  matrices are chosen to be

$$\Omega(x) \equiv \gamma_x \equiv \prod_{\mu=0}^3 (\gamma_\mu)^{x_\mu}, \quad (4.6)$$

or equivalently

$$\Omega(x) = \gamma_n \quad \text{for } n_\mu = x_\mu \pmod{2}; \quad (4.7)$$



which basically represent a rotation, or in other words a simple change of variables, in the spin space. As we learned in the previous chapter, they satisfy the following relations

$$\alpha_\mu(x) \equiv \Omega^\dagger(x) \gamma_\mu \Omega(x \pm \hat{\mu}) = (-1)^{x_\mu^<}, \quad (4.8)$$

$$1 = \Omega^\dagger(x) \Omega(x), \quad (4.9)$$

where  $\alpha_\mu(x)$  is a coordinate dependent phase with

$$x_\mu^< \equiv x_0 + x_1 + \cdots + x_{\mu-1}. \quad (4.10)$$

Note that there is an implicit  $4 \times 4$  unit matrix with spinor indices ( $\mathbf{1}_{\text{spinor}}$ ) on the left hand side of equations (4.8) and (4.9). “Staggering” the action through (4.5), therefore, has the effect of removing the gamma matrices and replacing them by a phase, as follows

$$\bar{\psi}(x) (\gamma \cdot \Delta + m) \psi(x) = \bar{\chi}(x) (\alpha(x) \cdot \Delta + m) \chi(x), \quad (4.11)$$

thereby decoupling the four components of the quark spinor fields. The four components of the staggered quark fields become degenerate as a direct consequence of the fact that the staggered action is diagonal in the spin space. They lead to identical quark physics on the lattice. The quark propagator in the staggered basis will therefore take the form

$$\langle \chi(x) \bar{\chi}(y) \rangle = g(x, y) \mathbf{1}_{\text{spinor}}; \quad (4.12)$$

a diagonal matrix with identical elements. Note that this is true for any background gauge field. Recall that on the lattice the staggered quark propagator  $g(x, y)$  is given by the inverse of the fermion operator

$$g(x, y) = M_{x,y}^{-1}, \quad (4.13)$$

where the matrix  $M$  carries the exact structure of the discretized quark action written as

$$\mathcal{S} = \sum_{x,y} \bar{\chi}(x) M_{x,y} \chi(y). \quad (4.14)$$

The staggered propagator above, is related to the quark propagator in the original Dirac basis through

$$\begin{aligned} S_F(x, y) &\equiv \langle \psi(x) \bar{\psi}(y) \rangle = \Omega(x) \langle \chi(x) \bar{\chi}(y) \rangle \Omega^\dagger(y) \\ &= g(x, y) \Omega(x) \Omega^\dagger(y), \end{aligned} \quad (4.15)$$

which simply follows from the definition of the staggering transformations (4.5). Examining this relation, one notices that the spinor structure of the fermion propagator is determined by the product  $\Omega(x) \Omega^\dagger(y)$  on the right hand side, which is a  $4 \times 4$  spinor matrix with exactly one non-zero element in every row and every column with a value of  $\pm 1$  or  $\pm i$ . Therefore,

the Dirac (or naive) propagator spinor matrix simply consists of a collection of 4 identical quarks, up to a phase, and hence is a scrambled but equivalent version of the diagonal staggered propagator.

This is a remarkable result. As we saw in the previous chapter, one can exploit this degeneracy and reduce the number of degrees of freedom in the Dirac formulation by a factor of 4, thereby also reducing the number of quark tastes down to 4. This degeneracy is a result of an underlying symmetry of the lattice action which we will turn to in the following section.

### 4.1.2 The Doubling Symmetry

During our discussion of the naive discretization approach and the doubling problem in subsection 3.1.1, we alluded to a general underlying symmetry of the action that gives rise to the creation of the doublers on the lattice. In this chapter we will present a formal treatment of this symmetry and attempt to describe the implications of the presence of the unphysical quark tastes by identifying and interpreting their contributions within the framework of the naive as well as the staggered quark action.

Before jumping into our discussion of the doubling symmetry, it will be helpful to quickly remind ourselves of some of the important properties of the gamma matrices and introduce a set of useful notation. Here we closely follow [9].

#### Gamma Matrices

Throughout this work we will be using the complete set of 16 spinor matrices denoted by  $\gamma_n$ , where the subscript  $n$  is a 4-component vectors with  $n_\mu \in \mathbb{Z}_2$ , introduced earlier in (4.4). These are equivalent to the following conventional set

$$\{1, \quad \gamma_5 \equiv \gamma_t \gamma_x \gamma_y \gamma_z, \quad \gamma_\mu, \quad \gamma_{5\mu} \equiv i\gamma_5 \gamma_\mu, \quad \gamma_{\mu\nu} \equiv \frac{i}{2}[\gamma_\mu, \gamma_\nu]\} \quad (4.16)$$

up to a  $\pm 1$  or  $\pm i$  phase. In the following we list a few useful relations which will be frequently referred to in the rest of this work and are reproduced in Appendix B. We adopt the notation used in [9].

- Orthonormality:

$$\text{Tr}(\gamma_n^\dagger \gamma_m) = 4\delta_{nm}, \quad (4.17)$$

- Multiplication properties:

$$\gamma_n \gamma_m = (-1)^{n \cdot m^<} \gamma_{n+m}, \quad (4.18)$$

where

$$m_\mu^< \equiv \sum_{\nu < \mu} m_\nu \pmod{2}, \quad (4.19)$$

and

$$n \cdot m^< = n^> \cdot m, \quad (4.20)$$

for  $n^>$  defined as

$$n_\mu^> \equiv \sum_{\nu > \mu} n_\nu \pmod{2}. \quad (4.21)$$

similar to  $m^<$ . A convenient notation reminiscent to  $\gamma_{5\mu}$  is to define

$$\gamma_{nm} \equiv \gamma_n \gamma_m. \quad (4.22)$$

Let us also include the relation

$$m^2 = \sum_{\mu} m_\mu^2 = \sum_{\mu} m_\mu \pmod{2}, \quad (4.23)$$

which is a handy shorthand notation for the sum of all components of the 4-vector  $m \in \mathbb{Z}_2^4$ .

- Hermitian conjugate:

$$\gamma_n^\dagger = (-1)^{n \cdot n^<} \gamma_n = \gamma_n^{-1}. \quad (4.24)$$

- Commutation relations:

$$\gamma_n \gamma_m = (-1)^{\bar{m} \cdot n} \gamma_m \gamma_n, \quad (4.25)$$

where

$$\begin{aligned} \bar{m}_\mu &\equiv m_\mu^< + m_\mu^> = \sum_{\nu \neq \mu} m_\nu \pmod{2} \\ &= \begin{cases} m_\mu & \text{if } m^2 \text{ even,} \\ (m_\mu + 1) \pmod{2} & \text{if } m^2 \text{ odd,} \end{cases} \end{aligned} \quad (4.26)$$

with the following properties

$$\bar{\bar{m}} \cdot n = m \cdot \bar{n}, \quad (4.27a)$$

$$\bar{\bar{m}} = m, \quad (4.27b)$$

$$(\bar{m} \cdot m) = 0 \pmod{2}; \quad (4.27c)$$

- Standard representation:

$$\gamma_0 = \begin{pmatrix} 1 & 0 \\ 0 & -1 \end{pmatrix}, \quad \gamma_i = \begin{pmatrix} 0 & \sigma_i \\ \sigma_i & 0 \end{pmatrix}, \quad (4.28)$$

$$\sigma_1 = \begin{pmatrix} 0 & 1 \\ 1 & 0 \end{pmatrix}, \quad \sigma_2 = \begin{pmatrix} 0 & -i \\ i & 0 \end{pmatrix}, \quad \sigma_3 = \begin{pmatrix} 1 & 0 \\ 0 & -1 \end{pmatrix}. \quad (4.29)$$

Let us finally point out that these  $\gamma_n$  matrices are like permutation operators with  $\pm 1$  or  $\pm i$  coefficients, whose effects when multiplying spinors is only to rearrange their components, up to a phase.

---

Having equipped ourselves with the above terminology let us now return to the naive action (4.1). One can easily confirm that this action is invariant under the following transformations

$$\begin{aligned}\psi(x) &\rightarrow \tilde{\psi}(x) \equiv \gamma_{5\rho}(-1)^{x_\rho}\psi(x) \\ &= \gamma_{5\rho} \exp(ix_\rho\pi)\psi(x),\end{aligned}\tag{4.30}$$

for  $\rho = 0, \dots, 3$ . In order to see this, consider a derivative term. We have

$$\begin{aligned}\bar{\psi}(x)\gamma_\mu\psi(x \pm \hat{\mu}) &\rightarrow \bar{\psi}(x)(\gamma_{5\rho})^\dagger(-1)^{x_\rho}\gamma_\mu\gamma_{5\rho}(-1)^{(x \pm \hat{\mu})_\rho}\psi(x \pm \hat{\mu}) \\ &= (-1)^{\delta_{\rho\mu}}\bar{\psi}(x) \left( (i\gamma_5\gamma_\rho)^\dagger\gamma_\mu(i\gamma_5\gamma_\rho) \right) \psi(x \pm \hat{\mu}) \\ &= \bar{\psi}(x)\gamma_\mu\psi(x \pm \hat{\mu}),\end{aligned}$$

where we have used

$$(i\gamma_5\gamma_\rho)^\dagger\gamma_\mu(i\gamma_5\gamma_\rho) = (-1)^{\delta_{\rho\mu}}\gamma_\mu,$$

which follows from the anti-commutation relation (4.3). We encountered this symmetry and its connection to the creation of the doublers, in our discussion leading to (3.22) in subsection 3.1.1.

It is now evident that the Dirac formulation of the QCD quark action has an exact “*doubling*” symmetry under the following unitary local transformations

$$\psi(x) \rightarrow \mathcal{B}_\zeta(x)\psi(x), \quad \bar{\psi}(x) \rightarrow \bar{\psi}(x)\mathcal{B}_\zeta^\dagger(x),\tag{4.31}$$

where

$$\mathcal{B}_\zeta(x) = \gamma_{\bar{\zeta}}(-1)^{\zeta \cdot x} \times \prod_\rho (\gamma_{5\rho})^{\zeta_\rho} \exp(ix \cdot \zeta\pi),\tag{4.32}$$

which is the result of successive applications of the transformation given by (4.30) along the 4 space-time dimensions. This symmetry has remarkable consequences. One can easily verify that

$$\mathcal{B}_\zeta(x)\Omega(x) = \Omega(x)\mathcal{B}_\zeta(0),\tag{4.33}$$

which implies that

$$\mathcal{B}_\zeta(x)\Omega(x)\Omega^\dagger(y)\mathcal{B}_\zeta^\dagger(y) = \Omega(x)\Omega^\dagger(y).\tag{4.34}$$

This, combined with (4.15) leads to

$$S_F(x, y) = \mathcal{B}_\zeta(x)S_F(x, y)\mathcal{B}_\zeta^\dagger(y),\tag{4.35}$$

for naive quark propagators in any background gauge field. In momentum space this translates to

$$S_F(p, q) = \mathcal{B}_\zeta(0) S_F(p + \zeta\pi, q + \zeta\pi) \mathcal{B}_\zeta^\dagger(0), \quad (4.36)$$

for any  $\zeta \in \mathbb{Z}_2^4$ . This clearly demonstrates that there is only 1/16-th as much information contained in the “naive” quark propagator as one would naively expect. This exact relationship once again captures the connection between the 16 different corners of the Brillouin zone, as discussed in section 3.1.

In the staggered basis the doubling transformation (4.31) becomes

$$\begin{aligned} \psi(x) &\rightarrow \mathcal{B}_\zeta(x) \psi(x) = \mathcal{B}_\zeta(x) \Omega(x) \chi(x) = (-1)^{\zeta \cdot x} \gamma_{\bar{\zeta}} \gamma_x \chi(x) \\ &= \gamma_x \gamma_{\bar{\zeta}} \chi(x) = \Omega(x) \mathcal{B}_\zeta(0) \chi(x), \end{aligned}$$

where we have used (4.32), (4.27b) and the commutation relation (4.25). The doubling symmetry of the quark action in the staggered basis (4.11) is then given by

$$\chi(x) \rightarrow \mathcal{B}_\zeta(0) \chi(x), \quad (4.37)$$

where  $\mathcal{B}_\zeta(0)$  permutes the 4 equivalent components of the staggered  $\chi$  field multiplying them by  $\pm 1$ , or  $\pm i$ .

Finally, we would like to re-stress the importance of the somewhat surprising consequence of the doubling symmetry, that the exact relation (4.36) holds for *any background gauge field*. This is essentially what allows us to discard all but one component of the staggered fermion field, thereby significantly reducing simulation costs. Quark propagators are computed in simulation by solving for the inverse fermion matrix  $M_{x,y}^{-1}$ . On an  $L^3 \times T$  lattice, this is a  $12L^3T \times 12L^3T$  square matrix in the naive basis, accommodating 4 spinor degrees of freedom times 3 color components on every lattice site. Whereas, in the staggered basis with only one spinor component per quark field, the matrix  $M$  is reduced to  $3L^3T \times 3L^3T$ . This together with the fact that the chiral symmetry of the staggered quarks preserve the positive definiteness of  $M$  result in a substantial increase in simulation efficiency.

### 4.1.3 Meson Propagators

This section shows two simple examples of computing meson propagators on the lattice using staggered quarks. A pseudo-scalar meson can be created using the bilinear operator

$$J_5(x) = \bar{\psi}(x) \gamma_5 \psi(x), \quad (4.38)$$

in the Dirac basis. A pion correlator constructed using this operator then becomes

$$\begin{aligned}
\langle J_5^\dagger(x) J_5(0) \rangle &= \overline{\langle \bar{\psi}(x) \gamma_5 \psi(x) \bar{\psi}(0) \gamma_5 \psi(0) \rangle} \\
&= \text{Tr}(\gamma_5 S_F(x, 0) \gamma_5 S_F(0, x)) \\
&= \text{Tr}(\gamma_5 S_F(x, 0) \gamma_5 \gamma_5 S_F^\dagger(x, 0) \gamma_5) \\
&= \text{Tr}(\Omega(x) \Omega^\dagger(0) \Omega(0) \Omega^\dagger(x)) \text{tr}(|g(x, 0)|^2) \\
&= 4 \text{tr}(|g(x, 0)|^2),
\end{aligned} \tag{4.39}$$

where  $g(x, 0)$  is the 1-component staggered quark propagator. Here,  $\text{Tr}()$  denotes the trace over spinor indices, and  $\text{tr}()$  color indices. In deriving the third equality in this relation we have used the following general property of the propagator

$$S_F(y, x) = \gamma_5 S_F^\dagger(x, y) \gamma_5, \tag{4.40}$$

which is a result of another underlying symmetry of the action known as  $\gamma_5$  *hermiticity*

$$M_{y,x} = \gamma_5 M_{x,y}^\dagger \gamma_5, \tag{4.41}$$

where  $M$  is the fermion matrix. In the staggered basis (4.40) becomes

$$g(y, x) \Omega(y) \Omega^\dagger(x) = \gamma_5 \left( g(x, y) \Omega(x) \Omega^\dagger(y) \right)^\dagger \gamma_5 = g^\dagger(x, y) \left( \gamma_5 \Omega(y) \Omega^\dagger(x) \gamma_5 \right),$$

therefore

$$g(y, x) \mathbf{1}_{\text{spinor}} = g^\dagger(x, y) \left( \Omega^\dagger(y) \gamma_5 \Omega(y) \right) \left( \Omega^\dagger(x) \gamma_5 \Omega(x) \right) = g^\dagger(x, y) (-1)^{y^2} \gamma_5 (-1)^{x^2} \gamma_5,$$

which results in

$$g(y, x) = (-1)^{x^2 - y^2} g^\dagger(x, y), \tag{4.42}$$

where once again the spinor structure of the propagator is encapsulated in a coordinate dependent phase. A vector meson can be created by a vector operator such as

$$J_i(x) = \bar{\psi}(x) \gamma_i \psi(x), \tag{4.43}$$

where  $i$  specifies the spatial orientation of its spin. The vector correlator then becomes

$$\begin{aligned}
\langle J_i^\dagger(x) J_i(0) \rangle &= \overline{\langle \bar{\psi}(x) \gamma_i \psi(x) \bar{\psi}(0) \gamma_i \psi(0) \rangle} \\
&= \text{Tr}(\gamma_i S_F(x, 0) \gamma_i \gamma_5 S_F^\dagger(x, 0) \gamma_5) \\
&= \text{Tr}(\gamma_i \Omega(x) \Omega^\dagger(0) \gamma_i \gamma_5 \Omega(0) \Omega^\dagger(x) \gamma_5) \text{tr}(|g(x, 0)|^2) \\
&= 4(-1)^{x_i} \text{tr}(|g(x, 0)|^2),
\end{aligned} \tag{4.44}$$

where the spin state of the vector meson, characterized by the  $\gamma_i$  matrix in the Dirac basis, is preserved in the staggered basis through the coordinate dependent phase  $(-1)^{x_i}$ . Spinor structure information is thus carried by a phase in the staggered formalism.

Here we only used the simplest operators in order to provide some examples. However, these operators aren't unique. One could of course use a range of different interpolating operators to create and destroy mesons, including non-local operators. We will discuss in detail various issues involving the choice of operators, such as selection rules, relationship between Dirac and staggered operators, and between different operators used to create the same hadron state, etc., in the remainder of this chapter and subsequent chapters.

## 4.2 Naive Currents; A Multitude of Mesons

So far we've seen the quark tastes in the staggered formalism. Now let us explore in more detail what happens when we use staggered quarks to build currents. In this section we discuss the implications of the quark doublers on studying mesons on the lattice using the staggered quark action. Here, we work with the naive basis which we find more intuitive. The formally equivalent and computationally more efficient but less intuitive staggered basis will be discussed in section 4.4.

In the ordinary continuum theory, a meson is simply created by a bilinear current operator such as  $J_n = \bar{\psi}\gamma_n\psi$ . On the lattice, however, naive quark bilinear operators give rise to a huge number of mesons. This is due to the doubling symmetry as well as point-splittings in the quark fields. For any single meson  $J_n$  in continuum QCD, one can get 16 different mesons on the lattice created by point-split currents of the form

$$\begin{aligned} J_n^{(s)}(x) &\equiv \bar{\psi}(x)\gamma_n^{(s)}\psi(x) \equiv \bar{\psi}(x)\gamma_n\psi(x + \delta x_{sn}) \\ &\propto \bar{\chi}(x)\gamma_s\chi(x + \delta x_{sn}), \end{aligned} \tag{4.45}$$

for 16 different 4-vectors  $s$  with  $s_\mu \in \mathbb{Z}_2$ , where

$$\delta x_{sn} \equiv s + n \pmod{2}, \tag{4.46}$$

determines the point-splitting structure of the current. Link variables  $U_\mu$  are implicit. The rationale behind our choice for the specific form of the shift in the coordinates of the quark field,  $\delta x_{sn}$ , in defining the current  $J_n^{(s)}$  will become increasingly more clear during the course of our discussion of mesons in the rest of this chapter.<sup>1</sup>

---

<sup>1</sup> The proportionality in (4.45) can be replaced by equality by including a coordinate dependent phase  $\phi(x) = \pm 1$ , whose value also depends on the spin structure  $n$ , as well as the point-splitting structure  $s$ :

$$\Omega^\dagger(x)\gamma_n\Omega(x + s + n) = \phi(x)\gamma_s.$$

The exact value of this phase is irrelevant in the following discussion, so even though easy to include, we've dropped it in order to avoid cluttering the equations.

Obviously, the 16 distinct point-splittings in (4.45), all collapse into the same meson  $\bar{\psi}\gamma_n\psi$  in the continuum limit. Thus, although point splitting would be unremarkable for Wilson fermions, one might expect for staggered quarks to create distinct mesons with different tastes, because the quark tastes are distributed across the Brillouin zone. Point-splitting therefore leads to a multitude of mesons on the lattice. The rest of this chapter will be focused on describing staggered mesons by identifying, classifying and finally interpreting these mesons.

### 4.2.1 Taste Selection Rules

Let us examine the meson tastes defined in (4.45). One can easily show that

$$J_n^{(s)} \rightarrow (-1)^{s\mu} J_n^{(s)}, \quad (4.47)$$

under doubling transformations

$$\psi(x) \rightarrow \mathcal{B}_{\zeta=\hat{\mu}}(x)\psi(x), \quad (4.48a)$$

$$\bar{\psi}(x) \rightarrow \bar{\psi}(x)\mathcal{B}_{\zeta=\hat{\mu}}^\dagger(x), \quad (4.48b)$$

and therefore, due to the exact doubling symmetry of the action, we have

$$\langle J_m^{(r)} J_n^{(s)\dagger} \rangle = (-1)^{r\mu+s\mu} \langle J_m^{(r)} J_n^{(s)\dagger} \rangle,$$

implying

$$\langle J_m^{(r)} J_n^{(s)\dagger} \rangle = 0 \quad \text{if } r \neq s, \quad (4.49)$$

which proves that the current operators  $J_n^{(s)}$  are orthogonal. This means that each of the 16 different point-splittings creates a different meson on the lattice. The binary 4-vector  $s$  is therefore called the ‘‘taste signature’’ of the meson. The orthogonality of these states shows that  $J_n^{(s)}$  operators correspond to 16 different variations of the same physical meson  $\bar{\psi}\gamma_n\psi$  in ordinary QCD. They are referred to as different ‘‘tastes’’ of mesons and have slightly different masses. Recall that one of the main purposes of the improvement program that we extensively discussed in subsection 3.2.2 was to suppress these taste splittings.

The orthogonality relation (4.49) imposes taste selection rules on meson two-point functions. In a similar manner, those selection rules can be extended to three-point functions

$$\langle J_l^{(r)} J_m^{(s)} J_n^{(t)} \rangle = 0 \quad \text{if } (r + s + t) \neq 0 \pmod{2}, \quad (4.50)$$

or, more generally, to any  $k$ -point function

$$\langle J_{n_1}^{(s_1)} \dots J_{n_k}^{(s_k)} \rangle = 0 \quad \text{if } (s_1 + \dots + s_k) \neq 0 \pmod{2}, \quad (4.51)$$



which means that only taste singlet  $k$ -point functions are allowed. Otherwise, the trace over the spinor indices that we encountered earlier in (4.39) and (4.44) would be zero and hence kill the correlator. These selection rules, therefore, dictate the choice of the interpolating operators one can use in simulations. We will be making use of these rules frequently in later chapters.

In addition to the 16 meson tastes due to point-splittings characterized by their taste signature  $s$ , there are an additional 16 mesons obtained by boosting a quark field to a different corner of the Brillouin zone labeled  $\zeta$ . The meson momentum will then be  $p_{\text{tot}} \approx \zeta\pi$ . Such a meson would be highly relativistic in the continuum. However, on the lattice, it is equivalent to a low energy one. For example, a flavor-nonsinglet meson with one low momentum quark and another with momentum  $\zeta\pi$ , is made by a momentum projection

$$\sum e^{ip_{\text{tot}} \cdot x} J_n^{(s)}(x) = \sum (-1)^{\zeta \cdot x} e^{ip \cdot x} J_n^{(s)}(x), \quad (4.52)$$

where  $p_{\text{tot}} = p + \zeta\pi$ , with  $|p_\mu| \leq \pi/2$ . As seen before, a Fourier sum with momentum equal to  $\zeta\pi$  looks like a doubling transformation. Thus such a boost in momentum changes the taste quantum numbers of the meson. Consider the current

$$\begin{aligned} J_n^{(\zeta, s)} &\equiv (-1)^{\zeta \cdot x} \bar{\psi}(x) \gamma_{\bar{\zeta}}^\dagger \gamma_n^{(s)} \psi(x) = \bar{\psi}(x) \mathcal{B}_{\bar{\zeta}}^\dagger(x) \gamma_n^{(s)} \psi(x) \\ &\propto \bar{\chi}(x) \gamma_{\bar{\zeta}}^\dagger \gamma_s \chi(x + \delta x_{sn}), \end{aligned} \quad (4.53)$$

whose taste signature is  $(\bar{\zeta} + s) \bmod 2$ . When summed over the entire lattice, it obviously has a momentum equal to  $\zeta\pi$ . However, for flavor-nonsinglet mesons such as  $\bar{u}d$ , the 16 different  $\zeta$ 's create identical states. This can be demonstrated by exploiting the doubling symmetry as follows

$$\begin{aligned} \langle J_n^{(\zeta, s)}(x) J_n^{(\zeta', s')\dagger}(y) \rangle &\equiv \langle \bar{u} \mathcal{B}_{\bar{\zeta}}^\dagger \gamma_n^{(s)} d \bar{d} \gamma_n^{(s')} \mathcal{B}_{\zeta'} u \rangle \\ &= \langle \bar{u} \gamma_n^{(s)} d \bar{d} \gamma_n^{(s')} u \rangle \equiv \langle J_n^{(s)}(x) J_n^{(s')\dagger}(y) \rangle. \end{aligned} \quad (4.54)$$

Momentum conservation combined with taste conservation (4.49) imply that

$$\sum_{x, y} \langle J_n^{(\zeta, s)}(x) J_n^{(\zeta', s')\dagger}(y) \rangle = 0 \quad \text{unless } \zeta = \zeta' \text{ and } s = s', \quad (4.55)$$

where the sum is over all space-time lattice points. However, in practice one normally only sums over all spatial points on a fixed single time slice of the lattice, projecting mesons onto a fixed 3-momentum. Therefore, only the spatial components of the boost vectors  $\zeta$  and  $\zeta'$  have to be equal;<sup>2</sup> allowing contribution from unequal time components

$$\zeta' - \zeta = \pm \hat{t}, \quad (4.56)$$

---

<sup>2</sup> The exact doubling symmetry still requires that  $s' = s$ , regardless of the summation range.

as well as equal boosts  $\zeta' = \zeta$ . Such contributions give rise to the so called oscillating states which will be discussed in the next section. But before doing so, let us recap what we have learned so far in this section.

For every ordinary meson  $\bar{\psi}\gamma_n\psi$  in continuum QCD, the corresponding naive bilinear currents give rise to a huge number of mesons on the lattice. There are 256 mesons in total, characterized by their taste  $s$  and by their habitat in the Brillouin zone labeled  $\zeta$ . That is, there are 16 distinct tastes, each with an additional 16 copies resulting from boosting it to various corners of the Brillouin zone. Thus, inside each of the 16 regions of the Brillouin zone  $\zeta$ , every one of the 16 meson tastes is represented exactly once. As shown in (4.49), these 16 tastes are orthogonal states and have different masses due to taste changing interactions. For flavor-nonsinglet mesons, (4.54) shows that the 16 different  $\zeta$ 's create identical mesons.

Flavor-singlet mesons such as  $\bar{u}u$  are more complicated. The trick we used in (4.54) to relate the  $J_n^{(\zeta,s)}$  currents with different  $\zeta$ 's to each other, does not work for them because the quark and the anti-quark fields do not have separate doubling symmetries. That is, a doubling transformation on the quark field in the bilinear operator must be accompanied by the same transformation on the anti-quark field, which would leave the meson in the same corner of the Brillouin zone. The only contributions that spoil this argument, however, are from valence quark pair annihilations into gluons. Gluons created from valence quark pair annihilation occurring in the process

$$\sum_{\mathbf{x}} \langle J_n^{(\zeta,s)}(x) J_n^{(\zeta,s)\dagger}(0) \rangle, \quad (4.57)$$

obviously carry a momentum of  $\zeta\pi$ . Therefore, they are far off shell and highly suppressed, unless  $\zeta = 0$ .<sup>3</sup> This means that quark pair annihilation contributions from the 16 different  $\zeta$ 's are different. Furthermore, due to the taste selection rules (4.51) imposed by the doubling symmetry, and given that  $J_n^{(\zeta,s)}$  has taste  $\bar{\zeta} + s$ , for each  $\zeta$  only one flavor-singlet current taste couples to pure gluons:

$$\langle J_n^{(\zeta,s)} \rangle \propto \text{Tr}(\gamma_{\bar{\zeta}+s}) = 0, \quad \text{unless } s = \bar{\zeta}. \quad (4.58)$$

Pair annihilation contributions from currents with non-zero taste,  $\zeta \neq 0$ , are clearly taste violating interactions and are removed by the contact term discussed in chapter 3. Therefore, only the taste-singlet current  $\zeta = s = 0$ , which is the only one with the correct coupling to the pure gluonic channel survives.

---

<sup>3</sup> Remember that gluons do not have doublers. Very high energy gluons are truly off shell.

### 4.3 Oscillating States

In chapter 3 we described how to deal with the doubling problem for the dynamical sea quarks. Section 3.1.1 introduced the 1/16-th root trick to account for the 16 *approximately* degenerate dynamical doublers and the Symanzik improvement program developed in section 3.2.2, was undertaken to suppress taste mixing interactions that break this degeneracy. In this section we finally address the implications of the doubling problem on valence quarks. We examine a relatively simple case of a heavy-light meson to demonstrate the appearance of the oscillating states with opposite parity [45, 46].

Consider a bilinear operator made of a light staggered quark field and a non-staggered heavy quark that does not exhibit the doubling problem, such as a  $b$  quark described by NRQCD. One can use

$$J_5(x) \equiv \bar{\psi}(x)\gamma_5\Psi_b(x), \quad (4.59)$$

to create a  $B$  meson with quantum numbers  $J^P = 0^-$ . The  $b$  quark will be far off shell at high energies  $E \approx \pi$  and will therefore resist those corners of the Brillouin zone. The staggered light quark, on the other hand, has a low energy doubler in those regions. Here the doubling symmetry will help us decode the situation through identifying the additional states that couple to this operator due to the light quark doubler, thereby enabling us to capture their contributions.

In simulations one normally sums over all spatial points when computing two-point correlators in order to project out a specific momentum. For instance, in

$$G_{55}(t) \equiv \sum_{\mathbf{x}} \langle 0 | J_5(\mathbf{x}, t) J_5^\dagger(\mathbf{0}, 0) | 0 \rangle, \quad (4.60)$$

the sum over  $\mathbf{x}$  guarantees that the three-momentum  $\mathbf{p} = \mathbf{0}$ . This takes care of the momentum doublers by explicitly projecting them out. The energy doubler, however, is still present. This means that the current  $J_5$ , couples to two different meson states containing two different light quark tastes

$$\zeta = 0 \leftrightarrow E \approx 0, \quad (4.61a)$$

$$\zeta = (1, 0, 0, 0) \leftrightarrow E \approx \pi. \quad (4.61b)$$

The tasteful energy doubler corresponds to a low-energy quark through the doubling transformation

$$\bar{\psi}(x) \Big|_{E \approx \pi} \rightarrow \bar{\psi}(x)(i\gamma_5\gamma_0)(-1)^t, \quad (4.62)$$

relating the current operator to

$$\bar{\psi}\gamma_5\Psi_b \Big|_{E \approx \pi} \rightarrow \bar{\psi}i\gamma_5\gamma_0\gamma_5\Psi_b(-1)^t = -\bar{\psi}i\gamma_0\Psi_b(-1)^t, \quad (4.63)$$

where the time dependent oscillating phase  $(-1)^t$  appearing in this doubling transformation is due to the boost in the energy by  $E = \pi$ , resulting in a momentum phase factor  $\exp(i\pi t)$ .

This demonstrates that in addition to the  $0^-$  state, the operator  $J_5$  also couples to a meson state with  $J^P = 0^+$ . It is still  $J = 0$  because there is no three-vector index and the parity is  $P = +$  because

$$P\gamma_0P = \gamma_0, \quad (4.64)$$

where  $P \equiv \gamma_0$  is the parity operator. This means that the correlator (4.60) contains contributions from states with opposite parity which enter with an oscillating sign at successive time-steps due to the  $(-1)^t$  factor. This corresponds to the same oscillating behavior that we encountered before in equation (3.31) on page 30. Therefore, the correlator takes the form

$$\begin{aligned} G_{55}(t) \rightarrow & \left| \langle 0 | \bar{\psi} \gamma_5 \Psi_b | 0^- \rangle \right|^2 e^{-E_- t} \\ & - (-1)^t \left| \langle 0 | \bar{\psi} i \gamma_0 \Psi_b | 0^+ \rangle \right|^2 e^{-E_+ t}, \end{aligned} \quad (4.65)$$

where  $E_{\pm}$  represent the masses of bottom meson states  $|0^{\pm}\rangle$ . In particular, we find that the light quark's high energy doubler component (4.61b), results in the coupling of  $J_5$  to a low energy meson with the opposite parity.

One can repeat this analysis for a vector meson. A spatial component of a vector current such as

$$J_i(x) \equiv \bar{\psi}(x) \gamma_i \Psi_b(x), \quad (4.66)$$

can be used to create a  $B^*$  meson with  $J^P = 1^-$  since it has one three-vector index; and

$$P\gamma_iP = \gamma_0\gamma_i\gamma_0 = -\gamma_i,$$

implies that it has parity  $P = -$ . However, under a temporal doubling transformation

$$\bar{\psi} \gamma_i \Psi_b \Big|_{E \approx \pi} \rightarrow \bar{\psi} i \gamma_5 \gamma_0 \gamma_i \Psi_b (-1)^t. \quad (4.67)$$

Hence, this current has additional contributions from coupling to a low energy state created by  $\bar{\psi} \gamma_5 \gamma_0 \gamma_i \Psi_b$ , which is a  $1^+$  state, because  $P\gamma_5\gamma_0\gamma_iP = \gamma_5\gamma_0\gamma_i$ . Therefore, the two-point meson correlator will take the form

$$\begin{aligned} G_{ii}(t) \equiv & \sum_{\mathbf{x}} \langle 0 | J_i(\mathbf{x}, t) J_i^\dagger(\mathbf{0}, 0) | 0 \rangle \\ \rightarrow & \left| \langle 0 | \bar{\psi} \gamma_i \Psi_b | 1^- \rangle \right|^2 e^{-E_- t} - (-1)^t \left| \langle 0 | \bar{\psi} i \gamma_5 \gamma_0 \gamma_i \Psi_b | 1^+ \rangle \right|^2 e^{-E_+ t}, \end{aligned} \quad (4.68)$$

where once again, the opposite parity state which in this case is a  $1^+$  pseudo-vector meson is oscillating in time.

We saw that for a heavy-light meson one can easily identify the contributions of the quark doublers using the doubling symmetry, which enter in the form of couplings to oppo-

site parity states that oscillate in time. One can follow a similar analysis for the light-light mesons as well. Though, since both quark fields in such mesons have doublers, they are slightly more complicated. Nevertheless, they too exhibit the same coupling to oscillating states. That is with the exception of zero-momentum flavor-singlet Goldstone pseudoscalar mesons which don't have an oscillating partner due to the mass degeneracy between constituent quarks.

## 4.4 Staggered Currents

So far we have been studying mesons in the naive basis where they are more intuitive. However, simulations are done in the staggered basis where they are much more efficient thanks to the four-fold reduction in the number of degrees of freedom. This section presents a treatment of mesons in the staggered basis which is formally equivalent to the naive basis.

There are 256 naive mesons on the lattice, consisting of 16 different tastes defined by  $s$ , each of which having 16 identical copies labeled by  $\zeta$ . However, after staggering the quarks and discarding the extra degrees of freedom, only one of the 16 identical  $\zeta$ 's will survive. This leads to a reduction in the number of mesons by a factor of 16. Therefore, there remains 16 distinct staggered mesons corresponding to the 16 tastes labeled  $s$ .

Consider the current introduced in (4.53). When staggered, it takes the form

$$J_n^{(\zeta,s)} \propto \bar{\chi} \gamma_{\zeta}^{\dagger} \gamma_s \chi \rightarrow \bar{\chi} \chi, \quad (4.69)$$

where the second relation expresses the requirement that in the staggered basis there can be no mixing between different spinor indices. In other words, discarding the extra identical degrees of freedom in the quark fields results in discarding the extra identical mesons, and the surviving meson is the one that is diagonal in the staggered basis. Recall that  $\gamma_{\zeta}^{\dagger} \gamma_s$  is like a permutation operator which only shuffles the spinor indices of  $\chi$ . Thus, this spinor matrix must be proportional to the unit matrix  $\mathbf{1}_{\text{spinor}}$ . This implies that for any given  $s$  the only  $\zeta$  that survives staggering is

$$\zeta = \bar{s}, \quad (4.70)$$

which corresponds to the current

$$\begin{aligned} J_n^{(\bar{s},s)} &\equiv (-1)^{\bar{s} \cdot x} \bar{\psi}(x) \gamma_s^{\dagger} \gamma_n \psi(x + \delta x_{sn}) \\ &= \beta_n^{(s)}(x) \bar{\chi}(x) \chi(x + \delta x_{sn}), \end{aligned} \quad (4.71)$$

where  $\beta_n^{(s)}(x)$  is a coordinate dependent phase. This meson has momentum  $p_{\text{tot}} = \bar{s}\pi$ . Once again all the information about the spin and the taste structure of the meson in the

staggered basis is encapsulated in a phase

$$\begin{aligned}\beta_n^{(s)}(x) &= \frac{1}{4} \text{Tr}(\gamma_s^\dagger \gamma_x^\dagger \gamma_n \gamma_{x+s+n}) \\ &= (-1)^{x \cdot (s^< + n^>)} (-1)^{n \cdot (s+n)^<},\end{aligned}\tag{4.72}$$

where we have used the gamma matrix properties listed in subsection 4.1.2. Note also that the current (4.71) is tasteless, since  $\bar{\zeta} + s = \bar{s} + s = 0$ , and hence is obviously unchanged under doubling transformations (4.37).

It would be useful for formal analyses to introduce a notation that separates the spin and the taste structure of a current. Let us define the operator

$$\gamma_n \otimes \xi_s \psi(x) \equiv (-1)^{\bar{s} \cdot x} \gamma_s^\dagger \gamma_n \psi(x \oplus (n + s)),\tag{4.73}$$

where  $\oplus$  is defined as

$$(x \oplus n)_\mu \equiv x_{B\mu} + (x_\mu - x_{B\mu} + n_\mu) \pmod{2},\tag{4.74}$$

and represents the point-splitting of the quark field inside an elementary hypercube block that contains  $2^4$  lattice sites and is identified by the coordinates  $x_B$  of its all-even corner. That is,  $x_{B\mu} = 0 \pmod{2}$ . The  $\oplus$  operator ensures that the shifted quark field stays inside the hypercube.

Using this notation one can recast the naive mesons in terms of current operators

$$\bar{\psi}(x) \gamma_n \otimes \xi_s \psi(x),\tag{4.75}$$

where  $\gamma_n$  encodes the spin, and  $\xi_s$  encodes the taste which is determined by the shifting of the quark field in the hypercube.

Equations (4.73) and (4.74) define a very simple algebra. One can easily verify that

$$\gamma_n \otimes \xi_s \gamma_m \otimes \xi_r = \gamma_n \gamma_m \otimes \xi_s \xi_r.\tag{4.76}$$

Furthermore, the  $\xi_s$  taste matrices satisfy the same anti-commutation relations as the  $\gamma_n$  spinor matrices

$$\gamma_n \otimes \xi_s \xi_r = (-1)^{\bar{r} \cdot s} \gamma_n \otimes \xi_r \xi_s,\tag{4.77}$$

similar to (4.25). Thus, the same notation and set of matrices can be used for taste as those used for spin, introduced in (4.4).

Working in the naive basis, one may wish to restrict a meson to the  $\zeta = \bar{s}$  corner of the Brillouin zone by blocking the relevant operator on a hypercube

$$\mathcal{J}_n^{(s)}(x_B) = \frac{1}{16} \sum_{\delta x_\mu \in \mathbb{Z}_2} \bar{\psi}(x_B + \delta x) \gamma_n \otimes \xi_s \psi(x_B + \delta x),\tag{4.78}$$

where the current is averaged over  $2^4$  sites. Bear in mind, however, that unlike the reduced staggered basis, this blocking approach only approximately isolates a certain taste.

In the staggered basis, the current defined in (4.75) is related to

$$\bar{\psi}(x)\gamma_n \otimes \xi_s \psi(x) = \bar{\chi}(x)\gamma_s^\dagger \gamma_x^\dagger \gamma_n \gamma_{x+\delta x_{sn}} \chi(x \oplus \delta x_{sn}), \quad (4.79)$$

where  $\delta x_{sn}$  is the only shifting vector, among the  $2^4$  shifts in the hypercube unit, which results in a diagonal current and survives staggering. Therefore, it can be rewritten as

$$\sum_{\delta x_\mu \in \mathbb{Z}_2} \bar{\chi}(x) \frac{1}{4} \text{Tr}(\gamma_s^\dagger \gamma_x^\dagger \gamma_n \gamma_{x+\delta x}) \chi(x \oplus \delta x), \quad (4.80)$$

and the blocked average becomes

$$\frac{1}{16} \sum_{\delta x, \delta x'} \bar{\chi}(x_B + \delta x) \frac{1}{4} \text{Tr}(\gamma_s^\dagger \gamma_{\delta x}^\dagger \gamma_n \gamma_{\delta x'}) \chi(x_B + \delta x'), \quad (4.81)$$

where we have used  $\gamma_{x_B+\delta x} = \gamma_{\delta x}$ . Note again that only 16 of the total 256 terms in this sum are non-vanishing, since the rest involve traceless gamma matrices. However, we would like to emphasize that this kind of averaging over hypercubes is not necessary in constructing operators used in simulation.

We saw that the spin and the taste structure of mesons can be described by the same kind of algebra that the corresponding  $\gamma$  and  $\xi$  matrices satisfy. Thus, for instance, one can refer to the local meson  $\bar{\psi}(x)\gamma_5\psi(x)$  as a pseudo-scalar meson with ‘‘pseudo-scalar taste,’’ as made clear by this notation

$$\bar{\psi}(x)\gamma_5 \otimes \xi_5 \psi(x) = \beta_5^{(5)}(x) \bar{\chi}(x) \chi(x) = (-1)^{x \cdot x} \bar{\chi}(x) \chi(x), \quad (4.82)$$

since both its spin and its taste are determined by the 4-vector

$$n = s = (1, 1, 1, 1). \quad (4.83)$$

By the same convention, one can build one-link operators by using an  $s = 5\mu$  taste vector. And a pseudo-scalar meson,  $n = 5 \equiv (1, 1, 1, 1)$ , with zero taste,  $s = 0$ , would correspond to a four-link operator, and so on.

This notation can also be extremely useful in the formal analysis of the naive/staggered quark theory’s symmetries, such as the study of its chiral invariance in the case of massless quarks. Chiral transformations can be expressed as

$$\begin{aligned} \psi(x) &\rightarrow \exp(i\theta \gamma_5 \otimes \xi_5) \psi(x), \\ \bar{\psi}(x) &\rightarrow \bar{\psi}(x) \exp(i\theta \gamma_5 \otimes \xi_5), \end{aligned} \quad (4.84)$$

where the  $\xi_5$  coupled to the  $\gamma_5$  in the exponent codifies the fact that the chiral transformations do not translate the quark field  $\psi(x)$ . We will return to the chiral symmetry in chapter 6.



# Chapter 5

## Methodology

In this chapter we explain how to get answers from the action. The previous three chapters developed an elaborate theoretical framework for doing nonperturbative calculations in low energy hadronic physics. With that in place, in this chapter we describe how one actually does a numerical simulation on the lattice to extract interesting physical quantities such as hadronic masses and decay rates. We will illustrate our methodology by computing a few interesting quantities, and also describe some diagnostics that were used to test the code developed for this thesis.

Although they're not physical "observables," we begin in section 5.1 by calculating quark propagators. They constitute the main ingredients of two-point and three-point correlation functions used in section 5.2 to compute hadron spectra and matrix elements. A select few of the most important numerical techniques employed in this work to enhance performance and increase precision are described in section 5.3. Periodic and twisted boundary conditions are discussed in section 5.4. Finally, section 5.5 explains Bayesian methods for curve fitting that are used to extract physical quantities from the simulation data.

This completes a full recipe for numerical calculation of a quantity whose experimentally measured value may or may not be on the PDG. The goal is that given a lattice action, and of course a computing cluster, one would be able to produce theoretical estimates for physical observables. Before moving on to our main calculations we close our pedagogical discussion of the methodology in section 5.6 by putting together everything we learned in this thesis up to that point and apply it to a few problems.

### 5.1 Quark Propagators

We saw in chapter 4 that the quark propagator in the staggered basis is

$$g(x, y) = \langle \chi(x) \bar{\chi}(y) \rangle = M_{x,y}^{-1}, \quad (5.1)$$

where  $M$  is the fermion matrix and encodes the structure of the lattice action:

$$\mathcal{S} = \sum_x \bar{\chi}(x) (\alpha(x) \cdot \mathcal{D} + m) \chi(x) \equiv \sum_{x,y} \bar{\chi}(x) M_{x,y} \chi(y). \quad (5.2)$$

It is related to the propagator in the spinor basis through  $S(x, y) = g(x, y) \Omega(x) \Omega^\dagger(y)$ .

The simplest way to compute the inverse fermion matrix  $M_{x,y}^{-1}$ , is to use a *point source* vector

$$b(x) = \mathbf{I}_3 \delta_{x,x_0} \quad (5.3)$$

where  $\mathbf{I}_3$  is the  $SU(3)$  color unit matrix, and solve the linear equation

$$M\phi = b \Rightarrow \phi = M^{-1}b. \quad (5.4)$$

The solution is the propagator on every lattice point  $y$ , of a quark propagating out of  $x_0$ :

$$\phi(y) = \sum_x M^{-1}(y, x) b(x) = M^{-1}(y, x_0) = g(y, x_0). \quad (5.5)$$

Note that there are no spinor indices and the color indices are made implicit.

The problem of calculating quark propagators is then reduced to solving a system of linear equations defined by the fermion matrix  $M$  and a source vector  $b$ . The structure of  $M$  is action specific and is exactly determined according to the finite difference implementation of the covariant derivative in the  $\mathcal{D} + m$  operator. Therefore,  $M$  is typically a large sparse square matrix whose elements connect the spin and color components of fermion fields defined on  $L^3T = V$  sites on the lattice.

The HISQ fermion matrix looks something like

$$M^{\text{HISQ}} = \begin{matrix} x - \hat{0} \\ x \\ x + \hat{0} \\ \vdots \\ \vdots \\ \vdots \end{matrix} \rightarrow \begin{pmatrix} m & & & & \vdots & & & & \\ & \ddots & & -\frac{9+\epsilon}{16} \alpha_0(x) U_0^\dagger(x - \hat{0}) & & & & & \\ & & & & \vdots & & & & \\ & \dots & & m & & \dots & & & \\ & & & & \vdots & & & & \\ & & & \frac{9+\epsilon}{16} \alpha_0(x) U_0(x) & & \ddots & & & \\ & & & & \vdots & & & & m \end{pmatrix}. \quad (5.6)$$

Every row and column has exactly 17 nonzero entries consisting of the diagonal mass term in addition to the forward and backward 1-step and 3-step separated terms along each of the 4 spacetime directions.

This is a  $3V \times 3V$  matrix since the 4 spinor degrees of freedom are diagonalized away in the staggered basis which is a big advantage. However, it's still a gigantic matrix.

This work has used  $20^3 \times 64$  lattices which makes  $M$  of size 512,000 times 3. Solving (5.4) is therefore computationally quite intensive. Apart from generating the gauge field configurations almost all of the simulation time is spent on inverting  $M$ .

The *conjugate gradient* family of numerical algorithms are best suited to solve large sparse linear systems efficiently. These are iterative methods that try to find a vector  $\phi$  for which  $M\phi - b$  is smaller than some pre-set tolerance level with variations optimized to handle different types of systems [47]. The number of iterations that the CG algorithm takes to converge is normally proportional to the condition number of  $M$ . As a result the computation slows down as the mass gets lighter thereby making simulations at physical light quark masses expensive and noisy.

The CG algorithm can be found in standard textbooks on numerical analysis such as [48] and therefore not repeated here. We almost doubled the performance of our code through *even-odd preconditioning* the matrix  $M$ . This method takes advantage of the fact that apart from the diagonal elements all nonzero elements of  $M$  belong to entries corresponding to lattice sites separated by an odd number of links. This allows one to reorganize  $M$  in such a way that (5.4) can be turned into a linear system with half the size which is also good news for the RAM. This method will also not be reproduced here.

## 5.2 Calculating Physical Quantities

Lattice theorists like other particle physicists are generally interested in hadronic masses and transition rates. These quantities are obtained from 2-point and 3-point correlation functions that are computed on the lattice by stitching quark propagators together. This section explains the connection.

### 5.2.1 Hadronic Masses and Two-Point Functions

Hadron spectroscopy is done by computing 2-point functions. Consider the correlator

$$G(t - t_0; \vec{p}) = \sum_{\vec{x}} e^{-i\vec{p}\cdot\vec{x}} \langle J_5^\dagger(\vec{x}, t) J_5(\vec{x}_0, t_0) \rangle \quad (5.7)$$

where  $J_5(x) = \bar{\psi}(x)\gamma_5\psi(x)$  is a pseudoscalar current that may be used to create an  $\eta_c$ . Fourier transforming into the momentum space and switching to the Euclidean Heisenberg picture one can write

$$\begin{aligned} G(t - t_0; \vec{p}) &= \sum_n \frac{\langle 0 | e^{Ht} J_5^\dagger(\vec{p}) e^{-Ht} | n \rangle \langle n | e^{Ht_0} J_5(\vec{p}) e^{-Ht_0} | 0 \rangle}{\langle n | n \rangle} \\ &= \sum_n |a_n|^2 e^{-E_n(\vec{p})(t-t_0)}. \end{aligned} \quad (5.8)$$

This relates the 2-point correlator to hadron energies. Generally, the  $a_n$  parameters

$$a_n = \frac{\langle n|J|0\rangle}{\sqrt{\langle n|n\rangle}} \quad (5.9)$$

are the overlaps between an *interpolating* operator  $J$  and the  $n$ -th meson state with energy  $E_n$ . This spectral decomposition follows from the completeness relation

$$\mathbf{1} = \sum_n |n\rangle \frac{1}{\langle n|n\rangle} \langle n| \quad (5.10)$$

and is simply obtained by inserting a complete set of states in the middle of the two interpolating operators.

These overlaps obviously depend on the choice of state normalization. One is free to adopt whatever normalization convention one wishes. It's important, however, to pick one and use it consistently throughout the analysis. We choose the relativistic normalization

$$\langle n(\vec{p})|n'(\vec{k})\rangle = \delta_{nn'} (2\pi)^3 2E_n(\vec{p}) \delta^{(3)}(\vec{p} - \vec{k}) \quad (5.11)$$

in all our formal analyses throughout this work.

Note that the time reversal symmetry requires that  $G(t) = G(-t)$ . However, in a finite box with temporal length  $L_t$ , time is limited to  $t \in [0, L_t)$  like a deadline. On a lattice with periodic boundary conditions,  $-t$  is mapped unto  $L_t - t$  and thus the time reversal condition is modified to  $G(t) = G(L_t - t)$ . Hence, the lattice 2-point function's time dependence is modified to<sup>1</sup>

$$G(t) = \sum_n a_n^2 \left( e^{-E_n t} + e^{-E_n(L_t - t)} \right). \quad (5.12)$$

In general, the two interpolating operators in a 2-point correlator can be different

$$G_{ab}(t) = \sum_{\vec{x}} e^{-i\vec{p}\cdot\vec{x}} \langle \Gamma_a^\dagger(x) \Gamma_b(0) \rangle \quad (5.13)$$

which results in different overlaps. Furthermore, recall that staggered bilinears also couple to states with opposite parity. These are the oscillating states discussed in section 4.3. A general staggered 2-point correlator is then of the form

$$G_{ab}(t) = \sum_{i_n, i_o} a_{i_n}^* b_{i_n} \text{fn}(E_{i_n}, t) - \tilde{a}_{i_o}^* \tilde{b}_{i_o} \text{fo}(\tilde{E}_{i_o}, t) \quad (5.14)$$

---

<sup>1</sup> This is just an intuitive explanation for the appearance of the second exponential, not a proof. For a formal derivation see [27, Section 4.2.5].

with shorthands for the normal and oscillating bi-exponentials defined as

$$\begin{aligned} \text{fn}(E, t) &\equiv e^{-Et} + e^{-E(L_t-t)}, \\ \text{fo}(E, t) &\equiv (-1)^t \text{fn}(E, t). \end{aligned} \quad (5.15)$$

The tilde parameters are associated with the oscillating states.

It is now clear how meson energies are calculated in lattice simulations. Consider the simple case of a pseudoscalar meson such as  $\eta_c$ . The interpolating operator

$$J_5(x) = \bar{\psi}(x)\gamma_5\psi(x) \quad (5.16)$$

is used to compute the 2-point function

$$G(t; \vec{p}) = \sum_{\vec{y}} e^{-i\vec{p}\cdot(\vec{y}-\vec{x}_0)} \langle J_5^\dagger(y) J_5(x_0) \rangle. \quad (5.17)$$

All one needs to do is then to compute  $G$  on the lattice. Using Wick's theorem, the correlator is obtained from contractions as follows

$$\begin{aligned} G(t; \vec{p}) &= \sum_{\vec{y}} e^{-i\vec{p}\cdot(\vec{y}-\vec{x}_0)} \overbrace{\langle \bar{\psi}(y)\gamma_5\psi(y)\bar{\psi}(x_0)\gamma_5\psi(x_0) \rangle} \\ &= \sum_{\vec{y}} e^{-i\vec{p}\cdot(\vec{y}-\vec{x}_0)} \text{Tr}(\gamma_5 S(x_0, y)\gamma_5 S(y, x_0)). \end{aligned} \quad (5.18)$$

The only other possible Wick contraction involves disconnected diagrams. These are OZI suppressed and expected to be negligibly small. They are also hugely expensive to include and are generally neglected in most lattice calculations.

Using the  $\gamma_5$  hermiticity property  $S^\dagger(y, x) = \gamma_5 S(x, y)\gamma_5$  and then spin diagonalizing into the staggered basis the trace will become

$$\text{Tr}\left(S^\dagger(y, x_0)S(y, x_0)\right) = \text{Tr}\left(\Omega(x_0)\Omega^\dagger(y)\Omega(y)\Omega^\dagger(x_0)\right) \text{tr}\left(g^\dagger(y, x_0)g(y, x_0)\right), \quad (5.19)$$

where the first  $\text{Tr}()$  is over spinor indices and  $\text{tr}()$  over color. This is simplified to

$$\begin{aligned} G(t; \vec{p}) &= 4 \sum_{\vec{y}} e^{-i\vec{p}\cdot(\vec{y}-\vec{x}_0)} \text{tr}\left(g^\dagger(y, x_0)g(y, x_0)\right) \\ &= 4 \sum_{\vec{y}} e^{-i\vec{p}\cdot(\vec{y}-\vec{x}_0)} \sum_{i,j} \left(|g_{ij}(y, x_0)|^2\right). \end{aligned} \quad (5.20)$$

The color indices  $i, j$  are made explicit in the second line.

This shows explicitly that one needs propagators of every initial and final color out of the source point  $x_0$ . Thus, three point sources are required one for each color. In (5.3) they were put together as columns of the  $3 \times 3$  components of the vector  $b$  for a compact notation.

In practice they're solved one color at a time in order to reduce memory requirements. The linear equation  $M\phi = b$  is then solved numerically to give  $\phi(y) = g(y, 0)$ . Finally, convolving  $\phi$  with itself using the appropriate momentum projection phase gives the correlator we were looking for

$$G(t; \vec{p}) = \sum_{\vec{y}} e^{-i\vec{p}\cdot\vec{y}} \phi^\dagger(\vec{y}, t) \phi(\vec{y}, t). \quad (5.21)$$

### Free Field

The simulation code for every single correlation function computed in this work has undergone extensive testing before being deployed for production run. One of the most useful tests of the simulation code would be to calculate free field correlators. This can be done both using the simulation code to compute the free propagators while setting all link variables equal to  $U_\mu(x) = \mathbf{I}_3$ , as well as (semi)-analytically as shown below. Setting all links equal to the unit matrix is tantamount to turning off interactions and equivalent to setting the coupling  $g = 0$ . This useful cross-check provides significant confidence in one's code. Here we show an example of an analytical free field 2-point function calculation.

Consider the simplest case of a local Goldstone pseudoscalar such as  $\eta_c$ . The free field propagator of a HISQ quark in the momentum space is given by

$$\begin{aligned} S_0^{-1}(p) &= \sum_{\mu} i\gamma_{\mu} \sin(p_{\mu}) \left[ 1 + \frac{1+\epsilon}{6} \sin^2(p_{\mu}) \right] + m_0 \\ &\equiv i\tilde{\not{p}} + m_0, \end{aligned} \quad (5.22)$$

where the shorthand notation  $\tilde{p}$  is introduced to represent the  $\mathcal{D}^{\text{HISQ}}$  operator in Fourier space

$$\tilde{p}_{\mu} \equiv \sin(p_{\mu}) \left[ 1 + \frac{1+\epsilon}{6} \sin^2(p_{\mu}) \right]. \quad (5.23)$$

The free field 2-point correlator is then

$$\begin{aligned} G^{(0)}(t; \vec{p}) &= \int d^3\vec{y} e^{-i\vec{p}\cdot(\vec{y}-\vec{x})} \overbrace{\langle \bar{\psi} \gamma_5 \psi(y) \bar{\psi} \gamma_5 \psi(x) \rangle} \\ &= \int d^3\vec{y} \frac{d^4 p_1}{(2\pi)^4} \frac{d^4 p_2}{(2\pi)^4} e^{-i\vec{p}\cdot(\vec{y}-\vec{x})} \text{Tr} \left( \gamma_5 \left[ \frac{e^{ip_1 \cdot (x-y)}}{i\tilde{\not{p}}_1 + m_0} \right] \gamma_5 \left[ \frac{e^{ip_2 \cdot (y-x)}}{i\tilde{\not{p}}_2 + m_0} \right] \right). \end{aligned} \quad (5.24)$$

One can write

$$\frac{1}{i\tilde{\not{p}} + m_0} = \frac{-i\tilde{\not{p}} + m_0}{D(\tilde{p})}, \quad (5.25)$$

where another shorthand notation is introduced to denote the denominator

$$D(\tilde{p}) \equiv \tilde{p}^2 + m_0^2. \quad (5.26)$$

Integrating first over  $\vec{y}$ , and then over  $\vec{p}_2$ , while noting that each yields a  $\delta^{(3)}$  function, one then finds

$$G^{(0)}(t; \vec{p}) = \int \frac{d^4 p_1}{(2\pi)^4} \frac{d p_2^0}{2\pi} e^{-i(p_2^0 - p_1^0)(t - t_0)} \frac{\text{Tr} \left( \gamma_5 (-i\vec{\not{p}}_1 + m_0) \gamma_5 (-i\vec{\not{p}}_2 + m_0) \right)}{D(\vec{p}_1) D(\vec{p}_2)} \Bigg|_{\vec{p}_2 = \vec{p}_1 - \vec{p}} \quad (5.27)$$

where it is understood that the integrand is evaluated at  $\vec{p}_2 = \vec{p}_1 - \vec{p}$ . The trace is

$$\begin{aligned} \text{Tr} \left( \gamma_5 (-i\vec{\not{p}}_1 + m_0) \gamma_5 (-i\vec{\not{p}}_2 + m_0) \right) &= \text{Tr} \left( (i\vec{\not{p}}_1 + m_0) (-i\vec{\not{p}}_2 + m_0) \right) \\ &= 4(\vec{p}_1 \cdot \vec{p}_2 + m_0^2). \end{aligned} \quad (5.28)$$

Thus, the free field correlator is given by

$$G^{(0)}(t; \vec{p}) = \int \frac{d^4 p_1}{(2\pi)^4} \frac{d p_2^0}{2\pi} e^{-i(p_2^0 - p_1^0)(t - t_0)} \left( \frac{4(\vec{p}_1 \cdot \vec{p}_2 + m_0^2)}{D(\vec{p}_1) D(\vec{p}_2)} \right) \Bigg|_{\vec{p}_2 = \vec{p}_1 - \vec{p}} \quad (5.29)$$

One can complete this calculation by evaluating this integral numerically.

The finite lattice extent simply converts the bounded momentum integrals  $\int_{-\pi/a}^{\pi/a}$  into discrete sums over a finite number of quanta of momentum allowed on the lattice. We will show in section 5.4 that these are integer multiples of  $2\pi/La$  where  $L$  is the lattice extent. Every correlator in this work passed the free field test, among many others. Our analytical and simulated results agreed perfectly up to roundoff errors at the level of machine precision.

## 5.2.2 Hadronic Matrix Elements and Three-Point Functions

Hadronic matrix elements are calculated on the lattice using 3-point functions that generally take the form

$$C(t, T; \vec{q}) = \sum_{\vec{y}, \vec{z}} e^{-i\vec{q} \cdot (\vec{y} - \vec{z})} \langle \Gamma_a^\dagger(y) V(z) \Gamma_b(x) \rangle. \quad (5.30)$$

where  $x^0 = t_0 = 0$ ,  $y^0 = T$  and  $z^0 = t$  are referred to as the source, the sink and the current insertion time respectively. Here the source is at rest. The correlation function is then related to physical observables through a spectral decomposition similar to that for the 2-point correlator

$$C(t, T; \vec{q}) = \sum_{m, n} \frac{\langle 0 | \Gamma_a^\dagger(T) | m \rangle \langle m | V(t) | n \rangle \langle n | \Gamma_b(0) | 0 \rangle}{\langle m | m \rangle \langle n | n \rangle} \quad (5.31)$$

Using the notation of the previous section, the right hand side takes the form

$$\begin{aligned}
C(t, T; \vec{q}) = & \sum_{i_n, j_n} a_{i_n}^* b_{j_n} V_{i_n j_n}^{nn} \text{fn}(E_{a, i_n}, T - t) \text{fn}(E_{b, j_n}, t) \\
& - \sum_{i_n, j_o} a_{i_n}^* \tilde{b}_{j_o} V_{i_n j_o}^{no} \text{fn}(E_{a, i_n}, T - t) \text{fo}(\tilde{E}_{b, j_o}, t) \\
& - \sum_{i_o, j_n} \tilde{a}_{i_o}^* b_{j_n} V_{i_o j_n}^{on} \text{fo}(\tilde{E}_{a, i_o}, T - t) \text{fn}(E_{b, j_n}, t) \\
& + \sum_{i_o, j_o} \tilde{a}_{i_o}^* \tilde{b}_{j_o} V_{i_o j_o}^{oo} \text{fo}(\tilde{E}_{a, i_o}, T - t) \text{fo}(\tilde{E}_{b, j_o}, t).
\end{aligned} \tag{5.32}$$

Despite its complicated looking form, the fit function is easily understood from the spectral decomposition. The 4 lines simply result from splitting up the normal and oscillating states in the double decomposition in (5.31). Accordingly, each term is made of the product of two exponential functions corresponding to the propagation of the initial and the final meson states before and after the current insertion at time  $t$ .  $a$  and  $b$  are the same overlap parameters as before. And finally, the hadronic matrix elements are

$$V_{ij} = \frac{\mathcal{Z} \langle i | V | j \rangle}{\sqrt{\langle i | i \rangle \langle j | j \rangle}}, \tag{5.33}$$

where  $\mathcal{Z}$  is the renormalization matching factor for the current. Note that the state normalization factors  $\sqrt{\langle i | i \rangle}$  were absorbed into the overlap parameters in (5.9) and the similar factors in the denominator make  $V_{ij}$  normalization independent.

### 5.2.3 The Conserved Current and the Ward Identity

The conserved current corresponding to the global  $U(1)$  symmetry of the fermion action is used as an example of a 3-point function calculation in this section. Let us first derive the conserved current for the HISQ action. Since there are no derivatives on the lattice, the usual procedure of the Noether's theorem for continuous symmetries can not be directly applied here. One can follow a discrete variational analysis without invoking the Euler-Lagrange equations or using field derivatives.

Let us introduce a convenient shorthand notation

$$\mathcal{D}_\mu^{\text{HISQ}} \equiv \mathcal{D}_\mu^{\text{forward}} - \mathcal{D}_\mu^{\text{backward}} \equiv (\mathcal{D}_{\mu,+} - \mathcal{D}_{\mu,3+}) - (\mathcal{D}_{\mu,-} - \mathcal{D}_{\mu,3-}) \tag{5.34}$$

with obvious definitions. Following the derivation presented in [49], consider a local  $U(1)$  infinitesimal phase transformation

$$\begin{aligned}
\psi(x) & \rightarrow e^{i\omega(x)} \psi(x) = \psi(x) + i\omega(x)\psi(x), \\
\bar{\psi}(x) & \rightarrow \bar{\psi}(x) e^{-i\omega(x)} = \bar{\psi}(x) - i\omega(x)\bar{\psi}(x).
\end{aligned} \tag{5.35}$$



The action varies like

$$\delta\mathcal{S}[\psi, \bar{\psi}] = \sum_{x,\mu} i\Delta_\mu\omega(x) \left[ \bar{\psi}(x) \gamma_\mu \left( \{ \mathcal{D}_{\mu,+} - 3\mathcal{D}_{\mu,3+} \} + \{ \mathcal{D}_{\mu,-} - 3\mathcal{D}_{\mu,3-} \} \right) \psi(x) \right] \quad (5.36)$$

where  $\Delta_\mu\omega(x) = \omega(x + \hat{\mu}) - \omega(x)$ . This yields a vector current

$$\begin{aligned} j_\mu^{(\text{cons.})}(x) &= -\frac{\delta\mathcal{S}(x)}{\delta(\Delta_\mu\omega(x))} \\ &= -i\bar{\psi}(x) \left[ \gamma \cdot (\{ \mathcal{D}_+ - 3\mathcal{D}_{3+} \} + \{ \mathcal{D}_- - 3\mathcal{D}_{3-} \}) \right] \psi(x). \end{aligned} \quad (5.37)$$

This current is conserved in the sense that  $\langle \delta\mathcal{S} \rangle = \langle \sum_\mu [j_\mu(x + \hat{\mu}) - j_\mu(x)] \rangle = 0$  on ensemble average, since it becomes a surface term.

Consider the conserved current inserted between two  $\eta_c$  operators

$$C(t, T; \vec{q}) = \sum_{\vec{y}, \vec{z}} e^{-i\vec{q} \cdot (\vec{y} - \vec{z})} \langle J_5^\dagger(y) j_0^{(\text{cons.})}(z) J_5(x) \rangle. \quad (5.38)$$

According to the Ward identity one expects

$$\mathcal{Z}(\vec{0}) = \frac{C(t, T; \vec{0})}{G(T; \vec{0})} = 1, \quad t_0 \leq t \leq T. \quad (5.39)$$

A similar shorthand notation for the corresponding correlator

$$C_\mu^{(\text{cons.})} \equiv \{ C_{\mu,+} - 3C_{\mu,3+} \} + \{ C_{\mu,-} - 3C_{\mu,3-} \} \quad (5.40)$$

is introduced to declutter the calculation and keep track of the 1-step and 3-step forward and backward shifted terms of the current.

The quark fields in the current Wick contract with those of the interpolating operators two different ways, corresponding to the coupling of the current to the quark or the antiquark. For instance, the 1-link forward term of the temporal component of the current inserted on the quark line takes the form

$$\begin{aligned} C_{0,+}(t, T; \vec{q}) &= \sum_{\vec{y}, \vec{z}} e^{-i\vec{q} \cdot (\vec{y} - \vec{z})} \langle \overbrace{\bar{\psi}(y) \gamma_5 \psi(y) \bar{\psi}(z) \gamma_0 U_0(z) \psi(z + \hat{0}) \bar{\psi}(x) \gamma_5 \psi(x)} \rangle \\ &= \sum_{\vec{y}, \vec{z}} e^{-i\vec{q} \cdot (\vec{y} - \vec{z})} \text{Tr} \left( \gamma_5 S(x, z) \gamma_0 U_0(z) S(z + \hat{0}, y) \gamma_5 S(y, x) \right) \\ &= \sum_{\vec{y}, \vec{z}} e^{-i\vec{q} \cdot (\vec{y} - \vec{z})} \text{Tr} \left( S^\dagger(z, x) \gamma_5 \gamma_0 U_0(z) S(z + \hat{0}, y) \gamma_5 S(y, x) \right) \end{aligned} \quad (5.41)$$

where the  $\gamma_5$  hermiticity trick has been used again. The trace becomes

$$\begin{aligned}\text{Tr}(\cdot) &= \text{Tr}\left(\Omega(x)\Omega^\dagger(z)\gamma_5\gamma_0\Omega(z+\hat{0})\Omega^\dagger(y)\gamma_5\Omega(y)\Omega^\dagger(x)\right)\text{tr}(g^\dagger(z,x)U_0(z)g(z+\hat{0},y)g(y,x)) \\ &= 4(-1)^{(z^2+y^2)}\alpha_0(z)\times\text{tr}(g^\dagger(z,x)U_0(z)g(z+\hat{0},y)g(y,x)).\end{aligned}\tag{5.42}$$

The trace over the spinor indices only returns a coordinate dependent *staggered* phase which encodes the specific structure of the operators in the correlation function.

The actual lattice calculation is then carried out in the staggered basis which involves only the staggered propagators  $g$ . The correlator to be computed on the lattice is then

$$C_0(t, T; \vec{q}) = 4 \sum_{\vec{y}, \vec{z}} e^{-i\vec{q}\cdot(\vec{y}-\vec{z})} (-1)^{(z^2+y^2)} \left[ \frac{9+\epsilon}{8} \text{tr} \left( g^\dagger(z, x) U_0(z) g(z + \hat{0}, y) g(y, x) \right) + \dots \right].\tag{5.43}$$

The ellipsis represents the 3-step and the backward shifted terms from the conserved current.

### Free Field

The semi-analytical calculation of the free field 3-point correlator for the conserved current is similar to that for a 2-point function and is undertaken as follows

$$\begin{aligned}C_{0,+}^{(0)}(t, T; \vec{q}) &= \int d^3\vec{y}d^3\vec{z} e^{-i\vec{q}\cdot(\vec{y}-\vec{z})} \overbrace{\langle \bar{\psi}(y)\gamma_5\psi(y)\bar{\psi}(z)\gamma_0U_0(z)\psi(z+\hat{0})\bar{\psi}(x)\gamma_5\psi(x) \rangle} \\ &= \int d^3\vec{y}d^3\vec{z} \frac{d^4p_1}{(2\pi)^4} \frac{d^4p_2}{(2\pi)^4} \frac{d^4p_3}{(2\pi)^4} e^{-i\vec{q}\cdot(\vec{y}-\vec{z})} \\ &\times \text{Tr} \left( \gamma_5 \left[ \frac{e^{ip_1\cdot(x-z)}}{i\tilde{\not{p}}_1 + m_0} \right] \gamma_0 \left[ \frac{e^{ip_2\cdot(z+\hat{0}-y)}}{i\tilde{\not{p}}_2 + m_0} \right] \gamma_5 \left[ \frac{e^{ip_3\cdot(y-x)}}{i\tilde{\not{p}}_3 + m_0} \right] \right).\end{aligned}\tag{5.44}$$

integrating over  $\vec{y}$  and  $\vec{z}$  followed by  $\vec{p}_2$  and  $\vec{p}_3$ , will take care of the momentum conservation and give

$$\begin{aligned}C_{0,+}^{(0)}(t, T; \vec{q}) &= \int \frac{d^4p_1}{(2\pi)^4} \frac{dp_2^0}{2\pi} \frac{dp_3^0}{2\pi} e^{ip_1^0(t_0-t)} e^{ip_2^0(t+1-T)} e^{ip_3^0(T-t_0)} \\ &\times \left\{ \frac{\text{Tr} \left( \gamma_5 (-i\tilde{\not{p}}_1 + m_0) \gamma_0 (-i\tilde{\not{p}}_2 + m_0) \gamma_5 (-i\tilde{\not{p}}_3 + m_0) \right)}{D(\tilde{p}_1)D(\tilde{p}_2)D(\tilde{p}_3)} \right\} \Bigg|_{\substack{\tilde{p}_2 = \tilde{p}_1 + \vec{q}, \\ \tilde{p}_3 = \tilde{p}_1}}.\end{aligned}\tag{5.45}$$

where the trace can be simplified to

$$\begin{aligned}\text{Tr}(\cdot) &= \text{Tr} \left( (-i\tilde{\not{p}}_1 + m_0) \gamma_0 (-i\tilde{\not{p}}_2 + m_0) (i\tilde{\not{p}}_3 + m_0) \right) \\ &= \text{Tr} \left( -i\tilde{\not{p}}_1 \gamma_0 \tilde{\not{p}}_2 \tilde{\not{p}}_3 - im_0^2 [\tilde{\not{p}}_1 \gamma_0 + \gamma_0 \tilde{\not{p}}_2 - \gamma_0 \tilde{\not{p}}_3] \right) \\ &= -4i \left( \tilde{p}_1^0 (\tilde{p}_2 \cdot \tilde{p}_3) - \tilde{p}_2^0 (\tilde{p}_1 \cdot \tilde{p}_3) + \tilde{p}_3^0 (\tilde{p}_1 \cdot \tilde{p}_2) + m_0^2 [\tilde{p}_1^0 + \tilde{p}_2^0 - \tilde{p}_3^0] \right).\end{aligned}\tag{5.46}$$

Thus, the correlation function is given by the following 6-dimensional integral in the momentum space

$$C_0^{(0)}(t, T; \vec{q}) = \int \frac{d^4 p_1}{(2\pi)^4} \frac{dp_2^0}{2\pi} \frac{dp_3^0}{2\pi} e^{ip_1^0(t_0-t)} e^{ip_2^0(t-T)} e^{ip_3^0(T-t_0)} \times \left( \frac{9+\epsilon}{8} \cos(p_2^0) - \frac{3(1+\epsilon)}{24} \cos(3p_2^0) \right) \left\{ \frac{\text{Tr}(\cdot)}{D(\tilde{p}_1)D(\tilde{p}_2)D(\tilde{p}_3)} \right\}. \quad (5.47)$$

Notice that the point-split structure of the current is captured in the trigonometric factor in the integrand. One can numerically compute this monster by summing over all momenta allowed on the lattice just like before.

### The Wrap-Around Effect

The Ward identity relation given earlier in (5.39) gets a small correction due to the finite size of the box and the boundary conditions. Recall that a second exponential in the form of  $\exp(-E(L_t - t))$  popped up inside the 2-point correlator fit function to  $G(t)$  in (5.14). This can be understood as the meson propagating the long way around between  $t_0$  and  $t$ , or between  $t$  and  $T$ . The extra contribution will be small due to the longer propagation time wrapping around the lattice.

It is easy to test this in the free field case. The correlator  $C(t, T)$  is almost constant both inside and outside of the source-sink interval. That is, it does not vary much as a function of the current insertion time  $t$ . Since the before and after states are identical, the dominant term in (5.32) is constant and the rest are suppressed by the exponential decay due to the long wrap-around propagation time. These two almost constants have different values but add up to exactly satisfy the Ward identity. To be precise, for  $0 \leq t \leq T < t' < L_t$  one has

$$\frac{C(t, T) - C(t', T)}{G(T)} = 1. \quad (5.48)$$

Needless to say, our calculations confirmed this relation to machine precision.

In practice, the wrap-around contribution is negligibly small due to the exponential time dependence of (5.32) for typical choices of the sink time compared with the temporal extent of the lattice. Nevertheless, they're automatically included in the fit function.

## 5.3 Lattice Calculation: Resources and Techniques

Having seen how physical quantities of interest can be accessed on the lattice through 2-point and 3-point correlation functions, in this section we will first quickly review the logistics and then introduce some of the most useful techniques that we employed to significantly enhance our statistics.

### 5.3.1 MILC Configurations and FNAL Computing Clusters

As discussed in section 2.4, Monte Carlo simulations of a physical observable involves the measurement of that observable on an ensemble of gauge field configurations sampled from a distribution given by (2.33). Creating such a large ensemble is quite expensive. Thankfully, the MILC collaboration have generated and made publicly available a sizable library of gauge field configurations at several lattice spacings, with several different sea quark masses and various lattice extents [16].

Quark vacuum polarization effects are included through the  $(\det M)^{1/4}$  factors, one for each flavor in the sea. They account for  $N_f = 2 + 1$  flavors of dynamical asqtad quarks including two light quarks and a strange where  $u$  and  $d$  are taken to be degenerate. This causes negligible errors of  $<1\%$  [16]. Simulations at physical light quark masses are too computationally expensive. Hence, the MILC collaboration generated a number of different ensembles at various heavier than physical  $m_{u/d}$  in order to enable an extrapolation to the chiral limit. The sea strange quark mass is close to its physical value in these ensembles. In order to ensure small finite volume errors due to pion self interaction across the boundary, the lattice extent of these configurations are chosen so as to satisfy  $Lm_\pi > 4$ .

The use of asqtad improved staggered quarks in the sea led to considerable success due to their high degree of improvements and relatively low computational cost. This work has primarily used MILC's *coarse* ensemble of  $20^3 \times 64$  lattices with an  $a = 0.12$  fm lattice spacing. More specific details on this ensemble is provided in Table 6.3.

All large scale simulations for this work have been run on Fermi National Accelerator Laboratory (FNAL) computing clusters through remote access. The simulation code developed in this work has been implemented in Fortran. The code was designed to optimize performance. A simple and flexible MPI application was also implemented to launch multiple instances of the simulation software in parallel depending on the CPU architecture of the worker nodes at Fermilab.

#### Autocorrelation

Successive gauge field configurations in an ensemble might be correlated with each other. This is because they are normally generated in a sequence by performing a series of algorithmic updates to a configuration to obtain the next one. Consequently, consecutive configurations in the chain that are separated by few updates look very much alike. Thus, depending on the specific algorithm, a minimum number of configurations are dumped in the intermediate steps before retaining one in the ensemble in order to ensure enough update operations have been performed to reduce autocorrelation.

The autocorrelation length can be measured for any quantity after the calculation in order to see whether the samples drawn from the distribution are truly independent. We measured it for a subset of our correlators and confirmed that they are indeed independent.

### 5.3.2 Random Wall Sources

Given the high computational cost of generating configurations, it would be highly desirable to extract as much information as possible out of every single one of them in an ensemble. In section 5.2 we saw that one can compute lattice 2-point correlators using a single point source. The statistical noise can be greatly reduced if one repeated this calculation with many different sources at different lattice sites on every configuration. For instance, one could average the correlation function over all spatial points on a time slice

$$G(t; \vec{p}) = \frac{1}{L^3} \sum_{\vec{y}, \vec{x}} e^{-i\vec{p} \cdot (\vec{y} - \vec{x})} \langle \Gamma^\dagger(\vec{y}) \Gamma(\vec{x}) \rangle. \quad (5.49)$$

This, however, will also be very expensive as it increases the simulation cost  $L^3$ -fold.

Instead, one can use a technique that delivers practically the same improvement in the statics while incurring little or no additional cost [50]. This technique uses *random wall sources* where the point source in (5.3) is replaced by

$$\tilde{b}(x) = \eta(\vec{x}) \delta_{t, t_0}, \quad (5.50)$$

where the columns of 3-dimensional matrices  $\eta(\vec{x})$  are now random vectors with unit norm in the color space. Solving the linear equation gives

$$\tilde{g}(y) = \sum_x g(y, x) \tilde{b}(x) = \sum_{\vec{x}} \eta(\vec{x}) g(\vec{y}, t; \vec{x}, t_0). \quad (5.51)$$

Following a similar procedure to before, and convolving the *noisy* propagator  $\tilde{g}$  with itself yields

$$\begin{aligned} \sum_{\vec{y}} \tilde{g}^\dagger(\vec{y}) \tilde{g}(\vec{y}) &= \sum_{\vec{y}, \vec{x}, \vec{x}'} \eta^\dagger(\vec{x}') \eta(\vec{x}) g^\dagger(\vec{y}, t; \vec{x}', t_0) g(\vec{y}, t; \vec{x}, t_0) \\ &= \sum_{\vec{y}, \vec{x}} g^\dagger(\vec{y}, t; \vec{x}, t_0) g(\vec{y}, t; \vec{x}, t_0) + \sum_{\vec{x}, \vec{x}' \neq \vec{x}} e(\vec{x}, \vec{x}'). \end{aligned} \quad (5.52)$$

On the second line, the double sum over the wall source is broken down into the  $\vec{x} = \vec{x}'$  terms corresponding to (5.20) which one is looking for and the extra  $\vec{x} \neq \vec{x}'$  unwanted error terms. Diagrammatically, this is equivalent to

$$\tilde{G} = \vec{x} \begin{array}{c} \curvearrowright \\ \curvearrowleft \end{array} \vec{y} + \eta^\dagger(\vec{x}') \eta(\vec{x}) \begin{array}{c} \vec{x}' \curvearrowright \\ \vec{x} \curvearrowleft \end{array} \vec{y} \quad (5.53)$$

with  $L^3(L^3 - 1)$  error terms that look like

$$e(\vec{x}, \vec{x}') = \left( \eta^\dagger(\vec{x}') \eta(\vec{x}) \right) \left( \sum_{\vec{y}} g^\dagger(\vec{y}, t; \vec{x}', t_0) g(\vec{y}, t; \vec{x}, t_0) \right) \quad (5.54)$$

$$\equiv f(\vec{x}, \vec{x}') \hat{g}(\vec{x}, \vec{x}').$$

The definitions of the shorthand notation introduced in the second line in  $f$  and  $\hat{g}$  are obvious. The dependence of  $\hat{g}$  on  $t$  and  $t_0$  is made implicit in the rest of this discussion to declutter the notation. On ensemble and spatial average one has

$$\tilde{G} = G + \mathcal{E} \equiv G + \frac{1}{NL^3} \sum_i e_i, \quad (5.55)$$

where the index  $i$  stands for

$$i \equiv \{i_{\text{cf}}, i_\eta, i_{\text{tsrc}}, \vec{x}, \vec{x}' \neq \vec{x}\}, \quad N = N_{\text{cf}} N_{\text{tsrc}} N_\eta. \quad (5.56)$$

Here  $N_{\text{cf}}$  denotes the number of configurations,  $N_{\text{tsrc}}$  time slices per configuration and  $N_\eta$  number of noisy sources per time slice.

One is seeking to obtain  $G$ . But using a random wall source gives  $\tilde{G}$ . Thus, one would like the error  $\mathcal{E}$  to vanish. Below we show that two factors combine forces to make this happen: the randomness of noise and gauge invariance. Furthermore, one is also interested to know how much additional statistical noise the error terms introduce.

First, we have

$$\langle \eta^\dagger(\vec{x}') \eta(\vec{x}) \rangle = \delta_{\vec{x}', \vec{x}} \mathbf{I}_3 \quad (5.57)$$

when averaged over a sufficiently large number of samples. This is simply a property of truly independent random variables. In addition, according to Elitzur's theorem the ensemble average of a non gauge invariant quantity vanishes. Thus we also have

$$\langle g^\dagger(y, x') g(y, x) \rangle = \delta_{x, x'} \langle g^\dagger(y, x) g(y, x) \rangle. \quad (5.58)$$

One can easily see from (5.53) that for  $\vec{x} \neq \vec{x}'$  this quantity is not gauge invariant due to the loose ends not being tied together by a path of connected link variables.

Let us make this concrete. But in order to avoid getting lost in a sea of indices and cluttered notation while demonstrating that random wall sources work, we will first consider an essentially identical case that is framed in a simpler way. Suppose that  $u$  and  $v$  are two independent normally distributed random variables with the following probability distribution functions

$$p_U(u) = \mathcal{N}(u | \mu_u = 0, \sigma_u^2), \quad (5.59)$$

$$p_V(v) = \mathcal{N}(v | \mu_v = 0, \sigma_v^2),$$

Then their product  $w = uv$  would also be a random variable with its own distribution. The product distribution of two normally distributed random variables is actually not normal.<sup>2</sup> In this case where each of the two parent distributions has zero mean, the product distribution is the modified Bessel function of the second kind. However, one is only concerned about the mean and variance of  $w$  and not the full distribution. These are in general easy to obtain from the pdfs of  $u$  and  $v$  as follows

$$\mu_w = \mu_u \mu_v \quad \Rightarrow \quad \mu_w = 0, \quad (5.61a)$$

$$\sigma_w^2 + \mu_w^2 = (\sigma_u^2 + \mu_u^2)(\sigma_v^2 + \mu_v^2) \quad \Rightarrow \quad \sigma_w^2 = \sigma_u^2 \sigma_v^2. \quad (5.61b)$$

According to the central limit theorem, the average of a large sample of these products  $w_i = u_i v_i$  approaches a normal distribution whose width is given by  $\sigma_{\langle w \rangle} = \sigma_w / \sqrt{N}$ , where  $N$  is the size of the sample. Thus, we have

$$p_{\langle W \rangle} \left( \langle w \rangle = \frac{1}{N} \sum_i W_i \right) = \mathcal{N} \left( w | 0, \frac{\sigma_u^2 \sigma_v^2}{N} \right) \quad (5.62)$$

provided that  $N$  is sufficiently large. It is important to bear in mind the distinction between the underlying pdf of a random variable denoted by  $p_W$  which is not normal and has a variance of  $\sigma_w$ , and the pdf of the average of  $N$  samples of the same variable denoted by  $p_{\langle W \rangle}$  which is asymptotically normal with a variance approaching  $\sigma_w / \sqrt{N}$ .

The simple discussion above can be applied directly to the case of random wall sources. The only difference being that there is a variety of indices in (5.56). Here we have two random variables we denote by  $f$  and  $\hat{g}$  whose product  $e$  has a probability distribution with zero mean. It follows from (5.61a) immediately that on ensemble average the error term  $\mathcal{E}$  does go away

$$\mu_e = \mu_f \mu_{\hat{g}} = 0. \quad (5.63)$$

The question now is how much extra variance does that introduce.

Its variance is also determined from those of  $f$  and  $\hat{g}$ . Note that  $\hat{g}(\vec{x}, \vec{x}')$  are highly correlated on a single time slice on a single configuration. This makes it complicated to work with them individually. Instead, consider the spatial average  $\sum_{\vec{x} \neq \vec{x}'} \hat{g}(\vec{x}, \vec{x}') / L^3(L^3 - 1)$  which can reasonably be taken as independent random samples from some distribution with variance

$$\sigma_{\hat{g}}^2 = \text{var} \left[ \hat{g} = \frac{1}{L^3(L^3 - 1)} \sum_{\vec{x} \neq \vec{x}'} \hat{g}(\vec{x}, \vec{x}') \right]. \quad (5.64)$$

---

<sup>2</sup> In general, the product distribution can be obtained from the parent distributions according to

$$p_W(w) = \int p_U(u) p_V(w/u) \frac{1}{|u|} du. \quad (5.60)$$

In contrast, all  $f(\vec{x}, \vec{x}')$  are truly independent from one another by construction. That is, except for those with the two ends swapped which are each others' complex conjugate and thus add up to a real number. Using a  $U(1)$  noise, for instance, gives the pdf of  $\text{Re}(f(\vec{x}, \vec{x}')) = \cos(\theta_{\vec{x}} - \theta_{\vec{x}'})$  and its mean and variance by

$$p_\eta(u) = \frac{1}{\pi\sqrt{1-u^2}} \Rightarrow \mu_\eta = 0, \quad \sigma_\eta^2 = \frac{1}{2}. \quad (5.65)$$

Similar to (5.64), averaging  $f(\vec{x}, \vec{x}')$  over spatial sites as well as the number of random noises on a single configuration we have

$$p_f\left(f = \frac{1}{N_\eta L^3(L^3 - 1)} \sum_{i_\eta, \vec{x} \neq \vec{x}'} f_{i_\eta}(\vec{x}, \vec{x}')\right) \approx \mathcal{N}\left(f | \mu_f = 0, \sigma_f^2 = \frac{2\sigma_\eta^2}{N_\eta L^3(L^3 - 1)}\right). \quad (5.66)$$

Note that this relation assumes that  $L^3(L^3 - 1)/2$  is large enough so that  $p_f$  is already approaching a Gaussian thanks to the central limit theorem. Though a very good assumption for typical lattices, this isn't necessary at this point yet. One can invoke the CLT on ensemble average later on.

Putting together (5.64) and (5.66) for the error term we have

$$\begin{aligned} \sigma_e^2 &\equiv \text{var} \left[ \frac{1}{N_\eta L^3(L^3 - 1)} \sum_{i_\eta, \vec{x} \neq \vec{x}'} f_{i_\eta}(\vec{x}, \vec{x}') \hat{g}(\vec{x}, \vec{x}') \right] = \sigma_f^2 \sigma_g^2 \\ &= \frac{2\sigma_\eta^2 \sigma_g^2}{N_\eta L^3(L^3 - 1)}. \end{aligned} \quad (5.67)$$

We have all the ingredients now. Going back to (5.55) and invoking CLT while convolving the pdfs of  $G$  and  $\mathcal{E}$  to obtain that of  $\tilde{G}$ , with  $N_{\text{tsrc}}$  time sources and  $N_{\text{cf}}$  configurations the sample variance (i.e. square of the statistical error) is

$$\tilde{\sigma}^2 = \frac{\sigma^2}{N_{\text{tsrc}} N_{\text{cf}}} + \frac{(L^3 - 1)\sigma_e^2}{N_{\text{tsrc}} N_{\text{cf}}} = \frac{\sigma^2}{N_{\text{tsrc}} N_{\text{cf}}} + \frac{2\sigma_\eta^2 \sigma_g^2}{N_{\text{cf}} N_{\text{tsrc}} N_\eta L^3}. \quad (5.68)$$

A number of important lessons can be learned from this relation. (1) The additional statistical error introduced by the random noise is tiny thanks to the  $1/L^3$  factor. (2) The random noise sitting on every site on a time slice is extremely crucial for fast convergence by significantly reducing the error term's variance through contributing a factor of  $2\sigma_\eta^2/N_\eta L^3$ . For instance, on our lattices with  $L = 20$ , with  $N_\eta = 1$  random  $U(1)$  noise per configuration that corresponds to a significant suppression of the variance by  $1/20^3$ .

Using a uniform wall source would also lead to an error with zero mean due to the gauge invariance constraint in (5.58) alone. But without the additional help from (5.57) it would result in a huge variance. This is somewhat counterintuitive in that adding random noise on individual configurations has the overall effect of a much smaller variance on aggregate.



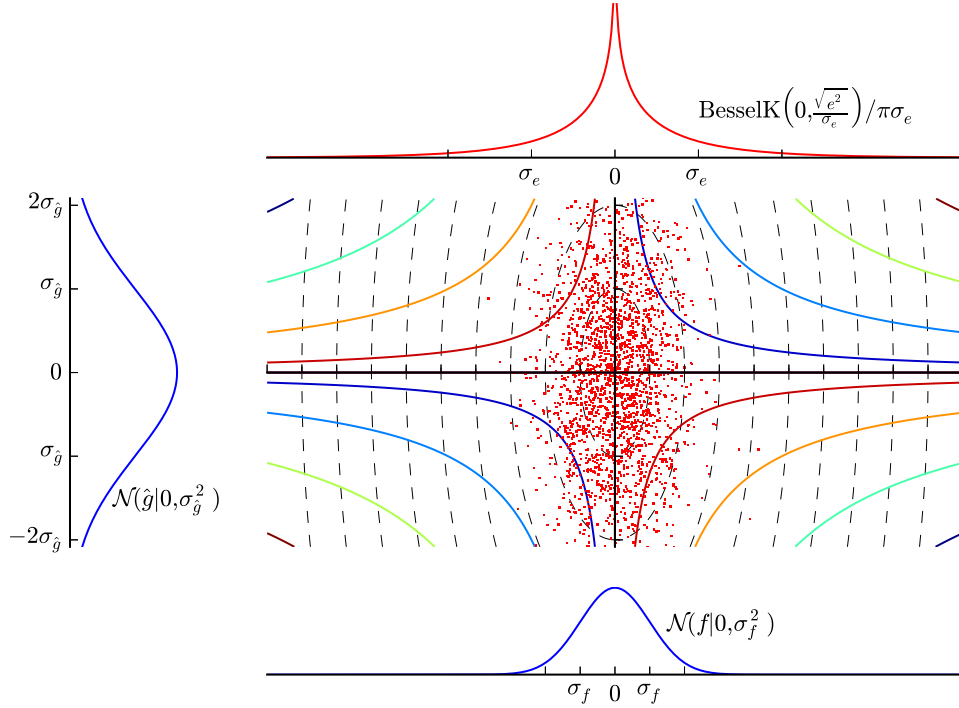


Figure 5.1: Random wall sources introduce errors due to loose propagators on individual configurations but produce correct results on ensemble average. The large panel in the middle shows 2112 random samples drawn from the bi-variate normal distribution whose contours are depicted by dashed ellipses with underlying random distributions of  $f$  and  $\hat{g}$  shown in the bottom and the side panels respectively. The product pdf is plotted in the top panel. The solid colored curves represent the contours of the product distribution.

That said, however, (5.68) also shows that (3) in simulations it's best to keep  $N_\eta = 1$  in favor of spending the computing resources to on a larger number of configurations and time sources. Increasing  $N_{\text{cf}}$  and  $N_{\text{tsrc}}$  brings down statistical errors in  $G$  as well as in  $\mathcal{E}$ , whereas doubling  $N_\eta$  only makes the already tiny  $\sigma_e$  slightly smaller. Figure 5.1 illustrates our explanation of why this technique produces the desired correlators and shows the important role of the small variance of the *random* noise in suppressing unwanted contributions.

For simplicity, the above discussion assumed that different time slices on the same configuration are uncorrelated. That's not really true but a reasonable assumption nonetheless, so long as they are separated by several time steps. In practice we see an improvement of almost  $1/\sqrt{N_{\text{tsrc}}}$  in the variance thanks to multiple time sources indicating small correlations. Nevertheless, the  $N_{\text{tsrc}}$  correlators computed on a single configuration are binned and

treated as one independent measurement to ensure correct analysis of correlations between data points.

Thanks to (5.68) it is clear that the optimal simulation strategy for a meson 2-point function is to first exhaust all available configurations in the ensemble using random wall sources, then add more time sources that are maximally separated along the temporal extent, and never bother using multiple noises on the same time slice of a single configuration.

To recap, the above discussion shows that using random wall sources produces the desired correlator on ensemble average and introduces a negligible error

$$\begin{aligned} \frac{1}{L^3} \sum_{\vec{y}} \langle \tilde{g}^\dagger(y) \tilde{g}(y) \rangle &= \frac{1}{L^3} \sum_{\vec{y}, \vec{x}} \langle g^\dagger(\vec{y}, t; \vec{x}, t_0) g(\vec{y}, t; \vec{x}, t_0) \rangle, \\ \tilde{\sigma}^2 &= \sigma^2 + \frac{2\sigma_\eta^2 \sigma_g^2}{N_\eta L^3}. \end{aligned} \tag{5.69}$$

Loose ends in (5.53) are tied. When compared with a point source, even though using random wall sources causes each configuration to be contaminated by errors, on ensemble average this added error vanishes and the extra noise has a very small contribution to the total statistical error. The benefit of effectively averaging over all spatial points on a time slice far outweighs the cost. Typically, one can achieve a reduction in statistical errors by a factor of 3–4 by using random wall sources.

We used a simple case of a local pseudoscalar flavorless meson at rest to explain this technique. In general, one might need more than one wall source in order to compute correlators of interest. Consider, for instance, a point-split<sup>3</sup> pion created by

$$P_{5x}(y) = \frac{1}{2} \bar{u}(y) \gamma_5 \{ U_1(y) d(y + \hat{1}) + U_1^\dagger(y - \hat{1}) d(y - \hat{1}) \}. \tag{5.70}$$

The corresponding 2-point correlator computed on the lattice is then given by

$$\begin{aligned} G_{5x}(t; \vec{p}) &= \frac{1}{L^3} \sum_{\vec{y}, \vec{x}} e^{-i\vec{p}\cdot(\vec{y}-\vec{x})} (-1)^{\beta(y)} (-1)^{\beta(x)} (-1)^{y^2-x^2} \\ &\times \text{tr} \left( \left\{ g_d(y + \hat{1}, x + \hat{1}) U_1^\dagger(x) \right\}^\dagger U_1^\dagger(y) g_u(y, x) + \dots \right) \end{aligned} \tag{5.71}$$

where  $\beta(x) = -(-1)^{x_0+x_1}$  is the staggered phase associated with the operator  $P_{5x}$  and the ellipsis represents the other three shifted convolutions. Due to the coordinate dependent phase, and depending on what else is being computed in the simulation it may be more computationally efficient to use two wall sources. One is plain and the other is shifted and

---

<sup>3</sup> This particular point splitting is chosen here because it will be used later on in the main simulation.

patterned by the appropriate momentum and staggered phase

$$\begin{aligned}\tilde{b}_1(x) &= \eta(\vec{x})\delta_{t,t_0} \\ \tilde{b}_2(x) &= e^{-i\vec{p}\cdot(\vec{x}+\hat{1})}(-1)^{\beta(x+\hat{1})-(x+\hat{1})^2} U_1(x)\tilde{b}_1(x+\hat{1}) \\ &\quad + e^{-i\vec{p}\cdot(\vec{x}-\hat{1})}(-1)^{\beta(x-\hat{1})-(x-\hat{1})^2} U_1^\dagger(x-\hat{1})\tilde{b}_1(x-\hat{1})\end{aligned}\tag{5.72}$$

while both use the *same* set of random noise  $\eta(\vec{x})$ . The resulting two noisy propagators are then combined to obtain the desired pion correlation function as

$$G(t; \vec{p}) = \frac{1}{L^3} \sum_{\vec{y}} e^{-i\vec{p}\cdot\vec{y}} (-1)^{\beta(y)-y^2} \text{tr} \left( \left\{ \tilde{g}_{d,2}^\dagger(y+\hat{1})U_1^\dagger(y) + \tilde{g}_{d,2}^\dagger(y-\hat{1})U_1(y-\hat{1}) \right\} \tilde{g}_{u,1}(y) \right).\tag{5.73}$$

### 5.3.3 Sequential Source Technique

We saw in section 5.2 that a typical 3-point correlator looks like

$$C(t, T; \vec{q}) = \sum_{\vec{y}, \vec{z}} e^{-i\vec{q}\cdot(\vec{y}-\vec{z})} (-1)^{\beta(x,y,z)} \text{tr}(g^\dagger(z, x)g(z, y)g(y, x))\tag{5.74}$$

where shifts and links are implicit and  $\beta$  is some staggered phase. This consists of 3 propagators tied together at three vertices called the source at  $t_0$ , the sink at  $T$  and the current insertion at  $t$ . The specific operators used in the correlator are encoded in the staggered phase and the shifts.

We also saw that the solution to the linear equation  $M\phi = b$  where  $b$  is a point source at  $x$  is the quark propagator from  $x$  to all points on the lattice

$$\phi(y) = g(y, x) = M_{y,x}^{-1}.\tag{5.75}$$

The  $\gamma_5$  hermiticity of the action can then be exploited to obtain  $g^\dagger(z, x)$  from the Hermitian conjugate of the first inversion. That leaves only the sink to current propagation  $g(z, y)$ . Notice also the sums over all spatial points  $\vec{y}$  on the sink wall. Thankfully, it is not necessary to compute  $L^3$  different propagators out of every sink point. Instead, one constructs a second “source” on the “sink” time slice as

$$b_{\text{sst}}(y) = e^{-i\vec{q}\cdot\vec{y}} (-1)^{\beta(y)} g(y, x) \delta_{y^0, T}.\tag{5.76}$$

The first propagator in (5.75) is used in constructing the *sequential source*. The solution to the linear equation  $M\phi_{\text{sst}} = b_{\text{sst}}$  with this source is therefore

$$\phi_{\text{sst}}(z) = \sum_y M_{z,y}^{-1} b_{\text{sst}}(y) = \sum_{\vec{y}} e^{-i\vec{q}\cdot\vec{y}} (-1)^{\beta(y)} g(\vec{z}, t; \vec{y}, T) g(\vec{y}, T; \vec{x}, t_0).\tag{5.77}$$

Its dot product with the first propagator yields

$$\phi^\dagger(z)\phi_{\text{sst}}(z) = \sum_{\vec{y}} e^{-i\vec{q}\cdot\vec{y}} (-1)^{\beta(y)} g^\dagger(\vec{z}, t; \vec{x}, t_0) g(\vec{z}, t; \vec{y}, T) g(\vec{y}, T; \vec{x}, t_0). \quad (5.78)$$

Thus, the desired 3-point correlator can be obtained from a convolution with appropriate momentum and staggered phases as well as the coordinate shifts corresponding to the current operator

$$C(t, T; \vec{q}) = (-1)^{\beta(x)} \sum_{\vec{z}} e^{i\vec{q}\cdot\vec{z}} (-1)^{\beta(z)} \text{tr}(\phi^\dagger(z)\phi_{\text{sst}}(z)). \quad (5.79)$$

Note that the specific current operator used in the 3-point function as determined by the staggered phase  $\beta(z)$  and its shifts did not enter until after the requisite propagators had been computed, which is the most expensive part of the calculation. This means that once committed to the choice of the interpolating operators to be used at the source and the sink whose quantum numbers are inscribed into the correlator through their staggered phase and point-splitting structure, one can insert any current between them so long as it satisfies the selection rules for no additional computing cost. We will take advantage of this later in our main calculation.

The sequential source technique is easily extended to random wall sources. Care must be taken to track all the coordinate dependent staggered and momentum phases as well as point-splittings of the operators to ensure the loose ends are tied at the right places with the right phases. The sequential source at  $T$  does not get an additional random noise.

## 5.4 Boundary Conditions

In simulations of lattice QCD we study the theory in a finite box of volume  $L^3 \times T$ . The finite volume leads to quantization of the momentum available on the lattice.<sup>4</sup> The specific values of the quantum of momenta allowed on the lattice are determined by the boundary conditions. The simplest and most common choice is the periodic boundary conditions (PBC), using which one can only access momenta with spatial components that are integer multiples of  $2\pi/L$ . This represents a severe limitation on the phenomenological reach of lattice simulations in the study of quantities and processes where access to precise hadronic momenta is required such as transitions with very small 4-momentum transfers. In order to accommodate such small momenta using PBC, one would need very large lattices which

---

<sup>4</sup> Momentum quantization imposes a lower bound on the size of the smallest non-zero momentum. There is also an upper limit on the magnitude of momenta accessible on the lattice. Though related to each other, these two effects—momentum quantization and its ultraviolet cutoff—have different causes. The finite volume necessitates some form of boundary conditions, which in turn lead to momentum quantization. The UV cutoff, on the other hand, is due to the discretization of spacetime which imposes a lower limit on particles' wavelength and therefore an upper limit on the energy-momentum.

can be prohibitively expensive. However, *twisted boundary conditions* (TBC) can be used to access arbitrarily small momenta. This is crucial in precise determination of form factors at zero momentum transfers on currently available lattices, where the smallest non-zero momentum allowed with PBC are generally not sufficiently small.

In order to understand clearly how this can be achieved using TBC, we first demonstrate the quantization of momentum and derive its allowed values. In subsection 5.4.1 we introduce the twisted boundary conditions and show how it can be used to tune hadronic momenta to arbitrary values.

Consider a fermion field  $\psi(x)$  on a finite 4-dimensional  $L^3 \times T$  box with lattice spacing  $a$ . Imposing periodic boundary conditions in all spatial dimensions implies

$$\psi(x + \hat{e}_i a L) = \psi(x), \quad i = 1, 2, 3. \quad (5.80)$$

Taking the Fourier transform of these conditions enforces the momentum components to satisfy  $\exp(ip_i a L) = 1$ . This determines the allowed quantum of momenta on the lattice

$$p_i = \frac{2\pi}{aL} n_i, \quad i = 1, 2, 3 \quad (5.81)$$

where  $n_i$  are integer numbers.

This means that the lowest non-zero momentum accessible on this lattice is  $2\pi/aL$ . This is a very large momentum on a typical lattice currently available. For instance, on the MILC collaboration's "coarse" ensemble of  $20^3 \times 64$  lattices with  $a = 0.12$  fm, the lowest allowed non-zero momentum is of the order of  $\approx 500$  MeV.

This is a significant problem in studying processes where it's necessary to reach a specific momentum through either precise tuning or approaching it from neighboring momenta. Either way, the momentum step sizes are too large to get sufficiently close to the desired momentum. In order to access smaller momenta with PBC by means of reducing the step size in momentum space one would have to use larger lattices for simulations, which can be prohibitively expensive. Fortunately, there is a much cheaper alternative where a generalized set of boundary conditions is used instead. We will describe this method below.

### 5.4.1 Twisted Boundary Conditions

This problem can be solved using a different set of boundary conditions called *twisted boundary conditions* [51, 52, 53, 54]:

$$\psi(x + \hat{e}_i a L) = e^{i\theta_i} \psi(x), \quad i = 1, 2, 3 \quad (5.82)$$

with a choice of an arbitrary topological 3-vector  $\vec{\theta}$ . One can determine the allowed momenta with these modified boundary conditions in a similar fashion. In momentum space this

condition translates to

$$e^{i(p_i aL - \theta_i)} = 1, \quad i = 1, 2, 3. \quad (5.83)$$

Therefore, the allowed momenta are shifted by the *twisting angles*

$$p_i = \frac{2\pi}{aL} n_i + \frac{\theta_i}{aL}, \quad i = 1, 2, 3. \quad (5.84)$$

The momentum is still quantized with the same step size as that under periodic boundary conditions. However, all momenta are now shifted by an arbitrary and *continuous* amount. One can therefore adjust the value of the twisting angles to tune the momentum to any arbitrary value.

It can be shown [53] that this is equivalent to simulating QCD with quarks satisfying periodic boundary conditions and interacting with a background of a constant fictitious magnetic vector potential whose strengths are determined by the twisting angles. An example of such a potential could be one that generates the magnetic field of a thin solenoid going around inside a 4-dimensional torus but vanishing everywhere on its surface where the lattice is. Due to the Aharonov-Bohm effect, the energy levels of quarks are shifted even though the magnetic field is zero everywhere on the lattice.

The twisted boundary conditions are imposed by doing an Abelian  $U(1)$  transformation generated by  $\Lambda_\theta(x) = \exp(i\theta \cdot x/L)$  on the quark fields, and then applying ordinary periodic boundary conditions on the resulting fields. This is like a field redefinition where the effects of the twist—that is the coupling with the fictitious magnetic potential—are separated from the ordinary quarks with periodic boundary conditions in the following way

$$\psi(x) \rightarrow \tilde{\psi}(x) \equiv \Lambda_\theta(x)\psi(x), \quad (5.85)$$

where  $\theta^0 = 0$ . Following (5.82), it is easy to verify that the redefined fields  $\tilde{\psi}(x)$  obey

$$\tilde{\psi}(x + \hat{e}_i L) = \tilde{\psi}(x), \quad i = 1, 2, 3 \quad (5.86)$$

which are precisely the periodic boundary conditions given in (5.80).

In terms of the redefined fields, the Euclidean Lagrangian is given by

$$\mathcal{L} = \bar{\tilde{\psi}}(x)\Lambda_\theta^\dagger(x)(\not{D} + m)\Lambda_\theta(x)\tilde{\psi}(x) = \bar{\tilde{\psi}}(x)(\Lambda_\theta^\dagger(x)\not{D}\Lambda_\theta(x) + m)\tilde{\psi}(x).$$

This can be written as

$$\mathcal{L} = \bar{\tilde{\psi}}(x) \left( \tilde{\not{D}} + m \right) \tilde{\psi}(x), \quad (5.87)$$

with

$$\tilde{D}_\mu = D_\mu + iB_\mu, \quad (5.88)$$

where  $B_\mu = \theta_\mu/L$  is the fictitious background magnetic potential.<sup>5</sup> On the lattice, this is simply equivalent to rephasing the gauge field links by the twisting angles

$$\tilde{U}_\mu(x) = e^{i\theta_\mu/L} U_\mu(x). \quad (5.89)$$

To better illustrate the effect of the twisted boundary conditions, we calculate free field quark propagators  $S(x, y) \equiv \langle \psi(x) \bar{\psi}(y) \rangle$ , using both field definitions.

First, we use the original quark fields which satisfy the twisted boundary conditions. When calculating the propagator in the momentum space one simply sums over all momenta allowed by the twisted boundary conditions as derived in (5.84)

$$S(x, 0) = \int \frac{dp^0}{2\pi} \frac{1}{L^3} \sum_{\vec{p}} \frac{e^{i(p + \frac{\theta}{L}) \cdot x}}{i(\vec{p} + \frac{\theta}{L}) + m}. \quad (5.90)$$

Alternatively, one can use the redefined quark fields to obtain the same quantity. These fields satisfy ordinary periodic boundary conditions. Therefore, the allowed momenta are unshifted, as given by (5.81). However, as shown above in (5.88), the field redefinition also transforms the Dirac operator. As a result, the  $\mathcal{B}$  term still shows up in the denominator

$$\tilde{S}(x, 0) \equiv \langle \tilde{\psi}(x) \tilde{\bar{\psi}}(0) \rangle = \int \frac{dp^0}{2\pi} \frac{1}{L^3} \sum_{\vec{p}} \frac{e^{ip \cdot x}}{i(\vec{p} + \mathcal{B}) + m}, \quad (5.91)$$

where  $\vec{p} = \frac{2\pi}{L} \vec{n}$  in both cases and the sums are over all 3-vectors of integers denoted by  $\vec{n}$ . It is now evident that

$$S(x, 0) = e^{-i\vec{\theta} \cdot \vec{x}/L} \tilde{S}(x, 0). \quad (5.92)$$

Once again, it is easy to see that  $S$  satisfies the twisted boundary conditions, while  $\tilde{S}$  satisfies the periodic boundary conditions:

$$S(x + \hat{e}_i L) = e^{i\theta_i} S(x), \quad \tilde{S}(x + \hat{e}_i L) = \tilde{S}(x). \quad (5.93)$$

The above discussion showed that rephasing the gauge fields and then applying ordinary periodic boundary conditions will result in shifted momenta. Thus, one can offset the allowed quantized momenta by an arbitrary continuous amount.

Note that this momentum is not projected by an exponential factor in an ordinary Fourier transformation sum over lattice sites. Rather, it is encoded in the gauge field link variables by a twisting phase  $\exp(i\theta_\mu/L)$ . Nevertheless, it acts as a true physical momentum. As a test, one can extract the physical energy of a meson obtained from a 2-point correlator created by pairing an ordinary propagator with a twisted one and demonstrate that the

---

<sup>5</sup> The presence of the background magnetic field does not affect the  $\gamma_5$  hermiticity of the action, which ensures that the determinant of the fermion matrix remains positive.

term  $\vec{\theta}/L$  enters the dispersion relation in exactly the same way as a physical momentum does [51].

Importantly, authors of [54] have shown that for *partially* twisted boundary conditions, where *some* valence quarks are twisted but other valence quarks and the sea quarks satisfy periodic boundary conditions finite volume corrections remain exponentially small, provided that there are no final state hadronic interactions. This is crucial since it eliminates the need to generate a new ensemble of gauge fields for every choice of the twisting angles and thereby making this useful technique practical.

## 5.5 Constrained Curve Fitting

So far we've learned how to calculate Monte Carlo estimates of two-point and three-point functions using lattice QCD. With these correlators at hand, one then uses curve fitting to extract physical quantities such as hadronic masses and matrix elements. In this section, we first briefly review the traditional maximum likelihood approach to curve fitting where we encounter its severe shortcomings. We next introduce an alternative approach to curve fitting based on Bayesian statistics and illustrate how it solves the problems encountered in the conventional approach in an elegant and systematic way.

Section 5.5.2 introduces some of the specific techniques and strategies that we employ in our analyses throughout this work. Finally, subsection 5.5.3 describes in detail the methods used in our error analysis.

A quick and accessible introduction to general Bayesian analysis can be found in [55]. A more comprehensive and rigorous, yet remarkably clear treatment of data modeling is presented in the excellent [56]. Numerical methods such as SVD are covered in the well known [57]. Our discussion on the applications of Bayesian methods to lattice QCD closely follows those presented in [58], [46, Appendix], [59], and [60, Appendix].

The curve fitting tools used for our analyses utilize powerful packages created by G. Peter Lepage (Cornell University) who has kindly made them publicly available online under the GNU General Public License as free software. We have extensively used the *lsqfit* package [61], which is a general purpose Bayesian least-squares fitter, as well as the *corrfitter* package [62] which is an extension to the *lsqfit* that specializes in fitting lattice two-point and three-point correlators.

### 5.5.1 A Bayesian Approach

Consider Monte Carlo data  $G^{\text{MC}}(t)$  obtained from a meson two-point correlator

$$\sum_{\mathbf{x}} \langle 0 | J(\mathbf{x}, t) J(\mathbf{0}, 0) | 0 \rangle. \quad (5.94)$$



One can extract hadronic masses from this correlator by fitting it to a model given by a multi-exponential function

$$f^{\text{theory}}(t; A_n, E_n) = \sum_{n=0}^{\infty} A_n e^{-E_n t}. \quad (5.95)$$

One way to do this is to use the standard maximum likelihood fitting procedure, which involves a least squares fit to minimize the chi-squared from the data given by

$$\chi^2(A_n, E_n) \equiv \sum_{t, t'} \Delta y(t) \sigma_{t, t'}^{-2} \Delta y(t'), \quad (5.96)$$

where

$$\Delta y(t) \equiv \langle G(t) \rangle - f(t; A_n, E_n) \quad (5.97)$$

is the difference between the data and the fit function, and

$$\sigma_{t, t'}^2 \equiv \langle G(t)G(t') \rangle - \langle G(t) \rangle \langle G(t') \rangle \quad (5.98)$$

is the covariance matrix between the data points. The fit parameters  $\{A_n, E_n\}$  are varied to minimize  $\chi^2(A_n, E_n)$ .

This fitting procedure, however, is singular. There are infinitely many fit parameters in the sum (5.95) but only a finite number of data points  $G(t)$ . In other words, we have a problem: there are more fit parameters than degrees of freedom from input data. Our model is too complex. More information is needed.

## A Bad Solution

The traditional approach to address this problem is to truncate both the model and the data. The justification for this is based on the assumption from prior knowledge, that the overlap amplitudes  $A_n$  can't be too large. Therefore, due to the exponential form of the fit function (5.95), contributions from high energy terms are suppressed at large times. This means that, there exists some minimum time  $t_{\text{min}}$ , above which only the first few terms in the model make statistically significant contributions. So one can reduce the number of fit parameters by truncating the sum in (5.95), effectively ignoring high energy terms. This is allowed so long as enough data points at small times  $t < t_{\text{min}}$  are discarded to ensure that systematic errors introduced by truncating the model will be small enough to be statistically insignificant.

The question, then, is to choose the best  $t_{\text{min}}$ . Too small a  $t_{\text{min}}$  biases the fit results for low  $n$  parameters due to contributions from high energy terms that aren't sufficiently suppressed yet. Too large a  $t_{\text{min}}$ , on the other hand, inevitably inflates statistical errors,

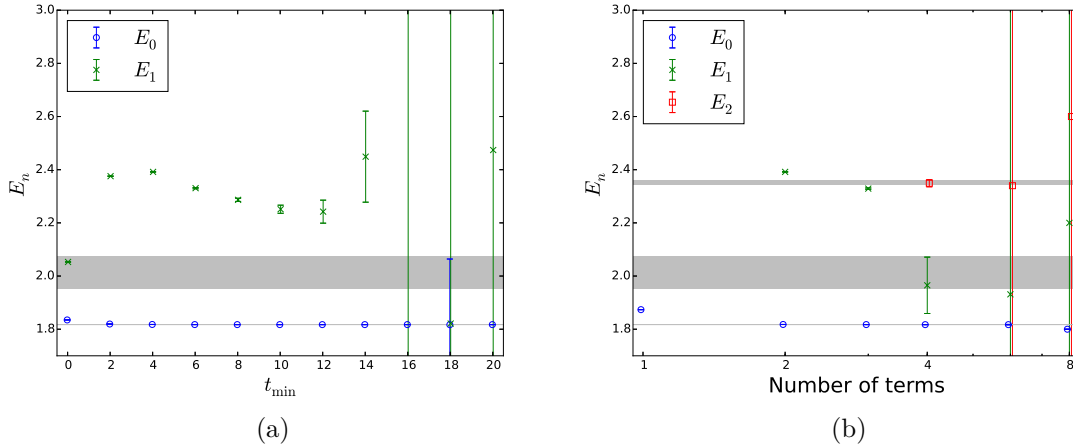


Figure 5.2: (a) The two lowest energies, obtained from unconstrained 2-term fits to  $\eta_c$  correlators plotted for various values of  $t_{\min}$ , in lattice units. Results for the first excited state’s energy,  $E_1$ , suffer from large systematic errors when obtained from fits with a small  $t_{\min}$ , due to insufficiently suppressed contributions from high energy states. A large  $t_{\min}$  results in huge error bars. (b) Results from unconstrained fits with a fixed  $t_{\min} = 4$ , plotted versus the number of terms in the model. The fits become unstable and uncertainties large with as few as 4 terms; far fewer than needed to get accurate results for  $E_1$ . The shaded gray bands represent more accurate results obtained from alternative analyses of the same data.

since useful data points are discarded. So the solution seems to be this:  $t_{\min}$  is increased until the systematic errors are masked by statistical errors.

Figure 5.2a illustrates this dependence on  $t_{\min}$ . The lowest two energies from a 2-term fit to  $\eta_c$  correlators are plotted for various  $t_{\min}$ s. The trade-off between systematic and statistical uncertainties is evident in the results for the first excited state’s energy,  $E_1$ . Fits with too few discarded data points have small error bars but are highly biased due to insufficiently suppressed contributions from higher energy states, while those with too many, result in huge statistical uncertainties.

We can already see that this isn’t the most optimal solution. The higher the quality of simulation data, the smaller the statistical errors, the more data points need be discarded to ensure high energy terms are drowned by statistical noise. Furthermore, since Monte Carlo data are in general considerably less noisy at small time steps, imposing a  $t_{\min} > 0$  would lose us our best quality data. This procedure increases both systematic and statistical uncertainties. Systematic errors are increased because part of the model which can conceivably be significant is omitted, while statistical uncertainties are increased because high quality data is discarded. Moreover, verifying that the right  $t_{\min}$  has been chosen, is necessarily post hoc, and hence prone to even further bias. This is a major weakness. We have no way of estimating the systematic errors due to omitting high energy states.

Monte Carlo data is expensive. So one would like to keep as much data as possible, ideally all of it, which entails keeping more terms in the fit function. This, however, can lead to severe over-fitting in conventional least squares fits. As more terms are added to the fit function, their corresponding fit parameters start to wander off in directions that are poorly constrained by the data. This results in unreasonably large and therefore unphysical values for high- $n$  amplitudes,  $A_n$ , which conspire to almost exactly cancel each other out. This can't be prevented as long as the fitter thinks that a model with  $a_3 \approx 10a_0$  is plausible.

This broad range of acceptable values in the parameter space leads to huge uncertainties in fit results. Figure 5.2b shows fits with various number of terms and a fixed  $t_{\min} = 4$ . They become very unstable very quickly. The fitter becomes extremely sensitive to the initial guess and often fails to converge, returning a huge  $\chi^2$ . The errors blow up before enough terms have been included in order to extract  $E_1$ .

We need a way to constrain the fit by teaching the fitter that the amplitudes must be of order 1, thereby preventing it from wandering off to unphysical regions in the parameter space. A standard way to do so is adding a regularization term to the  $\chi^2$ :

$$\chi^2 \rightarrow \chi^2 + \alpha \sum_n |A_n|^2. \quad (5.99)$$

The extra term regularizes the fit through penalizing large  $A_n$ . However, this raises the question of what is a suitable value for the regularization coefficient  $\alpha$ , which effectively controls the model complexity and flexibility. We can't tune  $\alpha$  by fitting it together with the original model parameters using the input data, since that would obviously result in  $\alpha = 0$ , because it minimizes the penalty term in the  $\chi^2$ . So we end up where we started with an unregularized model.

Even given a suitable  $\alpha$ , there remain problems that can't be solved by penalty terms, including the appearance of “fake” states or finding a real state multiple times. They occur simply because there's just not enough information in the data for the fitter to be able to find more than a couple of states. As a result, when forced to fit too many terms, it manufactures superfluous states. These fake states turn up in between the physical ones with amplitudes that are too small to have statistically significant contributions. Other states are split up into two or more with energies so close to one another that are numerically identical. Results for  $E_1$  from 4-term and 6-term fits shown in Figure 5.2b are examples of such problems.

Generally, one is only interested in the first couple of states. Nevertheless, as demonstrated above, higher energy terms are still needed in the model in order to get good estimates for the few parameters of actual interest. However, if left unconstrained, retaining these so called *nuisance parameters*, would break the fit. We also saw that conventional regularization terms aren't adequate. We need a better way to constrain the fit.

Clearly, this is not the right approach. Enter Bayes, and all of the above problems are solved in a surprisingly straightforward and natural way.

### A Better Solution; Bayesian Statistics

The maximum likelihood approach, tries to answer the following:

What are the parameters  $\{A_n, E_n\}$ , that the observed data  $G(t)$ , is most likely to have come from?

The question we are really trying to answer is:

Given the observed data  $G(t)$ , what is our best estimate for parameters  $\{A_n, E_n\}$  and their uncertainties?

Though subtle, these are two different questions. But intuitively, we know that these questions are logically related. They are best formulated in terms of conditional probabilities and the exact relationship between them is given by Bayes' theorem:<sup>6</sup>

$$\mathcal{P}(\lambda | G, I) = \mathcal{P}(\lambda | I) \frac{\mathcal{P}(G | \lambda, I)}{\mathcal{P}(G | I)}, \quad (5.100)$$

where  $\lambda$  denotes model parameters, and  $I$  represents all background information.  $\mathcal{P}(G | \lambda, I)$  on the right hand side is the probability of observing the data  $G$  given the parameters  $\lambda$  and is referred to as the *likelihood*. The prefactor  $\mathcal{P}(\lambda | I)$  is the probability distribution function (pdf) of the model parameters before new data is collected. It represents our a priori knowledge, and is called the *prior*. The left hand side  $\mathcal{P}(\lambda | G, I)$ , is the *posterior* probability distribution of the model parameters  $\lambda$  given the new data  $G$ .

The denominator on the right hand side  $\mathcal{P}(G | I)$  is the probability of the data arising from any model and is sometimes referred to as the *evidence*. Normally, we're not interested in this term.<sup>7</sup> Luckily, we don't actually need it. Once we have the prior and the likelihood, the posterior can be obtained by normalizing their product. So we drop it from the Bayes' formula and replace the equality by a proportionality:

$$\text{posterior} \propto \text{prior} \times \text{likelihood}. \quad (5.101)$$

---

<sup>6</sup> The proof simply follows from the product rule of probabilities applied to the joint probability of two independent events  $A$  and  $B$ :

$$\mathcal{P}(A, B) = \mathcal{P}(A | B)\mathcal{P}(B) = \mathcal{P}(B | A)\mathcal{P}(A).$$

<sup>7</sup> It becomes useful in the context of model selection. When uncertain about the choice of model—7-th degree polynomial or 6-term multi-exponential?—the “evidence” is used to compare different models, and to assess which one is preferred by the data. Particularly, when there is too little prior knowledge to assign a prior pdf, one may use the data to find a reasonable one. This procedure is known as *empirical Bayes*. Note that, implicit in  $I$  is the model itself, though not its parameters' values.

Essentially, Bayesian statistics is nothing more than consistently following the sum and product rules of probability. The Bayes' formula (5.100) provides clear instructions on how to systematically update our state of knowledge in light of new information.

Let us now return to our curve fitting problem with a Bayesian approach. We begin by writing down the likelihood function, i.e. the probability of getting the Monte Carlo data  $G(t)$  given  $\{A_n, E_n\}$ , viewed as a function of those parameters. We then explicitly specify our prior knowledge of and assumptions about  $\{A_n, E_n\}$ , in the prior pdf. Multiplying these two pdfs gives the posterior up to a normalization constant.

We will make two assumptions while assigning these probabilities. First, we assume that enough simulation data has been accumulated that the central limit theorem applies and therefore the likelihood can be taken to be a Gaussian. Thus, we can write

$$\mathcal{P}(G(t) | f(t; \boldsymbol{\lambda}), I) \propto \exp\left(-\frac{\chi_{\text{MC}}^2}{2}\right), \quad (5.102)$$

where  $\chi_{\text{MC}}^2$  is the same as before, given in (5.96), and the model parameters are collectively denoted by a vector  $\boldsymbol{\lambda}$ :

$$\boldsymbol{\lambda} \equiv (a_0, E_0, a_1, E_1, \dots). \quad (5.103)$$

Our second assumption is that the prior can also be approximated by a Gaussian

$$\begin{aligned} \mathcal{P}(f(t; \boldsymbol{\lambda}) | I) &= \prod_i \frac{1}{\sqrt{2\pi}\tilde{\sigma}_{\lambda_i}} \exp\left(-\frac{(\lambda_i - \tilde{\lambda}_i)^2}{2\tilde{\sigma}_{\lambda_i}^2}\right) \\ &\propto \exp\left(-\frac{\chi_{\text{prior}}^2}{2}\right), \end{aligned} \quad (5.104)$$

where  $\tilde{\lambda}_i$  and  $\tilde{\sigma}_i$  are *a priori* estimates for means and widths of the model parameters and are collectively referred to as the *priors*.

This is a somewhat arbitrary choice but a reasonable one nonetheless. Once the means and standard deviations of the model parameters have been specified, the least biased choice for the complete distribution, or equivalently, the least informative prior is Gaussian.<sup>8</sup> Moreover, since the likelihood is Gaussian, then a Gaussian prior would give us a Gaussian posterior as well. Hence, a preferable choice.

Putting together (5.102) and (5.104), the posterior takes the form:

$$\mathcal{P}(f(t; \boldsymbol{\lambda}) | G, I) \propto \exp\left(-\frac{\chi_{\text{aug}}^2}{2}\right). \quad (5.105)$$

---

<sup>8</sup> Given the constraints  $\langle \lambda_i \rangle = \tilde{\lambda}_i$ , and  $\langle \lambda_i^2 \rangle - \langle \lambda_i \rangle^2 = \tilde{\sigma}_i^2$ , the Gaussian distribution maximizes the entropy

$$S \equiv - \int \mathcal{P}(\boldsymbol{\lambda}) \ln \mathcal{P}(\boldsymbol{\lambda}) d^M \boldsymbol{\lambda}.$$

Essentially, we have augmented the original  $\chi^2$  from the Monte Carlo data by extra terms, thereby injecting additional a priori information into the analysis

$$\chi^2 \rightarrow \chi_{\text{aug}}^2 \equiv \chi_{\text{MC}}^2 + \chi_{\text{prior}}^2, \quad (5.106)$$

which in effect constrains the fit parameters. We have

$$\begin{aligned} \chi_{\text{aug}}^2(G; \boldsymbol{\lambda}, \{\tilde{\boldsymbol{\lambda}}, \tilde{\boldsymbol{\sigma}}\}) &\equiv \chi_{\text{MC}}^2(G; \boldsymbol{\lambda}) + \chi_{\text{prior}}^2(\boldsymbol{\lambda}, \{\tilde{\boldsymbol{\lambda}}, \tilde{\boldsymbol{\sigma}}\}) \\ &= \sum_{t,t'} \Delta y(t) \sigma_{t,t'}^{-2} \Delta y(t') + \sum_i \frac{(\lambda_i - \tilde{\lambda}_i)^2}{\tilde{\sigma}_{\lambda_i}^2}. \end{aligned} \quad (5.107)$$

Rewriting (5.105), the augmented  $\chi_{\text{aug}}^2$  is related to the posterior through

$$\chi_{\text{aug}}^2 \propto -2 \ln \mathcal{P}(f(t; \boldsymbol{\lambda}) | G, I). \quad (5.108)$$

Thus, minimizing  $\chi_{\text{aug}}^2$  gives us posterior best estimates for the model parameters.

In terms of energies and amplitudes the prior portion of  $\chi_{\text{aug}}^2$  is given by

$$\chi_{\text{prior}}^2 \equiv \sum_n \frac{(A_n - \tilde{A}_n)^2}{\tilde{\sigma}_{A_n}^2} + \sum_n \frac{(E_n - \tilde{E}_n)^2}{\tilde{\sigma}_{E_n}^2}. \quad (5.109)$$

Reasonable values are chosen for  $\{\tilde{A}_n, \tilde{\sigma}_{A_n}, \tilde{E}_n, \tilde{\sigma}_{E_n}\}$  based on our *prior* knowledge. These extra terms have the effect of favoring amplitudes in the range of  $\tilde{A}_n \pm \tilde{\sigma}_{A_n}$ , and energies in  $\tilde{E}_n \pm \tilde{\sigma}_{E_n}$ .

Note that (5.109) is similar to the regularization term we considered earlier in (5.99). However, unlike before, in a Bayesian framework these constraints arise in a more natural way. The widths  $\tilde{\sigma}_{A_n}$  and  $\tilde{\sigma}_{E_n}$  reflect the level of our prior knowledge, (or ignorance), and play the role of the regularization coefficient  $\alpha$ . The less we know about a parameter, the wider the prior widths, the less constrained it will be in the fit.

Having chosen the priors we do a least squares fit to the augmented  $\chi_{\text{aug}}^2$ , with a fixed small  $t_{\text{min}}$  and as many terms as we wish. Unlike previously, we do not need to optimize the number of terms. They are added until the fit results converge and return a  $\chi_{\text{aug}}^2/\text{DoF} \approx 1$ . If, however, this ratio remains significantly larger than 1 after convergence, then there is likely a mistake in either the data, the priors or the model. As can be seen in Figure 5.3a, fits are greatly improved and remain completely stable. Once converged, adding more terms will have no effect on the results.

The Bayesian analysis works so well because it makes use of crucial information in the form of the extra terms in the augmented  $\chi_{\text{aug}}^2$ , that would otherwise have been neglected. These terms give some curvature to the  $\chi^2$  function along directions that are poorly constrained by the data, thereby preventing the fit from going off to unphysical regions, while having little effect on those that are well determined by the data.

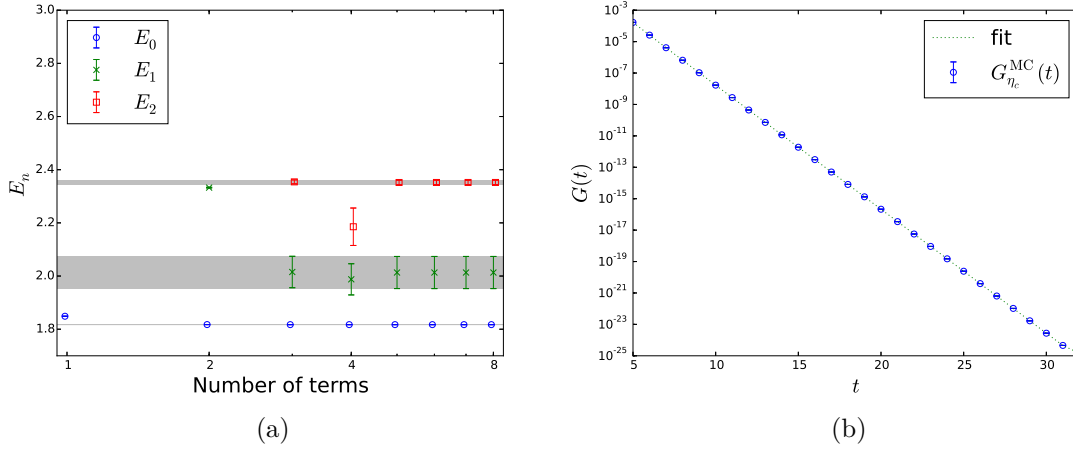


Figure 5.3: (a) Energies from Bayesian fits to  $\eta_c$  correlators plotted for various number of terms. Once converged, adding more terms has no effect. (b) Fit function (dotted line) plotted together with the Monte Carlo data. The fitted correlator is in excellent agreement with the data. Error bars on the data points are too small to be resolved.

The two pieces in the  $\chi_{\text{aug}}^2$  defined in (5.106), combine the statistical uncertainties from the input data and the systematic uncertainties due to our ignorance as specified in the  $\chi_{\text{prior}}^2$ . As a result, the uncertainties returned by the fit have two sources: the Monte Carlo data and the priors. Refitting the data with the prior widths doubled can give us a measure of how much error is due to each source. The results for the first 4 energies change as follows

$$\begin{aligned}
 E_0 &= 1.817302(54) & \rightarrow & 1.817306(54) \\
 E_1 &= 2.246(20) & \rightarrow & 2.251(19) \\
 E_2 &= 2.74(14) & \rightarrow & 2.79(16) \\
 E_3 &= 3.09(23) & \rightarrow & 3.13(39).
 \end{aligned}
 \tag{5.110}$$

The first 3 states are well determined by the data and mostly unaffected by changing the priors, while the error in the third excited state's energy is almost doubled. This indicates that  $E_3$  is largely determined by the priors. As more terms are added, the fit simply reproduces the priors without biasing the rest of the parameters. That is, it returns whatever information we put in it. This perfectly captures the power of Bayes. It allows one to fit 666 parameters to 42 data points.

One can build additional hard constraints directly into the fit function through its specific parameterization, in order to improve the quality and efficiency of the fit. The amplitudes in the  $\eta_c$  correlator, for instance, are actually given by  $A_n = |a_n|^2$ , where  $a_n$  is the overlap between the interpolating operator  $J$  used in (5.94) and the  $n$ -th state. So using  $a_n$  as fit parameters instead of  $A_n$ , avoids the potential cost of the fitter searching negative parts of the parameter space for values that we know are positive. However,

this parameterization introduces a degeneracy due to the symmetry  $a_n \rightarrow -a_n$ , hence making it difficult for the fitter to find either. We restrict the overlap to positive values by reparameterizing the fit function in terms of  $\log a_n$ .

In the same vein, one can build in a priori requirements for the energies to be positive, ordered and sufficiently spaced out to be physically distinct. Using  $\varepsilon_n \equiv \log(E_n - E_{n-1})$  for  $n > 1$ , and  $\varepsilon_0 \equiv \log E_0$  as fit parameters accomplishes that.

This specific parameterization then forces  $a_n > 0$  and  $E_n > E_{n-1}$ , while guiding the analysis towards level spacings that are consistent with physical states known from numerous previous analyses and experiments. Reasonable priors are normally easy to find. Incorrect priors lead to terrible  $\chi_{\text{aug}}^2$  which do not converge by adding more terms, and thus are immediately evident. We choose fairly generous widths to avoid biasing the results. For the  $\eta_c$  fit shown in Figure 5.3b, we took a rough estimate of the “effective mass” from the data as the central value for  $E_0$ , with a prior width of 500 MeV. For mass splittings between excitations, we used a prior of 600 MeV with various widths in the range of 300–600 MeV. The overlaps’ priors were taken to be  $0.5 \pm 0.5$ . In lattice units these are

$$\begin{aligned} E_0 &\approx 1.81 \pm 0.3, \\ E_n - E_{n-1} &\approx 0.36 \pm (0.18 - 36), \\ a_n &\approx 0.5 \pm 0.5. \end{aligned} \tag{5.111}$$

Table 5.1 lists some results from fits done with various number of terms using the above priors and parameterization. The results demonstrate the quick convergence of fits illustrated in Figure 5.3, as well as the effect of adding terms after convergence.

Let us make a couple of remarks regarding Bayesian analysis before going into a detailed discussion of the specific techniques we use in our fits. In a maximum likelihood fit, the number of degrees of freedom, is equal to the number of data points minus the number of fit parameters. We saw that maximum likelihood is highly prone to over-fitting. So, one is forced to limit the number of fit parameters.

However, it is deeply unsatisfying to choose the number of fit parameters according to the size of the data set, instead of the underlying model. Bayesian analysis completely avoids this problem and has no difficulty fitting models whose number of parameters exceeds that of data points. By adopting a Bayesian approach, the effective number of degrees of freedom is automatically adapted to the input information. It is both possible and permissible to have more parameters than data points. This is simply due to the fact that each prior is effectively like an additional data point. Since there is a prior for every fit parameter, the net number of degrees of freedom can be taken to be the number of data points.<sup>9</sup>

---

<sup>9</sup> In general, the *effective number of DoF* depends on the exact prior pdf. So in a Bayesian fit, ensuring that the minimized  $\chi^2/\text{DoF}$  is strictly less than 1 is of secondary importance behind convergence. In practice, it suffices to take each prior to be effectively equivalent to one input and seek to obtain a  $\chi^2/\text{DoF} \approx 1$ .



Table 5.1: Priors and fit results in lattice units for hadronic masses from Bayesian fits to  $\eta_c$  with various number of terms indicated in the first column. Columns 3 and 4 show the priors and the best-fit values for parameters  $\varepsilon_0 = \log(E_0)$  and  $\varepsilon_i = \log(E_i - E_{i-1})$  that were actually used in the fit. Columns 6 and 7 list their equivalent values converted back into hadronic masses. Note the quick convergence of results with as few as 3 terms, after which results for the first couple of states and the  $\chi^2$  remain the same. Note also that the addition of further terms has no effect and simply returns the prior, as is evident in both  $\varepsilon_3$  and  $\varepsilon_{13}$  entries from a 4-term and a 14-term fit respectively. Results for the overlaps exhibit a similar convergence pattern.

$N$	$\varepsilon_i$	prior	fit result	$E_i$	prior	fit result	$\chi^2/\text{DoF}$
1	$\varepsilon_0$	0.59(17)	0.607001(24)	$E_0$	1.81(30)	1.834920(44)	$10^4$
2	$\varepsilon_0$	0.59(17)	0.597430(28)	$E_0$	1.81(30)	1.817441(51)	5.5
	$\varepsilon_1$	-1.02(50)	-0.6637(45)	$E_1$	2.17(35)	2.3324(23)	
3	$\varepsilon_0$	0.59(17)	0.597353(30)	$E_0$	1.81(30)	1.817303(54)	0.58
	$\varepsilon_1$	-1.02(50)	-0.846(45)	$E_1$	2.17(35)	2.246(19)	
	$\varepsilon_2$	-1.02(50)	-0.69(24)	$E_2$	2.53(39)	2.75(14)	
4	$\varepsilon_0$	0.59(17)	0.597353(30)	$E_0$	1.81(30)	1.817302(54)	0.58
	$\varepsilon_1$	-1.02(50)	-0.847(45)	$E_1$	2.17(35)	2.246(19)	
	$\vdots$	$\vdots$	$\vdots$	$\vdots$	$\vdots$	$\vdots$	
	$\varepsilon_3$	-1.02(50)	-1.03(50)	$E_3$	2.89(43)	3.10(23)	
14	$\varepsilon_0$	0.59(17)	0.597353(30)	$E_0$	1.81(30)	1.817302(54)	0.58
	$\vdots$	$\vdots$	$\vdots$	$\vdots$	$\vdots$	$\vdots$	
	$\varepsilon_{13}$	-1.02(50)	-1.02(50)	$E_{13}$	6.49(71)	6.69(61)	

Finally, let us briefly comment on the perceived “subjectivity” of Bayesian fitting. Using priors may make one uneasy because it may seem that it undermines the objectivity of the analysis. After all, different people using different priors might obtain different results given the same input data. Whereas, one would rightly expect that an objective analysis of the same data should produce the same outcome.

Note however that, given the infinite parameter space and choices of models, all analyses necessarily involve assumptions in addition to the observed data and therefore strictly speaking are subjective. This is of course true for the Bayes probabilities which are interpreted as degree of belief, and naturally depend on the person who is assigning them. However, once all the underlying assumptions that go into the analysis in addition to the observed data are made explicit in the Bayes priors, the Bayesian analysis that follows will be objective. In other words, the use of Bayesian priors does not in itself make the analysis any less or more objective; it only makes one’s assumptions transparent. Not using priors like in traditional analyses, is in fact a special case of Bayes with infinitely wide priors for

parameters included in the fit and infinitely sharp priors centered at zero for those omitted. Bayesian priors are arguably far more realistic, and the analysis is no less objective merely due to their use.

Thus, the Bayes approach is concerned not with whether prior information should be used, arguing that they are inherently unavoidable. Rather, the focus is on assigning the priors dispassionately and making them explicit in order to assess their effect on the results. Accordingly, we will justify our priors in all our analyses and study how sensitive our fit results are to their choice.

### 5.5.2 Fitting Techniques

In most situations one wants to fit several two-point and three-point functions which share several parameters. For instance, extracting a transition form factor involves one or more three-point correlators, likely with various momenta and sink times, together with each one's parent two-point correlators, possibly obtained from different interpolating operators. In between them these correlators share many of the same fit parameters for energies, overlaps and matrix elements. Furthermore, the correlators are usually calculated on the same ensemble of configurations and therefore are correlated with one another.

In order to properly take into account all correlations, one must do a simultaneous fit to all correlators involved. Such a large data set leads to an unwieldy covariance matrix. The fit also involves a large number of parameters and as a result can be extremely slow to converge. We use a number of techniques and strategies to deal with convergence issues and to speed up our fits. These methods include singular value decomposition (SVD), chaining and marginalization and are described in Appendix C.

### 5.5.3 Error Analysis: Partial Error Budgets, Bootstrap

We've seen how to obtain the posterior probability distribution of parameters of interest using the Bayes' theorem, or equivalently (5.101) and (5.105). Given the posterior, one can in theory calculate the expected value of any arbitrary function of these parameters by evaluating Bayes integrals

$$\langle g(\lambda) \rangle = B^{-1} \int e^{-\chi_{\text{aug}}^2(\lambda)/2} g(\lambda) d^M \lambda. \quad (5.112)$$

No minimization necessary! Here,  $B$  is the normalization coefficient, (the evidence):

$$B \equiv \int e^{-\chi_{\text{aug}}^2(\lambda)/2} d^M \lambda, \quad (5.113)$$

and  $M$  is the number of model parameters. The error is also computed from  $\sigma_g^2 = \langle g^2 \rangle - \langle g \rangle^2$ .

In practice, however, the Bayes integrals are often prohibitively costly to evaluate due to the integrand being sharply peaked along long high narrow ridges in parameter space.

Approximations are needed. One can use the Laplace approximation in these situations:  $\chi_{\text{aug}}^2$  is assumed to be quadratic around its minimum

$$\chi_{\text{aug}}^2 \approx \chi_{\text{aug},\text{min}}^2 + \sum_{i,j} (\lambda - \lambda^*)_i C_{ij}^{-1} (\lambda - \lambda^*)_j, \quad (5.114)$$

where  $\lambda_i = \lambda_i^*$  minimize  $\chi_{\text{aug}}^2$ , and  $C$  is the covariance matrix for the model parameters. This obviously assumes a Gaussian posterior. Assuming that  $g$  is sufficiently smooth, the Bayes integrals are then approximated by the contributions from the dominant region

$$\begin{aligned} \langle g(\lambda) \rangle &\approx g(\lambda^*), \\ \sigma_g^2 &\approx \sum \partial_i g(\lambda^*) C_{ij} \partial_j g(\lambda^*). \end{aligned} \quad (5.115)$$

The second relation between  $\sigma_g^2$  and individual elements of the covariance matrix can then be used to constitute an *error budget* for  $g$ . That is, the aggregate error in our estimate for  $g$  is broken down to partial errors due to different sources, including statistical errors, priors and individual fit parameters.

There is an alternative, more general and more robust method for estimating errors known as the *bootstrap* analysis [46, 57]. This method is particularly useful in identifying and handling non-Gaussian distributions, which might for example arise out of low-statistics data sets. One constructs  $N_{\text{bs}}$  bootstrap copies of the Monte Carlo data by randomly drawing configurations from the original ensemble, allowing for duplicates. The entire analysis is repeated for each bootstrap copy and results are accumulated. The error is then taken to be the half-width of the middle 68% of the total spread in the bootstrap results.

Remember that in a Bayesian setting, priors are data. Therefore, for each bootstrap fit, in addition to constructing the standard bootstrap copy from the Monte Carlo data, one must also sample the priors at random. Prior means are thus drawn from their original distribution for each bootstrap, while their covariances are kept intact.

Note that, in general, drawing  $k$  configurations at random from an ensemble of  $N$  distinct configurations while allowing for repeat draws is equivalent to distributing  $k$  indistinguishable balls into  $N$  distinct boxes. There are  $\binom{N+k-1}{k}$  ways to do this.<sup>10</sup> Each bootstrap copy has the same number of configurations  $N$  as the original ensemble, but likely with some configurations repeated and hence some others omitted. Therefore, there are  $\binom{2N-1}{N} \sim N^N$  possible bootstrap copies, which is a huge number for a decent sized ensemble.

Luckily, one need not generate all possible samples. Typically, a bootstrap ensemble of  $N_{\text{bs}} = N_{\text{cf}}$  for relatively small statistics or  $N_{\text{bs}} \approx 500$  for larger data sets would be sufficient for the purpose of obtaining a reliable estimate of the underlying probability distribution. Results from each bootstrap copy are essentially samples from the underlying distribution of

---

<sup>10</sup> Placing  $x_i$  balls in the  $i$ -th box corresponds to the  $i$ -th configuration selected  $x_i$  times, where  $x_i \geq 0$  and  $x_1 + \dots + x_N = k$ . This is equivalent to filling  $N + k - 1$  blanks with  $N - 1$  box separators (or plus signs) and  $k$  balls, which can be done in  $\binom{N+k-1}{N-1} = \binom{N+k-1}{k}$  distinct ways.

corresponding random variables. This means that, one can determine a random variable's distribution by directly generating it via bootstrapping. This will be visually demonstrated through histogram plots in later chapters. For truly Gaussian distributions the bootstrap error estimates are consistent with (5.115) approximations.

It is worth stressing that not only the bootstrap analysis is useful for parameters directly used in the fit, it is also extremely useful for the error analysis of arbitrary functions of them which sometimes cannot be accurately estimated by simple error propagation. Whereas, in a bootstrap analysis every quantity of interest can be evaluated on each sample and thus accumulated to represent its distribution.

Also, importantly, the bootstrap method is better equipped to properly handle extreme outliers, since its estimation depends on the median and the spread of the sample as opposed to its average and size. One or two extreme outliers in the data can significantly skew the average and pull it away from the true mean. The median is clearly immune to this weakness.

Finally, it's important to note that the bootstrap error estimate is determined from the width of the spread of the results as opposed to the standard estimate of  $\sigma/\sqrt{N_{\text{bs}}}$ . The latter is clearly incorrect since the error can be artificially beaten down by jacking up the number of bootstrap samples.

## 5.6 Putting It All Together; A Case Study

We have now developed all the different components of a typical lattice calculation. chapter 2 presented the foundations of lattice QCD. The next two chapters reviewed the discretization of quarks and the improvement program that led to the formulation of a theoretical framework describing hadrons on the lattice. In this chapter we have so far explained the practical aspects of running computer simulations and extracting physical quantities from the resulting numerical data. In this section we put everything together and apply it to an interesting problem before getting to our main calculations in the next chapter.

### 5.6.1 Electric Form Factor and Charge Radius of Mesons

Here we compute the quark density distribution of  $\eta_c$  and  $D_s$  pseudoscalar mesons by calculating vector current form factors. This quantity is experimentally unobservable but physically interesting. It can be used to make a theoretical estimate for the “charge radius” of a valence quark inside a meson and thus infer the “size” of the meson [63, 5].

We used local pseudoscalar operators of the form  $\bar{\psi}(x)\gamma_5\psi(x)$  to create and destroy the  $\eta_c$  and  $D_s$  mesons and the conserved current  $j^\mu$  derived in subsection 5.2.3 to probe into them. The meson form factor for  $\eta_c$ , for instance, is defined in terms of the matrix element

$$\langle \eta_c(k) | j^\mu(q) | \eta_c(p) \rangle = f(q^2)(p+k)^\mu. \quad (5.116)$$

It can then be extracted from 3-point correlation functions computed on the lattice at various momentum transfers. One can then fit the result to a monopole form given by

$$f(q^2) = \mathcal{Q} \left( 1 + \frac{1}{6} |\vec{q}|^2 \langle r^2 \rangle \right)^{-1}, \quad (5.117)$$

where  $\mathcal{Q}$  is the electric charge of the current and  $\langle r^2 \rangle$  is the mean square of the charge radius.

We simulated at the four smallest momenta allowed on the lattice, i.e.  $\vec{q} = 2\pi\vec{n}/L$  where  $\vec{n}^2 = 0, 1, 2, 3$ . Our fit result for the root mean square (rms) of the quark density distribution radius for  $\eta_c$  is

$$\sqrt{\langle r^2 \rangle_{\eta_c}} = 0.1804(83) \text{ fm}. \quad (5.118)$$

The lattice spacing of the MILC coarse ensemble used in this work is  $a = 0.12$  fm and its length is  $L = 20$ . The above estimate of the “size” of  $\eta_c$  provides an a posteriori justification for the box size of 2.4 fm.

Similarly for  $D_s$  we get

$$\begin{aligned} \sqrt{\langle r_s^2 \rangle_{D_s}} &= 0.468(60) \text{ fm}, \\ \sqrt{\langle r_c^2 \rangle_{D_s}} &= 0.128(81) \text{ fm}. \end{aligned} \quad (5.119)$$

As expected we find the strange quark’s rms charge radius to be larger than that of the charm.

## Chapter 6

# Radiative and Pionic Transitions

In this chapter we present our original calculations. So far in this thesis we have reviewed the foundations of lattice QCD and learned how gluons and fermions can be simulated in a discretized spacetime. We encountered a number of improved formalisms to deal with different physical scales and degrees of freedom. We also learned the practical side of carrying out Monte Carlo simulations and extracting physical quantities from the numerical data and applied them to a few case studies.

Having gone through the development of a highly improved theoretical framework in the form of the HISQ action [9], and having developed the technology for calculating physical observables in chapter 5, we are now in a position to tackle the main problems that we set out to study. Recall from chapter 1 that this project was motivated by the curious suppression of the radiative decay of the charged vector charmed meson  $D^{*+} \rightarrow D^+\gamma$ , as compared with that of its neutral counterpart.

The experimentally measured branching ratios of the decay modes of heavy-light mesons taken from the PDG [1] are listed in Table 6.1. Notice first that as is evident from the branching fractions of  $D^{*0}$  and  $D_s^{*+}$ , their hadronic modes are not as dominant as one would normally expect from strong decays. As described in chapter 1, this can be explained by the kinematics of these processes involving small phase spaces. This can be seen in Table 6.2 where experimental values for the masses of these mesons are listed along with other physical quantities of relevance in this work.

This leads to the second curious observation where the radiative decay ratio of the charged vector charmed meson  $D^{*+} = c\bar{d}$  is observed to be only 1.6(4)%, while the neutral  $D^{*0} = c\bar{u}$  decays via a photon 38.1(2.9)% of the time despite their comparable phase spaces.

This discrepancy is due to a different kind of suppression that distinguishes the charged charm-light mesons, i.e.  $D^{*+} = c\bar{d}$  and  $D_s^{*+} = c\bar{s}$ , from the neutral  $D^{*0} = c\bar{u}$  and is due to the fact that, as shown in (1.1), individual contributions from the photon's coupling to each valence quark's magnetic moment have opposite signs for the charged mesons and

Table 6.1: Decay modes and branching ratios of  $D^*$  and  $D_s^*$  mesons [1].

$D^{*+}$ modes	Fraction (%)	$D^{*0}$ modes	Fraction (%)	$D_s^{*+}$ modes	Fraction (%)
$D^+\gamma$	1.6(4)	$D^0\gamma$	38.1(2.9)	$D_s^+\gamma$	94.2(7)
$D^0\pi^+$	67.7(5)	$D^0\pi^0$	61.9(2.9)	$D_s^+\pi^0$	5.8(7)
$D^+\pi^0$	30.7(5)				

Table 6.2: Experimental values for meson masses and other relevant quantities [1]. All values quoted in MeV unless indicated otherwise. Errors in pion masses are omitted since they're much smaller than those of the rest of the quantities listed below. The two momenta  $|\vec{q}_{\pi^+}|$  and  $|\vec{q}_{\pi^0}|$  in the bottom row correspond to pionic decays of the charge  $D$  meson  $D^{*+} \rightarrow D\pi$  whose branching ratios are given in the first two columns of Table 6.1 and are discussed in section 6.2. Finally,  $f_\pi$  is the decay constant of the pion.

Charged $D$	$m_{D^{*+}}$	$m_{D^+}$	$m_{D^{*+}} - m_{D^+}$	$ \vec{q}_\gamma $	$\Gamma_{\text{tot}}$ (keV)
Expt.	2010.26(7)	1869.61(10)	140.66(8)	137.1(1)	83.4(1.8)
Neutral $D$	$m_{D^{*0}}$	$m_{D^0}$	$m_{D^{*0}} - m_{D^0}$	$ \vec{q}_\gamma $	$\Gamma_{\text{tot}}$
Expt.	2006.96(10)	1864.84(7)	142.12(7)	135.7(1)	< 2.1
Charmed strange	$m_{D_s^{*+}}$	$m_{D_s^+}$	$m_{D_s^{*+}} - m_{D_s^+}$	$ \vec{q}_\gamma $	$\Gamma_{\text{tot}}$
Expt.	2112.1(4)	1968.30(11)	143.8(4)	138.9(4)	< 1.9
Charmonium	$m_{J/\psi}$	$m_{\eta_c}$	$m_{J/\psi} - m_{\eta_c}$	$ \vec{q}_\gamma $	$\Gamma_{\text{tot}}$ (keV)
Expt.	3096.916(11)	2983.6(7)	113.32(70)	111.24(67)	92.9(2.8)
Pions	$m_{\pi^+}$	$m_{\pi^0}$	$ \vec{q}_{\pi^+} $	$ \vec{q}_{\pi^0} $	$f_{\pi^+}$
Expt.	139.57	134.98	39.3(3)	38.1(4)	130.41(20)

happen to nearly cancel each other out while for the neutral system they have constructive contributions.

The third curious entry in Table 6.1 is the suppression of the pionic decay mode of  $D_s^{*+}$  which as explained in chapter 1 is a result of it being isospin violating in addition to the small phase space. Thus, despite the suppression of its radiative mode due to the near cancellation between the photocouplings with the effective magnetic moments of its constituent quarks the branching ratio is still dominant at 94.2(7)%.

These observations indicate that there is plenty of interesting hadron physics to be probed in the radiative and pionic decays of these charmed mesons. In this chapter we investigate these processes by directly calculating radiative and pionic transitions via lattice simulations. Though not limited to those, a major point of focus in our studies is the calculation of the decay modes of the charged  $D^{*+}$ .

A recent experiment by BaBar [11] measured the full width

$$\Gamma(D^{*+}) = (83.3 \pm 1.2 \pm 1.4) \text{ keV}. \quad (6.1)$$

The full width consists of three modes

$$\Gamma(D^{*+}) = \Gamma(D^{*+} \rightarrow D^+ \gamma) + \Gamma(D^{*+} \rightarrow D^0 \pi^+) + \Gamma(D^{*+} \rightarrow D^+ \pi^0). \quad (6.2)$$

We will directly calculate the radiative transition as well as the decay into the charged pion. We avoid complications due to the anomalous terms in the case of the neutral pion by invoking the approximate isospin symmetry. It provides an estimate for the third and last mode by simply relating the two pionic modes through iso-Clebsch-Gordon coefficients

$$\frac{\Gamma(D^{*+} \rightarrow D^0 \pi^+)}{\Gamma(D^{*+} \rightarrow D^+ \pi^0)} \approx \frac{|\langle \frac{1}{2}, \frac{1}{2} | \frac{1}{2}, -\frac{1}{2}; 1, 1 \rangle|^2}{|\langle \frac{1}{2}, \frac{1}{2} | \frac{1}{2}, \frac{1}{2}; 1, 0 \rangle|^2} = 2. \quad (6.3)$$

Compared with experimental observations given in Table 6.1 it is evident that this approximation introduces a systematic error of about 10%. Note also that since our estimate of the neutral pionic modes relies on the isospin symmetry it cannot be extended to the isospin violating pionic decay of  $D_s^*$  which is not studied in this work.

In order to examine the near cancellation that takes place between the two quarks' couplings to photon in heavy-light mesons as a function of quark mass we simulated transition processes for a range of light and heavy quark masses. Furthermore, we complemented our calculations with the radiative transition of charmonium.

In section 6.1 we describe our approach to calculating radiative transition rates. Section 6.2 lays out the theoretical basis we use to access pion couplings. We provide the details of our simulation data in section 6.3 followed by a detailed description of our analysis and present our final results. In section 6.4 we come back to Table 6.1 and discuss the phenomenology of our results. Finally, we close this chapter with our results for the radiative transitions of heavy-strange  $H_s$  mesons in section 6.5.

## 6.1 Radiative Transition

The decay amplitude can be written as

$$\langle D(k) \gamma(q, \eta_{\lambda'}) | D^*(p, \epsilon_{\lambda}) \rangle = \varepsilon_{\mu\nu\rho\sigma} \eta_{\lambda'}^{\mu} k^{\nu} \epsilon_{\lambda}^{\rho} p^{\sigma} g_{D^* D \gamma}, \quad (6.4)$$

where  $g_{D^* D \gamma}$  represents the  $D$  meson's coupling to photon. Inspecting the quantum numbers of the particles involved, while keeping in mind that the photon has odd intrinsic parity, one can see that this process has an overall odd intrinsic parity:  $\langle 0^- \otimes 1^- | 1^- \rangle$ .

There are four independent 4-vectors available out of which one needs to construct a Lorentz invariant quantity with the required odd parity. This dictates the form of the right hand side of (6.4), where the correct parity is imposed by the antisymmetric Levi-Civita tensor  $\varepsilon_{\mu\nu\rho\sigma}$ . Here,  $\epsilon_{\lambda}$  and  $\eta_{\lambda'}$  are the polarization vectors of the  $D^*$  and the photon respectively, while  $p$  and  $k$  are taken as the two independent momenta corresponding to  $D^*$



and  $D$  respectively. Conservation of momentum then implies that the photon's momentum is  $q = p - k$ .

The following subsection introduces our notation and outlines the strategy used in the calculation. Specific details of the lattice approach are then presented in subsection 6.1.2. In particular, general considerations that go into the operator selection process in going from continuum to lattice are discussed in detail. The discussion can therefore be viewed as a sample step by step recipe for translating a physical process as understood in the continuum theory into a lattice simulation formulated in the language of the staggered quarks.

Throughout this chapter the notation explicitly uses  $D^*$  and  $D$  to denote the hadrons involved. However, the exact same procedure can be used for all magnetic dipole (M1) transitions  $V \rightarrow P\gamma$  where a vector meson decays into its pseudoscalar counterpart and a photon.

### 6.1.1 Hadronic Matrix Elements

The coupling corresponding to this decay process is accessed on the lattice via the matrix element of the electromagnetic current

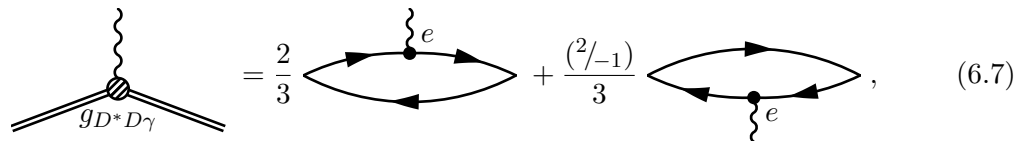
$$\mathcal{Z}\langle D(k)|J_\mu^{\text{em}}(q)|D^*(p, \lambda)\rangle = \frac{2eV(q^2)}{(m_{D^*} + m_D)}\varepsilon_{\mu\nu\rho\sigma}k^\nu\epsilon_\lambda^\rho p^\sigma, \quad (6.5)$$

where  $J_\mu^{\text{em}}$  is given by

$$J_\mu^{\text{em}} = eQ_c \bar{c}\gamma_\mu c + eQ_l \bar{l}\gamma_\mu l \equiv \frac{2e}{3}\mathcal{V}_\mu^c + \frac{(2/-1)e}{3}\mathcal{V}_\mu^l, \quad (6.6)$$

and  $\mathcal{Z}$  is its lattice renormalization matching factor. It is made up of two underlying quark bilinear vector currents  $\mathcal{V}_\mu^{c,l}$ , where  $c$  is the charm quark field and  $l$  a light quark field,<sup>1</sup> i.e. either  $u$  or  $d$ . They are combined together into  $J_\mu^{\text{em}}$ , each weighted by an appropriate electric charge coefficient. Here  $e = \sqrt{4\pi\alpha_{\text{QED}}}$  is the electromagnetic coupling, and  $Q_c = 2/3$  and  $Q_l = (2/3 \text{ or } -1/3)$  are the constituent quarks' electric charge in units of  $e$ .

Equivalently, this is expressed in the form of Feynman diagrams as



$$= \frac{2}{3} \left[ \text{loop with } e \text{ at top} \right] + \frac{(2/-1)}{3} \left[ \text{loop with } e \text{ at bottom} \right], \quad (6.7)$$

<sup>1</sup> There are no leptons in this study. Hence, there's no potential for confusion caused by having  $l$  stand for light. Throughout this work we use  $l$ ,  $q$ ,  $u$  and  $d$  interchangeably to denote light quarks depending on how specific we need to be in the context, or on which one would cause the least conflict. Note that this is more than just a shorthand notation. The  $u$  and  $d$  quarks are in fact treated as degenerate in some lattice QCD calculations that involve only strong interactions, thanks to the approximate chiral symmetry which will be discussed at length in subsection 6.2.1.

where we've wrapped up the  $D^*$  vector meson's photocoupling in a Lorentz invariant package represented in this diagram by a blob. The coupling is therefore

$$g_{D^{*+}D^+\gamma} = \frac{2}{m_{D^{*+}} + m_{D^+}} \frac{|V_l(0) - 2V_c(0)|}{3}, \quad (6.8a)$$

$$g_{D^{*0}D^0\gamma} = \frac{2}{m_{D^{*0}} + m_{D^0}} \frac{|2V_l(0) + 2V_c(0)|}{3}. \quad (6.8b)$$

All the information about the photocoupling is then encoded in  $V(q^2)$  on the right hand side of (6.5), which is a dimensionless Lorentz invariant function of the momentum transfer.<sup>2</sup> This is the essence of our calculation. The unknown quantity  $g_{D^*D\gamma}$ , is obtained from underlying processes whose coupling  $e$  is known.

The decay width is given by

$$\Gamma(D^* \rightarrow D\gamma) = \alpha_{\text{QED}} \frac{4|\vec{q}_\gamma|^3}{3(m_{D^*} + m_D)^2} |V(0)|^2. \quad (6.9)$$

The on-shell photon's momentum in the phase space factor is given by

$$|\vec{q}_\gamma| = \frac{m_{D^*}^2 - m_D^2}{2m_{D^*}} \quad (6.10)$$

and its physical value for both the charged and the neutral  $D$  is listed in Table 6.2, along with the corresponding quantity for other radiative transitions studied in this work.

Broken down into photon's coupling with each valence quark, the decay widths for the charged and the neutral  $D$  mesons are then given by

$$\Gamma(D^{*+} \rightarrow D^+\gamma) = \alpha_{\text{QED}} \frac{4|\vec{q}_\gamma|^3}{3(m_{D^{*+}} + m_{D^+})^2} \frac{|V_l(0) - 2V_c(0)|^2}{9}, \quad (6.11a)$$

$$\Gamma(D^{*0} \rightarrow D^0\gamma) = \alpha_{\text{QED}} \frac{4|\vec{q}_\gamma|^3}{3(m_{D^{*0}} + m_{D^0})^2} \frac{|2V_l(0) + 2V_c(0)|^2}{9}, \quad (6.11b)$$

where  $V_l(q^2)$  and  $V_c(q^2)$  capture contributions due to  $l$  and  $c$  quarks respectively and weighted accordingly in the overall radiative form factor.

Notice the relative sign between the two form factors above. The  $D^{*+}$  is made up of a  $c$  quark with charge  $+2/3$  and a  $d$  antiquark with  $+1/3$ . An additional factor of  $(-1)$  arises due to the spin flip that converts the vector meson with a symmetric spin configuration ( $|\uparrow\uparrow\rangle$ ), into a pseudoscalar with an antisymmetric one ( $|\uparrow\downarrow\rangle - |\downarrow\uparrow\rangle)/\sqrt{2}$ . Combined together, this leads to an overall relative sign in (6.11a) between contributions from  $c$  and  $d$  quarks inside the  $D^{*+}$ , which then conspire to suppress its radiative decay. It is this near cancellation that this work strives to probe.

---

<sup>2</sup> It is sometimes parameterized with the vector meson mass  $m_{D^*}$  in the denominator instead of the mass average  $(m_{D^*} + m_D)/2$ . This is just an arbitrary convention to make the form factor dimensionless.

In terms of the  $g_{D^*D\gamma}$  couplings with inverse-mass dimensions, the decay widths can be written as

$$\Gamma(D^{*+} \rightarrow D^+\gamma) = \frac{\alpha_{\text{QED}}}{3} g_{D^{*+}D^+\gamma}^2 |\vec{q}_\gamma|^3, \quad (6.12a)$$

$$\Gamma(D^{*0} \rightarrow D^0\gamma) = \frac{\alpha_{\text{QED}}}{3} g_{D^{*0}D^0\gamma}^2 |\vec{q}_\gamma|^3, \quad (6.12b)$$

which are equivalent to expressions (6.11) in terms of dimensionless form factors. They are included here for easy comparison with studies that quote these values as their results.

### 6.1.2 Lattice Correlation Functions

Correlation functions are the bread and butter of lattice theorists. In order to obtain the matrix element (6.5) one calculates a 3-point function of the form

$$C_{\mu\nu}^{(3)}(t, T; \vec{q}) = \sum_{\vec{y}, \vec{z}} e^{-i\vec{q}\cdot(\vec{y}-\vec{z})} \langle P^\dagger(\vec{y}, T) \mathcal{V}_\mu(\vec{z}, t) V_\nu(\vec{x}, 0) \rangle, \quad (6.13)$$

where  $V_\nu(x)$  and  $P(y)$  are interpolating operators that create a vector and a pseudoscalar meson respectively, while  $\mathcal{V}_\mu(z)$  is the vector current introduced in (6.6).

The kinematics is set up as follows. The antisymmetric tensor in (6.5) forces the four involved momenta to all point in different directions. The vector meson is kept at rest. Thus, its momentum  $p = (m_{D^*}, \vec{0})$  is purely along  $\hat{0}$ . Its polarization vector is chosen to be along the  $z$  axis and the vector current  $\mathcal{V}$  along  $y$ . This configuration then requires the momentum  $\vec{q} = -\vec{k}$  to have a non-zero component along the  $x$  axis in order for the matrix element of interest not to vanish.

### Choice of Operators; Decisions on Taste

Recall from subsection 4.2.1 that the taste symmetry requires correlation functions to be tasteless. The resulting taste selection rules given by (4.50), state that a 3-point correlator will vanish unless the total taste of the three operators add up to zero. That is, the overall taste signature must satisfy the condition  $s_P + s_V + s_{\mathcal{V}} = 0$ . As we saw before, it is much easier to think about operator selection in the Dirac (naive) basis, which we find more intuitive, before spin diagonalizing into the staggered basis in which the simulation is ultimately carried out.

Taste selection rules together with the spin and kinematical properties of the particles will narrow down, but not uniquely determine the set of operators that may be used in (6.13). Generally one would like to keep the number of point-splittings to a minimum in order to optimize the statistical errors. This is because point-split operators usually tend to be noisier than local ones [4].

Given the spin of the particles involved, one needs three bilinear operators with  $\gamma_5$ ,  $\gamma_2$  and  $\gamma_3$ . Thus, in order to prevent a vanishing trace over spinor indices (i.e. due to taste selection rules), an additional  $\gamma_0\gamma_1$  must somehow be conjured up inside that trace: cue for point-splits.

In order to avoid too many shifts, however, and since a bilinear with  $\gamma_0\gamma_3$  also creates a vector meson, a benign extra  $\gamma_0$  is dropped on the  $D^*$  operator  $V_3(x) = \bar{l}(x)\gamma_0\gamma_3c(x)$ . This saves us a shift along the temporal axis.  $V_3$  has a taste signature  $s_V = (1, 0, 0, 1)$ , or equivalently, a spin-taste structure of  $\gamma_0\gamma_3 \otimes \gamma_0\gamma_3$  according to the convention introduced in (4.73).

The requisite extra  $\gamma_1$  is produced through an unavoidable 1-link split along the  $x$  axis. It is convenient<sup>3</sup> to choose a local operator as the vector current  $\mathcal{V}_2(z) = \bar{\psi}(z)\gamma_2\psi(z)$ . Between the other two operators the shift along the  $x$  axis is given to the pseudoscalar operator  $P(y) = \bar{l}(y)\gamma_5c(y \pm \hat{1})$  where an appropriate link variable is implicit. These correspond to taste signatures  $s_V = (0, 0, 1, 0)$  and  $s_P = (1, 0, 1, 1)$ , which are equivalent to spin-taste  $\gamma_2 \otimes \gamma_2$  and  $\gamma_5 \otimes \gamma_5\gamma_2$  respectively.

Let us summarize the above discussion by listing the operators that are going to be used in the 3-point correlator (6.13) all in one place

$$D_\lambda^* : \quad V_3(x) = \bar{l}(x)\gamma_0\gamma_3c(x), \quad (6.14a)$$

$$J_\mu^{\text{em}} : \quad \mathcal{V}_2(z) = \bar{\psi}(z)\gamma_2\psi(z), \quad \psi = c \text{ or } l, \quad (6.14b)$$

$$D : \quad P(y) = \bar{l}(y)\gamma_5\{U_1(y)c(y + \hat{1}) + U_1^\dagger(y - \hat{1})c(y - \hat{1})\}. \quad (6.14c)$$

Let us now turn to the momentum  $q$ . Table 6.2 quotes the physical value of the photon's momentum  $|\vec{q}_\gamma|$  for various radiative decays studied in this work. It shows that they all involve very soft photons with momenta smaller than 140 MeV. This is a very small value which is not accessible on typical lattices currently available. However, one can tune the momentum by using twisted boundary conditions described in section 5.4.

This is done through rephasing the gauge field link variables by

$$U_\mu(x) \rightarrow U_\mu^\theta(x) = e^{i2\pi\theta_\mu/L}U_\mu(x), \quad (6.15)$$

where  $\theta = (0, \vec{\theta})$ . This has the effect of inducing a momentum of

$$\vec{q} = \frac{2\pi}{L}\vec{\theta}. \quad (6.16)$$

The twisting angle  $\vec{\theta}$  is an arbitrary 3-vector and is tuned to produce the desired momentum. This encodes the momentum into the gauge field link variables and therefore the usual momentum projection phase  $\exp(-i\vec{q} \cdot (\vec{y} - \vec{z}))$  in (6.13) is no longer needed.

<sup>3</sup> This choice is motivated by the fact that the local current's  $\mathcal{Z}$  factor has been calculated in [4] and [3] for  $c$  and  $s$  quarks, and shown to be very close to 1 within about 1%.

In practice one calculates the target momentum using (6.10) with mass inputs obtained from fits to separate zero momentum 2-point functions for the vector and the pseudoscalar mesons computed with the same operators as those that are going to be used in the main simulation. Remember also that the momentum must have a non-zero component along the  $x$  axis. Thus, the twisting phase is simply taken to be  $\vec{\theta} = (|\vec{q}|L/2\pi, 0, 0)$ .

The 3-point functions calculated are then given by

$$\begin{aligned}
C_{D^* \rightarrow D\gamma}^{(3,c)}(t, T; \vec{q}) &= \frac{1}{L^3} \sum_{\vec{x}, \vec{y}, \vec{z}} \langle \overbrace{\{\bar{c}(y + \hat{1})\gamma_5 U_1^{\theta\dagger}(y) l(y)\}_{\text{symm.}} \bar{c}(z)\gamma_2 c(z) \overbrace{l(x)\gamma_0\gamma_3 c(x)}^{\theta}} \rangle \\
&= \frac{4}{L^3} \sum_{\vec{x}, \vec{y}, \vec{z}} (-1)^{\phi(x,y,z)} \text{tr} \left( g_c^\dagger(z, x) g_c^\theta(z, y + \hat{1}) U_1^{\theta\dagger}(y) g_l(y, x) \right) \\
&\quad + \{g_c^\theta(z, y + \hat{1}) U_1^{\theta\dagger}(y) \leftrightarrow g_c^\theta(z, y - \hat{1}) U_1^\theta(y - \hat{1})\},
\end{aligned} \tag{6.17}$$

and its partner  $C^{(3,l)}$  which acts on the opposite quark line. Let us unpack this relation. The time-slice  $x^0 = t_0 = 0$  is called the source time,  $t = z^0$  the current insertion time and  $T = y^0$  the sink or the propagation time. The source and the sink are fixed and the current is inserted on every time step on the lattice.

The subscript ‘‘symm.’’ indicates a symmetrized point-splitting in the pseudoscalar operator  $P(y)$  as explicitly given in (6.14c). Switching to the staggered basis gives rise to a coordinate dependent staggered phase  $\phi(x, y, z)$ . The factor of 4 is due to the trace over spinor indices. The three quark propagators denoted by  $g$  are then computed in the staggered basis. The  $\text{tr}()$  is therefore over color indices.

The diagram in Figure 6.1 illustrates the first term of the (6.17) correlator. The downward line connecting  $y + \hat{1}$  to  $y$  is a link variable as clearly labeled and is not to be confused with a quark propagator. The *twisted* quark line labeled by  $\theta$  and propagating from the sink at  $y + \hat{1}$  to the current insertion point at  $z$ , represents a propagator computed using twisted boundary conditions

$$g^\theta(x, y) \equiv g(x, y; U^\theta) \equiv \langle \chi(x) \bar{\chi}(y) \rangle_\theta = e^{-2\pi i \vec{\theta} \cdot (\vec{y} - \vec{x})/L} g(y, x). \tag{6.18}$$

This injects the desired external momentum into the quark line at the current insertion time and takes it out at the sink. The other two propagators are not twisted and therefore only carry the internal momentum flowing around inside the quark loop. Notice also that the propagator between the source and current insertion is obtained in the simulation from the Hermitian conjugate of the one between the source and the sink  $g^\dagger(z, x)$  using (4.42). This gives one two propagators for the price of one.

Actually, (6.17) is not exactly what is calculated in the simulation. The average over all spatial lattice sites  $\vec{x}$  on the source time-slice is in fact estimated indirectly by using one random wall source, described in subsection 5.3.2, which on ensemble average will approach

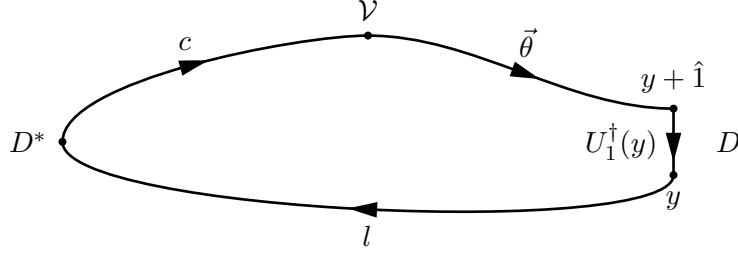


Figure 6.1: The 3-point correlator in (6.17) for the calculation of the radiative transition of  $D^*$ . A  $D^*$  at rest is created at the source. It decays into a  $D$  that is destroyed at the sink and a photon that couples to the  $c$  quark via a vector current  $\mathcal{V}$  inserted at time  $t$ , when the momentum is injected and is then carried to the sink along the twisted quark line. This is achieved by using twisted boundary conditions. The  $D$  meson operator has a 1-link split along the  $x$  axis. The loop is closed by the link variable  $U_1^\dagger(y)$ , thereby preserving the gauge invariance.

to the sum of  $L^3$  point sources. Whereas, sums over  $\vec{y}$  and  $\vec{z}$  are a direct result of those carried out when the propagators are contracted.

Finally, the 2-point functions

$$G_D^{(2)}(t; \vec{q}) = \frac{1}{L^3} \sum \langle P^\dagger(y) P(x) \rangle_\theta, \quad (6.19)$$

and

$$G_{D^*}^{(2)}(t; \vec{0}) = \frac{1}{L^3} \sum \langle V_3^\dagger(y) V_3(x) \rangle, \quad (6.20)$$

with the same interpolating operators used in (6.17) and given by (6.14) are calculated in order to extract the overlaps and energies of the hadronic states. Note that the meson correlator (6.19) is computed at  $\vec{q}$  by twisting one of its two quark propagators.

Let us now turn to the pionic decay. The analysis and results of both calculations will be presented in section 6.3.

## 6.2 Pionic Decay

Lattice simulation of the pionic decay  $D^* \rightarrow D\pi$  is less straightforward. Multi-hadron processes are difficult to deal with on the lattice since final state hadronic interactions are different in Euclidean and Minkowski space, and require more complicated methods. As was pointed out in subsection 5.4.1, in addition to the usual difficulties of dealing with non gold-plated quantities, *partially* twisted boundary conditions have large finite volume corrections in the presence of final state hadronic interactions [54].

Fortunately these problems can be avoided for decays to a single pion by relating the coupling  $g_{D^*D\pi}$  to the form factors of the axial current matrix elements. This strategy was first used in [64] to compute  $g_{B^*B\pi}$  using static heavy  $b$  quarks, and has since been adopted

in [65] for heavy quarks and in [66, 8, 67, 68] to compute  $g_{D^*D\pi}$  with relativistic propagating  $c$  quarks.

In this section we will lay out the theoretical basis of this strategy before describing our lattice calculation. As stated before we focus on the charged pionic decay to avoid anomalous terms in the neutral axial current.

### 6.2.1 Theory and Definitions

The width of the pionic decay of the vector  $D^*$  meson is given by

$$\Gamma(D^* \rightarrow D\pi) = \frac{C}{24\pi m_{D^*}^2} g_{D^*D\pi}^2 |\vec{q}_\pi|^3, \quad (6.21)$$

where the pion coupling  $g_{D^*D\pi}$  is defined as

$$g_{D^*D\pi}(q^2)(\epsilon_\lambda \cdot q) = \langle D(k)\pi(q) | D^*(p, \lambda) \rangle. \quad (6.22)$$

The isospin Clebsch-Gordon coefficient  $C$  has been factorized out. Here we take the coupling to represent the decay to a charged pion

$$g_{D^*D\pi} \equiv g_{D^{*+}D^0\pi^+}(m_{\pi^+}^2), \quad (6.23)$$

which according to (6.3), implies that  $C = 1$  for the charged pion and  $C = 1/2$  for the neutral. The pion momentum appearing in the phase space factor above is given by

$$|\vec{q}_\pi| = \frac{([m_{D^*}^2 - (m_D - m_\pi)^2][m_{D^*}^2 - (m_D + m_\pi)^2])^{1/2}}{2m_{D^*}} \quad (6.24)$$

with values given in Table 6.2.

The following is a detailed discussion of the theoretical basis and justification of our strategy. Readers familiar with the topic can jump ahead to the end of this subsection where the entire discussion is summarized in (6.50).

The coupling can be related to the form factors of the axial-vector current for on-shell charged pions. The idea is based on the Goldstone theorem, with pions identified as the Goldstone bosons associated with the *spontaneously broken approximate*  $SU(2)_L \times SU(2)_R$  *chiral symmetry*.

In the limit of exact chiral symmetry, i.e. massless  $u$  and  $d$  quarks, the Goldstone theorem implies [69], that there exist massless bosons which have non-vanishing overlap with the axial-vector current  $A^{\mu,a} = \bar{l}\gamma^\mu\gamma^5\tau^a l$  where  $\tau^a$  is the flavor operator. In reality the  $u$  and  $d$  quarks aren't massless. Therefore, the chiral symmetry is not exact. This means that the spontaneously broken *approximate* symmetry entails the existence of *approximately* massless Goldstone bosons. Pions have the correct quantum numbers to be candidates, and

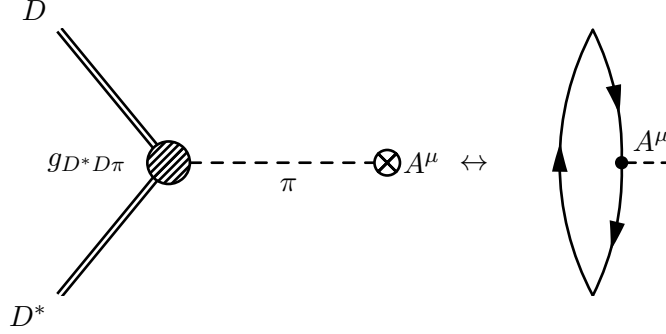


Figure 6.2: The pion coupling  $g_{D^*D\pi}$  is related to the form factors of the axial vector current.

are light on the hadronic scale. In fact they are the lightest of all hadrons. We shall see that  $m_\pi^2$  is proportional to light quark masses.

The overlap between the pion and the axial current then takes the form

$$\langle 0 | A^{\mu,a}(x) | \pi^b(q) \rangle = -iq^\mu f_\pi \delta^{ab} e^{-iq \cdot x} \quad (6.25)$$

where  $a$  and  $b$  are isospin indices and  $f_\pi$  is the charged pion decay constant,<sup>4</sup> which is determined from the weak decay  $\pi^+ \rightarrow l^+ \nu$ , and is measured to be 130.41(20)(3) MeV. The divergence of the axial current then gives

$$\langle 0 | \partial_\mu A^{\mu,a} | \pi^b \rangle = -f_\pi m_\pi^2 \delta^{ab}. \quad (6.26)$$

The generalization of this result for a matrix element of the axial divergence, into an operator relation

$$\partial_\mu A^{\mu,a} = f_\pi m_\pi^2 \pi^a(x), \quad (6.27)$$

where  $\pi^a(x)$  is an operator that creates a pion with normalization  $\langle \pi^a | \pi^b \rangle = \delta^{ab}$ , is known as the *partially conserved axial current* (PCAC) hypothesis.

It is crucial to understand that in and of itself, this assumption is meaningless. It can be shown [70, Chapter 10], that *any* operator with non-vanishing matrix element between the vacuum and a pion may be regarded as a pion field. So in that regard there's nothing particularly special about the axial current. The point of the PCAC assumption is not that  $\partial_\mu A^\mu$  couples to the pion. The important point is that the divergence of the axial-vector current is *small*, of order  $m_\pi^2$ , except near the pion pole where its smallness is compensated by the pole [69, Section 19.4]. As we move forward it'll become clear that this is precisely what's most important in this plan of attack.

<sup>4</sup> See [12, Section 19.3 and Problem 19.2] or [10, Section 10.4] for details on pion's weak decay and its decay constant.



In reality the chiral symmetry is *explicitly* broken as well as being *spontaneously* broken. This is due to the light quark mass terms such as  $m_q \bar{q}q$  in the Lagrangian. Therefore, it can be shown that (6.26) leads to

$$m_\pi^2 = (m_u + m_d) \frac{M^2}{f_\pi}. \quad (6.28)$$

where  $M^2 = \langle \bar{u}u + \bar{d}d \rangle / 2f_\pi$ , is an invariant quantity. The value of  $M$  is estimated to be of order 500 MeV [12], which implies that one needs an  $(m_u + m_d) \sim 10$  MeV, in order to give pion its observed mass of approximately 140 MeV. This is indeed a tiny perturbation on the scale of strong interactions of hadrons.

This is a remarkable result for a number of reasons. First, note that as promised earlier, we see that the *square* of the pion mass is proportional to the mass of the light quarks. Second, and more strikingly, the masses of the charged and the neutral pions turn out to be the same even though we've made no assumptions about the masses of the individual  $u$  and  $d$  quarks. The observed mass difference between the pion isotriplets is actually not only from the mass difference between the constituent light quarks, but from electromagnetism, and is successfully calculated from one-photon exchange interactions [69].

Third, and most importantly, note that isospin is a good symmetry not precisely because  $u$  and  $d$  have approximately equal masses, but because they are so light that their mass difference is also small as a result. In fact we do not make any assumptions about the relative sizes of  $m_u$  and  $m_d$ . As long as they're both small, inside hadrons they behave as approximately degenerate quarks, regardless of their relative size.

Our discussion so far suggests that both the axial current as well as its divergence may be used to create a pion in lieu of a pseudoscalar current one would normally use. What's more, a "polological" examination of any correlation function indicates that it can be well approximated by contributions from a single pole in the vicinity of that pole, provided that the operators inside the correlation function have non-zero matrix elements with the one-particle state associated with it.

Applied to the axial current, this implies that near the pion pole we have

$$\int_x e^{-iq \cdot x} \langle T \{ A^\mu(x) \dots \} \rangle \rightarrow \frac{iq^\mu}{q^2 - m_\pi^2} \times \langle 0 | A^\mu | \pi(q) \rangle \langle \pi(q) | T \{ \dots \} | 0 \rangle \delta^4(q + \dots). \quad (6.29)$$

where  $T$  is the time ordering operator and  $(\dots)$  stand for an arbitrary number of operators which have a combined non-zero overlap with pion. For a proof of this theorem see [70, Chapter 10]. This is the basis for the famous LSZ reduction formula<sup>5</sup> that makes a

---

<sup>5</sup> Named after three German physicists Harry Lehmann, Kurt Symanzik and Wolfhart Zimmermann [71].

connection between  $S$ -matrix elements and correlation functions:

$$N\text{-point correlator} \underset{q^2 \rightarrow m^2}{\sim} \prod \left( \frac{i\sqrt{Z}}{q^2 - m^2} \right) \times (S\text{-matrix element}). \quad (6.30)$$

Here  $Z$  is the wavefunction renormalization factor. This is just like the usual perturbative Feynman diagram prescription for computing the  $S$ -matrix for the emission of a particle except for the additional *renormalization* factor for the on-shell particle. Let us re-emphasize that the particle with mass  $m$  in this relation need *not* correspond to an elementary field that appears in the Lagrangian and which directly enters in a single Feynman diagram. It can also be a composite particle which couples to operators in the correlation function and arises from an infinite sum of diagrams. This is a *non-perturbative* result.

Stated in words, this theorem spells out instructions on how to calculate an  $S$ -matrix element: compute an appropriate correlation function, look for the region in momentum space where all external particles are on-shell, go to the pole and strip away the propagator. So that's what we're going to do next. We will omit the wavefunction  $Z$  factor of the external particles in the rest of our discussion since in the end they are absorbed into overlap parameters of our fit functions which will be divided out and therefore won't affect our final results.

The pion reduction of the axial current then gives

$$\int_x e^{iq \cdot x} \langle D(k) | \pi(x) | D^*(p, \lambda) \rangle = \frac{-i}{m_\pi^2 - q^2} \langle D(k) \pi(q) | D^*(p, \lambda) \rangle. \quad (6.31)$$

Using the PCAC relation (6.27), or equivalently

$$\pi(x) = \frac{1}{f_\pi m_\pi^2} \partial_\mu A^\mu(x) \quad (6.32)$$

we have

$$\frac{-i f_\pi m_\pi^2}{m_\pi^2 - q^2} \langle D(k) \pi(q) | D^*(p, \lambda) \rangle \simeq \langle D(k) | \partial_\mu A^\mu | D^*(p, \lambda) \rangle. \quad (6.33)$$

The  $S$ -matrix element of our interest which contains the pion coupling, is thus related to the matrix element of the axial current between the  $D^*$  and  $D$ , near the pion pole:

$$g_{D^* D \pi}(q^2) (\epsilon_\lambda \cdot q) = q_\mu \frac{m_\pi^2 - q^2}{f_\pi m_\pi^2} \langle D(k) | A^\mu | D^*(p, \lambda) \rangle. \quad (6.34)$$

The axial matrix element is expressed in terms of three form factors

$$\begin{aligned}
\langle D(k)|A^\mu|D^*(p,\lambda)\rangle &= 2m_{D^*}F_0(q^2)\frac{\epsilon_\lambda\cdot q}{q^2}q^\mu \\
&+ (m_{D^*}+m_D)F_1(q^2)\left(\epsilon_\lambda^\mu-\frac{\epsilon_\lambda\cdot q}{q^2}q^\mu\right) \\
&+ F_2(q^2)\frac{\epsilon_\lambda\cdot q}{m_{D^*}+m_D}\left(p^\mu+k^\mu-\frac{m_{D^*}^2-m_D^2}{q^2}q^\mu\right),
\end{aligned}
\tag{6.35}$$

where  $F_{0,1,2}(q^2)$  are Lorentz invariant functions of  $q^2$ . This is the standard parameterization used in the literature, whose specific form one may attempt to justify as follows.

The left hand side is a 4-vector. We have three independent 4-vectors on the roster to use:  $q^\mu$ ,  $\epsilon_\lambda^\mu$  and  $(p+k)^\mu$ ; hence, three form factors. Note that thanks to momentum conservation  $p=q+k$ , only two of the three momenta are independent. According to (6.25), the axial current's overlap with a one-pion state is proportional to the momentum  $q^\mu$ , which motivates one to choose it as one of the two independent momenta. This leaves  $p+k$  as the other independent 4-momentum. This can be seen from

$$(p+k)\cdot q = m_{D^*}^2 - m_D^2, \tag{6.36}$$

where we've used the fact that  $|D^*(p,\lambda)\rangle$  and  $|D(k)\rangle$  represent on-shell states. The mass-dimensioned factors  $2m_{D^*}$  and  $(m_{D^*}+m_D)$  in front are there to make the form factors dimensionless. The  $(\epsilon_\lambda\cdot q)$  factors in the  $F_0$  and  $F_2$  terms make those terms' invariant dependence on the polarization vector of  $D^*$  explicit. And finally, this parameterization has elected to make the  $F_1$  and  $F_2$  terms perpendicular to  $q$  by projecting out  $\epsilon_\lambda$  and  $(p+k)$ 's components along  $q$ . This will pack all contributions of the divergence of the axial current into  $F_0$ , at the expense of scattering the pion overlap of the axial current itself across all three form factors.

Given this convention, let us now describe how the pion coupling can be extracted from the form factors. It will be instructive to first consider the chiral limit where the pion is massless and therefore the axial divergence vanishes. We have

$$q_\mu\langle D(k)|A^\mu|D^*(p,\lambda)\rangle = 0, \tag{6.37}$$

from which it would be a mistake to conclude that its form factors also vanish. In terms of the form factors this translates to

$$2m_{D^*}F_0(0)(\epsilon_\lambda\cdot q) = 0. \tag{6.38}$$

The pion reduction of the axial current itself gives

$$\langle D(k)|A^\mu|D^*(p, \lambda)\rangle = -\frac{q^\mu f_\pi}{q^2}\langle D(k)\pi(q)|D^*(p, \lambda)\rangle + \dots, \quad (6.39)$$

near the pion pole  $q^2 \sim 0$ , where  $(\dots)$  are terms that are negligible compared to the pole term. In terms of the form factors this is

$$\frac{(\epsilon_\lambda \cdot q)}{q^2} \left[ 2m_{D^*}F_0(q^2) - (m_{D^*} + m_D)F_1(q^2) - (m_{D^*} - m_D)F_2(q^2) \right] \rightarrow -\frac{f_\pi}{q^2}g_{D^*D\pi}(\epsilon_\lambda \cdot q). \quad (6.40)$$

Combined with (6.38), this gives

$$g_{D^*D\pi} = \frac{m_{D^*} + m_D}{f_\pi}F_1(0) + \frac{m_{D^*} - m_D}{f_\pi}F_2(0). \quad (6.41)$$

This shows that even though the divergence of the axial current is killed by pion's zero mass, its form factors are kept alive by its pole.<sup>6</sup> Therefore, in the limit of exact chiral symmetry, the pion coupling  $g_{D^*D\pi}(0)$  does not vanish as one might have worried otherwise.

Let us now get back to reality where the light quark mass is not zero. That is, the chiral symmetry is explicitly broken before being spontaneously broken. Therefore, instead of assuming that the divergence of the axial current is zero, one assumes that it is small, i.e. of order  $m_\pi^2$ , except near the pion pole where the smallness is compensated by the pole. The equation (6.37) is then modified to

$$q_\mu \langle D(k)|A^\mu|D^*(p, \lambda)\rangle \simeq \frac{f_\pi m_\pi^2}{m_\pi^2 - q^2}g_{D^*D\pi}(\epsilon \cdot q). \quad (6.42)$$

Writing the left hand side in terms of the form factors then gives

$$2m_{D^*}F_0(q^2)(\epsilon_\lambda \cdot q) \simeq \frac{f_\pi m_\pi^2}{m_\pi^2 - q^2}g_{D^*D\pi}(\epsilon_\lambda \cdot q). \quad (6.43)$$

This relationship is valid near the pole, i.e. for  $q^2 \sim m_\pi^2$ . Therefore, at this stage it is not yet justified to take the limit of  $q^2 = 0$  and extrapolate to the on-shell momentum. The subdominant terms dropped from the right hand side of this relation come in suppressed by a relative factor of  $(m_\pi^2 - q^2)/m_\pi^2$  compared to the pole, and therefore can be ignored near it. Moving away from the pole all the way to  $q^2 = 0$ , however, the subdominant terms will no longer be suppressed and become relevant since the suppression (inverse pole) factor becomes equal to 1, which is not really much of a suppression. In fact we shall see shortly that the pion coupling is indeed extracted from the other non-pole form factors  $F_{1,2}$ .

In other words, (6.43) is a relation between two large quantities which live at the top of the pole and have steep momentum dependence. Both sides remain high so long as they're

---

<sup>6</sup> On this basis, the author proposes that the partially conserved currents be renamed to zombie currents.

around the pole. In order to estimate the coupling  $g_{D^*D\pi}$  by extrapolating from  $q^2 = 0$ , one must descend from the pole and identify the smooth terms' contributions.

Concretely, this is done by removing the pole from (6.43) through combining it with the pion reduction of the axial current just as was done above for the massless pion. That is, (6.40) is modified to

$$\frac{(\epsilon_\lambda \cdot q)}{q^2} \left[ 2m_{D^*}F_0(q^2) - (m_{D^*} + m_D)F_1(q^2) - (m_{D^*} - m_D)F_2(q^2) \right] \simeq \frac{f_\pi}{m_\pi^2 - q^2} g_{D^*D\pi} (\epsilon_\lambda \cdot q) \quad (6.44)$$

where the position of the pion pole on the right hand side is shifted from zero to that of a massive pion at  $q^2 = m_\pi^2$ . Note that the  $q^2$  at the bottom on the left hand side is unchanged in going from exact to approximate chiral symmetry, since it is just a parameterization convention that got in there as part of the 4-momentum projection explained above. It has nothing to do with poles.

Finally, combining the two pole-ful relations (6.43) and (6.44) for the form factors obtained from two separate LSZ reductions of the axial current and its divergence, removes the pole and gives us the coupling

$$g_{D^*D\pi}(q^2) \simeq \frac{m_{D^*} + m_D}{f_\pi} F_1(q^2) + \frac{m_{D^*} - m_D}{f_\pi} F_2(q^2). \quad (6.45)$$

This is now a pole-less, i.e. smooth, quantity that one may safely extrapolate down to  $q^2 = 0$ :

$$g_{D^*D\pi} = \frac{m_{D^*} + m_D}{f_\pi} F_1(0) + \frac{m_{D^*} - m_D}{f_\pi} F_2(0). \quad (6.46)$$

This is the analogue to the famous Goldberger-Treiman relation<sup>7</sup> for pion-nucleon coupling  $g_{\pi NN}$ , which is accurate to within 10% of experimental measurements [72]. This deviation is due to the error in extrapolating from off-shell momentum  $q^2 = 0$  to on-shell pion  $q^2 = m_\pi^2$ , and is a measure of the size of the effects of the chiral symmetry breaking terms.

The success of the Goldberger-Treiman relation is not surprising. The (6.45) function is roughly constant over the short range of  $q^2 = 0$  to  $m_\pi^2$ , since it has no one-pion pole and there's nothing else that can give it much variation. In fact, given its quantum numbers, a close look at the polography of  $\langle D(k) | A^\mu | D^*(p, \lambda) \rangle$  indicates that the next poles show up at the  $a_1(1260)$  and  $\pi(1300)$  mesons; long ways away.

The axial current  $A^\mu$  has parity  $P = -(-1)^\mu$ , using the shorthand  $(-1)^\mu \equiv 1$  for  $\mu = 0$  and  $(-1)^\mu \equiv -1$  for  $\mu = 1, 2, 3$ , charge conjugation  $C = +1$ , and isospin  $I = 1$ . Here it's sandwiched between a  $\langle D^0, 1/2(0^-) |$  and a  $| D^{*+}, 1/2(1^-) \rangle$ , where the applicable quantum numbers are expressed in the form of  $I^G(J^{PC})$ . This means that it can couple to  $1^-(0^-)$

<sup>7</sup> For a quick review of its derivation see [72] or [73]. Our derivation above follows the excellent treatment of the PCAC presented in [69], which contains a more careful, rigorous and detailed discussion.

mesons, i.e. pions and their heavy cousins  $\pi(1300)$ , and to  $1^-(1^+)$  mesons the lightest of which is the  $a_1(1260)$ .

The  $G$ -parity here is the useful version of charge conjugation for the light unflavored mesons. Only the neutral mesons are eigen-states of  $C$ , which makes it useful only for a few mesons. However, combining it with a rotation along the  $I_2$  axis in isospin space, will for instance take the  $\pi^+$  first to  $\pi^-$  and then back to itself. Isospin and charge conjugation are both preserved in strong interactions, making  $G$  a very useful quantum number. Its eigenvalues for members of an isomultiplet is given by

$$G = (-1)^J C \tag{6.47}$$

where  $C$  is the charge conjugation number of the neutral member of the multiplet.  $G$  violation rules out a pole at  $\rho(770)$  with  $1^+(1^{--})$ .

The coupling is now related to the form factors  $F_1$  and  $F_2$  of the axial current's matrix element at  $q^2 = 0$ . Note also that since the current can't couple to a massless particle there mustn't be a singularity on the right hand side of (6.35) at  $q^2 = 0$ . This imposes the following constraint between the three form factors

$$2m_{D^*}F_0(0) - (m_{D^*} + m_D)F_1(0) - (m_{D^*} - m_D)F_2(0) = 0, \tag{6.48}$$

which would ensure that the dangerous terms add up to cancel each other out. Thus, from (6.46) we get

$$g_{D^*D\pi} = \frac{2m_{D^*}}{f_\pi}F_0(0). \tag{6.49}$$

This turns out to be the  $q^2 = 0$  limit of (6.43) taking which we had initially warned against. Thus, the extrapolation we alluded to earlier is correct.

Why not work directly at  $q^2 = m_\pi^2$  and avoid extrapolation errors? In principle one can do that on the lattice with one caveat. The quantities directly computed on the lattice are the correlation functions. Thus, care must be taken in designing the calculation to ensure that they are not contaminated by  $F_0(q^2)$ . This may be done through choosing the right operators, polarization vectors and spatial orientations of momenta which together conspire to filter out the unwanted form factor. This is necessary because as shown above  $F_0$  has a steep momentum and light quark mass dependence and therefore a slight mistuning of parameters can result in large errors.

On the other hand, the success of the Goldberger-Treiman relation assures one of small extrapolation errors while also avoiding steep changes. Our other major reason is a practical one. Since we needed to tune the momentum to  $q^2 = 0$  for the radiative decay, this calculation also came along on the ride for free.

## Recap

$$\begin{aligned}
g_{D^*D\pi}(q^2) &\equiv \langle D\pi|D^* \rangle \xrightarrow{q^2 \rightarrow m_\pi^2} i(m_\pi^2 - q^2) \int_x e^{iq \cdot x} \langle D|\pi(x)|D^* \rangle \quad (\text{Polology + LSZ}) \\
&= q_\mu \frac{m_\pi^2 - q^2}{f_\pi m_p^2} \int_x e^{iq \cdot x} \langle D|A^\mu|D^* \rangle \quad (\text{Goldstone + PCAC}) \\
&\approx \frac{m_{D^*} + m_D}{f_\pi} F_1(0) + \frac{m_{D^*} - m_D}{f_\pi} F_2(0) \quad (\text{Polography} \Rightarrow \text{Goldberger-Treiman}) \\
&= \frac{2m_{D^*}}{f_\pi} F_0(0) \quad (\text{No massless pole}).
\end{aligned} \tag{6.50}$$

### 6.2.2 Lattice Correlation Functions

The correlation functions that are calculated for the pionic decay are similar to those computed for the radiative transition described in subsection 6.1.2, except that the vector current is swapped with appropriate axial currents. That is, the interpolating operators responsible for creating the vector and the pseudoscalar mesons are taken to be the same as those in the radiative calculation given in (6.14a) and (6.14c). This choice is due to a purely practical reason: it comes for free.

This is because, as shown in chapter 5, the calculation is designed in such a way that the current operator doesn't affect the simulation until after all the propagators are computed. This means that once the source and sink interpolating operators are fixed, basically all 3-point correlators allowed by the taste selection rules can be obtained for the cost of one. Thus, for any continuum current with a given spin all one needs to do is to find the right taste of the corresponding lattice current that would make the whole thing tasteless.

Here, the axial current  $A^\mu = \bar{l}\gamma^5\gamma^\mu l$ , is replacing the vector current (6.14b) whose taste signature is given by  $s_V = (0, 0, 1, 0)$  and which was specifically designed to form a tasteless trio with  $P$  and  $V$ . Thus,  $A$  must have the same taste as  $V$  had. This can be easily achieved. Total taste is determined by two factors: spin and point-splitting. Thus the discrepancy in their spin is simply compensated by an equal disparity in the point-splitting department to get its taste back to  $s_A = s_V$ .

At least two different polarizations of the axial current are needed in order to extract all three form factors in (6.35).  $A^0$  and  $A^3$  will do. The overall taste signature uniquely dictates two different shifts for each, given by

$$\begin{aligned}
A_0(z) &= \bar{u}(z \pm \hat{1})\gamma_5\gamma_0 d(z \pm \hat{3})|_{\text{symmetrized}}, \\
A_3(z) &= \bar{u}(z \pm \hat{0})\gamma_5\gamma_3 d(z \pm \hat{1})|_{\text{symmetrized}},
\end{aligned} \tag{6.51}$$

where the link variables are implicit. The shifts are chosen to be symmetrized. This is optional but useful nonetheless.

The following 3-point correlators are then calculated

$$C^0(t, T; \vec{q}) = \frac{1}{L^3} \sum_{\vec{x}, \vec{y}, \vec{z}} \langle P^\dagger(y) A^0(z) V_3(x) \rangle_\theta, \quad (6.52a)$$

$$C^3(t, T; \vec{q}) = \frac{1}{L^3} \sum_{\vec{x}, \vec{y}, \vec{z}} \langle P^\dagger(y) A^3(z) V_3(x) \rangle_\theta, \quad (6.52b)$$

where the subscript  $\theta$  indicates that the momentum is reached through the use of twisted boundary conditions for one of the three propagators involved in each correlation function in a similar fashion as that described in subsection 6.1.2.

## 6.3 Results

The previous two sections introduced the main physical processes of interest and described the lattice approach employed to attack each problem. We are now in a position to carry out the final analysis of the numerical data generated by the Monte Carlo simulation performed on the lattice. This section begins with a summary of this numerical data. The final results are then presented with a detailed description of the analysis.

All fits are done using the Bayesian curve fitting methods described in section 5.5. We explored several different fitting strategies for consistency checks and to ensure robust results. Our main criterion has been obtaining consistent results after convergence of the fit regardless of the specific fitting method used. We then settled on the most efficient method for the final fits and ran a large number of bootstraps. Results presented here are primarily obtained from chained marginalized fits to all relevant correlators with all correlations taken into account. All plots throughout this document have been produced using python’s *matplotlib* plotting library [74].

### 6.3.1 Lattice Calculation

This calculation is done on an ensemble of gauge field configuration generated by the MILC collaboration. The details of the ensemble are provided in Table 6.3. In order to probe the quark mass dependence of the radiative and pionic form factors using the HISQ formalism, the decay processes were simulated for a number of various heavy-light mesons, including both physical and fictitious states.

The “heavy” member of all mesons in this part of the study is the charm quark with a fixed mass of  $am_c = 0.63$  tuned to its physical value so as to give the correct mass for  $\eta_c$  [77]. For the “light” member we used four different masses the lightest of which is  $am_l = 0.0142$  tuned to pionically coincide with the sea light quark mass (see the caption of Table 6.3). This corresponds to a pion mass of  $\approx 370$  MeV [16]. Thus, using  $m_\pi^2 \propto m_l$  obtained in (6.28), the physical light quark mass can be roughly estimated to be  $am_l^{\text{phys.}} \approx 0.002$  on this lattice, making the simulated light quark about 7 times heavier than the physical one.



Table 6.3: Details of the “coarse” ensemble of  $N_f = 2 + 1$  asqtad gauge field configurations [16]. This ensemble has been generated and made publicly available by the MILC collaboration and consists of  $N_{\text{cf}} = 2259$  configurations with two degenerate flavors of light quarks (up and down) and one heavier flavor (strange) in the sea. The first column specifies the size of lattices where  $L_s$  and  $L_t$  denote the number of lattice sites along the spatial and temporal dimensions respectively. The lattice spacing  $a$  is used to convert lattice units to physical units. It is determined through computing its value in units of  $r_1$  given in column 2, with  $r_1 = 0.3133(23)$  fm [75]. Column 4 gives the sea quark masses in the MILC convention where  $u_0$  is the plaquette tadpole factor. Column 6 gives the mass of the HISQ valence light quark tuned to produce the same Goldstone pion mass as that obtained from an asqtad valence light quark with a mass equal to the mass of the sea light quark, and given in column 5 [76]. Columns 7 and 8 give the HISQ valence masses of the strange and charm tuned to their physical values [3, 77]. The last column is the HISQ coefficient of the Naik term for the charm quark.

$L_s^3 \times L_t$	$r_1/a$	$a$ (fm)	$au_0m_{l/s}^{\text{sea}}$	$L_s m_\pi$	$am_l$	$am_s$	$am_c$	$1 + \epsilon$
$20^3 \times 64$	2.618(3)	0.12	0.01/0.05	4.48	0.0142	0.0496	0.63	0.774

Table 6.4: Quark masses used in the simulation each in combination with a charm quark to form a meson. The bottom row gives the size of the twisting angle used for each mass combination to put the photon on shell. The  $l$ ,  $s$  and  $c$  quark masses are the same as those listed in Table 6.3 (see caption).  $D_{s/2}$  and  $D_{2s}$  are fictitious states corresponding to a charm bound to a fake quark with half and twice the strange mass respectively.

Label	$D$	$D_{s/2}$	$D_s$	$D_{2s}$	$J/\psi$
Mass	$am_l = 0.0142$	$am_{s/2} = 0.0248$	$am_s = 0.0496$	$am_{2s} = 0.0992$	$am_c = 0.63$
$ \vec{\theta} $	0.2225	0.2681	0.2698	0.2542	0.1913

The strange quark mass is also tuned to its physical value given in [3]. In addition, we use two other “light” masses at half and twice the strange mass. These are fictitious quarks and together with charm bound into fictitious  $D$  states, here labeled by  $D_{s/2}$  and  $D_{2s}$ . Table 6.4 lists the quark masses used in the simulation, as well as the twisting phases used to tune the momentum for each mass combination. In addition to heavy-light mesons, the radiative decay of the  $J/\psi$  has also been studied.

The 3-point correlators computed on the coarse ensemble with mass combinations specified in Table 6.4 are summarized in Table 6.5, together with the statistical information of each data set. Parent 2-point functions to all 3-point functions are included. Notice that  $C_\gamma^z$  and  $C^{0,x}$  are not listed since they vanish due to kinematical factors.

With the simulation data at hand, let us now turn to the analysis and extract the physical results. We begin with the radiative transition.

Table 6.5: Three-point correlators computed in the simulation. The first column introduces descriptive shorthand labels for later reference. Column 2 specifies the current inserted between the two mesons created by  $P$  and  $V$  defined earlier in (6.14). The third column gives the spatial orientation of the momentum transfer. Column 4 lists the size of each data set. The lower number of time sources in the first row refers to the  $J/\psi$  data set, which also has only one current insertion  $\mathcal{V}_2^c$ , and those in rows 2, 4 and 7 correspond to data sets with fake quarks. All correlators come in at two sink times and are accompanied by parent 2-point functions.

Correlator	Current	$\vec{\theta}/ \vec{\theta} $	$N_{\text{cf}} \times N_{\text{tsrc}}$	$T_{\text{sink}}$
$C_\gamma^x$	$\mathcal{V}_2^{c,l}$	(1, 0, 0)	$2256 \times 16(8)$	15,18
$C_\gamma^{xz}$	$\mathcal{V}_2^{c,l}$	(1, 0, 1)/ $\sqrt{2}$	$2256 \times 8(4)$	15,18
$C^{0,z}$	$A^0$	(0, 0, 1)	$2256 \times 16$	15,18
$C^{0,xz}$	$A^0$	(1, 0, 1)/ $\sqrt{2}$	$2256 \times 8(4)$	15,18
$C^{3,x}$	$A^3$	(1, 0, 0)	$2256 \times 16$	15,18
$C^{3,z}$	$A^3$	(0, 0, 1)	$2256 \times 16$	15,18
$C^{3,xz}$	$A^3$	(1, 0, 1)/ $\sqrt{2}$	$2256 \times 8(4)$	15,18

### 6.3.2 Radiative Transition

Recall from subsection 5.2.1 that 2-point correlation functions are related to meson energies through

$$G^{(2)}(t) = \sum_{i_n, i_o} a_{i_n}^2 \text{fn}(E_{i_n}, t) - \tilde{a}_{i_o}^2 \text{fo}(\tilde{E}_{i_o}, t), \quad (6.53)$$

where

$$\begin{aligned} \text{fn}(E, t) &\equiv e^{-Et} + e^{-E(Lt-t)}, \\ \text{fo}(E, t) &\equiv (-1)^t \text{fn}(E, t). \end{aligned} \quad (6.15)$$

The lowest normal (non-oscillating) state  $i_n = 0$  will then correspond to the meson of interest. Thus, energies are extracted by fitting (6.53) to the Monte Carlo data.

The fit function for a 3-point correlator computed using staggered quarks is given by

$$\begin{aligned} C^{(3)}(t, T) &= \sum_{i_n, j_n} a_{i_n} b_{j_n} V_{i_n j_n}^{nn} \text{fn}(E_{a, i_n}, T-t) \text{fn}(E_{b, j_n}, t) \\ &\quad - \sum_{i_n, j_o} a_{i_n} \tilde{b}_{j_o} V_{i_n j_o}^{no} \text{fn}(E_{a, i_n}, T-t) \text{fo}(\tilde{E}_{b, j_o}, t) \\ &\quad - \sum_{i_o, j_n} \tilde{a}_{i_o} b_{j_n} V_{i_o j_n}^{on} \text{fo}(\tilde{E}_{a, i_o}, T-t) \text{fn}(E_{b, j_n}, t) \\ &\quad + \sum_{i_o, j_o} \tilde{a}_{i_o} \tilde{b}_{j_o} V_{i_o j_o}^{oo} \text{fo}(\tilde{E}_{a, i_o}, T-t) \text{fo}(\tilde{E}_{b, j_o}, t). \end{aligned} \quad (6.54)$$

We saw in subsection 5.2.2 that this fit function is understood as the result of a spectral decomposition split up between the normal and oscillating states at each side of the current

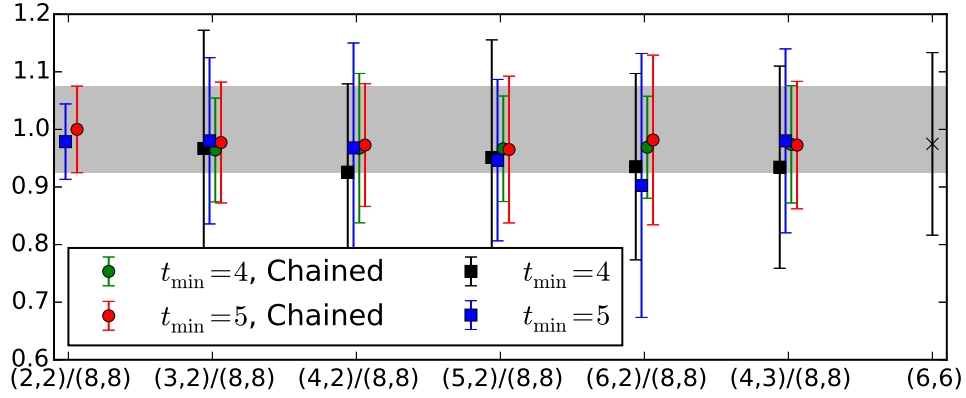


Figure 6.3: Comparison of various fitting strategies. The radiative matrix element from current insertion on the light quark in the  $D^{*+}$  meson is plotted for various methods and models. Marginalized fits with various number of terms retained with and without chaining to time ranges starting at  $t_{\min} = 4$  and 5 compared with a 6+6 standard fit to data from the shorter time range. Results are normalized by that obtained from a chained marginalized fit with  $t_{\min} = 5$  and 2 + 2 terms retained, for easier comparison. Error bars are obtained from bootstrapping. Results are clearly consistent. However, due to long propagation time to the sink excited states are suppressed and therefore higher number of terms become increasingly harder to fit. Hence, larger error bars reflecting more contribution from priors and less from numerical data. Chained marginalized fits produce better quality results more efficiently.

insertion time. Hence the four sums. They connect the before and after states via the  $V_{i_r j_s}^{rs}$  matrix elements where  $r$  and  $s$  superscripts indicate whether each state is of regular ( $n$ ) or opposite ( $o$ ) parity.

Here  $a$  and  $b$  are the overlaps between the interpolating operators and normal states with energies  $E_a$  and  $E_b$  at the sink and the source respectively. The overlap and energy parameters corresponding to oscillating states are distinguished by a tilde. Note that these are the same parameters as those appearing in the 2-point fit function (6.53) since the same interpolating operators  $P$  and  $V$  are used in the 2-point and 3-point correlators.

The fit function is actually parameterized in terms of  $\log(E_n - E_{n-1})$  and  $\log(a_n)$  for reasons explained in section 5.5. Reasonable priors with generous widths were chosen in our fits. Assigning priors to energy and overlap parameters is straightforward. For the ground state energy we use a rough estimate for the effective mass  $\frac{1}{2} \log(G(t)/G(t+2))$  from our 2-point correlator data at some intermediate time step where it has reached a plateau. Its width is set to 500 MeV.

For the level spacing between excited states  $E_n - E_{n-1}$ , the first oscillating state and the normal ground state  $\tilde{E}_0 - E_0$ , and between the oscillating tower  $\tilde{E}_n - \tilde{E}_{n-1}$  we use priors of  $600 \pm 300$  MeV. The overlaps were assigned priors of 0.5(5) to 0.6(6). These are well justified based on a wealth of past experimental and theoretical knowledge in  $D$  and charmonium

Table 6.6: Results for energies and masses of mesons obtained from fits to our 2-point functions given in lattice units. Columns 2 and 3 list masses of the vector and the pseudoscalar. Column 4 is the momentum transfer in the radiative decay carried by an on-shell photon and the pseudoscalar meson in the vector meson’s rest frame and is tuned using twisted boundary conditions. The last column is the energy of the pseudoscalar after the decay.

Mesons	$am_V$	$am_P$	$a \vec{q} $	$aE_P^0$
$D$	1.2549(40)	1.16513(41)	0.070	1.16723(41)
$D_{s/2}$	1.2661(23)	1.17713(27)	0.084	1.18014(27)
$D_s$	1.2930(15)	1.20550(15)	0.085	1.20848(15)
$D_{2s}$	1.34650(53)	1.26159(10)	0.080	1.26412(10)
$J/\psi, \eta_c$	1.878642(94)	1.817441(52)	0.060	1.818395(53)

spectroscopy. The prior widths are wide enough to ensure no region in the parameter space is excluded. They also prevent duplicate and superfluous states showing up in our fits. For the matrix elements  $V_{ij}$  we used priors with zero mean. Assigning the widths is slightly less obvious. Motivated by [4, 3], we chose widths in the range of 0.25–0.50.

We performed extensive empirical Bayes studies on our data sets to ensure appropriate priors were chosen. This was done for the prior widths of each of the three collective sets of parameters<sup>8</sup> corresponding to energies, overlaps and matrix elements by maximizing the logarithm of the Gaussian Bayes factor (the evidence). This is a useful cross check to verify that priors are appropriately assigned and are not inconsistent with the data. In some cases empirical Bayes suggested that widths as tight as 0.10 would maximize the  $\log(\text{GBF})$ . However, we refrained from tightening the constraints so aggressively in order to avoid biasing our error estimates. Although results did not depend strongly on prior widths of  $V_{ij}$ .

An SVD cut of  $10^{-3}$  or  $10^{-4}$  was used. We also found that while completely consistent with each other fits to data in the time range with a  $t_{\min} = 5$  generally produced slightly better  $\chi^2$  than with  $t_{\min} = 4$ . All error estimates are obtained from bootstrap analyses with at least  $N_{\text{bs}} = 500$  or higher. Figure 6.3 illustrates the robustness of our fits and consistency of results by comparing best fitted results for a matrix element obtained using various fitting strategies.

The model for 2-point correlator fits given in (6.53) is symmetrical around the lattice temporal mid-point  $L_t/2$ . However, due to statistical fluctuations the correlator is only symmetrical within statistical errors. We avoid potential additional uncertainties in our fit results due to lopsided correlators by folding them over unto themselves and fitting to the average  $(G(t) + G(L_t - t))/2$  with  $t \in [t_{\min}, L_t/2]$ . This also reduces the number of degrees of freedom by a factor of 2 thereby speeding up the fit.

<sup>8</sup> Not individual parameters. Tuning priors for each fit parameter separately using empirical Bayes can lead to nonsense results.

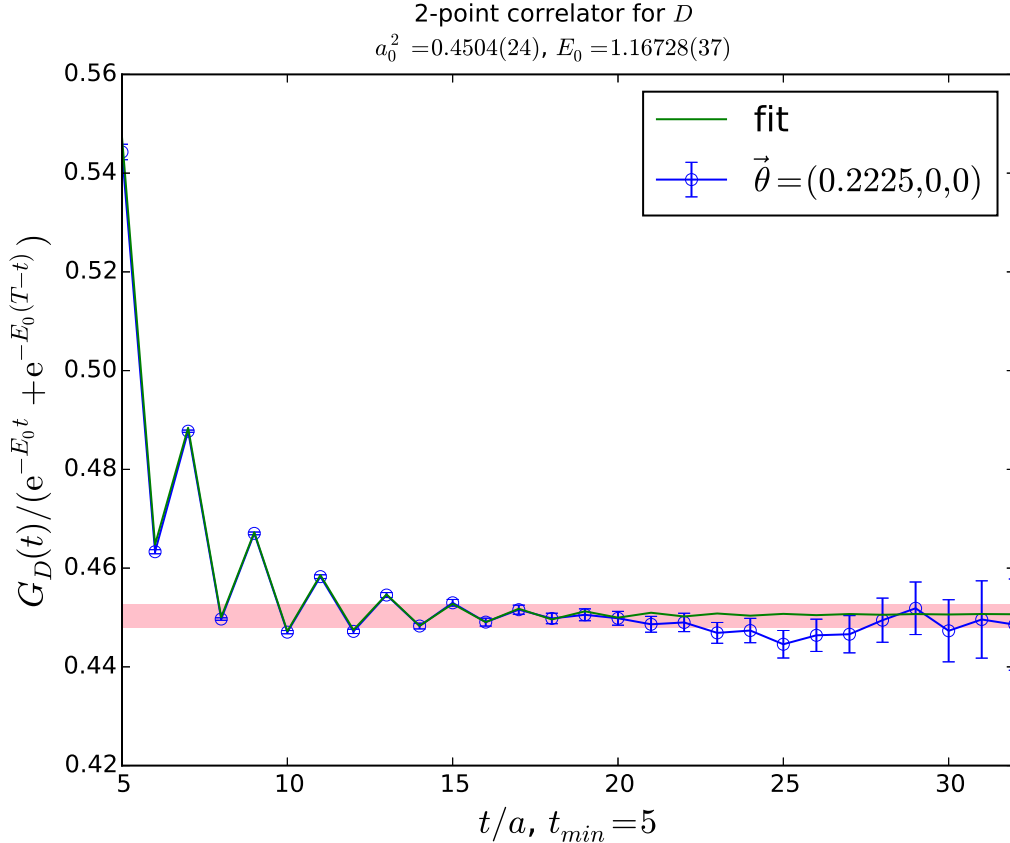


Figure 6.4: Fit to 2-point function data for the pseudoscalar  $D$  meson. The exponential fall-off of  $G(t)$  is largely canceled by dividing out the ground state’s time dependence. The presence of oscillating states with opposite parity (scalar mesons) is evident. Once higher energy states have died off the correlator is dominated by the ground state and the plotted ratio reaches a plateau that isolates the overlap  $a_0^2$  represented by the shaded band.

Table 6.6 lists our results for the energies in lattice units. Even though the mass results are presented in a separate table they have all been obtained from simultaneous fits to 2-point and 3-point functions together with the matrix elements. Our results are in excellent agreement with published studies of  $D_s$  [3] and charmonium [4] using HISQ.

Figure 6.4 provides a plot as an example that demonstrates the quality of our fits by showing an excellent agreement between the Monte Carlo 2-point function data for the pseudoscalar  $D$  meson and the fitted values overlaid on top of the data points. The effective mass plot for the same correlator is also shown in Figure 6.5 which demonstrates consistency with the best fitted ground state energy in the plateau region. While these plots correspond to our noisiest data sets since they contain the lightest light quarks among our correlators, they are typical of all our fits. Fits to other correlators exhibit the same qualitative features but have increasingly smaller error bars and better agreements. They also demonstrate that chaining and marginalization work well: they produce accurate results faster.

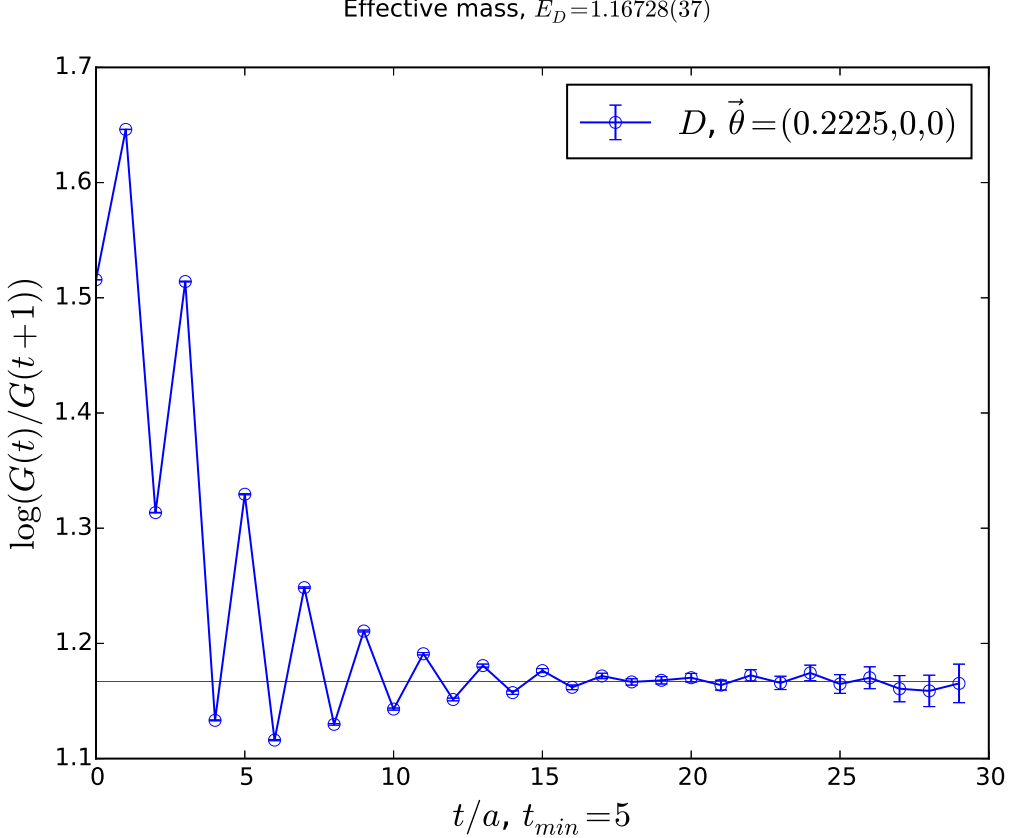


Figure 6.5: Effective mass plot for the pseudoscalar  $D$  meson 2-point function. The shaded band is the ground state energy and passes right through the data points that roughly approximate it in the plateau region. The narrow width of the band indicates small fit uncertainties obtained from bootstrap error analyses. The oscillation amplitude dies off at large time steps as expected.

The ground state mesons  $i_n = 0$  and  $j_n = 0$  correspond to  $|D(k)\rangle$  and  $|D^*(p, \lambda)\rangle$ . Adopting the relativistic normalization convention and following (5.33), the electromagnetic matrix element is then extracted from the fit through

$$V_{00}^{nn} = \frac{\langle D(k) | \mathcal{V}_2 | D^*(p, \lambda) \rangle}{2\sqrt{m_{D^*} E_D}}. \quad (6.55)$$

Using (6.5), the radiative form factor is therefore given by

$$\frac{V(0)}{\mathcal{Z}} = \frac{(m_{D^*} + m_D)}{2m_{D^*} q_x} 2\sqrt{m_{D^*} E_D} V_{00}^{nn}. \quad (6.56)$$

This form factor encapsulates the decay amplitude and is thus the quantity that our lattice simulation sought to examine.

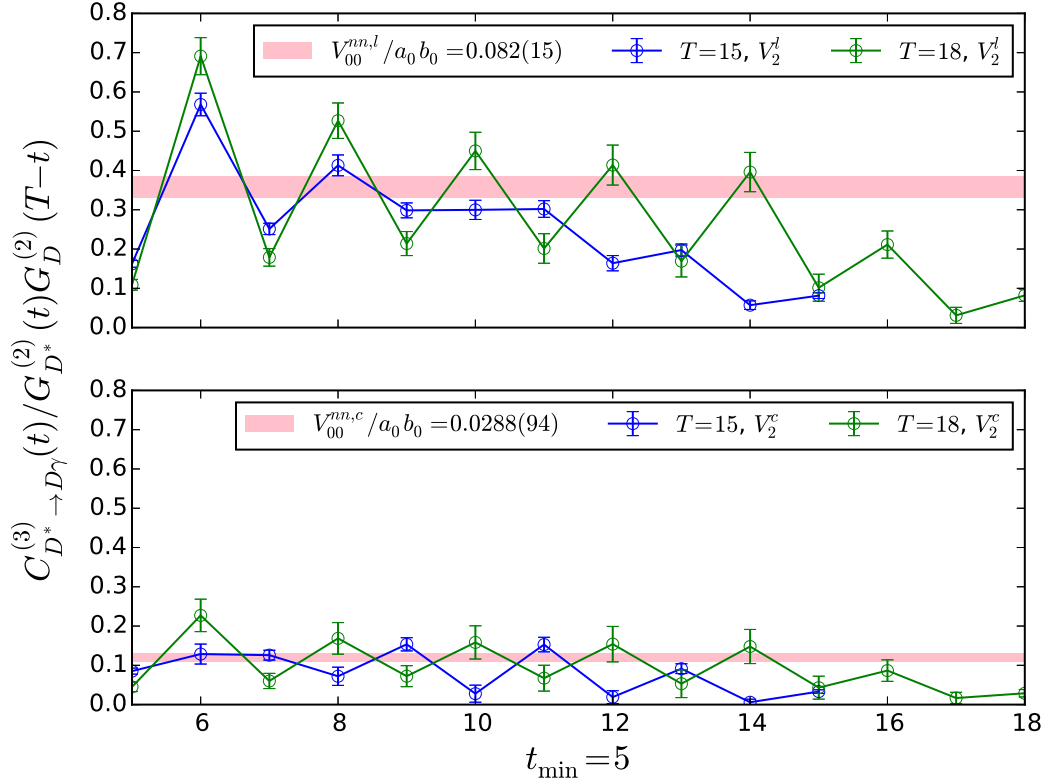


Figure 6.6: Ratios of 3-point to 2-point correlators plotted as a function of current insertion time. The product of the two 2-point correlators corresponding to the initial (vector) and final (pseudoscalar) mesons in the denominator divides out the dominant time dependence of the 3-point function, thereby roughly isolating  $V_{00}^{nn}/a_0 b_0$  whose fitted values and uncertainties are shown as shaded bands. The top panel is for insertion on light and the bottom on charm. Both plots are drawn on the same scale, but split up to disentangle and declutter.

Figure 6.6 shows ratios of 3-point correlators divided by appropriate products of parent 2-point correlators that take out the dominant time dependence due to ground state contributions to the models in (6.53) and (6.54), and isolate  $V_{00}^{nn}/a_0 b_0$ . Note that these 3-point correlators all involve a combined meson propagation of  $T = 15$  or  $18$  and therefore have highly suppressed contributions from excited states. Thus, while a larger number of terms are normally retained in marginalized fits to 2-point correlators we find that retaining  $2 + 2$  terms was sufficient and produced accurate results.

Table 6.7 lists our raw fit results for the  $V_{00}^{nn}$  matrix elements for current insertion on each quark line together with the corresponding form factors as well as appropriate combinations pertaining to the charged and neutral mesons. The current renormalization matching factors  $\mathcal{Z}_{cc} = 0.9894(8)$  for charm and  $\mathcal{Z}_{ss} = 1.003(9)$  for strange were computed

Table 6.7: Fit results for radiative transition matrix elements and form factors of charmed mesons. The first column is the light quark mass. Columns 2 and 3 list our fit results for the matrix elements corresponding to current insertion on light and charm respectively. Columns 4 and 5 convert them into photon coupling form factors. These are then combined according to  $V^+(0) = (V_l(0) - 2V_c(0))/3$  and  $V^0(0) = (2V_l(0) + 2V_c(0))/3$  to give the charged and neutral meson's radiative form factors. Some results from other sources are provided for comparison when available. Empty cells correspond to quantities that are either not applicable or not available in external sources.

$am_l$	$V_{00}^{nn,l}$	$V_{00}^{nn,c}$	$V_l(0)/\mathcal{Z}_{ll}$	$V_c(0)/\mathcal{Z}_{cc}$	$V^+(0)$	$V^0(0)$
0.0142	0.1044(78)	0.0348(31)	3.49(26)	1.16(10)	0.39(11)	3.10(19)
[8, $\beta=5.29$ ]					0.1(1.4)	5.3(2.3)
[8, $\beta=5.40$ ]					0.4(6)	3.9(1.1)
Expt. [1]					0.89(11)	< 36
0.0248	0.1194(46)	0.0425(25)	3.34(13)	1.189(69)	0.321(64)	3.021(96)
0.0496	0.1127(23)	0.0443(11)	3.213(64)	1.262(32)	0.229(29)	2.984(50)
[3]	–	–	3.24(12)	1.33(6)	0.203(40)	–
Expt. [1]					< 35	–
0.0992	0.0932(12)	0.04151(91)	2.945(37)	1.312(29)	0.107(20)	2.838(35)
$am_c = 0.63$	–	0.03179(15)	–	1.9232(92)	–	–

by the authors of [3]. Each deviates from 1 by only about 1%. Thus, bearing in mind the size of our systematics we can safely ignore these factors in the rest of this thesis.

One can then convert this form factor into the physical decay width using the phase space relationship (6.9) given at the beginning of this chapter and reproduced here

$$\Gamma(D^* \rightarrow D\gamma) = \alpha_{\text{QED}} \frac{4|\vec{q}|^3}{3(m_{D^*} + m_D)^2} |V(0)|^2.$$

An ambiguity arises as to what values one should use in the phase space factor in going from  $|V(0)|^2$  obtained on the lattice to the physical width in the continuum. Usually, lattice estimates of hadronic masses and momenta differ from the measured values for the same quantities due to a number of different reasons including discretization errors, working at a larger than physical light quark mass and imperfect tuning of simulation parameters.

The combined 5 powers of  $|\vec{q}|^3$  and  $(m_{D^*} + m_D)^2$  in this conversion, can compound quickly and turn a slight mismatch in each quantity into wildly different estimates for the decay width. The ambiguity goes away, however, as one focuses on the central quantity of interest. What's being probed here is the coupling of photon to a meson bound state of two quarks while causing a spin flip inside the meson. This interaction is independent of the phase space and is captured by the form factor, which was specifically made dimensionless in order to have weak mass and phase space dependence.



Table 6.8: Results for radiative decay widths of charged and neutral  $D$  mesons. <sup>†</sup>The width reported in [8] for the charged meson’s decay was 0.8(7) keV which was inconsistent with the rest of their results. We suspect that it was likely a typo. In order to avoid misrepresenting their work while staying faithful to it, here we have quoted the width we calculated from their coupling which is listed in column 4.

Transition	Ref.	Method	$g$ (GeV) <sup>-1</sup>	$\Gamma$ (keV)
$D^{*+} \rightarrow D^+\gamma$	self	HISQ	0.200(58)	0.25(15)
	[8]	Wilson	0.2(3)	0.2(7) <sup>†</sup>
	[1, 11]	Expt.	0.461(57)	1.33(33)
$D^{*0} \rightarrow D^0\gamma$	self	HISQ	1.598(96)	15.6(1.9)
	[8]	Wilson	2.0(6)	27(14)
	[1]	Expt.	< 18.3	< 2.1 MeV

Therefore, although results are in the end converted into decay widths for easy and complete comparison, we focus on the form factors. Thus, when available, physical values are used in (6.9) to obtain the “experimental” value of the form factor  $V(0)_{\text{expt.}}$  which is then compared with the lattice result, thereby isolating it from unwanted errors.

In contrast, in going from the matrix element  $V_{00}^{nn}$  to form factors we use lattice values. Importantly, the explicit momentum factor  $q_x$  in (6.56) used in the conversion must be the lattice value used in the simulation.

Table 6.8 lists our results converted into the dimensionful photon coupling  $g_{D^*D\gamma}$  and the radiative decay width  $\Gamma(D^* \rightarrow D\gamma)$  of both charged and neutral  $D^*$  mesons along with available experimental data and lattice results obtained using different formalisms. In addition, Table 6.9 presents our results for the radiative decay of the charmed strange  $D_s^* \rightarrow D_s\gamma$  as well as that for the charmonium  $J/\psi \rightarrow \eta_c$  along with available measurements and other calculations as a sanity check.

We find that when combined to form the total form factor  $V^+(0)$  for the charged charmed meson, the individual form factors  $V_l(0)$  and  $V_c(0)$  do in fact nearly but not quite cancel each other out for all four light quark masses studies in this work. Furthermore, given our error analysis this fine cancellation is very well resolved. That is, our result is highly suppressed and yet clearly differs from zero by a statistically significant amount.

Our final result for the radiative form factor of the charged charm-light meson at our lightest light quark mass is

$$V^+(0) = 0.39(11). \tag{6.57}$$

The experimental form factor obtained from the measured decay rate divided by kinematical phase space factors is estimated to be  $V_{\text{expt.}}^+(0) = 0.89(11)$ . This can be considered a remarkable success for the HISQ formalism. The suppression is clearly demonstrated in the

Table 6.9: Results for the radiative decay widths of  $D_s^*$  and  $J/\psi$  included in this study as a sanity check. Our results compare well with published theoretical studies and in the case of charmonium are not inconsistent with the experimental value. The latt. and phys. superscripts pertain to the choice of lattice or physical values used in the phase space factor in each reference when applicable.

Transition	Ref.	Method	$\Gamma$ (keV)
$D_s^{*+} \rightarrow D_s^+ \gamma$	self	HISQ	0.083(21)
	[3]	HISQ	0.066(26)
	[1]	Expt.	$< 1.9$ MeV
$J/\psi \rightarrow \eta_c \gamma$	self	HISQ	2.383(49)
	[4]	HISQ	2.49(19)
	[6]	Twisted mass	2.64(11)(3)
	[5]	Quenched domain-wall	2.57(11) <sup>phys.</sup> 1.61(7) <sup>latt.</sup>
	[78]	Quenched clover	2.51(8) <sup>phys.</sup>
	[7]	Twisted mass	2.84(6) <sup>phys.</sup> 1.99(6) <sup>latt.</sup>
	[79]	Expt.	1.84(29)
	[1]	Expt.	1.58(37)

ratio between the charged and the neutral  $D$  mesons radiative form factor. We find

$$\frac{V^+(0)}{V^0(0)} = 0.126(36). \quad (6.58)$$

Not only did we accomplish to resolve the near cancellation from zero by a statistically significant amount in our simulations, our statistical errors are comparable with experimental measurements. As seen in Table 6.7 and Table 6.8, the Wilson method used in [8] resulted in errors larger than 100%.

Figure 6.7 shows the radiative form factor of the charged charm-light with various *light* quark masses ranging from our lightest at  $m_l \approx m_s/4 \approx 7m_{u/d}^{\text{phys.}}$  up to  $2m_s$  plotted as a function of pion mass, i.e. the square root of the quark mass  $\sqrt{am_l}$  which is packed with physical insight into heavy-light mesons. Notice in particular the perfect agreement between our results for  $D_s^*$  and those obtained in [3]. We used different tastes for our interpolating operators than those used in [3] and our radiative form factors are in excellent agreement with theirs, both listed in Table 6.7.

Given that our goal here is not a couple percent precision calculation due to inherent systematics of this process, we do not include a full-fledged chiral extrapolation analysis. Nevertheless, in order to shed some light on the quality of our results compared with physical

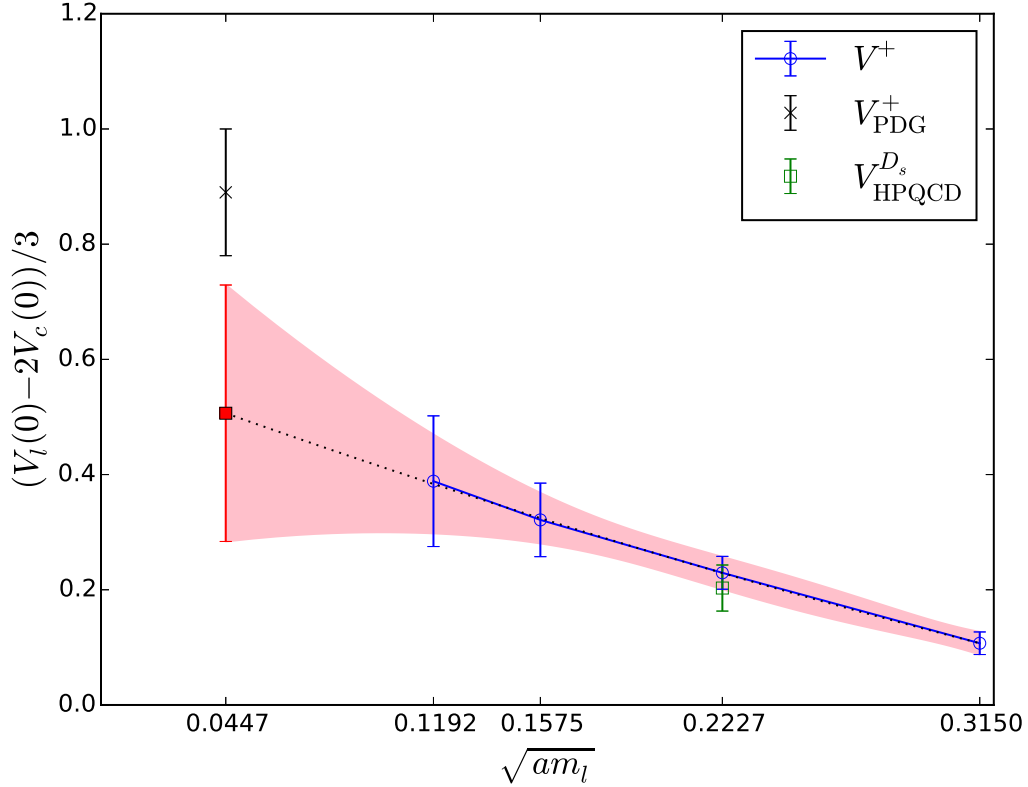


Figure 6.7: Radiative transition form factor  $V^+(0)$  of the charged charm-light meson at various light quark masses plotted as a function of the corresponding pion mass, or equivalently  $\sqrt{am_l}$ . Blue circles represent our results. The green square at the strange mass is the HPQCD collaboration’s result for the radiative decay of the  $D_s^*$  using HISQ and published in [3] while this work was in progress. The black cross is the experimental form factor at the physical light quark mass inferred from the measured branching ratio and total decay width of the  $D^{*+}$  taken from [1] and with the kinematical phase space factors stripped off according to (6.9). A simple quadratic extrapolation in terms of  $\sqrt{am_l}$  is plotted to guide the eye. The dotted line is the fit function and the shaded area its uncertainty. The red filled square is the form factor extrapolated to the physical point.

observations, while we do not use this extrapolated value as our final result, it is included here as a visual approximation of where the form factor is headed. Given the upward trend, the distance to the physical point and the size of theoretical and experimental error bars, our results suggest a  $2\sigma$  agreement upon extrapolation. This will be discussed further in chapter 7.

### 6.3.3 Pionic Decay

There are three form factors in the axial correlators as defined in (6.35). Given the lattice correlators listed in Table 6.5 the form factors are extracted as follows. The kinematical configuration of the lattice calculation is summarized as

$$\begin{aligned}\epsilon_\lambda &= \hat{3}, \\ p &= (m_{D^*}, \vec{0}), \\ k &= (E_D^\theta, -\vec{q}), \\ q &= (m_{D^*} - E_D^\theta, \vec{q}),\end{aligned}\tag{6.59}$$

with three different spatial orientations for  $\vec{q}$  tagged by self explanatory labels:  $x$ ,  $z$  and  $xz$ .

The divergence of the axial current is

$$\langle D(k) | q_\mu A^\mu | D^*(p, \lambda) \rangle = 2m_{D^*} F_0(0) (\epsilon_\lambda \cdot q).\tag{6.60}$$

which directly gives  $F_0(0)$ . Thus, fitting (6.54) to the linear combination

$$C^{\text{div}} \equiv q^0 C^{0,z} - q^3 C^{3,z}\tag{6.61}$$

made out of correlators computed with momentum purely along  $z$  gives

$$F_0(0) = -\frac{2\sqrt{m_{D^*} E_D}}{2m_{D^*} q_z} V_{00}^{nn,\text{div}}.\tag{6.62}$$

The value used for  $q^0 = m_{D^*} - E_D$  in this linear combination is obtained from fits to 2-point functions. Note also that according to (6.59), we have  $\epsilon_\lambda \cdot q = -q_z$ .

The  $F_1(0)$  form factor is directly obtained from the  $C^{3,x}$  correlator

$$F_1(0) = \frac{2\sqrt{m_{D^*} E_D}}{m_{D^*} + m_D} V_{00}^{nn,3x}.\tag{6.63}$$

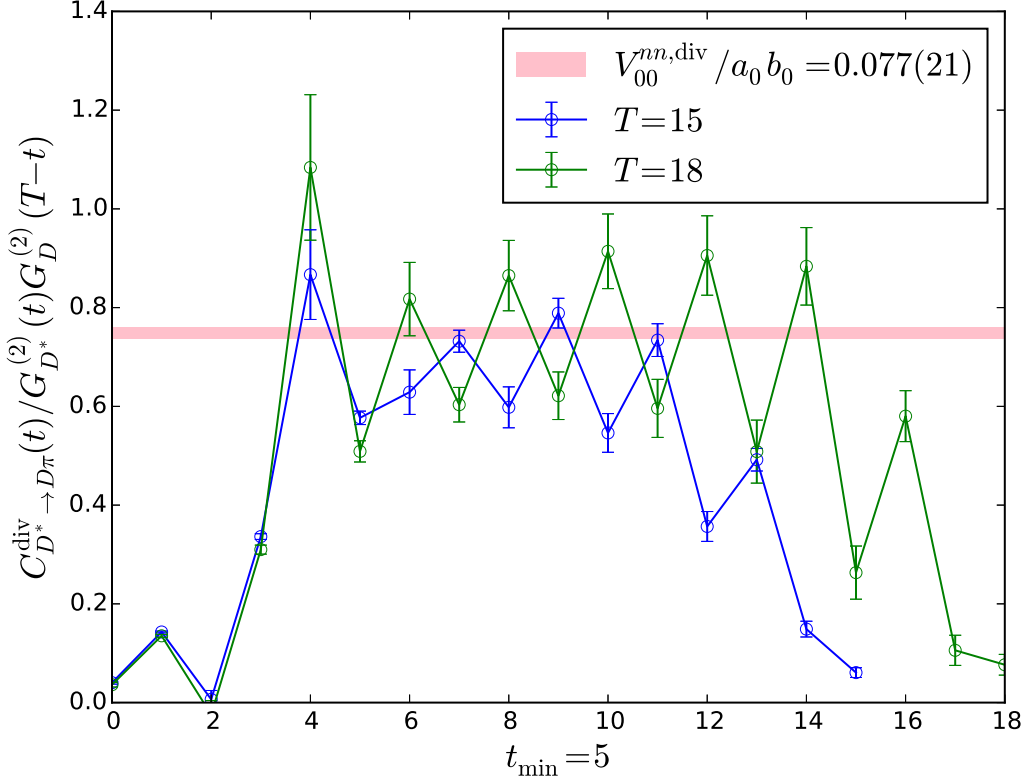


Figure 6.8: Ratio of 3-point to 2-point axial correlators as a of current insertion time. Dominant time dependence is divided out isolating  $V_{00}^{nn}/a_0 b_0$ . Other pionic correlators exhibit similar qualitative behaviors.

Extracting  $F_2(0)$  is a bit more tricky. Separating  $q^\mu$  terms we have

$$\begin{aligned} \langle D|A^0|D^* \rangle &= F_2(0) \frac{(\epsilon_\lambda \cdot q)}{m_{D^*} + m_D} (m_{D^*} + E_D) + (\dots) \frac{\epsilon_\lambda \cdot q}{q^2} q^0, \\ \langle D|A^3|D^* \rangle &= (m_{D^*} + m_D) F_1(0) + F_2(0) \frac{(\epsilon_\lambda \cdot q)}{m_{D^*} + m_D} (-q^3) + (\dots) \frac{\epsilon_\lambda \cdot q}{q^2} q^3. \end{aligned}$$

Thus, one can eliminate all  $q^\mu$  terms from the right hand side of (6.35), by cross multiplying opposite components of the momentum and the axial correlator and subtract them to form the linear combination  $q^0 A^3 - q^3 A^0$  which then takes the form

$$\langle D(k)|(q^0 A^3 - q^3 A^0)|D^*(p, \lambda) \rangle = q^0 (m_{D^*} + m_D) F_1(0) - \frac{2m_{D^*} q_z (\epsilon_\lambda \cdot q)}{m_{D^*} + m_D} F_2(0). \quad (6.64)$$

One can then remove the  $F_1(0)$  from this combination using  $C^{3,x}$ :

$$C^{F_2} \equiv q^0 C^3 - q^3 C^0 - q^0 C^{3,x} \quad (6.65)$$

Table 6.10: Fit results for axial matrix elements and pionic form factors. Note that as discussed before the form factors computed at the strange quark mass does not correspond to the actual pionic decay of  $D_s^*$ .

$am_l$	$V_{00}^{nn,\text{div}}$	$V_{00}^{nn,F_1}$	$V_{00}^{nn,F_2}$	$F_0(0)$	$F_1(0)$	$F_2(0)$
0.0142	0.2197(37)	0.2250(28)	-0.056(63)	0.5323(91)	0.5450(69)	-0.14(15)
0.0248	0.2216(19)	0.2303(20)	0.002(34)	0.5421(46)	0.5636(50)	0.006(82)
0.0496	0.2332(11)	0.23621(88)	0.188(17)	0.5835(27)	0.5909(22)	0.470(44)
0.0992	0.24745(58)	0.24913(57)	0.186(13)	0.6461(15)	0.6505(15)	0.487(33)

fitting which gives the third form factor

$$F_2(0) = \frac{m_{D^*} + m_D}{2m_{D^*}q_z^2} 2\sqrt{m_{D^*}E_D} V_{00}^{nn,F_2}. \quad (6.66)$$

Note that for a perfectly tuned momentum where  $q^0 = q^3 = \frac{m_{D^*}^2 - m_D^2}{2m_{D^*}}$ , the right hand side of (6.64) would have nicely simplified to

$$q^0(m_{D^*} + m_D)F_1(0) + q^3(m_{D^*} - m_D)F_2(0) \quad (6.67)$$

which demonstrates that as we saw throughout subsection 6.2.1,  $F_1(0)$  and  $F_2(0)$  always show up with a factor of  $m_{D^*} + m_D$  and  $m_{D^*} - m_D$  respectively. However,  $|\vec{q}|$  is not perfectly tuned. So, in order to avoid unnecessarily introducing additional errors due to mistuning, one should stay true to the  $q_z$  parameter that was used in the simulation in (6.66) to get  $F_2(0)$ . Either way, the coefficient is small and therefore the contribution of the dimensionless  $F_2$  form factor to the pion coupling given by (6.46), is suppressed relative to that from  $F_1$ .

Our fitting procedure is the same as that described above for the radiative transition. Figure 6.8 shows a 3-point to 2-point ratio plot for the  $C^{\text{div}}$  correlator similar to those in Figure 6.6. Our fit results for the raw matrix elements and the corresponding form factors are listed in Table 6.10. We observe that  $F_2(0)$  at our two lightest masses comes out already suppressed compared to  $F_1(0)$ . This suppression is further exacerbated by the relative kinematical coefficient of  $(m_{D^*} - m_D)/(m_{D^*} + m_D)$ , which is consistent with similar findings in other studies.

Recall from (6.50) in subsection 6.2.1 that the pion coupling  $g_{D^*D\pi}$  can be accessed at  $q^2 = 0$  two different ways; one using  $F_0(0)$  and the other using a combination of  $F_1(0)$  and  $F_2(0)$ . This theoretical expectation is verified by our results. This is demonstrated in Figure 6.9 where the two independent estimates of the pion coupling almost lie on top of each other all the way up to twice the strange quark mass. Figure 6.10 consolidates these independent estimates into one by simply averaging them and shows a quadratic

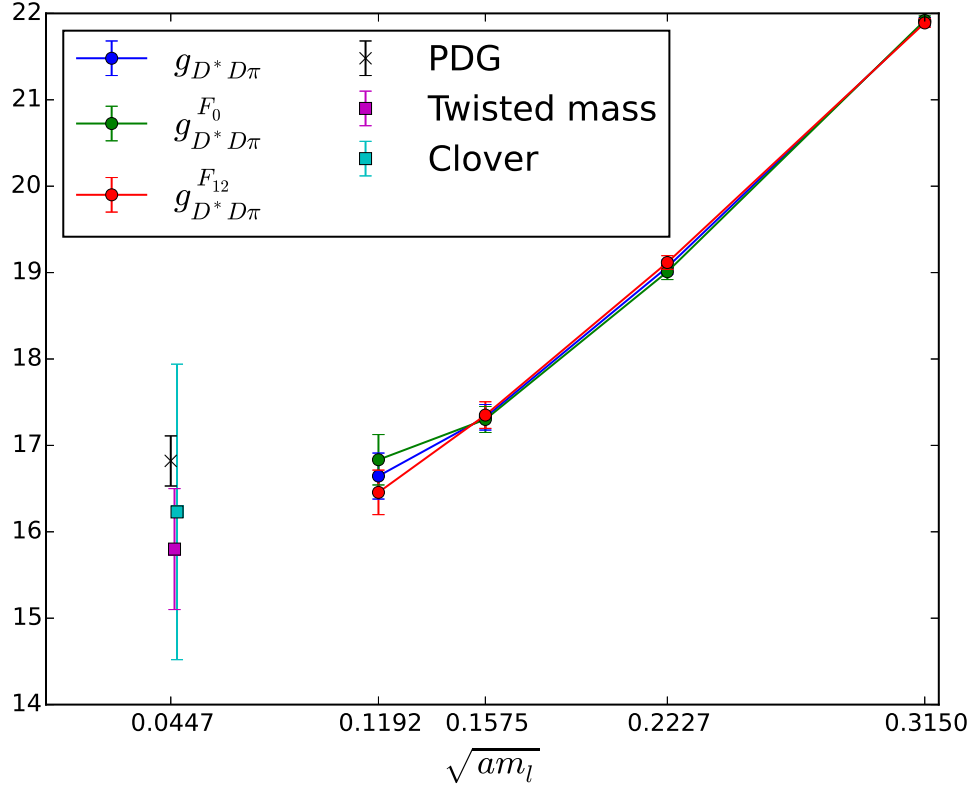


Figure 6.9: Pion coupling of the charged  $D^{*+}$  meson at various light quark masses plotted as a function of pion mass, or equivalently  $\sqrt{am_l}$ . The green and red circles are extracted from the  $F_0(0)$  form factor and the combination of  $F_1(0)$  and  $F_2(0)$  respectively, as clearly labeled, and perfectly agree with each other within errors. The blue circles are the average of the two and taken as our best estimate for  $g_{D^*D\pi}$ . The black cross is the observed coupling [1] and the squares are theoretical results obtained in other studies [67, 68] using different lattice formalisms.

extrapolation in  $\sqrt{am_l}$  to the physical point only as a visual aid to see where the coupling might be headed.

The pion coupling of a heavy-light meson denoted here by  $g_{D^*D\pi}$  as defined in (6.22) at the beginning of section 6.2, is often in the literature converted into  $g_c$  given by

$$g_{D^*D\pi} \equiv \frac{2\sqrt{m_{D^*}m_D}}{f_\pi} g_c. \quad (6.68)$$

This is a convenient convention in the heavy quark limit [67] and therefore is included here for easy comparison with related studies. The subscript  $c$  is to distinguish the charm-light pion coupling from that of bottom-light which corresponds to  $g_{B^*B\pi}$ .

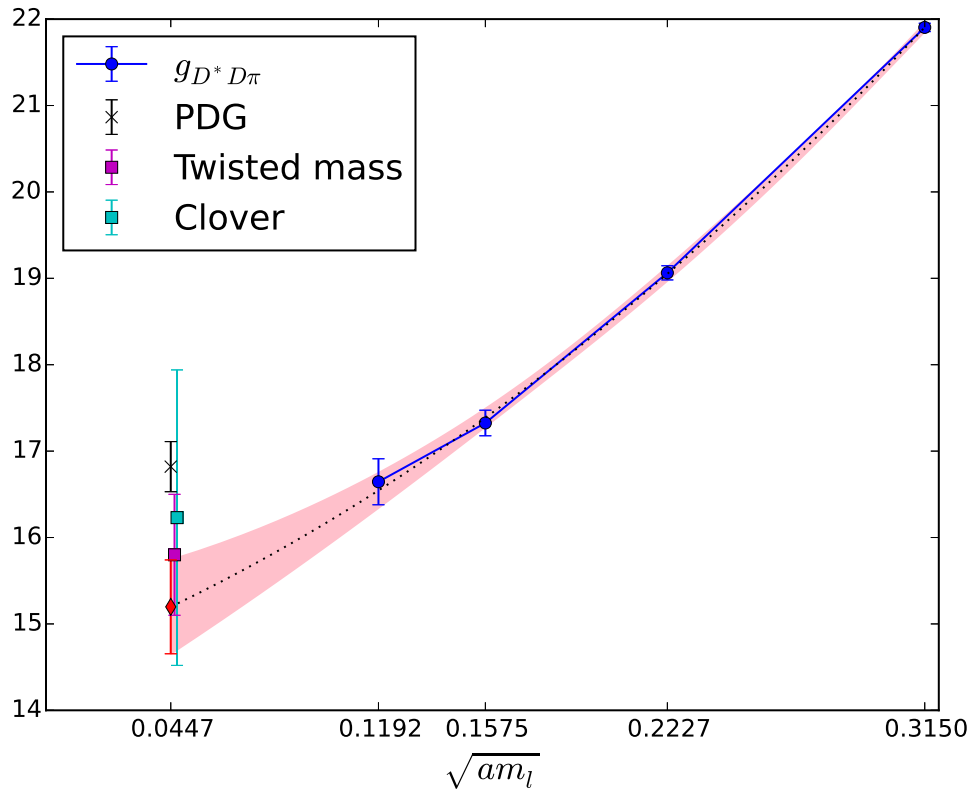


Figure 6.10: A quadratic extrapolation of the pion coupling in terms of the pion mass, i.e.  $\sqrt{am_l}$ , is added to the plot shown in Figure 6.9 to guide the eye towards the chiral limit. The red diamond is where our crude extrapolation intersects the physical point. This serves only as a visual representation. We take the coupling at obtained at the lightest quark mass as our final result, not the red diamond.



Table 6.11: Results for the pion coupling and pionic decay width of  $D^{*+}$ . Columns 3, 4 and 5 are directly related to one another through simple conversions. Theoretical results for all three quantities are obtained from the same underlying matrix elements and form factors computed on the lattice. The experimental values are inferred from the measured width given in column 5. <sup>†</sup>Entries indicated by a dagger were not provided in [68] and are calculated here from related quantities reported in the original reference.

Ref.	Method	$g_{D^{*+}D^0\pi^+}$	$g_c$	$\Gamma(D^{*+} \rightarrow D^0\pi^+)$ keV
self	HISQ	16.65(27)	0.5465(87)	55.2(2.2)
[67]	Twisted mass	15.8(7)(3)	0.53(3)(3)	50(5)(6)
[68]	Clover	16.23(1.71)	0.546(58) <sup>†</sup>	52(11) <sup>†</sup>
[1]	Expt.	16.82(29)	0.5657(98)	56.5(1.3)

Finally, Table 6.11 lists our results for the pion coupling  $g_{D^*D\pi}$  as well as  $g_c$  and our estimate for the decay width along with other lattice results employing different quark actions [67, 68] and the experimental values [1].

## 6.4 Phenomenology

Having computed the radiative and pionic transitions that we set out to, let us now return to the curious Table 6.1 and see how our results fit in. We have directly calculated the following radiative decay widths of  $\Gamma(D^{*+} \rightarrow D^+\gamma) = 0.25(15)$  keV,  $\Gamma(D^{*0} \rightarrow D^0\gamma) = 15.6(1.9)$  keV and  $\Gamma(D_s^{*+} \rightarrow D_s^+\gamma) = 0.083(21)$  keV, as well as the pionic decay width  $\Gamma(D^{*+} \rightarrow D^0\pi^+) = 55.2(2.2)$  keV.

All errors here are pure statistical lattice errors. Evidence from other studies indicate that systematic errors due to the continuum and sea-quark chiral extrapolations are small. Our rough valence quark extrapolation in Figure 6.7 indicates that our systematics increase our errors by roughly 50%.

Using these results together with the approximate isospin symmetry and additional input from related existing experimental data, we can now make estimates for other decay modes of these charmed mesons and propagate our results to fill the rest of Table 6.1.

- As we showed earlier in (6.3), the isospin symmetry predicts that the neutral pionic decay of  $D^{*+}$  is approximately twice as wide as its charged pionic decay due to

$$g_{D^{*+}D^+\pi^0}^2 = 2g_{D^{*+}D^0\pi^+}^2, \quad (6.69)$$

which simply follows from calculating the appropriate iso-Clebsch-Gordon coefficient. This enables one to estimate the neutral pionic width using this coupling and the

relevant phase space factor

$$\Gamma(D^{*+} \rightarrow D^+\pi^0) = \frac{|\vec{q}_{\pi^0}|^3}{48\pi m_{D^{*+}}^2} g_{D^{*+}D^+\pi^0}^2 = 25.2(1.1) \text{ keV}. \quad (6.70)$$

- Combining our results for each of the three modes the total width is then given by

$$\Gamma_{\text{tot.}}(D^{*+}) = 80.7(2.5) \text{ keV}. \quad (6.71)$$

Our theoretical result is in good agreement with BaBar's measurement of 83.4(1.8) keV [11].

- Alternatively, using the recent measurement of the total width

$$\Gamma_{\text{tot}}(D^{*+}) = \Gamma(D^{*+} \rightarrow D^+\gamma) + \Gamma(D^{*+} \rightarrow D^0\pi^+) + \Gamma(D^{*+} \rightarrow D^+\pi^0) \quad (6.72)$$

and our direct results for two out of the three modes, one can infer  $\Gamma(D^{*+} \rightarrow D^+\pi^0) \approx 28.0(2.8) \text{ keV}$ . Comparing these two estimates—one using isospin, one the total width—provides a measure of isospin violation. The two agree with each other within about 10%. This is a remarkable agreement considering our pion mass is about 2.5 times heavier than physical.

- One can also exploit the isospin symmetry to estimate the pionic decay rates of the neutral  $D^{*0}$ . The charged pionic mode  $\Gamma(D^{*0} \rightarrow D^-\pi^+)$  is kinematically forbidden. The neutral pionic mode is predicted to be

$$\Gamma(D^{*0} \rightarrow D^0\pi^0) = \frac{|\vec{q}'_{\pi^0}|^3}{48\pi m_{D^{*0}}^2} g_{D^{*0}D^0\pi^0}^2 = 36.3(1.2) \text{ keV}. \quad (6.73)$$

Here  $|\vec{q}'_{\pi^0}|$  in the phase space is 43 MeV.

- Combining this with the radiative decay width of  $D^{*0}$  computed in this work we can predict its total width

$$\Gamma_{\text{tot.}}(D^{*0}) = 51.9(2.2) \text{ keV}. \quad (6.74)$$

At the moment there exists only an upper bound for this width available by experiment  $\Gamma_{\text{tot.}}^{\text{expt.}}(D^{*0}) < 2.1 \text{ MeV}$  [1].

- Combining our direct calculation of  $D^{*0} \rightarrow D^0\gamma$ , our indirect theoretical estimate of  $D^{*0} \rightarrow D^0\pi^0$  using isospin symmetry and experimentally observed branching fractions, provides another rough measure of isospin violation. Using the experimental branching ratios we have

$$\Gamma(D^{*0} \rightarrow D^0\pi^0) = \Gamma(D^{*0} \rightarrow D^0\gamma) \times \frac{\text{BR}(D^0\gamma)}{\text{BR}(D^0\pi^0)} = 25.3(4.4) \text{ keV}. \quad (6.75)$$

Table 6.12: Results for the branching ratios of  $D^{*+}$  and  $D^{*0}$  mesons decay modes compared with observed ratios [1].

$D^{*+}$ modes	Latt. (%)	Expt. (%)	$D^{*0}$ modes	Latt. (%)	Expt. (%)
$D^+\gamma$	0.31(19)	1.6(4)	$D^0\gamma$	30.1(2.7)	38.1(2.9)
$D^0\pi^+$	68.4(1.3)	67.7(5)	$D^0\pi^0$	69.9(2.7)	61.9(2.9)
$D^+\pi^0$	31.2(1.3)	30.7(5)			

The uncertainty is larger here at about 17% due to both our radiative width uncertainty and experimental branching fraction errors. The agreement with the width calculated above from lattice + isospin given by 36.3(1.2) keV is less good than what we found in the case of  $D^{*+}$  neutral pionic decay.

- The total decay width of the vector charmed strange meson  $D_s^*$  can be predicted from our direct calculation of its radiative decay combined with its experimentally measured branching ratio

$$\Gamma(D_s^*) = \frac{\Gamma(D_s\gamma)}{\text{BR}(D_s\gamma)} = 0.088(22) \text{ keV}. \quad (6.76)$$

The only other mode is the isospin violating OZI suppressed decay via a neutral pion. The narrow total width we find here is consistent with the HPQCD collaboration's result 0.066(26) keV, also obtained using HISQ [3], as expected given the earlier agreement between the radiative widths.

Finally, having calculated the width of every decay mode for both  $D^{*+}$  and  $D^{*0}$  in this work we can simply obtain the branching fractions. Table 6.12 lists our results for the ratios alongside the experimentally observed values [1]. The radiative branching ratio of  $D^{*+}$  is suppressed as expected. We see excellent agreement with experiment for our  $D^{*+}$  pionic modes. The agreement is less good for the  $D^{*0}$  with an error of roughly 15%. However, note that the pionic width of the  $D^{*0}$  was inferred from the charged pionic of  $D^{*+}$  using the isospin symmetry which as discussed before causes an error of roughly 10%.

## 6.5 Heavy-Strange

We studied the mass dependence of the magnetic moment of the light quark inside a heavy-light meson in subsection 6.3.2 by computing lattice correlators for charmed mesons with the charm quark fixed at its physical mass and various light quark masses. Additionally, in order to study the heavy quark's magnetic moment's mass dependence in heavy-light mesons, we have also explored the heavy mass axis.

This would be of particular interest in studies of the bottom strange vector meson  $B_s^*$ . The radiative decay width of this meson is not measured but is seen to be dominant since its pionic decay is kinematically forbidden [1]. However, the MILC collaboration’s “coarse” ensemble with  $a = 0.12$  fm utilized in this work is too coarse for studying the  $b$  quark using the HISQ formalism. In fact, in order to have valence HISQ  $b$  quarks with  $am_b < 1$ , one would require much finer lattices with  $a < 0.044$  fm, while a spacing of  $a = 0.03$  would bring  $am_b$  down to around 0.5 where precision calculations begin to become possible [80].

In contrast, NRQCD and Fermilab actions are capable of handling  $b$  quarks on coarser lattices, by construction. Nevertheless, in order to push the limits of HISQ and explore the possibility of studying the radiative decay of  $B_s^*$  by approaching the physical  $b$  mass from below we investigated radiative transitions of heavy-strange vector mesons with fictitious lighter than bottom quarks, denoted here by  $H_s^*$ . To that end, we fixed the light member at the physical strange mass  $am_s = 0.0496$  and pushed the heavy member’s mass up from charm’s  $am_c = 0.63$  to  $am_h \in \{0.75, 0.85, 1.0\}$ . The effective magnetic moment of each quark was obtained from the radiative form factors through a similar procedure to that described in subsection 6.3.2.

In the limit of static heavy quark one expects the quark magnetic moment to be

$$\mu_h \approx \frac{1}{2M_h}. \quad (6.77)$$

A very crude estimate using a simple constituent quark model picture suggests that the strange quark’s magnetic moment is roughly

$$\mu_s \approx \frac{1}{2M_s}, \quad (6.78)$$

where the mass parameters in (6.77) and (6.78) are the so called *constituent mass* of these quarks. This rough approximation can be justified by, for instance, viewing  $s$  in this simple model as a quark moving about inside the meson while surrounded by a cloud of gluons that bind it to the other quark, thereby giving it an effective (constituent) mass larger than its bare mass.

We estimated the heavy constituent mass from our heavyonium results as  $M_h \approx m_{\Upsilon_h}/2$  at each heavy quark mass, where  $\Upsilon_h = h\bar{h}$  denotes a vector heavyonium meson. The strange constituent mass was then taken as  $M_s \approx m_{H_s^*} - m_{\Upsilon_h}/2$  using our results for heavy-strange mesons at various heavy quark masses. We found it to be roughly constant over that range at about  $M_s \approx 590$  MeV, which is in the same ball park as the more direct estimate of  $m_\phi/2 \approx 510$  MeV, where  $\phi = s\bar{s}$  is a vector meson made of a strange quark and its antiquark.

Figure 6.11 shows our results for each quark’s magnetic moment as a function of inverse heavy mass:  $1/am_h$ . The plotted quantity pertaining to the heavy quark’s magnetic mo-

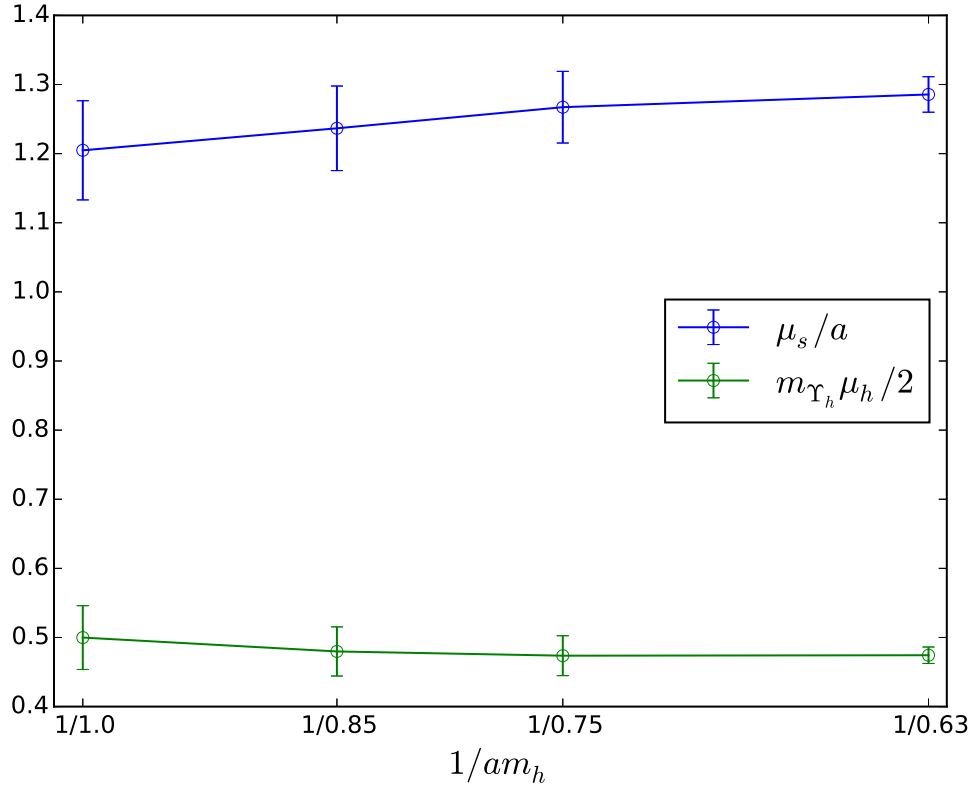


Figure 6.11: Magnetic moment of heavy HISQ quarks inside heavy-strange, multiplied by their constituent mass, plotted as a function of inverse heavy quark mass  $1/am_h$ . The blue circles are the magnetic moment of the strange quark in lattice units.

ment, i.e.  $m_{\gamma_h} \mu_h$ , is expected to approach asymptotically to 0.5 in the infinite mass limit. In contrast, a crude quark model picture suggests that in the infinite quark mass limit, the strange quark's dynamics is decoupled from that of the heavy member and it simply orbits around a static quark. Consequently, one would expect the magnetic moment of the strange quark to be roughly independent of  $m_h$  with a value of  $\mu_s/a \approx 1/2aM_s \approx 1.4$ . Figure 6.11 demonstrates that our exploratory results for heavy HISQ are in the same ballpark as the simplest quark model approximations.

# Chapter 7

## Conclusion

### 7.1 Summary

We accomplished to resolve the accidental near cancellation between the photocoupling of the two valence quarks that takes place in the radiative decay of the charged charmed vector mesons  $D^{*+}$  and  $D_s^{*+}$ . Our result for the radiative form factor for the  $D^{*+}$  at our closest to physical light quark mass is  $V_+^{\text{latt.}}(0) = 0.39(11)$ . Compared with that for the neutral  $D^{*0}$  meson given by  $V_0^{\text{latt.}}(0) = 3.10(19)$ , we find that the charged meson's radiative form factor is indeed highly suppressed, by a factor of  $0.126(36)$ , and yet clearly resolved by a statistically significant amount. This had been difficult to achieve previously as shown in [8] where the Wilson method yielded results with larger than 100% errors. This small ratio illustrates the fact that the charged radiative form factor is intrinsically noisy due to the near cancellation with errors dominated by lattice statistical uncertainties.

The experimentally measured decay width of  $D^{*+}$  allowed us to infer its radiative form factor  $V^{\text{expt.}}(0) = 0.89(11)$  with an uncertainty of 12% [1]. As illustrated by Figure 6.7, our study of the mass dependence of this form factor clearly indicates an upward trend in the right direction as the light quark mass approaches the physical point and suggests that an agreement within  $2\sigma$  can be reached.

In terms of the decay width we find  $\Gamma(D^{*+} \rightarrow D^+\gamma) = 0.25(15)$  keV while the experimental value is  $1.33(33)$  keV which has somewhat large errors at 25%. Furthermore, we predict the radiative decay width of the neutral  $D$  to be  $\Gamma(D^{*0} \rightarrow D^0\gamma) = 15.6(1.9)$  keV. Compared with  $27(14)$  keV obtained in [8] using the Wilson method our errors are much smaller. There is only an upper bound available for the decay width of the neutral  $D$  from the experiment  $\Gamma^{\text{expt.}}(D^{*0} \rightarrow D^0\gamma) < 0.8$  MeV. Thus, new and more accurate measurements can shed more light on our understanding of charm physics.

We also calculated the charged pionic decay of the charged vector  $D$  meson and at our lightest mass found  $\Gamma(D^{*+} \rightarrow D^0\pi^+) = 55.2(2.2)$  keV. This is in excellent agreement with experiment as well as other lattice calculations using different methods than ours [1, 67, 68].

Once again our errors are smaller than other lattice results. Together with our estimate of its neutral pionic decay width  $\Gamma(D^{*+} \rightarrow D^+\pi^0) = 25.2(1.1)$  keV, our result for the total width of the charged  $D$  is  $\Gamma(D^{*+}) = 80.7(2.5)$  keV, which is in good agreement with BaBar’s observed value of 83.4(1.8) keV [11].

Using our estimate for the pionic decay width of the neutral vector  $D$  meson  $\Gamma(D^{*0} \rightarrow D^0\pi^0) = 36.3(1.2)$  keV, we predict its full width to be  $\Gamma_{\text{tot.}}(D^{*0}) = 51.9(2.2)$  keV. The current experimental upper bound is  $< 2.1$  MeV.

Additionally, we computed the radiative decay width of  $D_s^*$ . This meson is expected to have a very narrow width due to a number of reasons. Our calculation resulted in  $\Gamma(D_s^* \rightarrow D_s\gamma) = 0.083(21)$  keV which implies a total width of 0.088(22) keV. Our result is consistent with that reported in another HISQ study [3] published as we were finalizing our analysis. Currently there is only an upper bound of  $< 1.9$  MeV available for its full width from experiment. Given the narrow width predicted in this work, an accurate measurement of the  $D_s^*$  meson’s decays will be of significant value.

In addition to our original studies of various decay processes of charm-light mesons, we also performed complementary studies of charmonium physics as a sanity test while building up the tools that were necessary for our main calculations. We computed the hyperfine mass splitting, the electric charge form factor and charge radius of  $\eta_c$  and the radiative transition rate  $\Gamma(J/\psi \rightarrow \eta_c\gamma) = 2.383(49)$  keV, which were all in good agreements with the published lattice and experimental results.

Moreover, we performed an exploratory study to evaluate the large mass behavior of the HISQ formalism in the context of simulations of radiative transitions of heavy-light vector mesons. While far from the physical  $b$  quark, our exploratory results for  $H_s^*$  with a range of quark masses heavier than charm obtained using MILC’s *coarse* ensemble, were reasonable and exhibited the overall qualitative behavior that we expected to see in both heavy and strange quark’s effective magnetic moment.

As a primary point of focus in our original calculations using the HISQ formalism, we employed an array of theoretical and numerical tools and techniques in carrying out large scale simulations of the radiative and pionic decays of charmed mesons at various light quark masses ranging from  $m_l \approx m_s/4$  up to  $2m_s$ . And this enabled us to gain theoretical insight into the internal structure of charmed hadrons. Particularly, we examined the light quark mass dependence of each constituent quark’s effective magnetic moment inside a charm-light meson.

## 7.2 Further Studies

The lattice radiative form factor at our lightest quark mass around  $m_l \approx 7m_{u/d}^{\text{phys.}}$ , computed in chapter 6 using HISQ, is  $V^{\text{latt.}}(0) = 0.39(11)$ . This error is purely statistical and does not take into account the systematic uncertainties such as chiral and continuum extrapolations.

It is worth emphasizing the contrast between the 28% error in the charged meson’s form factor and the 6% error in the neutral form factor  $V_{D^{*0}}^{\text{latt.}}(0) = 3.10(19)$  obtained from the exact same numerical data. This is a consequence of the strong suppression of the signal to noise ratio in the charged case due to the aforementioned near cancellation.

Although this result underestimates the physical value, Figure 6.7 clearly demonstrates that the form factor is trending up in the right direction as the light quark mass approaches the physical point. A rough extrapolation attempt suggests that an agreement within  $2\sigma$  can be reached at the chiral point. It is therefore highly desirable to improve this calculation by reducing the errors and going to lighter masses. However, upon close inspection, Figure 6.7 reveals another barrier. Once again we reach a point where the brute force approach, here reducing  $am_l$ , is not sufficient and one needs to employ new methods.

This is due to a number of reasons affecting both statistical and systematic errors. With our lightest quark approximately 7 times heavier than physical and a pion mass of around 370 MeV [16], we are not quite close enough to the real world to perform a reliable chiral extrapolation. There is also plenty of evidence, for instance from calculations of  $\pi$  and  $K$  meson masses and decay constants, that chiral perturbation theory results in poor convergence at masses larger than about half the strange mass  $m_l > m_s/2$  [22]. This leaves us with only two data points whose error bars are somewhat large due to the signal cancellation, one of which is on the cusp of being useful for chiral extrapolation.

The ensemble used in this study is statistically exhausted. We used 16 time sources per every configuration. That is a wall source on every 4th time step. As they get closer to each other, correlations among the time sources grow and that leads to diminishing return in noise reduction. Given the size of our errors and the fact that normally the statistical noise increases as the quark mass decreases, adding a new data point at a smaller mass is unlikely to improve the chiral extrapolation. Furthermore, typically the computation cost of a quark propagator scales like  $1/am_l$ , which means that not only are they noisier at lighter masses, they’re also more expensive. Therefore, adding a data point at a new lighter mass to the current calculation will cost a lot but likely help little unless other methods are employed to significantly reduce statistical errors.

In addition to the array of theoretical and numerical techniques employed in this study—which indeed ultimately proved perfectly adequate for achieving our goals—in order to take this any further one will need to expand the current simulation strategy in various dimensions so as to bring under control the systematic errors and beat down the statistical uncertainties. To that end, one can use additional ensembles of gauge field configurations at several various sea quark masses and lattice spacing, preferably lighter and finer than used here. The MILC collaboration has been generating a sizable library of  $N_f = 2 + 1 + 1$  HISQ ensembles which, as discussed in chapter 3, will have smaller discretization errors than asqtad configurations. Simulations on several ensembles with different masses and lattice spacings will enable one to perform chiral and continuum extrapolations.



In addition, on each ensemble one may use distinct sets of interpolating operators and currents to compute a large number of different correlators from which the same matrix elements of interest can be extracted. For instance, one can boost the statistics by using a similar setup to ours but with different polarizations or operator tastes. The resulting data can then be analyzed by incorporating more involved eigenbasis methods into the Bayesian approach described in chapter 5, to handle the large data set of correlators corresponding to several different operators which couple to the same mesons.

Another potential candidate is to use *smearred sources* where instead of a point source with a  $\mathbf{1}$  at a single site and zeros everywhere else, one constructs a source vector that has a larger overlap with the ground state and much smaller overlaps with excited states. As a result, the ground state signal is magnified and higher energy states are almost eliminated. More recently, the same idea has also been employed in studies of excited state mesons which use different appropriately designed smeared sources to enhance the signal that would otherwise have been drowned by the dominant ground state and the noise. Smeared sources may be used in conjunction with random wall sources which adds an extra layer of complexity as well as improvement.

All of these constitute an significant undertaking both in terms of computing and human resources. Nonetheless, our results in this thesis make a compelling case that it is worthwhile.

# Bibliography

- [1] **Particle Data Group**, K. Olive *et al.*, “Review of Particle Physics,” *Chin.Phys.* **C38** (2014) 090001. ix, 1, 2, 51, 107, 108, 133, 134, 135, 136, 140, 142, 143, 144, 145, 147
- [2] R. Woloshyn, “VECTOR MESON RADIATIVE DECAY IN LATTICE QCD,” *Z.Phys.* **C33** (1986) 121. 1
- [3] G. Donald, C. Davies, J. Koponen, and G. Lepage, “Prediction of the  $D_s^*$  width from a calculation of its radiative decay in full lattice QCD,” *Phys.Rev.Lett.* **112** (2014) 212002, [arXiv:1312.5264 \[hep-lat\]](#). 1, 113, 126, 129, 130, 133, 135, 136, 144, 148
- [4] G. Donald, C. Davies, R. Dowdall, E. Follana, K. Hornbostel, *et al.*, “Precision tests of the  $J/\psi$  from full lattice QCD: mass, leptonic width and radiative decay rate to  $\eta_c$ ,” *Phys.Rev.* **D86** (2012) 094501, [arXiv:1208.2855 \[hep-lat\]](#). 1, 51, 112, 113, 129, 130, 135
- [5] J. J. Dudek, R. G. Edwards, and D. G. Richards, “Radiative transitions in charmonium from lattice QCD,” *Phys.Rev.* **D73** (2006) 074507, [arXiv:hep-ph/0601137 \[hep-ph\]](#). 1, 105, 135
- [6] D. Becirevic and F. Sanfilippo, “Lattice QCD study of the radiative decays  $J/\psi \rightarrow \eta_c \gamma$  and  $h_c \rightarrow \eta_c \gamma$ ,” *JHEP* **1301** (2013) 028, [arXiv:1206.1445 \[hep-lat\]](#). 1, 135
- [7] Y. Chen, D.-C. Du, B.-Z. Guo, N. Li, C. Liu, *et al.*, “Radiative transitions in charmonium from  $N_f = 2$  twisted mass lattice QCD,” *Phys.Rev.* **D84** (2011) 034503, [arXiv:1104.2655 \[hep-lat\]](#). 1, 135
- [8] D. Becirevic and B. Haas, “ $D^* \rightarrow D \pi$  and  $D^* \rightarrow D \gamma$  decays: Axial coupling and Magnetic moment of  $D^*$  meson,” *Eur.Phys.J.* **C71** (2011) 1734, [arXiv:0903.2407 \[hep-lat\]](#). 1, 116, 133, 134, 135, 147
- [9] **HPQCD Collaboration**, **UKQCD Collaboration**, E. Follana *et al.*, “Highly improved staggered quarks on the lattice, with applications to charm physics,” *Phys.Rev.* **D75** (2007) 054502, [arXiv:hep-lat/0610092 \[hep-lat\]](#). 1, 9, 23, 40, 46, 47, 48, 49, 50, 51, 52, 53, 55, 107
- [10] D. J. Griffiths, *INTRODUCTION TO ELEMENTARY PARTICLES*. 1987. 3, 117
- [11] **BaBar Collaboration**, J. Lees *et al.*, “Measurement of the  $D^*(2010)^+$  meson width and the  $D^*(2010)^+ - D^0$  mass difference,” *Phys.Rev.Lett.* **111** no. 11, (2013) 111801, [arXiv:1304.5657 \[hep-ex\]](#). 4, 108, 134, 143, 148

- [12] M. E. Peskin and D. V. Schroeder, *An Introduction to quantum field theory*. 1995. 5, 12, 15, 16, 20, 117, 118
- [13] K. G. Wilson, “Confinement of quarks,” *Phys. Rev. D* **10** (Oct, 1974) 2445–2459. <http://link.aps.org/doi/10.1103/PhysRevD.10.2445>. 5, 15, 17
- [14] G. P. Lepage, “Redesigning lattice QCD,” *Lect. Notes Phys.* **479** (1997) 1–48, [arXiv:hep-lat/9607076](https://arxiv.org/abs/hep-lat/9607076) [hep-lat]. 5, 12, 18, 20, 38
- [15] **Fermilab Lattice, HPQCD, UKQCD, MILC**, C. T. H. Davies *et al.*, “High precision lattice QCD confronts experiment,” *Phys. Rev. Lett.* **92** (2004) 022001, [arXiv:hep-lat/0304004](https://arxiv.org/abs/hep-lat/0304004) [hep-lat]. 6, 7
- [16] **MILC**, A. Bazavov *et al.*, “Nonperturbative QCD simulations with 2+1 flavors of improved staggered quarks,” *Rev.Mod.Phys.* **82** (2010) 1349–1417, [arXiv:0903.3598](https://arxiv.org/abs/0903.3598) [hep-lat]. 7, 8, 22, 39, 81, 125, 126, 149
- [17] G. P. Lepage, “Flavor symmetry restoration and Symanzik improvement for staggered quarks,” *Phys.Rev.* **D59** (1999) 074502, [arXiv:hep-lat/9809157](https://arxiv.org/abs/hep-lat/9809157) [hep-lat]. 7, 39, 43
- [18] K. G. Wilson, “Quarks and strings on a lattice,” in *New Phenomena in Subnuclear Physics*, A. Zichichi, ed., vol. 13 of *The Subnuclear Series*, pp. 69–142. Springer US, 1977. [http://dx.doi.org/10.1007/978-1-4613-4208-3\\_6](http://dx.doi.org/10.1007/978-1-4613-4208-3_6). 8, 24, 32
- [19] J. B. Kogut and L. Susskind, “Hamiltonian Formulation of Wilson’s Lattice Gauge Theories,” *Phys.Rev.* **D11** (1975) 395–408. 8, 35
- [20] T. Banks, L. Susskind, and J. B. Kogut, “Strong Coupling Calculations of Lattice Gauge Theories: (1+1)-Dimensional Exercises,” *Phys.Rev.* **D13** (1976) 1043. 8, 35
- [21] L. Susskind, “Lattice Fermions,” *Phys.Rev.* **D16** (1977) 3031–3039. 8, 35
- [22] C. Davies, “Lattice QCD: A Guide for people who want results,” [arXiv:hep-lat/0509046](https://arxiv.org/abs/hep-lat/0509046) [hep-lat]. 8, 149
- [23] G. P. Lepage, L. Magnea, C. Nakhleh, U. Magnea, and K. Hornbostel, “Improved nonrelativistic QCD for heavy quark physics,” *Phys.Rev.* **D46** (1992) 4052–4067, [arXiv:hep-lat/9205007](https://arxiv.org/abs/hep-lat/9205007) [hep-lat]. 8, 158
- [24] A. X. El-Khadra, A. S. Kronfeld, and P. B. Mackenzie, “Massive fermions in lattice gauge theory,” *Phys.Rev.* **D55** (1997) 3933–3957, [arXiv:hep-lat/9604004](https://arxiv.org/abs/hep-lat/9604004) [hep-lat]. 9, 158
- [25] K. Symanzik, “Continuum Limit and Improved Action in Lattice Theories. 1. Principles and  $\phi^4$  Theory,” *Nucl.Phys.* **B226** (1983) 187. 9, 14, 38
- [26] H. Rothe, *Lattice gauge theories: An Introduction*, vol. 59 of *World Sci.Lect.Notes Phys.* World Scientific, 2nd ed., 1997. 12, 23
- [27] I. Montvay and G. Münster, *Quantum fields on a lattice*. Cambridge monographs on mathematical physics. Cambridge Univ. Press, Cambridge, 1994. 12, 23, 73

- [28] J. Smit, “Introduction to quantum fields on a lattice: A robust mate,” *Cambridge Lect.Notes Phys.* **15** (2002) 1–271. 12, 23
- [29] G. P. Lepage, “Lattice QCD for novices,” in *Strong interactions at low and intermediate energies. Proceedings, 13th Annual Hampton University Graduate Studies, HUGS’98, Newport News, USA, May 26-June 12, 1998*, pp. 49–90. 1998. [arXiv:hep-lat/0506036 \[hep-lat\]](#). 12, 22
- [30] M. Luscher and P. Weisz, “Computation of the Action for On-Shell Improved Lattice Gauge Theories at Weak Coupling,” *Phys. Lett.* **B158** (1985) 250. 18
- [31] M. Luscher and P. Weisz, “On-Shell Improved Lattice Gauge Theories,” *Commun. Math. Phys.* **97** (1985) 59. [Erratum: *Commun. Math. Phys.* 98,433(1985)]. 18
- [32] G. P. Lepage and P. B. Mackenzie, “On the viability of lattice perturbation theory,” *Phys.Rev.* **D48** (1993) 2250–2264, [arXiv:hep-lat/9209022 \[hep-lat\]](#). 18, 19
- [33] G. P. Lepage, “On the Absence of  $O(a)$  Errors in Staggered-Quark Discretizations,” [arXiv:1111.2955 \[hep-lat\]](#). 31
- [34] B. Sheikholeslami and R. Wohlert, “Improved Continuum Limit Lattice Action for QCD with Wilson Fermions,” *Nucl. Phys.* **B259** (1985) 572. 33, 35
- [35] MILC, K. Orginos and D. Toussaint, “Testing improved actions for dynamical Kogut-Susskind quarks,” *Phys.Rev.* **D59** (1999) 014501, [arXiv:hep-lat/9805009 \[hep-lat\]](#). 39, 42
- [36] MILC, D. Toussaint and K. Orginos, “Tests of improved Kogut-Susskind fermion actions,” *Nucl.Phys.Proc.Suppl.* **73** (1999) 909–911, [arXiv:hep-lat/9809148 \[hep-lat\]](#). 39, 42
- [37] P. Lepage, “Perturbative improvement for lattice QCD: An Update,” *Nucl.Phys.Proc.Suppl.* **60A** (1998) 267–278, [arXiv:hep-lat/9707026 \[hep-lat\]](#). 39
- [38] J. Lagae and D. Sinclair, “Improving the staggered quark action to reduce flavor symmetry violations,” *Nucl.Phys.Proc.Suppl.* **63** (1998) 892–894, [arXiv:hep-lat/9709035 \[hep-lat\]](#). 39
- [39] J. Lagae and D. Sinclair, “Improved staggered quark actions with reduced flavor symmetry violations for lattice QCD,” *Phys.Rev.* **D59** (1999) 014511, [arXiv:hep-lat/9806014 \[hep-lat\]](#). 39
- [40] A. Hasenfratz and F. Knechtli, “Flavor symmetry and the static potential with hypercubic blocking,” *Phys.Rev.* **D64** (2001) 034504, [arXiv:hep-lat/0103029 \[hep-lat\]](#). 40
- [41] S. Naik, “On-shell Improved Lattice Action for QCD With Susskind Fermions and Asymptotic Freedom Scale,” *Nucl.Phys.* **B316** (1989) 238. 40
- [42] T. Blum, C. E. Detar, S. A. Gottlieb, K. Rummukainen, U. M. Heller, *et al.*, “Improving flavor symmetry in the Kogut-Susskind hadron spectrum,” *Phys.Rev.* **D55** (1997) 1133–1137, [arXiv:hep-lat/9609036 \[hep-lat\]](#). 42

- [43] J. Shigemitsu. Personal communication. 45
- [44] <http://www.wolframalpha.com/>. 46
- [45] H. Sharatchandra, H. Thun, and P. Weisz, “Susskind Fermions on a Euclidean Lattice,” *Nucl.Phys.* **B192** (1981) 205. 64
- [46] M. Wingate, J. Shigemitsu, C. T. Davies, G. P. Lepage, and H. D. Trottier, “Heavy light mesons with staggered light quarks,” *Phys.Rev.* **D67** (2003) 054505, [arXiv:hep-lat/0211014](https://arxiv.org/abs/hep-lat/0211014) [[hep-lat](#)]. 64, 93, 104
- [47] A. Frommer, V. Hannemann, B. Nockel, T. Lippert, and K. Schilling, “Accelerating Wilson fermion matrix inversions by means of the stabilized biconjugate gradient algorithm,” *Int. J. Mod. Phys.* **C5** (1994) 1073–1088, [arXiv:hep-lat/9404013](https://arxiv.org/abs/hep-lat/9404013) [[hep-lat](#)]. 72
- [48] Y. Saad, *Iterative Methods for Sparse Linear Systems*. Society for Industrial and Applied Mathematics, Philadelphia, PA, USA, 2nd ed., 2003. 72
- [49] W. Wilcox and R. Woloshyn, “Lattice Results on the Meson Electric Form-factor,” *Phys.Rev.Lett.* **54** (1985) 2653. 77
- [50] MILC, C. Aubin, C. Bernard, C. E. DeTar, J. Osborn, S. Gottlieb, E. B. Gregory, D. Toussaint, U. M. Heller, J. E. Hetrick, and R. Sugar, “Light pseudoscalar decay constants, quark masses, and low energy constants from three-flavor lattice QCD,” *Phys. Rev.* **D70** (2004) 114501, [arXiv:hep-lat/0407028](https://arxiv.org/abs/hep-lat/0407028) [[hep-lat](#)]. 82
- [51] G. de Divitiis, R. Petronzio, and N. Tantalo, “On the discretization of physical momenta in lattice QCD,” *Phys.Lett.* **B595** (2004) 408–413, [arXiv:hep-lat/0405002](https://arxiv.org/abs/hep-lat/0405002) [[hep-lat](#)]. 90, 93
- [52] D. Guadagnoli, F. Mescia, and S. Simula, “Lattice study of semileptonic form-factors with twisted boundary conditions,” *Phys.Rev.* **D73** (2006) 114504, [arXiv:hep-lat/0512020](https://arxiv.org/abs/hep-lat/0512020) [[hep-lat](#)]. 90
- [53] P. F. Bedaque, “Aharonov-Bohm effect and nucleon nucleon phase shifts on the lattice,” *Phys.Lett.* **B593** (2004) 82–88, [arXiv:nucl-th/0402051](https://arxiv.org/abs/nucl-th/0402051) [[nucl-th](#)]. 90, 91
- [54] C. Sachrajda and G. Villadoro, “Twisted boundary conditions in lattice simulations,” *Phys.Lett.* **B609** (2005) 73–85, [arXiv:hep-lat/0411033](https://arxiv.org/abs/hep-lat/0411033) [[hep-lat](#)]. 90, 93, 115
- [55] D. Sivia and J. Skilling, *Data Analysis: A Bayesian Tutorial*. Oxford science publications. Oxford University Press, 2006. 93
- [56] C. Bishop, *Pattern Recognition and Machine Learning*. Information Science and Statistics. Springer, 2006. 93
- [57] W. Press, *Numerical Recipes 3rd Edition: The Art of Scientific Computing*. Cambridge University Press, 2007. 93, 104, 164
- [58] G. Lepage, B. Clark, C. Davies, K. Hornbostel, P. Mackenzie, *et al.*, “Constrained curve fitting,” *Nucl.Phys.Proc.Suppl.* **106** (2002) 12–20, [arXiv:hep-lat/0110175](https://arxiv.org/abs/hep-lat/0110175) [[hep-lat](#)]. 93

- [59] K. Hornbostel, G. Lepage, C. Davies, R. Dowdall, H. Na, *et al.*, “Fast Fits for Lattice QCD Correlators,” *Phys.Rev.* **D85** (2012) 031504, [arXiv:1111.1363 \[hep-lat\]](#). 93, 166, 167
- [60] C. Bouchard, G. P. Lepage, C. Monahan, H. Na, and J. Shigemitsu, “ $B_s \rightarrow K\ell\nu$  form factors from lattice QCD,” *Phys.Rev.* **D90** no. 5, (2014) 054506, [arXiv:1406.2279 \[hep-lat\]](#). 93, 165, 166
- [61] P. Lepage and C. Gohlke, “lsqfit: lsqfit version 6.0,” Nov., 2014. <http://dx.doi.org/10.5281/zenodo.12803>. 93
- [62] P. Lepage, “corrfitter v4.1,” June, 2014. <http://dx.doi.org/10.5281/zenodo.10714>. 93
- [63] W. Wilcox and R. Woloshyn, “Meson Electric Form-factor on the Lattice,” *Phys.Rev.* **D32** (1985) 3282. 105
- [64] **UKQCD**, G. de Divitiis *et al.*, “Towards a lattice determination of the  $B^* B \pi$  coupling,” *JHEP* **9810** (1998) 010, [arXiv:hep-lat/9807032 \[hep-lat\]](#). 115
- [65] A. Abada, D. Becirevic, P. Boucaud, G. Herdoiza, J. Leroy, *et al.*, “Lattice measurement of the couplings affine  $g$  infinity and  $g(B^* B \pi)$ ,” *JHEP* **0402** (2004) 016, [arXiv:hep-lat/0310050 \[hep-lat\]](#). 116
- [66] A. Abada, D. Becirevic, P. Boucaud, G. Herdoiza, J. Leroy, *et al.*, “First lattice QCD estimate of the  $g(D^* D \pi)$  coupling,” *Phys.Rev.* **D66** (2002) 074504, [arXiv:hep-ph/0206237 \[hep-ph\]](#). 116
- [67] D. Becirevic and F. Sanfilippo, “Theoretical estimate of the  $D^* \rightarrow D\pi$  decay rate,” *Phys.Lett.* **B721** (2013) 94–100, [arXiv:1210.5410 \[hep-lat\]](#). 116, 140, 142, 147
- [68] K. Can, G. Erkol, M. Oka, A. Ozpineci, and T. Takahashi, “Vector and axial-vector couplings of  $D$  and  $D^*$  mesons in 2+1 flavor Lattice QCD,” *Phys.Lett.* **B719** (2013) 103–109, [arXiv:1210.0869 \[hep-lat\]](#). 116, 140, 142, 147
- [69] S. Weinberg, *The quantum theory of fields. Vol. 2: Modern applications*. 1996. 116, 117, 118, 122
- [70] S. Weinberg, *The Quantum theory of fields. Vol. 1: Foundations*. 1995. 117, 118
- [71] H. Lehmann, K. Symanzik, and W. Zimmermann, “On the formulation of quantized field theories,” *Nuovo Cim.* **1** (1955) 205–225. 118
- [72] T. Cheng and L. Li, *GAUGE THEORY OF ELEMENTARY PARTICLE PHYSICS*. 1984. 122
- [73] C. Itzykson and J. Zuber, *QUANTUM FIELD THEORY*. 1980. 122
- [74] J. D. Hunter, “Matplotlib: A 2d graphics environment,” *Computing In Science & Engineering* **9** no. 3, (May-jun, 2007) 90–95. 125
- [75] **HPQCD**, C. Davies, E. Follana, I. Kendall, G. P. Lepage, and C. McNeile, “Precise determination of the lattice spacing in full lattice QCD,” *Phys.Rev.* **D81** (2010) 034506, [arXiv:0910.1229 \[hep-lat\]](#). 126

- [76] J. Koponen, C. Davies, G. Donald, E. Follana, G. Lepage, *et al.*, “The shape of the  $D \rightarrow K$  semileptonic form factor from full lattice QCD and  $V_{cs}$ ,” [arXiv:1305.1462 \[hep-lat\]](#). 126
- [77] C. Davies, C. McNeile, E. Follana, G. Lepage, H. Na, *et al.*, “Update: Precision  $D_s$  decay constant from full lattice QCD using very fine lattices,” *Phys.Rev.* **D82** (2010) 114504, [arXiv:1008.4018 \[hep-lat\]](#). 125, 126
- [78] J. J. Dudek, R. Edwards, and C. E. Thomas, “Exotic and excited-state radiative transitions in charmonium from lattice QCD,” *Phys.Rev.* **D79** (2009) 094504, [arXiv:0902.2241 \[hep-ph\]](#). 135
- [79] **CLEO**, R. Mitchell *et al.*, “ $J/\psi$  and  $\psi(2S)$  Radiative Decays to  $\eta(c)$ ,” *Phys.Rev.Lett.* **102** (2009) 011801, [arXiv:0805.0252 \[hep-ex\]](#). 135
- [80] C. McNeile, C. T. H. Davies, E. Follana, K. Hornbostel, and G. P. Lepage, “Heavy meson masses and decay constants from relativistic heavy quarks in full lattice QCD,” *Phys. Rev.* **D86** (2012) 074503, [arXiv:1207.0994 \[hep-lat\]](#). 145
- [81] M. B. Oktay and A. S. Kronfeld, “New lattice action for heavy quarks,” *Phys. Rev.* **D78** (2008) 014504, [arXiv:0803.0523 \[hep-lat\]](#). 158
- [82] C. McNeile, C. Davies, E. Follana, K. Hornbostel, and G. Lepage, “High-Precision  $c$  and  $b$  Masses, and QCD Coupling from Current-Current Correlators in Lattice and Continuum QCD,” *Phys.Rev.* **D82** (2010) 034512, [arXiv:1004.4285 \[hep-lat\]](#). 167

## Appendix A

# Heavy Quarks on the Lattice

In chapter 3 we talked about lattice artifacts and discretization errors in general and their magnitude at various energy scales. As mentioned in chapter 1, the six different flavors of quark found in nature come in vastly different masses ranging from  $m_{u/d}$  at a few MeV to  $m_s \approx 100$  MeV to  $m_{c/b} \approx 1\text{--}4$  GeV to the top which with  $m_t \approx 160$  GeV is too short lived to form bound states with others. Such a wide range will naturally give rise to physical systems that exhibit dynamical behaviour of entirely different characteristics. Consequently, as discussed earlier different physical degrees of freedom become important at different scales. Therefore, errors of various type will also be of varying degrees of significance and relevance. Which means that different systems call for different kinds of improvements to correct for their most dominant sources of error.

The focus of this work is primarily on the charm quark which along with the bottom is on the heavy side of the mass spectrum. Ultimately, we used a highly improved version of the staggered quark action in our calculation. However, since the broader topic of interest is the study of heavy quarks on the lattice, it is important to make a connection to other widely used formulations with overlapping domain of application. The improvement program of the staggered quarks was reviewed in great detail in section 3.2. In this appendix we very briefly touch upon a couple of other methods that have shown considerable success in simulations of heavy quarks.

To be clear, we do not intend to become experts in all the details and subtleties of these actions. The goal is to compare and contrast other relevant approaches with the formalism used here.

The main problem that sets apart the heavy quarks is that on typical lattices  $am$  is of order 1. In other words, the Compton wavelength is of order the lattice spacing. As a result the heavy quark's dynamics cannot be resolved well and  $\mathcal{O}((am)^n)$  discretization errors will be too large. This motivates the idea of developing effective theories specializing in heavy quarks that somehow deal with the large mass outside of the computer simulation. For instance, the heavy quark effective theory (HQET) integrates the mass out of the theory and then tries to capture the dynamics through an expansion in inverse mass. That is, one could start from a heavy quark effective theory and then proceed to systematically correct it to desired order in  $\alpha_s^n M_Q^{-m}$ .



The Fermilab action proposed in [24] adopts a different approach by designing a unified framework that is valid for all mass scales allowing a smooth interpolation between light and heavy quarks. It encompasses all masses by making all couplings in the action mass dependent. The dominant mass contributions are encoded in the coefficients and therefore not directly simulated on the computer. Fermilab fermions approach the SW action and the HQET at the two extreme mass limits. In order to accommodate all masses, the axis interchange symmetry is broken. The  $a^2$  improvement of Fermilab fermions is undertaken in [81]. The resulting theory known as the OK action extends the Fermilab formulation to dimension-6 and 7 operators. The Fermilab and OK family avoid targeting specific mass scales and organize their systematic improvement solely based on the dimensionality of correction operators up to desired order in  $a^n$ .

In what follows we present a cursory overview of nonrelativistic QCD without getting into much details. Of particular interest is the development of power counting rules which informs those used for the study of higher dimension operators for the HISQ action in subsection 3.2.5.

## A.1 NRQCD

As a consequence of their large mass heavy quarks tend to be nonrelativistic in most physical systems of interest. Lepage and co used this to develop a nonrelativistic formulation of QCD known as NRQCD [23].

The potential sources of error in the effective nonrelativistic lattice theory include those due to relativity, radiative corrections, finite lattice spacing and finite volume. In principle, lattice NRQCD can be corrected to exactly match ordinary continuum relativistic QCD by adding an infinite number of correction terms. In practice, however, exact agreement is unnecessary and only a finite number of corrections will suffice to improve the theory to any desired accuracy. The question is how to find the most important ones. One needs some sort of criterion to assess the importance of corrections as a guide to a systematic improvement.

As an example, consider the size of an operator's contribution to the *heavyonium* energy as a guide in designing the corrected effective theory. Quarkonia are flavorless mesons consisting of a quark and an antiquark of the same flavor. The power counting rules described below were developed for the purpose of ranking possible correction operators according to their importance. These rules serve as the guiding criterion in the formulation of the improved lattice action and can shed light on similar principles used in improvement of the staggered quarks. The following discussion is partial and only limited to constructing NRQCD in the continuum. Derivations and the subsequent discretization of it are not included here. Interested readers are referred to [23] for the details.

Correction terms are organized in a nonrelativistic expansion in terms of the quark velocity. The effect of  $\delta\mathcal{L}$  on the energy of a quarkonium state is

$$\delta E = -\langle n | \int d^3x \delta\mathcal{L}(x) | n \rangle. \quad (\text{A.1})$$

The important dynamical scales in quarkonium states such as  $\psi$  and  $\Upsilon$  are the momentum and the kinetic energy of the constituent quarks. These are of order 1–2 GeV and 500 MeV respectively and are related to the quark mass by

$$p \sim Mv, \quad K \sim Mv^2. \quad (\text{A.2})$$

It is important to note here that it is the order in  $v$  rather than the dimension of an operator that determines its numerical importance. This is a major distinguishing factor in the way corrections are organized between NRQCD and the Fermilab approach which will be discussed in the next section.

The Lagrangian is built from fields and operators. Their magnitude can be roughly estimated in terms of  $p$  and  $K$ . In this section  $\psi$  represents a 2-spinor for the quark. Charge conjugation uniquely relates the quark part of the action to the antiquark part normally denoted by  $\chi$ . Hence, everything said about  $\psi$  will be applied to  $\chi$  identically. The magnitude of the number operator acting on a quarkonium is of order 1:

$$\int d^3x \psi^\dagger(x)\psi(x) \sim 1. \quad (\text{A.3})$$

Since the quark is localized in a region of size  $\Delta x \sim 1/p$  one can estimate

$$\int d^3x \sim \frac{1}{p^3}, \quad \psi^\dagger(x)\psi(x) \sim p^3. \quad (\text{A.4})$$

By definition, the operator for kinetic energy should be of order  $K$ , which implies

$$\int d^3x \psi^\dagger(x) \frac{\mathbf{D}^2}{2M} \psi(x) \sim K \quad \Rightarrow \quad \mathbf{D} \sim (2MK)^{1/2} \sim p. \quad (\text{A.5})$$

The lowest order approximation to the field equation is used to estimate  $D_t$  giving

$$\left( iD_t + \frac{\mathbf{D}^2}{2M} \right) \psi(x) = 0 \quad \Rightarrow \quad D_t \sim \frac{\mathbf{D}^2}{2M} \sim K. \quad (\text{A.6})$$

Next, using the Coulomb gauge while neglecting the vector potential which can easily be shown to be of higher order in  $v$ , one gets

$$\left( i\partial_t - g\phi(x) + \frac{\nabla^2}{2M} \right) \psi \approx 0. \quad (\text{A.7})$$

Together with (A.6) this implies that  $g\phi(x) \sim K$ . Also, the field equation for  $\phi$  gives

$$\nabla^2 g\phi(x) = -g^2 \psi^\dagger(x)\psi(x), \quad (\text{A.8})$$

which implies  $g\phi(x) \sim \frac{1}{p^2} g^2 p^3 \sim g^2 p$ . The coupling must therefore be

$$\alpha_s \sim g^2 \sim v. \quad (\text{A.9})$$

Finally, it is easy to see that for the *chromoelectric* and *chromomagnetic* fields one has

$$ig\mathbf{E} \equiv [D_t, \mathbf{D}] \sim pK, \quad -ig\epsilon_{ijk}B_k \equiv [D_i, D_j] \sim K^2. \quad (\text{A.10})$$

One can now use these simple power counting rules to build the NRQCD Lagrangian according to

$$\mathcal{L}_{\text{NRQCD}} = \mathcal{L}_0 + \delta\mathcal{L}_K + \delta\mathcal{L}_E + \delta\mathcal{L}_B + \dots \quad (\text{A.11})$$

where  $\mathcal{L}_0$  is the Schrödinger Lagrangian

$$\mathcal{L}_0 = \psi^\dagger(x) \left( iD_t + \frac{\mathbf{D}^2}{2M} \right) \psi(x), \quad (\text{A.12})$$

which being of order  $p^4v$  is the lowest order approximation to the Dirac Lagrangian.

The additional  $\delta\mathcal{L}_i$  terms are various corrections to  $\mathcal{L}_0$  and are constructed from fields and operators, whose magnitudes were estimated above, as their building blocks. For instance, there are four bilinear operators that are dimension 4 and order  $p^4v^3$ , hence suppressed by  $v^2$  relative to the zeroth order that one could add to the Lagrangian

$$\begin{aligned} \mathcal{L}_{\text{NRQCD}} = \psi^\dagger & \left( iD_t + \frac{\mathbf{D}^2}{2M} + c_1 \frac{\mathbf{D}^4}{M^3} + c_2 \frac{g}{M^2} (\mathbf{D} \cdot \mathbf{E} - \mathbf{E} \cdot \mathbf{D}) \right. \\ & \left. + c_3 \frac{ig}{M^2} \boldsymbol{\sigma} \cdot (\mathbf{D} \times \mathbf{E} - \mathbf{E} \times \mathbf{D}) + c_4 \frac{g}{M} \boldsymbol{\sigma} \cdot \mathbf{B} + \dots \right) \psi. \end{aligned} \quad (\text{A.13})$$

The new coefficients  $c_i$  are free parameters and can be tuned by matching simulation calculations of physical quantities to their observed values.

Treating every new coupling as an input parameter, however, reduces the predictive power of the theory. Alternatively, they can be determined from perturbative calculations. These couplings affect the small distance physics. Therefore, perturbation theory is valid provided that  $a$  is small.<sup>1</sup> Consider, for example, the nonrelativistic expansion that corrects the dispersion relation

$$E = M + \frac{\mathbf{p}^2}{2M} - \frac{\mathbf{p}^4}{8M^3} + \dots \quad (\text{A.14})$$

This determines the coefficient  $c_1 = -\frac{1}{8}$  of the kinetic correction term  $\delta\mathcal{L}_K$ . More interestingly  $c_4$  is obtained from matching the scattering amplitude of a quark off of a static gluon potential. The tree level amplitude is

$$\mathcal{M}_B(\mathbf{p}, \mathbf{q}) = -\bar{u}(\mathbf{q}) \boldsymbol{\gamma} \cdot g\mathbf{A}(\mathbf{q} - \mathbf{p}) u(\mathbf{p}), \quad (\text{A.15})$$

where  $\mathbf{p}^2 = \mathbf{q}^2$  due to energy conservation and the Dirac spinor with nonrelativistic normalization  $u^\dagger u = 1$  is

$$u(\mathbf{p}) = \left( \frac{E_p + M}{2E_p} \right)^{\frac{1}{2}} \begin{bmatrix} \psi \\ \frac{\boldsymbol{\sigma} \cdot \mathbf{p}}{E_p + M} \psi \end{bmatrix}. \quad (\text{A.16})$$

Plugging it in (A.15)

$$\begin{aligned} \mathcal{M}_B(\mathbf{p}, \mathbf{q}) &= -\frac{g}{2M} \left( 1 - \frac{\mathbf{p}^2}{2M^2} \right) \psi^\dagger [(\mathbf{p} + \mathbf{q}) \cdot \mathbf{A} + i\boldsymbol{\sigma} \cdot \mathbf{A} \times (\mathbf{p} - \mathbf{q})] \psi \\ &\equiv S_B(\mathbf{p}, \mathbf{q}) + V_B(\mathbf{p}, \mathbf{q}). \end{aligned} \quad (\text{A.17})$$

---

<sup>1</sup> But not too small. NRQCD is nonrenormalizable and has UV divergences like  $g^2/aM$  which will blow up if  $aM$  is too small.

The spin independent term  $S_B$  arises from the kinetic correction in (A.13) that is linear in  $g\mathbf{A}$  while the spin dependent term  $V_B$  must be generated by additional corrections of the form

$$\delta\mathcal{L}_B = \frac{g}{2M}\psi^\dagger\boldsymbol{\sigma}\cdot\mathbf{B}\psi + \frac{g}{8M^3}\psi^\dagger\{\mathbf{D}^2, \boldsymbol{\sigma}\cdot\mathbf{B}\}\psi. \quad (\text{A.18})$$

This gives  $c_4 = \frac{1}{2}$ . The second term is of order  $p^4v^5$  and will appear with a coupling  $\frac{1}{8}$  in the next order spin dependent correction term  $\delta\mathcal{L}_{\text{spin}}$ .

The procedure outlined above demonstrates a systematic and structured approach to constructing an effective framework designed to study physical systems of a specific type that is guided by their shared characteristics. This concludes our brief but instructive discussion of NRQCD.

## Appendix B

# Gamma Matrix Algebra

$$\gamma_5 \equiv \gamma_0 \gamma_1 \gamma_2 \gamma_3. \quad (\text{B.1})$$

$$\gamma_n \equiv \prod_{\mu=0}^3 \gamma_\mu^{n_\mu}. \quad (\text{B.2})$$

- Orthonormality:

$$\text{Tr}(\gamma_n^\dagger \gamma_m) = 4\delta_{nm}. \quad (\text{B.3})$$

- Multiplication properties:

$$\gamma_n \gamma_m = (-1)^{n \cdot m^<} \gamma_{n+m}. \quad (\text{B.4})$$

$$m_\mu^< \equiv \sum_{\nu < \mu} m_\nu \pmod{2}. \quad (\text{B.5})$$

$$n \cdot m^< = n^> \cdot m. \quad (\text{B.6})$$

$$n_\mu^> \equiv \sum_{\nu > \mu} n_\nu \pmod{2}. \quad (\text{B.7})$$

$$\gamma_{nm} \equiv \gamma_n \gamma_m. \quad (\text{B.8})$$

$$m^2 = \sum_{\mu} m_\mu^2 = \sum_{\mu} m_\mu \pmod{2}. \quad (\text{B.9})$$

- Hermitian conjugate:

$$\gamma_n^\dagger = (-1)^{n \cdot n^<} \gamma_n = \gamma_n^{-1}. \quad (\text{B.10})$$

- Commutation relations:

$$\gamma_n \gamma_m = (-1)^{\bar{m} \cdot n} \gamma_m \gamma_n. \quad (\text{B.11})$$

$$\begin{aligned} \bar{m}_\mu &\equiv m_\mu^< + m_\mu^> = \sum_{\nu \neq \mu} m_\nu \pmod{2} \\ &= \begin{cases} m_\mu & \text{if } m^2 \text{ even,} \\ (m_\mu + 1) \pmod{2} & \text{if } m^2 \text{ odd.} \end{cases} \end{aligned} \quad (\text{B.12})$$

$$\bar{m} \cdot n = m \cdot \bar{n}, \quad (\text{B.13a})$$

$$\overline{\bar{m}} = m, \quad (\text{B.13b})$$

$$(\bar{m} \cdot m) = 0 \pmod{2}. \quad (\text{B.13c})$$

- Standard representation:

$$\gamma_0 = \begin{pmatrix} 1 & 0 \\ 0 & -1 \end{pmatrix}, \quad \gamma_i = \begin{pmatrix} 0 & \sigma_i \\ \sigma_i & 0 \end{pmatrix}. \quad (\text{B.14})$$

$$\sigma_1 = \begin{pmatrix} 0 & 1 \\ 1 & 0 \end{pmatrix}, \quad \sigma_2 = \begin{pmatrix} 0 & -i \\ i & 0 \end{pmatrix}, \quad \sigma_3 = \begin{pmatrix} 1 & 0 \\ 0 & -1 \end{pmatrix}. \quad (\text{B.15})$$

# Appendix C

## Fitting Details

### C.1 SVD

The covariance matrix can be quite singular due to strong correlations between the data. This makes it difficult for the fitter to invert the covariance matrix and so it often fails to converge. Non-convergent fits are diagnosed and dealt with by a standard and powerful technique known as singular value decomposition (SVD) [57]. The covariance matrix  $C$  is decomposed into a product of three matrices

$$C = U \cdot W \cdot V^T, \tag{C.1}$$

where  $U$  and  $V$  are orthogonal:<sup>1</sup>  $U^T U = V^T V = \mathbf{1}$ , and  $W$  is a diagonal matrix with positive or zero elements referred to as the *singular values*:  $\text{diag}(w_i)$ .

Given this decomposition of the covariance matrix, its inverse is trivial to compute

$$C^{-1} = V \cdot \text{diag}(1/w_i) \cdot U^T. \tag{C.2}$$

The inversion fails only if one or more of the eigenvalues  $w_i$  is zero, making  $C$  singular. This is only analytically true. In practice, it is far more common for  $C$  to be *ill-conditioned*. That is, the *condition number* of the covariance matrix, defined as the ratio of the largest of the eigenvalues  $w_i$  to the smallest, is too large for a machine with finite precision to handle.

SVD not only diagnoses the problem, it also solves it. It identifies modes with  $w_i$  smaller than machine precision, who show up in the inverse as  $1/w_i \approx \infty$ . A common solution is then to drop these eigenmodes, by setting  $1/w_i = 0$ .<sup>2</sup> They are so corrupted by roundoff errors that their contribution is useless and pulls the solution away to infinity.

---

<sup>1</sup> SVD can be applied to any  $M \times N$  matrix. So in general,  $U$  is an  $M \times N$  *column*-orthogonal matrix. SVD of any matrix is unique up to trivial permutations of elements and corresponding columns, and linear combinations of columns corresponding to identical singular values.

<sup>2</sup>This may seem paradoxical. Just because something is infinite, it doesn't necessarily mean that it's zero! This is linear algebra, not QFT, one might say. Also, it seems counter-intuitive that discarding information results in better accuracy. There's no paradox, however. By zeroing these modes we're simply preventing compounded roundoff errors.

A minimum eigenvalue is introduced by an SVD cut multiplied by the largest eigenvalue. The conventional approach of discarding singular modes is equivalent to setting the variance associated with them to infinity. We adopt a more realistic implementation where instead any eigenvalue smaller than the minimum is set equal to the minimum eigenvalue. All modes are retained and the singular modes are regulated. This method yields more accurate results.

In our implementation we actually first rescale each block-diagonal sub-matrix of the covariance matrix to obtain the *correlation* matrix, whose diagonal elements are all equal to 1. The SVD cut is applied to the correlation matrix. We then rescale it back to reconstitute a less singular covariance matrix. For simple problems with few data points and parameters an SVD cut of the order of machine precision, e.g.  $\approx 10^{-15}$  for double precision, is enough. Many-parameter fits to highly correlated and large data sets, typically require larger cuts of the order of  $\approx 10^{-3(4)}$ .

## C.2 Chained Fits

Simultaneous fits to large and complicated multi-correlator problems can take a long time. Chained fits can simplify and accelerate such fits. A multi-correlator problem is broken down into a series of successive separate single-correlator fits. Fits are done to one data set at a time and results from each step in the sequence are used as priors for the next.

Chained fits are fairly straightforward in a Bayesian framework for uncorrelated data. Recall that the Bayes' formula (5.101), essentially provides a recipe for the analysis of *independent* input information as they come in. At each stage, our knowledge is represented by the results of the latest fit in the chain through the posterior. This knowledge will then serve as the prior for the analysis of the next correlator in the sequence. In this chain, one link's posterior is the next link's prior. Bayes' theorem implies that for uncorrelated input this is equivalent to a one-step simultaneous fit to all data.

The situation is more complicated when there is correlation between correlators, as is usually the case with our Monte Carlo data. These correlations must be carefully taken into account. This requires that fit parameters from each step must be included in all subsequent steps as fit parameters even if they are not explicitly needed by the models down the line, since there might be correlations between later data and previous parameters.

Correlations are preserved at every step throughout the analysis by including the covariance matrix between the best-fit parameters from the previous fit and the data for the next, as well as the parameter-parameter covariance matrix for the best-fit parameters returned by the previous fit. These account for possible prior-data and prior-prior correlations respectively. This is of course in addition to the data-data covariance matrix (5.98). Recall that in a Bayesian approach priors are effectively treated like data. So this is simply equivalent to consistently tracking correlations between *all data*; that is, new data (correlators) as well as what we've learned from old data (priors).

It is essential to include correlations between the data sets in chained fits. Authors of [60] demonstrate marked improvement in the accuracy of results when taking them into account. Chained fits are equivalent to simultaneous fits in the limit of large statistics (Gaussian), and the order of data sets in the sequence does not matter. For data sets with larger errors,



it is better to start with more accurate data. The total  $\chi^2$  is equal to the sum of individual  $\chi^2$ s from each step.

We will employ this technique throughout this work and will show examples of chained fits compared with simultaneous fits in later chapters. For more details on chained fits such as computing the relevant covariance matrices see [60, Appendix A].

### C.3 Marginalized Fits

So far in this section we've seen that one is forced to include several excited states when fitting multi-exponential models to hadronic correlators. But we're rarely interested in the excited states even though they are needed for good fits. The necessary presence of these “nuisance parameters” makes fits extremely slow and complicated, especially for large data sets consisting of several correlators.

We've also learned that these fits are doomed to fail without priors. The following describes how priors can also be used to accelerate and simplify such fits. The contributions of the excited states are removed from the data *before* fitting [59]. In other words, the nuisance parameters are *marginalized* or integrated out of Bayes pdfs.<sup>3</sup>

Again, the idea is straightforward in a Bayesian framework. There are two types of data that go into the fit, each with its own uncertainties: Monte Carlo data from simulation and priors. They are combined in the  $\chi^2_{\text{aug}}$  before minimizing, contributing  $\chi^2_{\text{MC}}$  and  $\chi^2_{\text{pr}}$  given by (5.96) and (5.109) respectively. The trick is how the priors are introduced.

They can be used to obtain *a priori* estimates for the correlators

$$G^{\text{pr}}(t; N) \equiv \sum_{i=0}^{N-1} \tilde{a}_i \tilde{b}_i e^{-\tilde{E}_i t}, \quad (\text{C.3})$$

where  $\tilde{a}_i$  and  $\tilde{b}_i$  are the prior means for the overlaps between the interpolating operators at the source and the sink, and  $\tilde{E}_i$  are for hadronic masses. The means and the covariance matrix of  $G^{\text{pr}}(t; N)$  are obtained from the prior means and variances through standard error propagation.

The key is now to use this estimate to explicitly remove the contributions of the excited states from the correlators. The *priors* are thus incorporated into the Monte Carlo data by subtracting from correlators our *a priori* estimate of the large- $i$  terms *prior* to fitting (the “difference” method)

$$\tilde{G}^{\text{MC}}(t; n) \equiv G^{\text{MC}}(t) - \Delta G^{\text{pr}}(t; n), \quad (\text{C.4})$$

where

$$\Delta G^{\text{pr}}(t; n) \equiv G^{\text{pr}}(t; N) - G^{\text{pr}}(t; n) = \sum_{i=n}^{N-1} \tilde{a}_i \tilde{b}_i e^{-\tilde{E}_i t}. \quad (\text{C.5})$$

---

<sup>3</sup> Using the *marginalization* rules of probability, for uncorrelated parameters we have

$$\mathcal{P}(\lambda | G) = \int \mathcal{P}(\lambda, \Lambda | G) d\Lambda \propto \mathcal{P}(\lambda) \int \mathcal{P}(G, \Lambda | \lambda) d\Lambda,$$

where  $\lambda$  and  $\Lambda$  stand for parameters corresponding to the first few terms and excited states respectively.

The covariance matrix of the modified data  $\tilde{G}^{\text{pr}}$  is also obtained from that of the original data combined with covariances of the priors through error propagation. That is, errors are added in quadrature in (C.4).

Having taken out large- $i$  excited states ( $n < i < N$ ), the modified data is then fitted with an  $n$ -term model, thereby replacing a difficult fit by a much simpler one. This is an approximation to the original fit. Though, they become equivalent in the high-statistics (Gaussian) limit. A proof is shown in [82, Appendix]. In other words, they are equivalent only insofar as the relevant probability distributions can be approximated by a Gaussian.

The rapid exponential drop of the correlators makes this approximation less good quite fast. As a result, small values of  $n$  may not work very well. This suggests an alternative marginalization scheme where one modifies the log of the data instead

$$\log \tilde{G}^{\text{MC}}(t; n) \equiv \log G^{\text{MC}}(t) - \Delta \log G^{\text{pr}}(t; n), \quad (\text{C.6})$$

where

$$\Delta \log G^{\text{pr}}(t; n) \equiv \log G^{\text{pr}}(t; N) - \log G^{\text{pr}}(t; n). \quad (\text{C.7})$$

Equivalently, the data is modified as follows (the “ratio” method)

$$\tilde{G}^{\text{MC}}(t; n) \equiv G^{\text{MC}}(t) \frac{G^{\text{pr}}(t; n)}{G^{\text{pr}}(t; N)}. \quad (\text{C.8})$$

Remarkably, as demonstrated in [59], marginalization works very well with a quite small  $n$ . The ratio method is also shown to require fewer terms retained than is needed by the difference method. The final results from either method agree with one another, as well as with those obtained from a standard fit, while the fits become 10–40 times faster.

The total number of terms  $N$  is chosen so that the size of  $j > N$  terms is negligible compared with the statistical errors. This also ensures that  $G(t; n)$  is independent of  $N$ . We normally start with 1 term and keep adding more until the fit results, their uncertainties and the  $\chi^2$  stop changing. Best-fit results from each step are used as the initial guess for the next, in order to further speed up the fit. Increasing the number of exponentials until convergence is reached is a standard technique commonly referred to as *sequential* fits, which is not to be confused with *chained* fits.

We will extensively employ this strategy to accelerate large multi-exponential fits to multiple correlators throughout this work. Examples will be shown to illustrate its agreement with standard analyses.

# Index

- $a$ , 13
- action
  - asqtad, 39
  - clover (Sheikholeslami-Wohlert), 35, 158
  - continuum, 12
  - Fermilab, 158
  - fermion, 20
  - HQET, 157, 158
  - Lüscher-Weisz, 18
  - naive, 24
  - NRQCD, 158
  - OK, 158
  - staggered, 38
  - Wilson fermions, 32
  - Wilson gluons, 17
- Aharonov-Bohm, 91
- $\alpha_0$ , 18
- $\alpha_\mu(x)$ , 36
- $\alpha_{\text{QED}}$ , 110
- $\alpha_s$ , 5, 14
- $a^2$  errors, 38
- asqtad, 39, 42, 43, 126
- asymptotic freedom, 5, 14
- autocorrelation, 81
- axial
  - correlator, 124
  - current, 116
- axis interchange symmetry, 158
  
- Bayes integrals, 103
- Bayes theorem, 97
- Bayesian fitting, 97
- bootstrap, 104
- Brillouin zone, 25, 41
  
- $c$  (speed of light), 44
- central limit theorem, 21, 84
- CG, *see* conjugate gradient
- chained, 129
- chained fits, 165
  
- charge form factor, 4
- charge radius, 105
- chiral symmetry, 110, 116
- $\chi^2$ , 94
  - augmented, 99
  - prior, 98
  - regularization, 96
- chromomagnetic fields, 159
- Clebsch-Gordon, 4
- Clifford algebra, 24
- clover, 158
- $C_{\mu\nu\rho}$ , 18
- comparator, 16
- condition number, 72, *see* SVD
- configuration, 21
- confinement, 5
- conjugate gradient, 72
- constrained curve fitting, *see* Bayesian fitting
- contour, 86
- correlation matrix, *see* SVD
- corrfitter, 93
- Coulomb gauge, 159
- coupling
  - photon, 109
  - pion, 116
- covariance matrix, 94
- covariant derivative, 16
- $c_{\text{SW}}$ , 35
- current
  - axial-vector, 116
  - electromagnetic, 110
  - insertion, 114
  - vector, 110
  
- Dirac matrices, 24
- dispersion relation, 44
- doubling, 8, 26
- dynamical quarks, 7
  
- $e$ , 2, 110

electric form factor, 105  
 electromagnetic  
     coupling, 110  
     current, 110  
     matrix element, 110  
 Elitzur's theorem, 83  
 $\epsilon$ , 44  
 $\epsilon_{\mu\nu\rho\sigma}$ , 110  
 error budget, 104  
 Euclidean space, 13, 23  
 even-odd preconditioning, 72  
  
 fat links, 42  
 fat7, 42  
 Fermilab, 158  
 fermion matrix, 20  
 finite difference, 13  
 FNAL, 81  
 form factor, 4  
     axial-vector current, 120  
     vector current, 111  
 Fortran, 81  
 free field, 75  
 functional democracy, 13  
  
 $G$ -parity, 123  
 $\gamma_5$  hermiticity, 59  
 $\gamma_n$ , 53  
 $g_{D^*D\gamma}$ , 109  
 $g_{D^*D\pi}$ , 116  
 Goldberger-Treiman, 122  
 Goldstone, 39, 116, 126  
 Grassmann variables, 20  
  
 heavyonium, 158  
 HISQ, 1, 40, 47  
 HQET, 157, 158  
 hypercube, 35  
 hyperfine splitting, 51  
  
 ignorance blob, 111  
 ill-conditioned, *see* SVD  
 interpolating operator, 73, 112  
 irrelevant operators, 15  
 isospin, 4, 109, 116, 142  
     Clebsch-Gordon, 116  
  
 $J_\mu^{\text{em}}$ , 110  
  
 $K$ , 159  
 kinetic mass, 45  
 Kogut-Susskind, *see* staggered quarks, 35  
  
 Lüscher-Weisz, 18  
 $\Lambda_{\text{QCD}}$ , 5  
 Laplace approximation, 104  
 least squares, 94  
 Lepage, 19  
 Lepage term, 42, 43  
 Levi-Civita tensor, 110  
 link, 15  
 lsqfit, 93  
 LSZ, *see* reduction formula  
  
 M1 transition, 3, 110  
 Mackenzie, 19  
 magnetic dipole transition, 3, 110  
 marginalized, 129  
 marginalized fits, 166  
     difference, 166  
     ratio, 167  
 matching factor, 110  
 matrix element  
     axial, 116, 120  
     electromagnetic, 110  
     scattering, 119  
 maximum likelihood, 94–96  
 mean link, 19  
 meson form factor, 105  
 Metropolis algorithm, 22  
 MILC, 22, 81  
 Minkowski space, 23  
 Monte Carlo, 21  
 MPI, 81  
  
 Naik, 40  
     coefficient, *see*  $\epsilon$   
 naive basis, 112  
 naive fermions, 24  
 non-perturbative, 119  
 nonrelativistic expansion, *see* NRQCD  
 normal distribution, 83  
 NRQCD, 158  
 nuisance parameters, 96, 166  
  
 OK, 158  
 $\Omega(x)$ , 36

operator selection, 112, 124  
opposite parity states, *see* oscillating states  
oscillating states, 30, 65  
over-fitting, 96  
overlap, 73  
  
 $\mathcal{P}$  (path ordering), 15  
parallel transporter, 16  
partial errors, 104  
partially conserved axial current, *see* PCAC  
partition function, 20  
path integral, 13  
path ordering, 15  
PCAC, 117, 119  
pdf, 83, 97  
periodic boundary conditions, 90  
photon  
    coupling, 109  
    intrinsic parity, 110  
pion  
    coupling, 116  
    decay constant, 117  
    Goldstone boson, 117  
    reduction, 119  
plaquette, 17  
 $P_{\mu\nu}$ , 17  
point-split, 60, 113  
pole mass, *see* rest mass  
polography, 123  
polology, 118  
posterior, 97  
power counting rules, 158  
preconditioning, 72  
priors, 98  
probability distribution, 21  
probability distribution function, *see* pdf  
product distribution, 83, 86  
  
 $\mathcal{Q}$ , 2, 110  
quarkonium, 158  
quenched, 7, 22  
  
 $r$  (Wilson parameter), 32  
radiative transition  
    form factor, 111  
random wall source, 82, 115  
reduction formula, 119, 122  
redundant operators, 33  
renormalization, 119  
rest mass, 45  
reunitarization, 47  
 $R_{\mu\nu}$ , 18  
  
Schrödinger Lagrangian, 160  
sea quarks, *see* dynamical quarks  
sequential fits, 167  
sequential source, 88  
Sheikholeslami-Wohlert, 35  
singular value decomposition, *see* SVD  
sink, 114  
 $S$ -matrix, 119  
smearing, 39, 41  
source, 71, 114  
spin diagonalization, 36  
spin-taste, 113  
spinor basis, 36  
spontaneous breaking of symmetry, 116  
staggered, 35  
staggered basis, 37  
staggered quarks, 8  
staple, 42  
SVD, 129, 164  
    correlation matrix, 165  
    covariance matrix, 164  
Symanzik improvement, 9  
Symanzik improvements, 14  
  
tadpole factor, 19  
tadpole improvement, 19, 43  
taste, 8, 26  
    exchange, 39  
    meson, 61  
    selection rules, 61, 112, 124  
    signature, 61, 112  
    splitting, 39, 51  
twisted boundary conditions, 90–93, 113, 125  
    partially, 93  
twisting angle, 113  
  
 $u_0$ , 19  
 $U_\mu$ , 15  
UV cutoff, 13  
  
 $v$ , 159  
vacuum polarization, 7  
variance, 21

vector current, 110  
 $\mathcal{V}_\mu$ , 110  
 $V(q^2)$ , 111

Ward identity, 16, 78  
Wick contraction, 74  
Wilson, 15  
    action  
        gluons, 17  
        line, 16  
        loop, 17  
Wilson fermions, 32

$\mathcal{Z}$ , 77  
 $Z$  (matching factor), 110  
 $Z$  (wavefunction renormalization), 119  
 $\mathbb{Z}_2$ , 41  
 $\zeta$ , 41